ABSTRACT

Title of Dissertation: MEASUREMENT AND SIMULATION OF SUPPRESSION EFFECTS IN A BUOYANT TURBULENT LINE FIRE

James Patrick White, Doctor of Philosophy, 2016

Dissertation directed by: Associate Professor, Peter B. Sunderland
Department of Fire Protection Engineering

An experimental and numerical study of turbulent fire suppression is presented. For this work, a novel and canonical facility has been developed, featuring a buoyant, turbulent, methane or propane-fueled diffusion flame suppressed via either nitrogen dilution of the oxidizer or application of a fine water mist. Flames are stabilized on a slot burner surrounded by a co-flowing oxidizer, which allows controlled delivery of either suppressant to achieve a range of conditions from complete combustion through partial and total flame quenching. A minimal supply of pure oxygen is optionally applied along the burner to provide a strengthened flame base that resists liftoff extinction and permits the study of substantially weakened turbulent flames. The carefully designed facility features well-characterized inlet and boundary conditions that are especially amenable to numerical simulation.

Non-intrusive diagnostics provide detailed measurements of suppression behavior, yielding insight into the governing suppression processes, and aiding the development and validation of advanced suppression models. Diagnostics include oxidizer composition analysis to determine suppression potential, flame imaging to quantify visible flame structure, luminous and radiative emissions measurements to assess sooting propensity and heat losses, and species-based calorimetry to evaluate global heat release and combustion efficiency. The studied flames experience notable suppression effects, including transition in color from bright yellow to dim blue, expansion in flame height and structural intermittency, and reduction in radiative heat emissions. Still, measurements indicate that the combustion efficiency remains close to unity, and only near the extinction limit do the flames experience an abrupt transition from nearly complete combustion to total extinguishment.

Measurements are compared with large eddy simulation results obtained using the Fire Dynamics Simulator, an open-source computational fluid dynamics software package. Comparisons of experimental and simulated results are used to evaluate the performance of available models in predicting fire suppression. Simulations in the present configuration highlight the issue of spurious reignition that is permitted by the classical eddy-dissipation concept for modeling turbulent combustion. To address this issue, simple treatments to prevent spurious reignition are developed and implemented. Simulations incorporating these treatments are shown to produce excellent agreement with the experimentally measured data, including the global combustion efficiency.

MEASUREMENT AND SIMULATION OF SUPPRESSION EFFECTS IN A BUOYANT TURBULENT LINE FIRE

by

James Patrick White

Dissertation submitted to the Faculty of the Graduate School of the
University of Maryland, College Park in partial fulfillment
of the requirements for the degree of
Doctor of Philosophy
2016

Advisory Committee:
Professor Peter Sunderland, Chair
Professor Christopher Cadou
Professor Marino diMarzo
Professor André Marshall
Professor Arnaud Trouvé

Acknowledgments

This project has been supported through a joint collaboration between the Department of Fire Protection Engineering at the University of Maryland, FM Global Research Division, and United Technologies Research Center, sponsored by the United States National Science Foundation (NSF GOALI Award #1236788). In addition to the material support provided by these organizations, thanks are owed to Joshua Sheffel, Vaidya Sankaran, May Corn, and Med Colket at UTRC; as well as Ning Ren, Bert Yu, and Yi Wang at FM Global. These individuals have provided countless hours of support and advisement throughout the minutia that make up the contributions of this work.

Foremost thanks are owed to the candidate's co-advisors: Peter Sunderland, Arnaud Trouvé, and André Marshall. Without their tireless support, the present work would simply not have been possible. Each of them has provided unique and essential advisement to the candidate throughout the course of this project. To Peter, for his confidence and trust in the candidate's abilities, his adherence to simplicity and practicality, and for the unique perspectives that he offers to challenging problems; to Arnaud, for his impressive expertise in computational fluid dynamics and numerical methods, for his timeliness and organization, his pragmatism, and for his attentiveness to detail; and to André, for his fearless ideas, his willingness to spend as much time as necessary to find clarity and insight in every situation no matter the complexity, and for his contagious motivation to grow the scope of the work to reach new-found broader impact; many heartfelt thanks.

Special thanks go to Eric Link, whose significant contributions to this project cannot be overstated. His ideas, insight, and effort lie within every aspect of the present work, with particular emphasis in the design and construction of the experimental apparatus, the recording of measurement data, and the development of the image-processing techniques utilized in the flame height and radiative emissions diagnostics. Special thanks are also owed to Sébastien Vilfayeau for his engaged interest in the quality of the experiment and for his leading role in defining and advising the scope of the simulations.

Further thanks are owed to Tim Western, for his assistance in the design, development, and construction of the calorimetry infrastructure necessary for completion of this project. Without his contributions, many of the measurements and analyses derived in this work would not have been possible. Additional thanks go to Vivien Lecoustre, for his expertise in spectral radiation and the RadCal numerical solver, and to Taylor Myers and Stephen Jordan for many inspiring discussions related to their work on the characterization of fire suppression sprays.

Special thanks in particular are owed to Randall McDermott for his specialized expertise, advisement, and support in all simulation-related work. His criticism and praise have greatly motivated the quality of the candidate's computational endeavors. His direct involvement has led to the development and implementation of the reignition models utilized in the present simulations. Without his generous dedication to the success of these efforts, the numerical contributions of this work would be significantly diminished. Special thanks also go to Marcos Chaos for founding and inspiring the multipoint radiation source model developed in the present work.

Additional thanks go to Christopher Cadou for his service on the candidate's committee and for permitting the use of the infrared camera used in the experiments. Further thanks go to Marino diMarzo, also for his service on the candidate's committee, but additionally for his longstanding support dating back to his role as the candidate's MS advisor.

Further thanks go to the faculty, staff, and students of the Department of Fire Protection Engineering: to James Milke, Stanislav Stoliarov, and Michael Gollner, for their continuous support of the candidate's academic pursuits; to Sharon Hodgson, Mary Lou Holt, Nicole Hollywood, and Pat Baker, for all of their work behind the scenes that has supported the candidate throughout his undergraduate and graduate careers; to Isaac Leventon, Mark McKinnon, Xuan Liu, Paul Anderson, Colin Miller, Wei Tang, Ajay Singh, and Fernando Raffan, for their shared time and experiences over past years; and to Elizabeth Keller and Devin Müller, whose immediate future efforts will continue the legacy of this work.

Final thanks go to the candidate's family: to his partner Katlyn, his mother Pollyanna, his father Bernard, and his brother Bernard, for their nurturing support and encouragement through all of the candidate's personal and professional trials.

Table of Contents

List of Tables

List of Figures

Nomenclature

Acronyms

AC	alternating current
CDG	carbon-dioxide-generation
CFD	computational fluid dynamics
CPU	central processing unit
DAQ	data acquisition
EDC	eddy-dissipation concept
FDS	Fire Dynamics Simulator
LES	large eddy simulation
LOI	limiting oxygen index
MEC	minimum extinguishing concentration
MPI	message passing interface
ND	neutral density
OC	oxygen-consumption
RH	relative humidity
RTE	radiative transfer equation
TLB	turbulent line burner
UHC	unburned hydrocarbons

Symbols, Roman

A	area	(m^2)
B	Planck distribution	$(\mathrm{W\,m^{-1}\,sr^{-1}})$
c_0	speed of light (in vacuum)	$(\mathrm{m\,s^{-1}})$
c_p	heat capacity (at constant pressure)	$(\mathrm{J\,kg^{-1}\,K^{-1}})$
C_d	drag coefficient	(-)
C_f	flow coefficient	(-)
C_u	model coefficient	(-)
C_v	model coefficient	(-)
d	diameter	(m)
d	differential operator	(-)
D	characteristic length scale	(m)
fn	functional relationship	(-)
F	weighting factor	(-)
g	gravitational acceleration constant	$(\mathrm{m\,s^{-2}})$
Gr	fire-source Grashof number	(-)
h	mass-specific sensible enthalpy	$(\mathrm{J\,kg^{-1}})$
h_P	Planck constant	$(\mathrm{J\,s})$
I	grayscale pixel intensity	(-)

I	radiative intensity	$(\mathrm{W\,m^{-2}\,sr^{-1}})$
k	mass-specific kinetic energy	$(\mathrm{m^2\,s^{-2}})$
k_B	Boltzmann constant	$(\mathrm{J\,K^{-1}})$
L	length	(m)
L^*	characteristic length scale	(m)
LR	flame luminosity ratio	(-)
m	mass	(kg)
$\dot{m}$	mass flow rate	$(\mathrm{kg\,s^{-1}})$
$\dot{m}'''$	volumetric mass reaction rate	$(\mathrm{kg\,s^{-1}\,m^{-3}})$
M	molar mass	$(\mathrm{kg\,mol^{-1}})$
M	turbulence resolution criterion	(-)
n	counting variable	(-)
N	flame height scaling parameter	(-)
N	sample size	(-)
N_θ	number of polar bands	(-)
N_ϕ	number of azimuthal bands	(-)
N_Ω	total solid angles	(-)
p	perturbation pressure	(Pa)
P	pressure	(Pa)
Pr	Prandtl number	(-)
$\dot{q}''$	heat flux	$(\mathrm{W\,m^{-2}})$
$\dot{Q}$	heat release rate	(W)
$\dot{Q}'$	heat release rate per-unit-length	$(\mathrm{W\,m^{-1}})$
$\dot{Q}'''$	volumetric heat release rate	$(\mathrm{W\,m^{-3}})$
$\dot{Q}^*$	fire-source Froude number	(-)
r	radial position	(m)
R	ideal gas constant	$(\mathrm{J\,mol^{-1}\,K^{-1}})$
Re	Reynolds number	(-)
s	stoichiometric oxidizer-to-fuel mass ratio	$(\mathrm{kg\,kg^{-1}})$
s_{O_2}	stoichiometric oxygen-to-fuel mass ratio	$(\mathrm{kg\,kg^{-1}})$
S	separation distance	(m)
Sc	Schmidt number	(-)
t	time	(s)
T	temperature	(K)
u	velocity magnitude, x-component	$(\mathrm{m\,s^{-1}})$
v	velocity magnitude, y-component	$(\mathrm{m\,s^{-1}})$
V	volume	$(\mathrm{m^3})$
$\dot{V}$	volumetric flow rate	$(\mathrm{m^3\,s^{-1}})$
w	velocity magnitude, z-component	$(\mathrm{m\,s^{-1}})$
W	width	(m)
x	position, x-coordinate	(m)
x	C atoms in arbitrary fuel molecule	(-)
X	mole fraction	$(\mathrm{mol\,mol^{-1}})$
y	position, y-coordinate	(m)

y	net combustion yield	$(\mathrm{kg\,kg^{-1}})$
y	H atoms in arbitrary fuel molecule	(-)
Y	mass fraction	$(\mathrm{kg\,kg^{-1}})$
$\hat{Y}$	reaction-mixture mass fraction	$(\mathrm{kg\,kg^{-1}})$
z	position, z-coordinate	(m)
z	O atoms in arbitrary fuel molecule	(-)

Symbols, Greek

α	flame height coefficient	$(\mathrm{m^{5/3}\,W^{-2/3}})$
α	absorptivity	(-)
β	thermal expansion coefficient	$(\mathrm{K^{-1}})$
β	spectral band-overlap parameter	(-)
Δ	LES filter width	(m)
Δh	mass-specific enthalpy differential	$(\mathrm{J\,kg^{-1}})$
Δh_f°	mass-specific standard enthalpy of formation	$(\mathrm{J\,kg^{-1}})$
$\Delta \bar{h}_f^\circ$	mole-specific standard enthalpy of formation	$(\mathrm{J\,mol^{-1}})$
ΔH	enthalpy differential	(J)
ΔP	pressure differential	(Pa)
ΔQ	heat differential	(J)
ΔT	temperature differential	(K)
Δx	numerical grid resolution, x-coordinate	(m)
Δy	numerical grid resolution, y-coordinate	(m)
Δz	numerical grid resolution, z-coordinate	(m)
$\Delta\Omega$	numerical angular space resolution	(sr)
ε	emissivity	(-)
ζ	source model ratio	(-)
η	efficiency	(-)
θ	angular position (polar)	(rad)
κ	absorption coefficient	$(\mathrm{m^{-1}\,Pa^{-1}})$
κ_E	effective absorption coefficient	$(\mathrm{m^{-1}})$
κ_P	Planck mean absorption coefficient	$(\mathrm{m^{-1}})$
λ	wavelength	(m)
μ	dynamic viscosity	$(\mathrm{kg\,m^{-1}\,s^{-1}})$
ν	kinematic viscosity	$(\mathrm{m^2\,s^{-1}})$
ν	molar reaction coefficient	$(\mathrm{mol\,mol^{-1}})$
ρ	mass density	$(\mathrm{kg\,m^{-3}})$
σ	Stefan-Boltzmann constant	$(\mathrm{W\,m^{-2}\,K^{-4}})$
τ	transmissivity	(-)
τ	time-averaging window	(s)
τ_{mix}	characteristic mixing time scale	(s)
ϕ	angular position (azimuthal)	(rad)
χ	heat-loss fraction	(-)
ω	wavenumber	$(\mathrm{m^{-1}})$

Subscripts / Superscripts

∞	ambient property
a	ambient entrainment
A	analyzer-measured
b	burner
B	blackbody
$comb$	combustion
$conv$	convective
$crit$	critical value
e	exhaust
ext	extinction
f	flame
fr	frame
$fuel$	fuel
g	gauge/transducer
ign	ignition
i	indexing variable
j	indexing variable
k	indexing variable
l	layer
m	water-mist
max	maximum
min	minimum
n	indexing variable
na	non-anchored
ox	oxidizer
pr	products
rad	radiative
rms	root-mean-square
rmv	removed
rxn	reaction
s	solid
sat	saturated/saturation
sgs	subgrid-scale
st	stoichiometric
sum	summation
t	turbulent
tc	thermocouple
$term$	terminal
vap	vaporization/evaporation
ω	spectral quantity

Chapter 1: Introduction

1.1 Motivation

Fire suppression systems are ubiquitous throughout the built environment as a means of protecting life and property from fire hazards. Despite their prevalence and reliability, there remains a limited understanding of the phenomena governing the performance of these systems. While the primary mechanisms of flame suppression are known, including thermal, aerodynamic, and kinetic quenching, detailed insight into how these mechanisms dictate fire behavior, for conditions ranging from complete combustion to total extinguishment, has yet to be attained.

The physical processes that govern fire suppression represent complex coupled phenomena that are worthy of exploration, including turbulence, multiphase thermodynamics, and intricate combustion chemistry. The complexity of these processes lends to the limited understanding of fire suppression behaviors, a profound result of which is the present absence of an established analytical framework for predicting suppression performance.

Without an analytical framework for performance-based design, the design process for fire suppression systems is mostly relegated to a prescriptive code-based approach [1–3]. By this methodology, systems are designed not based on their pre-

dicted performance relative to the application of interest, but rather are based on the results of qualification tests for representative configurations and hazards which are then extrapolated to the application of interest. This approach is grounded in empiricism and significantly limits the opportunity for design innovation. Furthermore, such prescriptive design guidelines become unclear for applications that deviate from previous design experience.

In recent years, design efforts in the fire protection engineering discipline have migrated away from prescriptive code-based approaches toward more performance-based methods. Performance-based methods are advantageous in that they potentially offer both cost savings and improvement in design performance by permitting engineers to develop systems based on specific design objectives. Certainly, in cases where design requirements differ significantly from the domain of the prescriptive codes, performance-based methods provide the only available solution. Unfortunately, due to the aforementioned absence of an established analytical framework for predicting suppression performance, performance-based design methods for fire suppression systems are currently limited to scaled or full-scale experiments, which are often prohibitively costly or time consuming for design applications, while offering limited insight into the true performance of the design.

An attractive alternative to the use of full-scale experiments for performance-based design is the use of computational fluid dynamics (CFD) fire modeling tools. While there are several open-source CFD packages available for fire modeling applications [4–6], current suppression models are largely incapable of accurately resolving or predicting fire response to modern suppression technologies. The limitations

of these models are largely due to the aforementioned complexity of the processes that govern suppression performance, particularly turbulence-induced separation of scales and intricate reaction chemistry. Another key factor contributing to the lack of advancement in current suppression models is the unavailability of experimental data for model validation. Though there have been numerous previous studies exploring the extinction behavior of flames (see Sec. 1.2), none has provided the detailed, comprehensive extinction measurements required for model validation.

Were a detailed understanding of fire suppression available, such knowledge could be applied toward the development of advanced suppression models that would ideally capture the essential global suppression behaviors without requiring the prohibitively costly resolution of the underlying turbulence and chemical processes. Implementation of such models as design tools would then require their validation against detailed experimental measurements. Appropriate measurements should capture variations in suppression behavior in a well-characterized configuration that may be easily represented in the numerical models, but also contains sufficient complexity for relation to realistic fire scenarios.

Following this insight, the primary motivations for the present work include the pursuit of an improved understanding of fire suppression phenomena in a context that facilitates the development of advanced suppression models, while concurrently developing an experimental database suitable for model validation. These motivations represent the obvious next steps toward realizing a truly performance-based approach for the design of fire suppression systems.

1.2 Review

The existing literature of fire research provides an established foundation for the investigation of suppression phenomena. Recent anthological works [7–9] provide useful summaries of the current fire suppression knowledgebase, identifying the principal mechanisms of suppression. These mechanisms include thermal quenching, whereby the flame is weakened due to heat losses; aerodynamic quenching, whereby the flame is weakened due to flow-induced perturbations in the fuel-oxidizer mixing rate; and kinetic quenching, whereby the flame is weakened due to interactions with chemically active agents. Numerous experimental and numerical studies have investigated the relative importance of these mechanisms in various applications [10–17].

Most experimental studies of diluent-based suppression utilize small-scale laminar flames [18–29]. These works have been particularly useful in exploring extinction theory, as well as establishing critical extinguishing limits for many fuels. Many of these studies utilize the cup-burner configuration, featuring small laminar flames immersed in a diluted co-flowing oxidizer [30]. Extinguishment for this configuration is observed primarily as flame detachment and liftoff from the burner, mainly due to weakening of the edge reaction kernel responsible for flame stabilization [31–35]. This type of suppression is believed to be more characteristic of partially-premixed flames, than of the diffusion flames encountered in typical fire applications. It is then questionable whether liftoff extinguishment relates to the suppression of larger-scale turbulent flames, where suppression is believed to result from progressive localized extinction throughout the main combustion region [36–46].

Many studies of water-mist suppression [47–53] have focused on variations in performance with spray characteristics, most of which reveal a non-monotonic variation in performance with droplet size. This behavior is due to evaporation, where small droplets evaporate before reaching the flame, while large droplets with high terminal velocities pass through the flame too quickly to evaporate. Maximum performance is noted for droplets that evaporate close to the flame, enhancing flame cooling. Unfortunately, any such findings are configuration dependent, where many studies offering conclusions of an ideal droplet size are of questionable value for general applications. Other studies have suggested that the more appropriate parameter to gauge mist performance is the mass fraction of droplets in the entrained flow [54–56]. Recent works have also investigated water-based suppression effects in large-scale fires of realistic configuration, primarily to evaluate suppression performance in specific scenarios [57–60]. Others have focused on developing scaling relationships to compare results from different sized configurations [61, 62].

Regarding the numerical modeling of fire suppression, several recent works have made progress in the development of simple formulations to model flame extinction in cases applicable to realistic fire scenarios [63–67]. Additional studies have highlighted the primary features of flame reignition events, which may follow localized extinction in large-scale turbulent flames [67–73]. As noted in these works, the primary difficulty associated with modeling flame extinction and reignition in fire applications is that both phenomena are controlled by small-scale quantities that are typically unresolved in the simulations, including the flame temperature and the fuel-oxidizer mixing rate at the flame sheet.

Despite the progress previous works have made toward an improved understanding of fire suppression processes, a number of questions remain unanswered and several areas require further research. Most previous studies, both experimental and numerical, are limited to simplistic configurations for which conclusions may not extrapolate to more realistic conditions. Experimental studies in particular are mostly limited to laminar flames and lack the integral measurements necessary for insight into model development. Unlike laminar flames, turbulent flames offer additional features including more intense radiative emissions, structural non-uniformity, flame-flame interactions, and a greater dynamic range of the dominant physical scales. It has not yet been demonstrated how or whether these features affect flame suppression behavior. Studies that have employed large-scale realistic configurations with turbulent fires often lack the detailed characterization and controlled conditions necessary for usefulness in fire modeling applications.

The fundamental fire suppression mechanisms have been established and suppression studies, both experimental and numerical, have been conducted over a range of scales and configurations. Visibly absent, however, are studies employing a well-characterized canonical configuration containing both the complexity required for relation to actual fire scenarios (turbulence, non-liftoff extinction) and the detailed diagnostics required for CFD model development and validation (integral measurements of suppression performance). In addition, most previous works have limited their focus to the extinction limit, which while critical, provides limited insight into how the noted suppression mechanisms dictate flame behaviors for conditions ranging from complete combustion through partial and total extinguishment.

1.3 Objective

The present research seeks to fill the void in the current understanding of the complex physical phenomena that govern fire suppression. This research features detailed experimental and numerical modeling efforts, focusing on the suppression of turbulent flames via nitrogen dilution of the oxidizer, but including a development of capability for future studies investigating suppression via fine water mist. Of specific interest in this study are observations and measurements of flame behaviors and suppression performance for variable suppressant-loading conditions from extinction-free through partial and total flame quenching.

Experimental efforts for the present work include the development of a canonical laboratory-scale facility for the observation and measurement of fire suppression phenomena applicable to realistic fire scenarios, and that provides well-characterized inlet and boundary conditions suitable for application to CFD fire simulations. Within this configuration, non-intrusive integral diagnostics measure the flame-suppressant interactions and suppression performance metrics of interest. With feedback from parallel numerical efforts, the experimental configuration and selected diagnostics are designed to provide a detailed dataset suitable to support the development and validation of predictive fire suppression models.

Numerical efforts focus on the evaluation and improvement of capability for current CFD fire modeling tools to accurately predict suppression behavior. To this end, the results of numerical simulations tailored to the designed configuration are compared with the measured experimental data. Based on these comparisons, the

proficiencies and limitations of the suppression models are assessed and recommendations for improvement are identified and implemented.

The primary deliverables for the present work include (1) the development of a well-characterized experimental facility for present and future studies of turbulent fire suppression phenomena; (2) the development of multiple non-intrusive integral diagnostics to provide insightful measurements of flame-suppressant interactions and global suppression performance; (3) the provision of a database of measurements, made available to the general fire modeling community and suitable to support the development and validation of advanced fire suppression models; (4) the analysis of high-fidelity CFD simulations to evaluate current suppression modeling capabilities via comparisons with the measured data; (5) the development and implementation of model improvements to bolster the accuracy and predictive capability of current fire suppression models; and (6) the dissemination of these and other results of interest through scientific journal publications and conference proceedings.

The long-term goal to which the present work aims is the successful realization of performance-based design methods for fire suppression systems. The achievement of this objective would equip fire protection engineers with analytical design tools based on a fundamental understanding of suppression phenomena. These tools would provide a framework for evaluating suppression performance as a function of design input, enhancing design efficiency for standard applications while permitting the design of innovative solutions for exotic applications. The hopeful broader impact of this would be the development of more cost-effective fire suppression technologies while promoting improved life safety and infrastructure protection from fire.

Chapter 2: Experiment

2.1 Overview

The primary objective for the experiment is the observation and measurement of flame behaviors and suppression effects across varying suppressant-loading conditions from extinction-free through partial and total flame quenching. The selected experimental configuration facilitates isolation of suppression effects, while producing flames with sufficient complexity for applicability to realistic fire scenarios. The careful design of the configuration also provides controlled and well-characterized inlet and boundary conditions, which are easily applied within CFD simulations.

The present facility features a slot burner flowing gaseous fuels to provide a low-strain, buoyant, turbulent diffusion flame in a canonical line-fire configuration. This burner permits well-controlled inlet conditions for the fuel stream, while introducing the complicating effects of buoyancy and turbulence characteristic of realistic large-scale fires. The selected two-dimensional line-fire configuration is also especially amenable to a variety of non-intrusive diagnostics suitable for the study of fundamental flame suppression phenomena. The burner is surrounded by a co-flowing oxidizer stream, which permits a well-controlled delivery of suppressants to the flame environment, while also isolating flame-suppressant interactions.

Two suppression capabilities are introduced, including a system for adding gaseous N_2 to the oxidizer, whereby the primary means of flame suppression is thermal quenching due to oxidizer dilution, and a system for adding a fine water mist to the oxidizer, whereby the primary means of flame suppression is thermal quenching due to a combination of oxidizer dilution (via water-vapor) and evaporative cooling. A comprehensive description of each component in the experimental configuration is provided in Sec. 2.2.

Present measurement capabilities include several non-intrusive integral diagnostics meant to capture essential flame features related to strength and behavior throughout the progression to extinction. Measurement methods utilize detailed analytical techniques to derive a depth of rich information from these relatively simple diagnostics. These measurements are useful for both probing flame-suppressant interactions and gauging global suppression performance. Measurements are also suitable as validation data for comparison with CFD simulation results.

Among the selected diagnostics, flame imaging provides visual observation and identification of flame suppression behaviors, as well as a means for quantitative evaluation of mean flame height. Luminous flame emissions give further information related to soot production and incandescence. Radiative flame emissions provide flame strength information related to radiative emissive power and heat losses. Finally, calorimetry techniques are used to measure flame heat release rate and combustion efficiency for direct analysis of global flame strength and suppression performance. Full descriptions of each measurement system are presented in Sec 2.3, while data collection and analysis procedures are discussed in Sec 2.4.

2.2 Configuration

2.2.1 Burner and Flame

The slot burner utilized in the present facility is specifically designed to produce buoyant, turbulent diffusion flames in a canonical line-fire configuration. As such, design attributes for the burner (dimensions and fuel mass flow rates) have been selected to ensure the studied flames meet the following line-fire, buoyancy, and turbulence constraints.

The line-fire constraint limits the mean flame height, L_f, relative to the burner length, L_b, so that $L_f/L_b < 1$, while also limiting the burner length-to-width aspect ratio so that $L_b/W_b > 10$ in order to minimize three-dimensional edge effects in the flame. For the purposes of the burner design, L_f is approximated via the following expression [74],

$$L_f = \alpha \left(\dot{Q}_{conv}/L_b \right)^{2/3}, \tag{2.1}$$

where α is an empirical correlation coefficient for the flame height and $\dot{Q}_{conv}$ is the convective portion of the flame heat release rate, given by

$$\dot{Q}_{conv} = (1 - \chi_{rad})\, \eta_{comb}\, \Delta h_{comb}\, \dot{m}_{fuel}, \tag{2.2}$$

where χ_{rad} is the flame radiative heat-loss fraction (here treated as a fuel property), η_{comb} is the combustion efficiency (here assumed to be unity), Δh_{comb} is the mass-specific enthalpy of combustion of the fuel, and $\dot{m}_{fuel}$ is the mass flow rate of fuel. For the purposes of the burner design, α has been determined based on preliminary experimental data as $\alpha \approx 0.0003\,\mathrm{m}^{5/3}/\mathrm{W}^{2/3}$ for the present configuration.

The buoyancy constraint requires that a characteristic fire-source Froude number, $\dot{Q}^*$, be less than a critical value defining transition from buoyancy-driven to momentum-dominated flow regimes so that

$$\dot{Q}^* = \frac{\left(\dot{Q}_{conv}/L_b\right)}{\rho_\infty \, c_{p,\infty} \, T_\infty \, g^{\,1/2} \, W_b^{\,3/2}} < \dot{Q}^*_{crit} \approx 10, \tag{2.3}$$

where ρ_∞, $c_{p,\infty}$, and T_∞ are respectively the mass density, heat capacity, and temperature of the ambient and g is the gravitational acceleration constant [75].

The turbulence constraint requires that a characteristic fire-source Grashof number, Gr, evaluated at one-tenth the flame height, be greater than a critical value defining transition from laminar to fully-turbulent flow regimes according to

$$Gr\,(z = L_f/10) = \frac{g \, \beta_\infty \, z^{\,3} \left(\dot{Q}_{conv}/L_b\right)}{\rho_\infty \, c_{p,\infty} \, \nu_\infty^3} > Gr_{crit} \approx 10^{10}, \tag{2.4}$$

where z measures elevation above the burner, β_∞ is the volumetric thermal expansion coefficient of the ambient, and ν_∞ is the ambient kinematic viscosity [76–81].

In the present study, the burner is fueled with either methane (CH_4) or propane (C_3H_8) gaseous fuel to yield respective flames with either minimal or appreciable net soot yield. Utilizing reference property values for these fuels, as well as those for ambient air at normal temperature and pressure, the preceding constraint expressions may be solved simultaneously to visualize the feasible design space for the burner. To simplify the analysis, the burner length-to-width aspect ratio is explicitly defined as $L_b/W_b = 10$. The preceding set of constraints can then be formulated to express $\dot{m}_{fuel}$ as a function of W_b, yielding the design spaces depicted in Fig. 2.1 for CH_4 and Fig. 2.2 for C_3H_8.

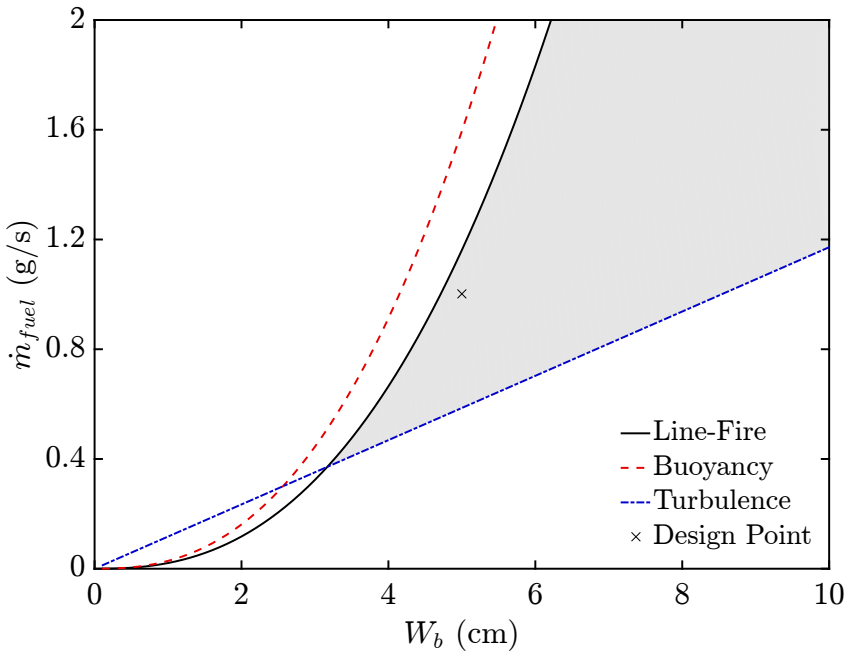

Figure 2.1: Burner design space for CH_4 fuel; W_b and $\dot{m}_{fuel}$ satisfying all design criteria lie within the shaded region.

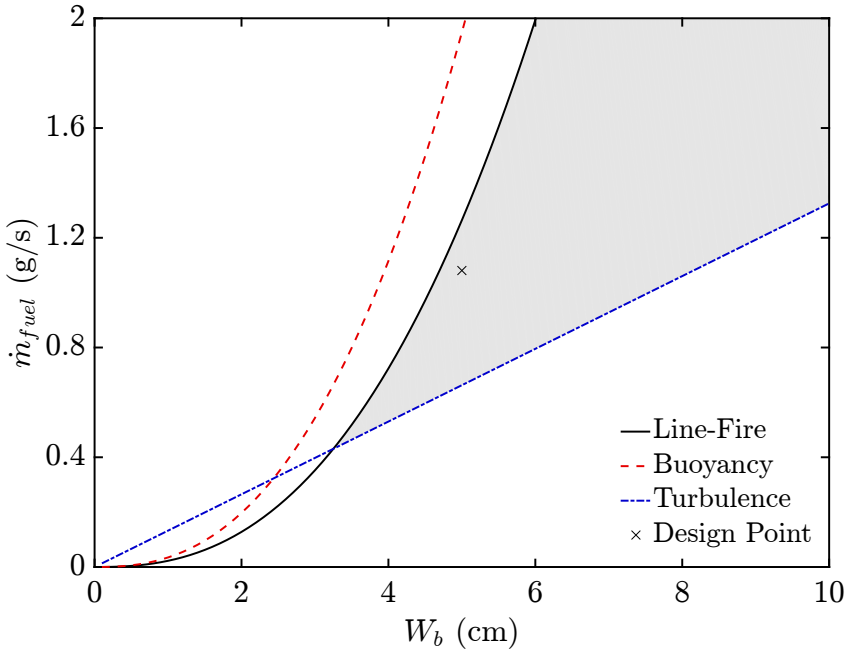

Figure 2.2: Burner design space for C_3H_8 fuel; W_b and $\dot{m}_{fuel}$ satisfying all design criteria lie within the shaded region.

The shaded regions in Figs. 2.1 and 2.2 identify the feasible design space within which burner attributes satisfy all design constraints. Note that for either fuel, the buoyancy constraint is inactive and the feasible design space is limited only by the bounds of the line-fire and turbulence constraints.

As guided by the preceding design model, and illustrated in Figs. 2.1 and 2.2, a slot burner with dimensions $W_b = 5\,\text{cm}$ and $L_b = 50\,\text{cm}$ is utilized in the present configuration. For these dimensions, solution of the constraint expressions indicates that flames for either fuel with $\dot{m}_{fuel} \approx 1\,\text{g/s}$ are sufficiently buoyant and turbulent with respect to the design criteria, and fit the desired line-fire geometry. A detailed schematic for the present design, which is denoted as the turbulent line burner (TLB), is presented in Fig. 2.3.

CH_4 and C_3H_8 fuels are each supplied to the burner at 99.5% purity from pressurized cylinders. Either fuel initially passes through a 7.5 m length of 6.4 mm outer-diameter copper tubing coiled in a water bath, warming to ambient temperature to facilitate steady flow measurement. The fuel next passes through a mass flow controller before entering the burner through two equally-spaced ports.

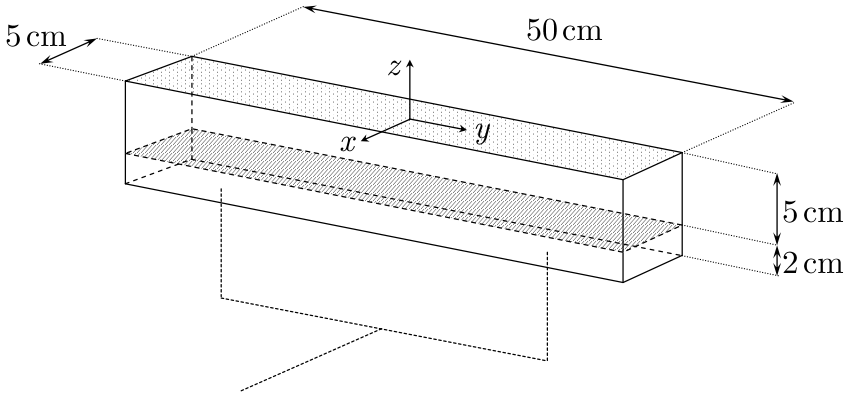

Figure 2.3: Schematic detailing the turbulent line burner (TLB) design.

The burner consists of a 5-cm-wide by 50-cm-long by 7-cm-tall stainless-steel slot with 1.5-mm-thick side walls. Within the burner, fuel enters at the bottom of a lower 2-cm-tall plenum space, then filters through a 5-cm-tall bed of ground glass (25–40 mesh size) to facilitate uniform fuel delivery. A perforated aluminum plate (40% open area) covered with a stainless-steel wire mesh (50 by 250 mesh size) separates the lower plenum space from the upper glass-filled section of the burner. Buried within the layer of ground glass, an exposed-junction K-type thermocouple probe positioned at the center of the fuel port measures the inlet temperature of the fuel with an uncertainty of $\pm 2\,\mathrm{K}$ and response time of roughly 3 s.

A nominal CH_4 flow rate of $1.00 \pm 0.02\,\mathrm{g/s}$ (6.0 cm/s from the fuel port) or a nominal C_3H_8 flow rate of $1.08 \pm 0.02\,\mathrm{g/s}$ (2.3 cm/s) is utilized for the present study. Assuming complete combustion, the total heat release rate is roughly 50 kW for either fuel in the unsuppressed flames. Representative images depicting simultaneous front and end views of a CH_4 flame produced in the present configuration are shown in Fig. 2.4. The flame resembles a line fire in that its length (y-direction, shown in front view) is much larger than its width (x-direction, shown in end view).

The entrance flow of the fuel stream is laminar for the specified fuel flow rates, and therefore the flame base is expected to be laminar. Transition to buoyancy-generated turbulence is estimated via a re-expression of Eq. 2.4 as

$$z_{crit} = \left(\frac{Gr_{crit}\,\rho_\infty\,c_{p,\infty}\,\nu_\infty^3}{g\,\beta_\infty \left(\dot{Q}_{conv}/L_b \right)} \right)^{1/3}, \tag{2.5}$$

where z_{crit} is the elevation above the fuel port at which flow-regime transition occurs and other quantities are as previously defined. Applied to the specified experimental

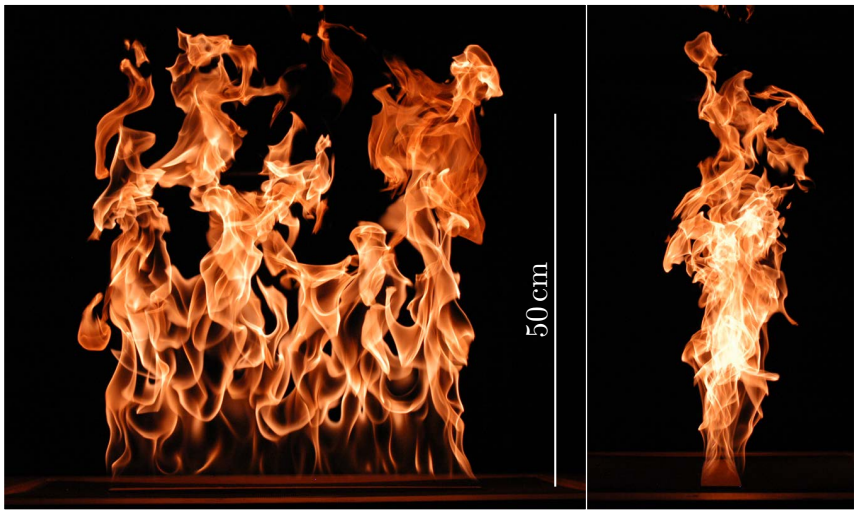

Figure 2.4: Front and end views of a representative CH_4 flame.

conditions, evaluation of Eq. 2.5 gives $z_{crit} = 1.2\,\text{cm}$ for laminar to transitional flow ($Gr_{crit} = 10^9$) and $z_{crit} = 2.7\,\text{cm}$ for transitional to turbulent flow ($Gr_{crit} = 10^{10}$) [76–81]. As shown in Fig. 2.4, these elevations reasonably match the length scales over which turbulent flame structures develop at the base of the flame.

2.2.2 Co-flowing Oxidizer

Surrounding the burner is an apparatus designed to produce a controlled, uniform co-flowing oxidizer, with capacity to deliver various suppressants to the flame. The oxidizer is intended to minimally impact the entrainment structure of the flame, while also shielding the flame from significant interaction with ambient air (thus ensuring that the flame interacts primarily with the suppressant-laden environment provided by the oxidizer). As such, design attributes for the oxidizer apparatus (dimensions and oxidizer mass flow rates) have been selected to ensure the oxidizer meets the following flame-interaction and ambient-occlusion constraints.

The flame-interaction constraint requires that the oxidizer velocity, w_{ox}, be significantly less than a characteristic buoyant velocity scale for the flame, w_f, so that

$$10\, w_{ox} < w_f = \left(\frac{g\, L_f\, \Delta T}{T_\infty} \right)^{1/2}, \tag{2.6}$$

where ΔT is a characteristic temperature rise for the fire plume gases over ambient, here assumed to be 500 K [82], and other terms are as previously defined. For the present flames, $w_f \approx 3\,\mathrm{m/s}$, and therefore by Eq. 2.6, $w_{ox} < 30\,\mathrm{cm/s}$.

The ambient-occlusion constraint then requires that fuel leaving the burner react predominantly with air supplied by the co-flowing oxidizer, rather than that entrained from the ambient. Formulated from the perspective of heat release rate (which is analogous to the chemical reaction rate), this constraint becomes

$$\eta_{ox} = \frac{\dot{Q}_{ox}}{\dot{Q}} > 0.9, \tag{2.7}$$

where η_{ox} is defined as the ambient-occlusion efficiency of the oxidizer, $\dot{Q}_{ox}$ is the rate of heat release by fuel reacting only with oxidizer air, and $\dot{Q}$ is the total rate of heat release by fuel reacting with oxidizer air and air entrained from the ambient.

While it is not feasible to measure or estimate η_{ox} experimentally, such may be achieved via CFD simulation. For the present design analysis, Eq. 2.7 is evaluated using the Fire Dynamics Simulator (FDS), an open-source CFD software tool for thermally driven flow [4]. As a CFD solver, FDS provides an adequate means of resolving the turbulent mixing dynamics that govern the variations in η_{ox} that should occur with changing oxidizer attributes. A detailed description of the FDS solver and the present numerical configuration is deferred to Chapter 3.

For the oxidizer design simulations, a dual-reaction formulation is developed for which one fuel species (here limited to CH_4) reacts with either of two distinct (but chemically equivalent) air species, the first representing the background ambient air, and the second representing air supplied by the co-flowing oxidizer. The heat release rates for these two reactions are readily distinguished in the simulation results, from which η_{ox} is evaluated via Eq. 2.7.

Simulations are conducted for two conditions, where the O_2 mole fraction in the oxidizer, $X_{O_2}^{ox}$, is varied to represent different suppressant-loading conditions of the N_2 suppression system (see Sec. 2.2.3). The first case, corresponding to $X_{O_2}^{ox} = 0.21$, represents an unsuppressed condition where the oxidizer comprises pure air. The second case, corresponding to $X_{O_2}^{ox} = 0.15$, then represents a partially-suppressed condition where the oxidizer includes a diluted mixture of air with added N_2. As the diluted oxidizer contains less O_2 available for reaction with the fuel, it may be expected that the flame be more susceptible to ambient interaction for the partially-suppressed case than for the unsuppressed case. This is confirmed in the following simulation results, where values for η_{ox} are generally lower at $X_{O_2}^{ox} = 0.15$ than at $X_{O_2}^{ox} = 0.21$.

Time-mean simulated η_{ox} are plotted versus oxidizer-port width (W_{ox}) in Fig. 2.5 and oxidizer-port length (L_{ox}) in Fig. 2.6. As shown, there is a non-monotonic variation in η_{ox} with changing oxidizer-port dimensions. Because the oxidizer flow rate ($\dot{m}_{ox}$) is held constant for these cases, variations in the size of the oxidizer port yield inverse variations in the oxidizer velocity (w_{ox}). Note that η_{ox} should tend to increase with increasing W_{ox} and L_{ox}, but also with increasing w_{ox},

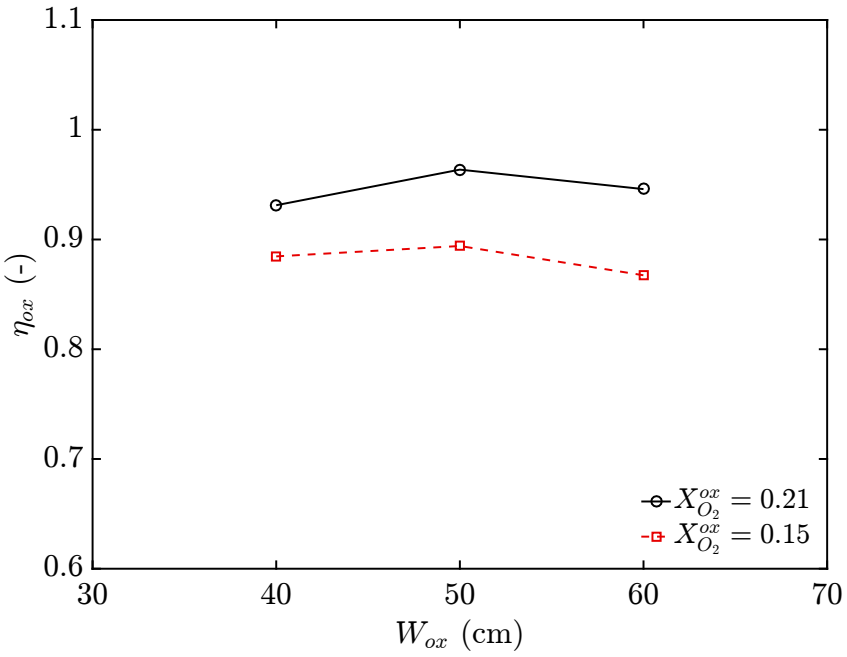

Figure 2.5: Simulated oxidizer ambient-occlusion efficiency (η_{ox}) plotted versus oxidizer-port width (W_{ox}); $L_{ox} = 75\,\text{cm}$, $\dot{m}_{ox} = 75\,\text{g/s}$.

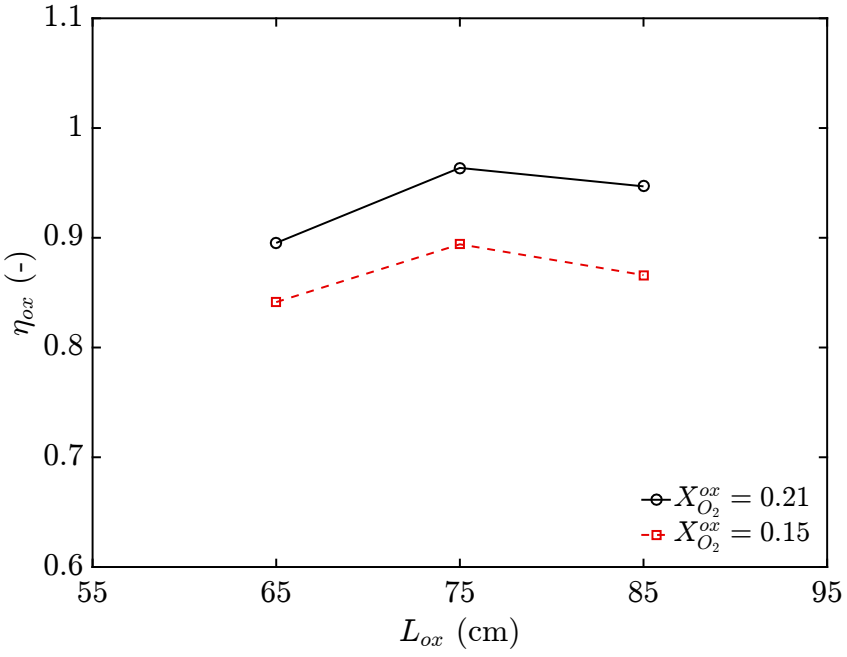

Figure 2.6: Simulated oxidizer ambient-occlusion efficiency (η_{ox}) plotted versus oxidizer-port length (L_{ox}); $W_{ox} = 50\,\text{cm}$, $\dot{m}_{ox} = 75\,\text{g/s}$.

as these variations should encourage isolation of the flame from the ambient. The peak values in η_{ox} may then be interpreted to indicate oxidizer-port dimensions for which w_{ox} is optimized at a given $\dot{m}_{ox}$. From their relationship to w_{ox}, optimum values of W_{ox} and L_{ox} should increase with increasing $\dot{m}_{ox}$ and decrease with decreasing $\dot{m}_{ox}$. For the present configuration, a representative $\dot{m}_{ox} = 75\,\mathrm{g/s}$ indicates optimum oxidizer-port dimensions of $W_{ox} \approx 50\,\mathrm{cm}$ and $L_{ox} \approx 75\,\mathrm{cm}$.

Simulated η_{ox} for the stated optimum W_{ox} and L_{ox} are plotted versus $\dot{m}_{ox}$ in Fig. 2.7. As shown, η_{ox} is an increasing function of $\dot{m}_{ox}$, as expected. From these results, the ambient-occlusion constraint is appropriately satisfied for $W_{ox} = 50\,\mathrm{cm}$ and $L_{ox} = 75\,\mathrm{cm}$ and with $\dot{m}_{ox} \approx 85\,\mathrm{g/s}$, limited by the partially-suppressed case at $X_{O_2}^{ox} = 0.15$. For these conditions, and accounting for the cross-section of the burner, $w_{ox} \approx 25\,\mathrm{cm/s}$, also satisfying the flame-interaction constraint given in Eq. 2.6.

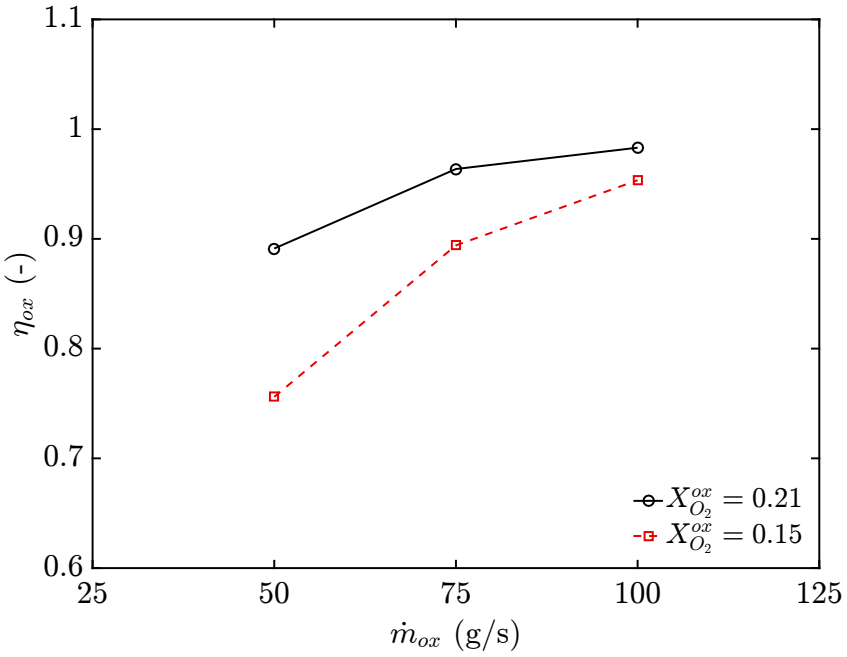

Figure 2.7: Simulated oxidizer ambient-occlusion efficiency (η_{ox}) plotted versus oxidizer mass flow rate ($\dot{m}_{ox}$); $W_{ox} = 50\,\mathrm{cm}$, $L_{ox} = 75\,\mathrm{cm}$.

Detailed simulation results are presented in Fig. 2.8, where simulated η_{ox} for $W_{ox} = 50\,\text{cm}$, $L_{ox} = 75\,\text{cm}$, and $\dot{m}_{ox} = 75\,\text{g/s}$, for both $X_{O_2}^{ox} = 0.21$ and $X_{O_2}^{ox} = 0.15$, are plotted versus elevation above the fuel port, z. Also plotted is the time-mean integrated total heat release rate per-unit-elevation above the fuel port, $\dot{Q}/dz$. As shown, $\dot{Q}/dz$ attains peak values for $z < 25\,\text{cm}$ ($\sim L_f/2$), but drops considerably thereafter, falling to zero for $z > 75\,\text{cm}$ ($\sim 3\,L_f/2$). Correspondingly, $\eta_{ox} = 1$ for $z < 25\,\text{cm}$, indicating that no ambient interaction occurs over the region of peak $\dot{Q}/dz$. For $z > 25\,\text{cm}$, η_{ox} decreases continuously as ambient entrainment begins to dominate the oxidizer. Still, the observed drop in η_{ox} with increasing z is outpaced by declining $\dot{Q}/dz$ so that any ambient interaction that occurs high in the flame represents only a small portion of the total combustion reaction.

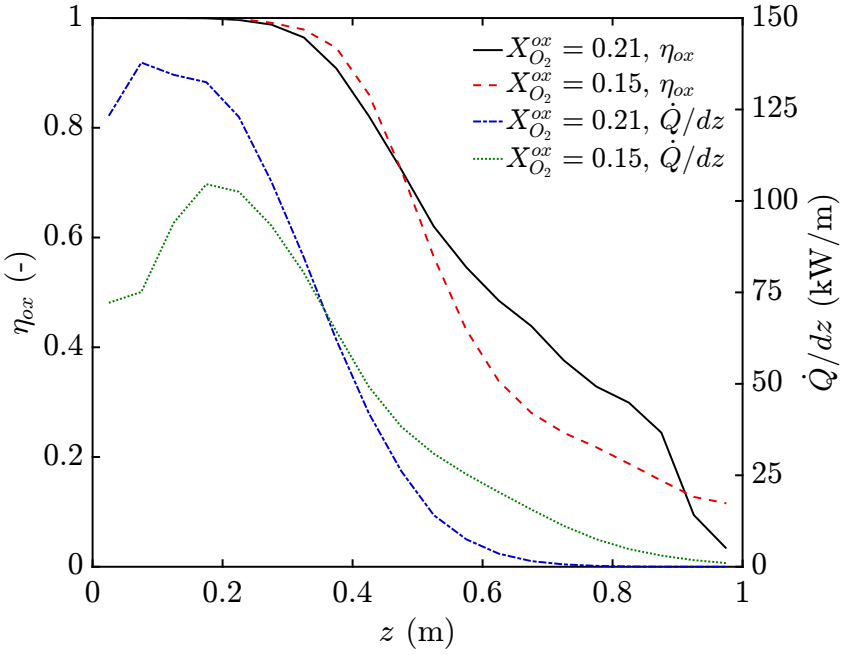

Figure 2.8: Simulated oxidizer ambient-occlusion efficiency (η_{ox}) and heat release rate per-unit-elevation ($\dot{Q}/dz$) plotted versus elevation above the fuel port (z); $W_{ox} = 50\,\text{cm}$, $L_{ox} = 75\,\text{cm}$, $\dot{m}_{ox} = 75\,\text{g/s}$.

As guided by the preceding analysis, the oxidizer apparatus and associated flow conditioning systems are illustrated in Fig. 2.9. The oxidizer apparatus comprises a sealed rectangular structure with internal dimensions 50-cm-wide by 75-cm-long by 100-cm-tall. Oxidizer enters at the base of the structure, mixing within its internal volume before passing through a 38-mm-thick aluminum honeycomb of 3.2 mm hexagonal cells. This honeycomb defines the oxidizer port at the top of the structure, conditioning the flow with a uniform vertical velocity profile. The oxidizer port sits 15 mm below the fuel port, while the 10-cm-wide perimeter of the oxidizer apparatus sits at the same elevation as the fuel port.

Also shown in Fig. 2.9, the N_2 and water-mist suppression systems represent integral components of the oxidizer apparatus. Detailed descriptions of these systems are presented respectively in Secs. 2.2.3 and 2.2.4.

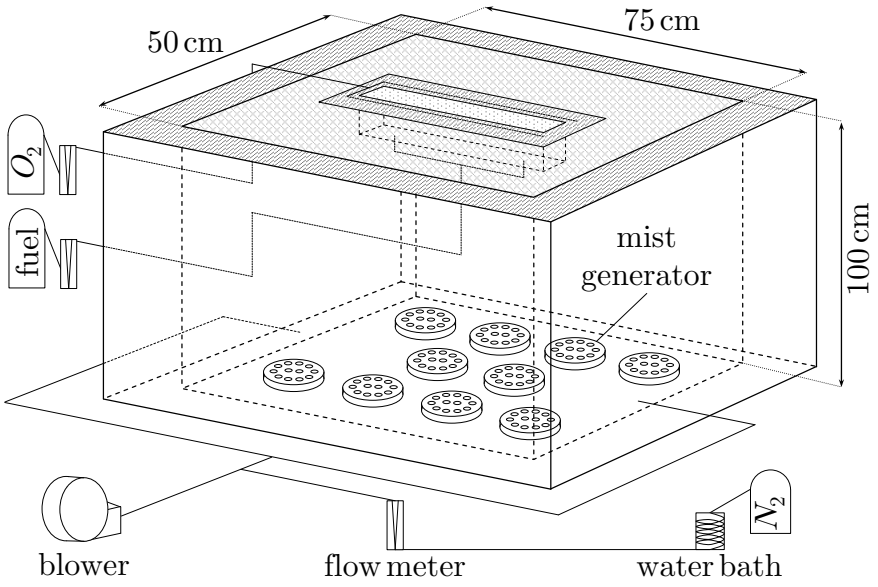

Figure 2.9: Schematic detailing the experimental configuration, including the turbulent line burner (TLB) and co-flowing oxidizer apparatus, as well as the integrated N_2 and water-mist suppression systems.

On top of the honeycomb and surrounding the burner lies a 5-mm-tall by 5-cm-wide strip of ceramic fiberboard, positioned so the top of the board is 10 mm below the fuel port. This board reduces the vertical component of the oxidizer velocity near the flame base, forcing the onset of buoyancy-generated turbulence upstream toward the fuel port and helping to prevent the oxidizer from impacting the entrainment structure of the flame (see Sec. 4.2.1 for a comparison of flame structure with and without the board). This configuration also yields horizontal entrainment conditions at the flame base that more closely resemble those of realistic buoyant liquid-pool and solid-fuel fires.

A plan-view illustration of the fuel and oxidizer ports is presented in Fig. 2.10. Also shown, an optional O_2-anchor sits on top of the fiberboard against each long edge of the burner. This device and its purpose are further described in Sec. 2.2.3.

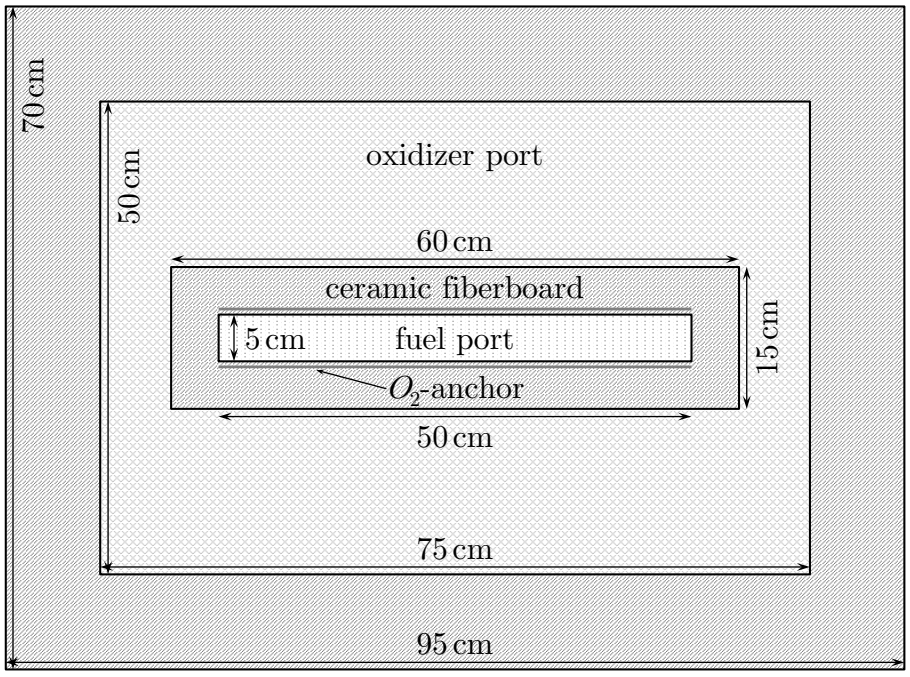

Figure 2.10: Plan-view illustration detailing the fuel and oxidizer ports.

Air for the oxidizer is supplied by an electric centrifugal blower through 8.9 cm outer-diameter piping, with flow rate controlled by a manual gate valve and measured using a United Sensor pitot-static probe connected to a Setra Model 264 differential pressure transducer. Sufficient lengths of straight piping are provided upstream (25 diameters) and downstream (5 diameters) of the pitot probe to ensure fully-developed flow and promote measurement stability.

The pitot probe is calibrated by adding measured amounts of gaseous N_2 into the oxidizer upstream of the pitot probe and measuring the resulting changes in $X_{O_2}^{ox}$ at the oxidizer port (see Sec. 2.2.3). From the measured variations in $X_{O_2}^{ox}$, the total oxidizer flow is determined via

$$\dot{m}_{ox} = \left(\dot{V}_{N_2} + \dot{V}_{N_2} \frac{X_{O_2}^{ox}}{X_{O_2}^{\infty} - X_{O_2}^{ox}} \right) \left(\frac{P_{ox}\, M_{ox}}{R\, T_{ox}} \right), \tag{2.8}$$

where $\dot{V}_{N_2}$ is the volumetric flow rate of N_2 added to the oxidizer, $X_{O_2}^{\infty}$ is the O_2 mole fraction in the ambient air, P_{ox} is the static pressure, M_{ox} the molar mass, and T_{ox} the temperature of the oxidizer mixture, and R is the ideal gas constant. Note that Eq. 2.8 utilizes the ideal gas law to estimate the mass density of the oxidizer.

The flow rate measured by the pitot probe is then determined via

$$\dot{m}_{ox} = C_f^{ox}\, A_{ox} \left(\frac{2\, \Delta P_{ox}\, P_{ox}\, M_{ox}}{R\, T_{ox}} \right)^{1/2}, \tag{2.9}$$

where ΔP_{ox} is the pitot-measured differential pressure and C_f^{ox} is a flow coefficient characterizing the velocity distribution across the cross-sectional area, A_{ox}, of the oxidizer piping at the probe location. Equation 2.9 relies on Bernoulli's principle to relate the measured differential pressure to the flow velocity, which is related to the mass flow rate via the flow density, again estimated using the ideal gas law.

Calibration of the pitot probe is then accomplished by determining an appropriate value for C_f^{ox} so that $\dot{m}_{ox}$ evaluated using both Eqs. 2.8 and 2.9 agree for a variety of flow conditions. A typical calibration curve corresponding to measurements in the present configuration is presented in Fig. 2.11, from which $C_f^{ox} = 0.8972$. As shown, the calibration measurements derived using Eq. 2.8 reasonably follow the trend produced using Eq. 2.9 across a wide range in pitot-measured ΔP_{ox}, indicating satisfactory calibration of the probe.

Adjacent to the pitot probe, an exposed-junction K-type thermocouple probe measures the oxidizer temperature with an uncertainty of $\pm 2\,\mathrm{K}$ and response time of roughly 3 s. Immediately downstream of the probes, the oxidizer piping is split, with each path delivering half the oxidizer to opposite sides of the oxidizer apparatus. The fixed total oxidizer flow of $\dot{m}_{ox} = 85 \pm 7\,\mathrm{g/s}$ (25 cm/s) provides roughly five-times the O_2 required for stoichiometric combustion of either fuel.

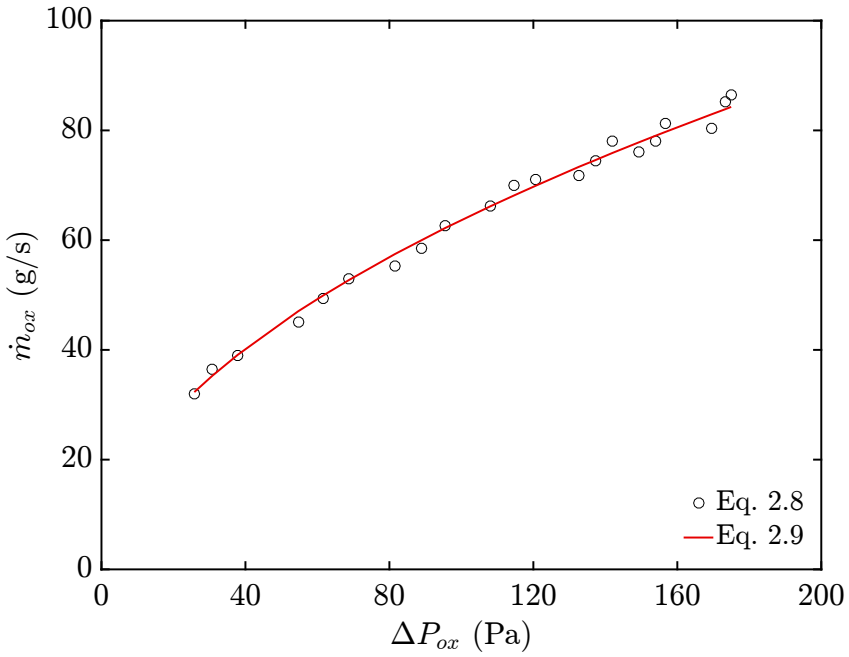

Figure 2.11: Calibration measurements for the oxidizer pitot probe.

To further characterize the oxidizer boundary condition, qualitative observations of the oxidizer flow patterns are performed using a flow-visualization technique derived from previous work [83]. By this technique, an electrically heated wire is used to flash-pyrolyze a thin film of mineral oil applied to the wire surface. This produces a line source of highly visible white smoke, which can be recorded using standard imaging devices to visualize flow patterns. A schematic illustrating the present implementation of this technique is presented in Fig. 2.12.

As depicted in Fig. 2.12, a 2 m length of 0.5 mm diameter Nickel-Chromium wire is suspended across the oxidizer port, supported by ceramic rods mounted on brackets at either end of the apparatus. The excess length of wire at each end is wound between two additional ceramic rods, which are attached to small 2 kg weights. The ceramic rods provide sufficient resistance to isolate the electrical current in the wire, while the weights hold the wire in tension, preventing undesirable movement of the wire during flow visualization as caused by thermal expansion.

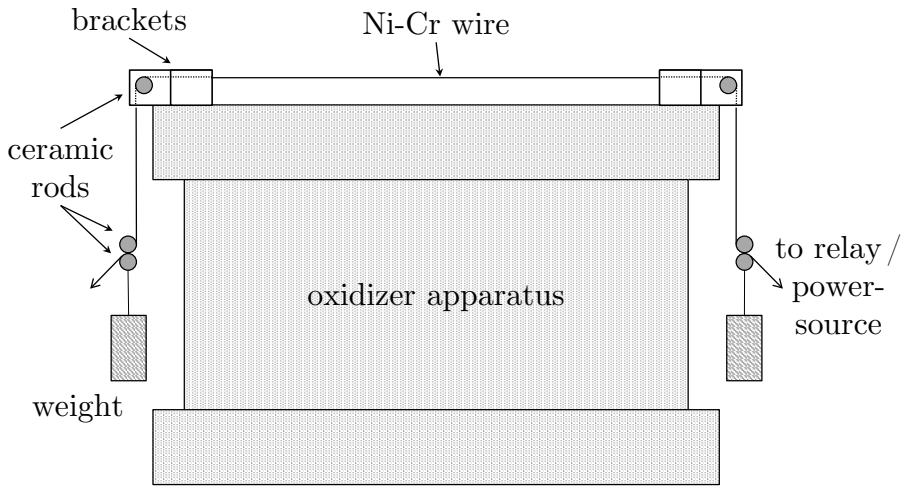

Figure 2.12: Technique to visualize flow patterns in the co-flowing oxidizer.

Each end of the wire is connected in an electrical circuit containing a 120-volt AC power supply and a relay switch. A thin film of mineral oil is uniformly applied to the portion of the wire suspended above the oxidizer port. Upon activation of the power source, the relay switch provides a 0.2 s duration of electrical current before opening the circuit. During this time, the wire is electrically heated to the point of pyrolyzing the mineral oil, producing an instantaneous line-source puff of visible white smoke, distributed along the length of the wire.

Images of the smoke-trace flow visualization are utilized to qualitatively characterize the oxidizer boundary condition. A sample image is presented in Fig. 2.13, depicting a smoke trace across the center of the fuel and oxidizer ports (x-direction). Note that the image presented in Fig. 2.13 has been post-processed via color inversion and gamma correction in order to enhance the visibility of the smoke. As shown, the smoke trace remains flat and even on either side of the fuel port and ceramic fiberboard, suggesting adequate uniformity in the oxidizer flow field.

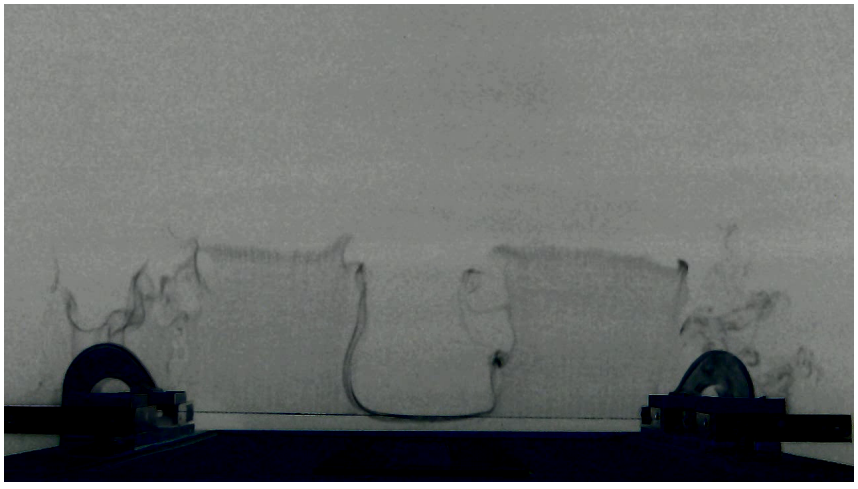

Figure 2.13: Smoke-trace flow visualization of the co-flowing oxidizer across the center of the fuel and oxidizer ports (x-direction), showing adequate uniformity in the oxidizer flow field.

2.2.3 Nitrogen Suppression

The N_2 suppression system provides controlled flame quenching by introducing a variable flow of gaseous N_2 into the oxidizer stream. As N_2 is added to the oxidizer, the O_2 mole fraction in the oxidizer ($X_{O_2}^{ox}$) is reduced, such that a greater volume of oxidizer must be entrained into the flame to supply the stoichiometric O_2 required for combustion. The additional N_2 in the oxidizer acts as an inert diluent in the combustion region, dissipating the heat released by the reaction and lowering the flame temperature. Flame suppression via oxidizer dilution then occurs primarily as thermal quenching, where the flame is extinguished once the flame temperature is reduced below a critical value necessary to sustain combustion [8].

For the present configuration, the N_2 suppression system is designed to provide a full range of controlled conditions from extinction-free through partial and total extinguishment of the flame. The central components of the system are illustrated in Fig. 2.9. Gaseous N_2 (99.99% purity) for suppression is furnished from a pressurized Dewar, passing through a 15 m length of 19 mm outer-diameter copper tubing coiled in a water bath, warming to ambient temperature to facilitate steady flow measurement. The flow rate of N_2 is controlled using a needle valve and measured using a calibrated variable-area rotameter. The N_2 is injected into the oxidizer piping downstream of the blower and upstream of the pitot probe used to measure the oxidizer flow rate. Air and N_2 in the oxidizer are thoroughly mixed, passing through a sufficiently long section of piping (> 50 diameters) to ensure fully-developed flow before the mixture enters the oxidizer apparatus.

The suppression potential of the N_2 suppression system is characterized by the quantity $X_{O_2}^{ox}$, where decreasing $X_{O_2}^{ox}$ indicates increasing suppression potential of the oxidizer. The flow rate of N_2 supplied by the system varies between 0–40 g/s yielding changes in $X_{O_2}^{ox}$ from the ambient $X_{O_2}^{ox} = 0.21$ to as low as $X_{O_2}^{ox} = 0.11$, a value sufficient to achieve global flame extinguishment for either CH_4 or C_3H_8 fuel.

Quantity $X_{O_2}^{ox}$ is measured using a Servomex 540E paramagnetic analyzer via a sampling probe located inside the oxidizer port. The oxidizer sample is drawn using a vacuum pump, through a length of 3.2 mm inner-diameter tubing toward the analyzer. The sample passes through a section of Drierite$^{\text{TM}}$ desiccant to remove H_2O, and a 2 μm particulate filter prior to analysis. The analyzer provides a measurement uncertainty of ±1250 ppm O_2 and response time of roughly 5 s. The characteristic transport time of the sampling system, measured to be roughly 22 s, is compensated to provide synchronous data collection with other diagnostics. Measurements of $X_{O_2}^{ox}$ at steady N_2 flow and with the sampling probe positioned at various locations across the oxidizer port confirm sufficient uniformity in the oxidizer composition.

The value of $X_{O_2}^{ox}$ at global flame extinction is termed the limiting oxygen index (LOI) and is used to characterize the extinction limit for a particular fuel. Similar to LOI is the minimum extinguishing concentration (MEC), defined as the mole fraction of added suppressant in the oxidizer at global extinction. LOI and MEC are used interchangeably in the literature and are simply related via

$$LOI = X_{O_2}^{\infty} \left(1 - MEC\right), \tag{2.10}$$

where $X_{O_2}^{\infty}$ is the mole fraction of O_2 in the ambient air. In the present work,

extinction conditions are reported using LOI, though the equivalent MEC may be determined using Eq. 2.10.

In agreement with previous works [27–35], preliminary extinction results in the present configuration have shown that weakened flames in co-flow may liftoff and detach from the fuel port prior to extinction. As introduced in Sec. 1.2, this extinction behavior is undesirable as it is questionable whether liftoff events relate to the extinction processes of large-scale turbulent fires.

To prevent liftoff extinction events in the present configuration and permit the study of substantially weakened flames, an O_2-anchor is optionally applied to strengthen the flame base (see Fig. 2.10). Gaseous O_2 (99.994% purity) is supplied to the anchor by a pressurized cylinder, with flow rate controlled using a needle valve and measured using a calibrated variable-area rotameter. The O_2-anchor comprises two 60-cm-long, 12.7 mm outer-diameter, sintered stainless-steel tubes. Each tube sits on top of the ceramic fiberboard, along opposite edges of the burner. The surface of each tube is wrapped with aluminum foil such that the O_2 flow is directed at a 45° angle toward the flame base through a 2 mm-wide by 50-cm-long port.

The fixed O_2 flow of 0.08 ± 0.0008 g/s (3 cm/s) provides less than 2% of the stoichiometric O_2 requirement for either fuel and less than 0.5% of the total O_2 content supplied by the oxidizer at ambient condition. Localized $X_{O_2}^{ox}$ measurements in the vicinity of the O_2-anchor verify that its direct region of influence is limited to within 1 cm from the tube surface. In the present work, experiments including this O_2 flow are referred as 'anchored', while those without are referred as 'non-anchored', with all other conditions being the same between the two cases.

2.2.4 Water-Mist Suppression

The water-mist suppression system provides controlled flame quenching by introducing a fine water mist into the oxidizer stream. Suppression via water-mist occurs primarily as thermal quenching, where evaporation of mist near the flame leads to direct flame cooling due to the high latent enthalpy of vaporization of H_2O ($\Delta h^{vap}_{H_2O} \approx 2260\,\mathrm{J/g}$). Evaporation of mist upstream from the flame also contributes to suppression by increasing the water-vapor mole fraction in the oxidizer ($X^{ox}_{H_2O}$), thereby lowering $X^{ox}_{O_2}$. This yields an oxidizer-dilution effect similar to N_2 suppression, where the additional gaseous H_2O in the combustion region dissipates heat from the reaction and lowers the flame temperature.

The cooling efficiency of water-vapor ($c_{p,H_2O} \approx 1870\,\mathrm{J/kg/K}$) is notably greater than that of N_2 ($c_{p,N_2} \approx 1040\,\mathrm{J/kg/K}$). Still, global dilution of the oxidizer via water-vapor is strictly limited by saturation, where $X^{ox}_{H_2O}$ cannot exceed an amount corresponding to 100% relative humidity in the oxidizer ($X^{sat}_{H_2O}$). This saturation limit is strongly temperature dependent, where $X^{sat}_{H_2O}$ at ambient temperature is too low to accomplish suppression, but near the flame where temperatures are elevated, $X^{sat}_{H_2O}$ increases significantly (see Fig. 2.14). For saturated oxidizer conditions, mist evaporation can only occur within this near-flame heated region.

Though H_2O is also known to exhibit chemical influence in the combustion reaction [10–15], such effects are comparatively slight. Through a combination of the prior mechanisms, the flame is extinguished once the flame temperature is reduced below a critical value necessary to sustain combustion [8].

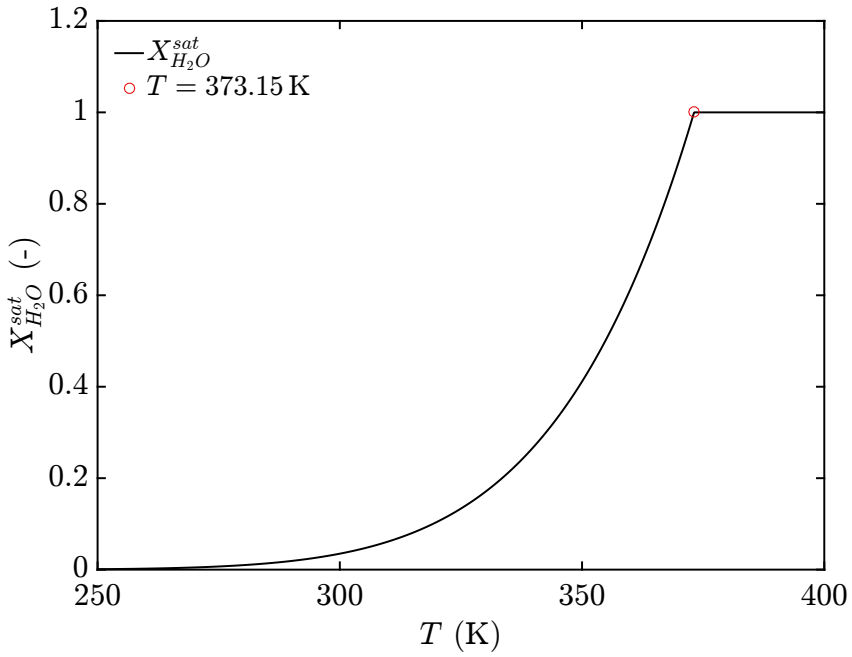

Figure 2.14: Saturated H_2O mole fraction ($X^{sat}_{H_2O}$) in ambient air (101,325 Pa) plotted versus temperature.

The dominance of either evaporative cooling or oxidizer dilution during water-mist suppression is strongly configuration dependent, related primarily to the location at which the mist evaporates relative to the flame. As mentioned in Sec. 1.2, the location of mist evaporation in a given configuration is mainly determined by delivery characteristics, most notably the droplet size distribution of the mist. For the present configuration, the provision of well-characterized boundary conditions necessitates that the mist be generated with low momentum to give a steady, uniform, mist-laden oxidizer that is naturally entrained into the flame. In this application, the droplet size distribution of the delivered mist is mostly limited by available mist-generation methods (low-momentum mist generation precludes most high-pressure nozzles), but also by the requisite capacity for the oxidizer to carry the mist.

A simple force balance on a spherical mist droplet suspended in the upward flowing oxidizer yields

$$\frac{\pi}{6}\,\rho_m\,g\,d_m^3 = \frac{\pi}{8}\,C_d\,\rho_{ox}\,d_m^2\,w_{term}^2, \tag{2.11}$$

where ρ_m is the mass density, d_m the diameter, and C_d the drag coefficient of the mist droplet, ρ_{ox} is the mass density of the oxidizer, and w_{term} is the terminal velocity of the droplet relative to the oxidizer velocity. The left-hand side of Eq. 2.11 represents the gravity force pulling the droplet downward against the flowing oxidizer, while the right-hand side represents the drag force of the oxidizer pulling the droplet upward.

For droplet Reynolds number less than unity, $C_d = 24/Re_d$. This treatment is presently valid for $d_m < 80\,\mu\text{m}$, but conservatively underestimates C_d for $d_m > 80\,\mu\text{m}$. Applied to Eq. 2.11, the solution for w_{term} becomes

$$w_{term} = \frac{\rho_m\,g\,d_m^2}{18\,\mu_{ox}}, \tag{2.12}$$

where μ_{ox} is the dynamic viscosity of the oxidizer (treated as ambient air). Using Eq. 2.12, w_{term} is plotted versus d_m in Fig. 2.15.

Note that w_{term} quantifies the minimum oxidizer velocity necessary to suspend a mist droplet of corresponding diameter d_m. Droplets with $w_{term} = w_{ox}$ are suspended in the oxidizer with zero net velocity, whereas droplets with $w_{term} > w_{ox}$ fall against the flowing oxidizer and only droplets with $w_{term} < w_{ox}$ may be carried with the flow. For the present configuration, for which $w_{ox} = 25\,\text{cm/s}$, droplets with $w_{term} > 25\,\text{cm/s}$ ($d_m > 90\,\mu\text{m}$, see Fig. 2.15) are too heavy to be carried by the oxidizer and cannot be delivered to the flame. Certainly, only droplets with $w_{term} \ll w_{ox}$ may be effectively transported with the flowing oxidizer.

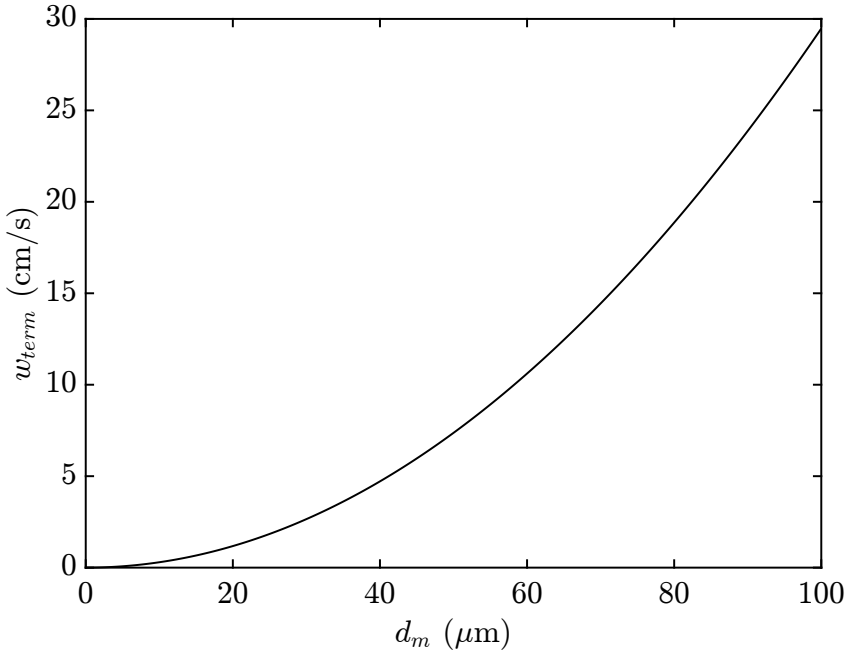

Figure 2.15: Terminal droplet velocity (w_{term}) plotted versus droplet diameter (d_m).

From Eq. 2.12, a droplet-size criterion for mist delivery may be defined as

$$d_m < \left(\frac{6\,\mu_{ox}\,w_{ox}}{\rho_m\,g} \right)^{1/2}, \tag{2.13}$$

formulated so that $w_{term} < w_{ox}/3$, and therefore droplets satisfying Eq. 2.13 are terminally carried at two-thirds the velocity of the background flow. For the present configuration, Eq. 2.13 gives $d_m < 53\,\mu\text{m}$.

As with the N_2 suppression system, the water-mist suppression system is designed to provide a full range of controlled conditions from extinction-free through partial and total extinguishment of the flame. From previous work [8,53], it is estimated that a mist mass fraction in the oxidizer, $Y_m^{ox} > 0.15$, is sufficient for flame extinguishment. For the present configuration, this criterion corresponds to a mist supply rate of $\dot{m}_m > Y_m^{ox}\,\dot{m}_{ox} = 12.8\,\text{g/s}$ (for $\dot{m}_{ox} = 85\,\text{g/s}$).

An additional criterion for water-mist flame extinction may be defined by

$$\dot{m}_m > \eta_{m,crit} \frac{\dot{Q}}{\Delta h_{H_2O}^{vap}}, \tag{2.14}$$

where $\dot{Q}$ is the flame heat release rate, $\Delta h_{H_2O}^{vap}$ is the mass-specific latent enthalpy of vaporization of H_2O, and $\eta_{m,crit}$ is a critical value defining the fraction of the flame heat release that is absorbed by mist evaporation at extinction. Equation 2.14 implicitly assumes the dominant suppression mechanism of the mist to be latent evaporative cooling, which may not apply in all configurations, though sensible cooling effects are conservatively neglected. Experimentally reported values for $\eta_{m,crit}$ vary considerably in the literature, from as low as 0.10, to as high as 0.70 [7]. Assuming a conservative value of $\eta_{m,crit} = 0.75$, applying Eq. 2.14 to the present configuration ($\dot{Q} = 50\,\mathrm{kW}$) gives $\dot{m}_m > 16.6\,\mathrm{g/s}$.

As designed in the present configuration, mist is generated using an array of ten model DK12-36 ultrasonic mist generators, submerged in a 7-cm-deep layer of water within the base of the oxidizer apparatus (see Fig. 2.9). Each mist generator includes twelve individual 20-mm-diameter piezoelectric atomizers, with each generator capable of producing mist at a maximum rate of 6 L/hr. The characteristic droplet size of the generated mist is roughly 10 μm, satisfying the droplet-size criterion given in Eq. 2.13. The maximum mist generation rate from this configuration is roughly $\dot{m}_m \approx 17\,\mathrm{g/s}$ ($Y_m^{ox} \approx 0.20$), satisfying the previously stated supply-rate criteria for flame extinguishment.

The water level inside the apparatus is precisely maintained using a float control valve that closes once the water level reaches a specified depth, and reopens

once the water level begins to recede. Here, proper maintenance of water level is a primary determining factor in the mist-generation efficiency of the atomizers. The base of the oxidizer apparatus additionally includes a drain for water removal.

Inside the apparatus, the oxidizer piping is redirected and redistributed to provide a downward flow of air across the cross section of the apparatus. This supports symmetric mixing of the oxidizer with the mist. The mist is entrained into the oxidizer and delivered through the oxidizer port directly at the flame base. Images depicting mist delivery via the oxidizer for varying mist-loading conditions are provided in Fig. 2.16. As shown, the mist behaves as a dense gas [84], exhibiting Rayleigh-Taylor instabilities with the lower-density ambient and, in the absence of buoyant flame entrainment, tending to spill over the sides of the oxidizer structure.

The suppression potential of the mist-laden oxidizer is primarily characterized by quantity Y_m^{ox}. Also of importance are the droplet size distribution of the mist and the mole fraction of water-vapor in the oxidizer ($X_{H_2O}^{ox}$). Variation of Y_m^{ox} (and correspondingly $X_{H_2O}^{ox}$) is achieved by either varying the total flow rate of the oxidizer at constant mist-loading capacity, or by varying mist-loading capacity at constant oxidizer flow. No significant variation in the droplet size distribution is permissible using the present ultrasonic mist generators. It is then desirable to maintain a constant droplet size distribution, thus isolating the variation of suppression potential to quantities Y_m^{ox} and $X_{H_2O}^{ox}$.

Quantity Y_m^{ox} and the corresponding droplet size distribution are measured using a Malvern Instruments Spraytec system, which uses a laser-diffraction technique to measure both quantities simultaneously [85]. For this technique, a collimated

(a)

(b)

(c)

(d)

(e)

Figure 2.16: Images depicting water-mist delivery at selected Y_m^{ox}; (a) $Y_m^{ox} = 0.00$, (b) $Y_m^{ox} \approx 0.03$, (c) $Y_m^{ox} \approx 0.06$, (d) $Y_m^{ox} \approx 0.09$, (e) $Y_m^{ox} \approx 0.12$.

Helium-Neon laser (632.8 nm) is passed through the mist, while a multifaceted ring detector collects and analyzes the resulting light scattering patterns produced by the laser-mist interactions. The droplet size distribution is evaluated from the beam scattering patterns, while the volumetric mist concentration is determined from the obscuration of the beam through the mist. This volumetric concentration is related to quantity Y_m^{ox} using a characteristic droplet mass density combined with the measured droplet size distribution and the droplet velocities, which are estimated from the droplet size distribution and the oxidizer velocity via Eq. 2.12. The Spraytec system resolves droplet diameters in a range between 0.1–2000 μm with a measurement accuracy of ±1%. This accuracy is retained across a wide range of Y_m^{ox}, permitting up to 95% obscuration of the laser.

For mist characterization measurements in the present configuration, the laser source and detector components of the Spraytec system are positioned so that they face each other from opposite sides of the oxidizer apparatus, located directly above the oxidizer port. The Spraytec is positioned so that the laser passes over the edge of the oxidizer port, without intersecting the space above the fuel port or ceramic fiberboard. The beam path-length is controlled so as to provide total laser obscuration within the accuracy limitations of the instrument.

Quantity $X_{H_2O}^{ox}$ is measured using a Michell Instruments PCMini52 relative humidity sensor mounted to the interior of the oxidizer apparatus. This sensor provides a measurement uncertainty of ±1% RH and response time of roughly 10 s. The measured relative humidity is related to absolute humidity via a thermodynamic state equation for the saturation pressure of H_2O as a function of temperature [86].

2.3 Instrumentation

2.3.1 Flame Imaging / Flame Height

Flame images are utilized to qualitatively identify and observe flame dynamics and extinction behaviors, and also to quantitatively evaluate mean visible flame height. Flame images are recorded using two digital single-lens reflex cameras, where a remote trigger-switch is used to capture simultaneous images (± 50 ms) of the front view (Canon EOS 40D) and end view (Nikon D100) of the flame.

For flame height measurements, an additional video camera (Casio Exilim EX-F1) records flame images continuously at 60 frames per second using variable exposure settings. Each frame is thresholded (via fixed gray value) to a binary black/white image wherein white pixels (value 1) correspond to luminous flame emissions and locate the flame, while black pixels (value 0) correspond to the absence of flame. Exposure settings are selected to maintain high contrast between the flame and background, minimizing thresholding errors and providing a clear demarcation of the visible flame location, accurate to within a few pixels (± 1 mm). The set of continuous frames is then divided into subsets of 600 sequential images (each representing a 10 s recording), where this sample size has been found sufficient to produce steady first-order flame shape statistics.

Within each subset, all 600 frames are averaged together to produce a single grayscale image, in which grayscale pixel intensities represent flame intermittency. An isocontour corresponding to a grayscale value of 0.5 then marks locations where a

visible flame is present 50% of the time. This contour fits the classical definition for the 50% intermittent flame height established in previous work [87], and is presently defined as the mean visible flame shape. The mean elevation of this contour above the central half of the fuel port (neglecting the end regions) then defines the mean visible flame height, L_f, as measured in the present configuration. A sample flame image depicting this technique is provided in Fig. 2.17.

The presently described image-based L_f measurements rely on luminous flame emissions, due predominantly to the incandescence of soot particles. Measurements reported by this technique then include regions of the combustion zone made visible by soot, and do not strictly define the location of the stoichiometric flame sheet. Using this technique, uncertainty in each L_f measurement is estimated to be less than $\pm 1.5\,\mathrm{cm}$, from statistical analyses of steady flame measurements.

Figure 2.17: Illustration of flame image-processing technique depicting a thresholded flame image (black/white regions) overlaid with the corresponding mean visible flame shape (gray contour); $L_f = 45\,\mathrm{cm}$.

Following classical scaling relationships [88,89], a correlation to predict L_f for a buoyant line fire in diluted oxidizer conditions may be derived as follows. The existing L_f scaling established in previous work [88] may be expressed as

$$\frac{L_f}{D} = fn\left(\frac{c_{p,\infty}\,T_\infty}{g\,\rho_\infty^2}\frac{s^3}{\chi_{conv}\,\Delta h_{comb}}\frac{\dot{m}_{fuel}^2}{D^5}\right), \tag{2.15}$$

where s is the stoichiometric oxidizer-to-fuel mass ratio, χ_{conv} is the convective fraction of the total heat release, D is a characteristic length scale of the fuel source, and other terms are as previously defined.

From Eq. 2.15, s may be expanded as $s = s_{O_2}/Y_{O_2}^{ox}$, where s_{O_2} is the stoichiometric oxygen-to-fuel mass ratio, and $Y_{O_2}^{ox}$ is the mass fraction of O_2 in the oxidizer. This substitution permits the extension of Eq. 2.15 to include diluted oxidizer environments. Further, χ_{conv} may be expanded as $\chi_{conv} = (1 - \chi_{rad})$, where χ_{rad} is the radiative fraction of the total heat release. Introducing the combustion efficiency, η_{comb}, as a product coefficient to $\dot{m}_{fuel}$ then accounts for partial suppression of the flame. Finally, fitting the present line-fire geometry, D may be defined as the width of the fuel source, W_b, and $\dot{m}_{fuel}$ may be expressed per-unit-length of the fuel source, $\dot{m}_{fuel}/L_b$. Applying this collection of substitutions to Eq. 2.15 yields

$$\frac{L_f}{W_b} = fn\left(\frac{c_{p,\infty}\,T_\infty}{g\,\rho_\infty^2\,Y_{O_2}^{ox\,3}}\frac{s_{O_2}^3}{(1-\chi_{rad})\,\Delta h_{comb}}\frac{\left(\eta_{comb}\,\dot{m}_{fuel}\right)^2}{L_b^2\,W_b^3}\right). \tag{2.16}$$

Defining the dimensionless group on the right-hand side of Eq. 2.16 as the parameter N,

$$N = \frac{c_{p,\infty}\,T_\infty}{g\,\rho_\infty^2\,Y_{O_2}^{ox\,3}}\frac{s_{O_2}^3}{(1-\chi_{rad})\,\Delta h_{comb}}\frac{\left(\eta_{comb}\,\dot{m}_{fuel}\right)^2}{L_b^2\,W_b^3}, \tag{2.17}$$

the scaling relationship becomes

$$\frac{L_f}{W_b} = fn\left(N\right). \tag{2.18}$$

As defined in Eq. 2.17, N characterizes the oxidizer environment (left term), the properties of the fuel (center term), and the configuration of the fuel source (right term). Note that N provides a generalized form of the more familiar scaling parameter $\dot{Q}^*$ (see Eq. 2.3), to which N is simply related via

$$N = \left(\frac{c_{p,\infty}\, T_\infty\, s_{O_2}}{Y_{O_2}^{ox}\,\left(1-\chi_{rad}\right)\,\Delta h_{comb}}\right)^3 \dot{Q}^{*\,2}. \tag{2.19}$$

Previous scaling analyses [74, 90] have established that for line-source flames, $L_f/W_b \propto \dot{Q}^{*\,2/3}$, but from Eq. 2.19, $N \propto \dot{Q}^{*\,2}$, therefore it follows that

$$\frac{L_f}{W_b} \propto N^{1/3}. \tag{2.20}$$

In applying Eq. 2.20 to the present configuration, $Y_{O_2}^{ox}$ (in Eq. 2.17) is derived from measured $X_{O_2}^{ox}$ via

$$Y_{O_2}^{ox} = \frac{X_{O_2}^{ox}\, M_{O_2}}{\sum_k \left(X_k^{ox}\, M_k\right)}, \tag{2.21}$$

where X_k^{ox} is the mole fraction and M_k the molar mass of each species, k, present in the oxidizer. Further, χ_{rad} and η_{comb} (in Eq. 2.17) are derived from experimental measurements via methods respectively described in Secs. 2.3.3 and 2.3.4. Other terms in Eq. 2.17 are defined by the configuration and testing conditions. A comparison of the L_f scaling predicted by Eq. 2.20 with presently measured data is presented in Sec. 4.2.3.

2.3.2 Luminous Flame Emissions

Luminous flame emissions result almost exclusively from the incandescence of soot particles (yellow-white in color), with minor contributions from the emission spectra of heated combustion radicals such as CH or C_2 (blue in color), which are often detectable only in the absence of the dominant soot emissions. Quantitative measurements of luminous flame emissions are then particularly well representative of flame sooting propensity, where previous work has shown a direct correlation between flame luminosity and the local soot volume fraction in the flame [91].

In the present configuration, luminous flame emissions are measured using a Hamamatsu S2281-01 photodiode and C9051 photosensor amplifier, positioned 2 m radially outward from the burner centroid, 5 cm above the fuel port, facing perpendicular to the long axis of the burner. This device provides a local measurement of the luminous flux at its sensor surface within a spectral range of 190–1000 nm, a maximum viewing angle of 90°, and a response time of 7 µs. Neutral density filters (total ND 5.0) shield the sensor to prevent saturation of the measurement signal, and background measurements are subtracted to correct for ambient interference and isolate flame emissions.

Using a steady, unsuppressed flame as a light source, the photodiode is calibrated by placing various neutral density filters in front of the photosensor and recording the resulting variations in the measured signal. Reductions in the signal strength are then correlated to the corresponding net filter transmittance, which defines the ratio of the measured luminosity to that of the unsuppressed flame. The

resulting calibration correlation then relates the measured signal to a dimensionless luminosity ratio, LR, normalized to a value of unity for the unsuppressed flame. Uncertainty in each LR measurement is estimated to be less than $\pm 15\%$.

2.3.3 Radiative Flame Emissions

Radiative flame emissions result from a combination of spectral emissions from heated combustion gases (particularly CO_2 and H_2O, as well as preheated unburned fuel), with additional contributions from soot incandescence. The relative contributions of soot and gas-phase emissions depend on the sooting propensity of the fuel, where for large, highly sooting fires, radiation from soot typically dominates. Measured variations in radiative flame emissions are representative of changes in flame temperature and/or the local composition of combustion products, both of which indicate effects of suppression and variations in flame strength.

Quantities of interest in characterizing radiative flame emissions include the flame emissive power, $\dot{Q}_{rad}$, defined as the rate of heat release in the form of thermal radiation, and the flame radiative heat-loss fraction, χ_{rad}, defined as

$$\chi_{rad} = \frac{\dot{Q}_{rad}}{\dot{m}_{fuel}\,\Delta h_{comb}}, \tag{2.22}$$

where the product $(\dot{m}_{fuel}\,\Delta h_{comb})$ characterizes the total chemical heat release potential for combustion based on the rate of fuel consumption.

Radiative flame emissions are presently measured using a factory-calibrated, water-cooled, MedTherm model 64-2-20 Schmidt-Boelter type heat flux transducer. This device provides a local measurement of the total incident heat flux at its sen-

sor surface with a hemispherical absorptance of 0.94 for a spectral range between 0.6-15.0 μm, a maximum viewing angle of 90°, a response time of 0.25 s, and a measurement uncertainty of ±3%.

The transducer is positioned 1 m radially outward from the burner centroid, 18 cm above the fuel port, facing perpendicular to the long axis of the burner. This location is sufficiently remote from the flame such that the temperature gradient between the water-cooled body of the sensor and the surrounding air is negligible. Neglecting this convective portion, the measured heat flux is interpreted as entirely radiative. As with the luminous emissions, background measurements are subtracted to correct for ambient irradiation and isolate flame emissions.

The measured heat flux data are related to the global radiative loss fraction (χ_{rad}) using a weighted multipoint source model [92], adapted to the present two-dimensional flame geometry from the original concepts put forth in previous work [93]. While relatively complex, the multipoint source model provides a more accurate representation of radiative emissions than that given by the simpler and more conventional single-point isotropic source model [94–99]. The single-point source model is reasonably accurate when the sensor is located sufficiently far from the source, but can suffer significant inaccuracies when the measurement is close enough for source geometry effects to be important.

Using the multipoint source model, the measured heat flux is assumed to be received from an array of isotropic point sources uniformly distributed over a two-dimensional plane oriented across the visible surface of the flame. A schematic illustrating this approach is presented in Fig. 2.18.

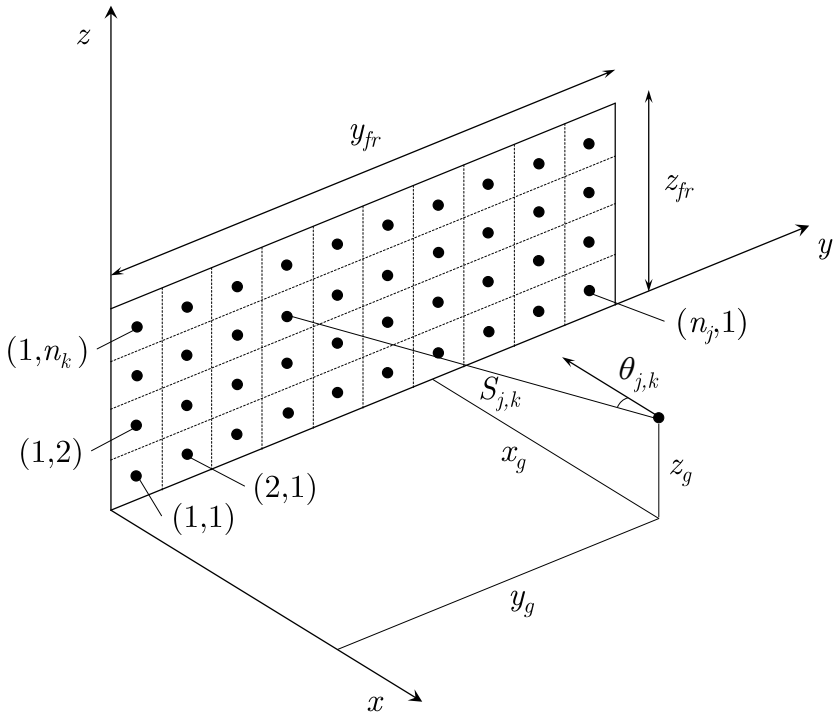

Figure 2.18: Schematic depicting the two-dimensional multipoint source model.

The radiative heat flux measured by the transducer, $\dot{q}''_g$, is evaluated as the weighted sum of radiation emitted by each individual point source so that

$$\dot{q}''_g = \frac{\chi_{rad}\,\dot{m}_{fuel}\,\Delta h_{comb}}{4\,\pi}\sum_{j=1}^{n_j}\sum_{k=1}^{n_k}\left(\frac{F_{j,k}\,\tau_{j,k}\,\cos\left(\theta_{j,k}\right)}{S_{j,k}^2}\right), \tag{2.23}$$

where $F_{j,k}$ is a weighting factor applied to the $(j,k)^{\text{th}}$ point source, n_j and n_k are respectively the number of point sources in the y and z directions, $\tau_{j,k}$ is the atmospheric transmissivity over the separation distance, $S_{j,k}$, between the $(j,k)^{\text{th}}$ point source and the heat flux transducer, and $\theta_{j,k}$ is the angle between the normal out of the transducer surface and the line of sight to the $(j,k)^{\text{th}}$ point source.

Note that the weighting factors, $F_{j,k}$, must always satisfy

$$\sum_{j=1}^{n_j}\sum_{k=1}^{n_k} F_{j,k} = 1. \tag{2.24}$$

From Fig. 2.18, geometric arguments yield

$$\cos\left(\theta_{j,k}\right) = \frac{x_g}{S_{j,k}}, \tag{2.25}$$

$$S_{j,k}^2 = x_g^2 + \left[y_g - \frac{y_{fr}}{n_j}\left(j - \frac{1}{2}\right)\right]^2 + \left[z_g - \frac{z_{fr}}{n_k}\left(k - \frac{1}{2}\right)\right]^2, \tag{2.26}$$

where (x_g, y_g, z_g) is the location of the heat flux transducer, and (y_{fr}, z_{fr}) gives the boundary dimensions of an arbitrary two-dimensional frame containing the flame.

Inserting Eq. 2.25 into Eq. 2.23 and solving for χ_{rad} then gives

$$\chi_{rad} = \frac{4\,\pi\,\dot{q}_g''}{\dot{m}_{fuel}\,\Delta h_{comb}\,x_g} \sum_{j=1}^{n_j}\sum_{k=1}^{n_k}\left(\frac{S_{j,k}^3}{F_{j,k}\,\tau_{j,k}}\right). \tag{2.27}$$

For the present study, the weighting factors, $F_{j,k}$, are determined via spatially-resolved flame images recorded using a FLIR ThermaCAM SC3000 infrared camera. The camera sensor has a spectral range between 8–9 μm, providing a maximum image resolution of 320 by 240 pixels at 60 frames per second. A sample grayscale infrared flame image is presented in Fig. 2.19.

Recorded flame images are synchronized with $\dot{q}_g''$ measurements and averaged over the response time of the transducer. The array of $F_{j,k}$ applicable to each $\dot{q}_g''$ measurement is then determined from the corresponding array of grayscale pixel intensities, $I_{j,k}$, in the synchronized image so that

$$F_{j,k} = \frac{I_{j,k}}{\sum_{j=1}^{n_j}\sum_{k=1}^{n_k} I_{j,k}}. \tag{2.28}$$

The array of point sources (n_j, n_k) is conveniently bounded by the frame of each image, where y_{fr} and z_{fr} are defined as the outer dimensions of each frame. As a result, it is not necessary to assume the flame shape a priori, provided the entire

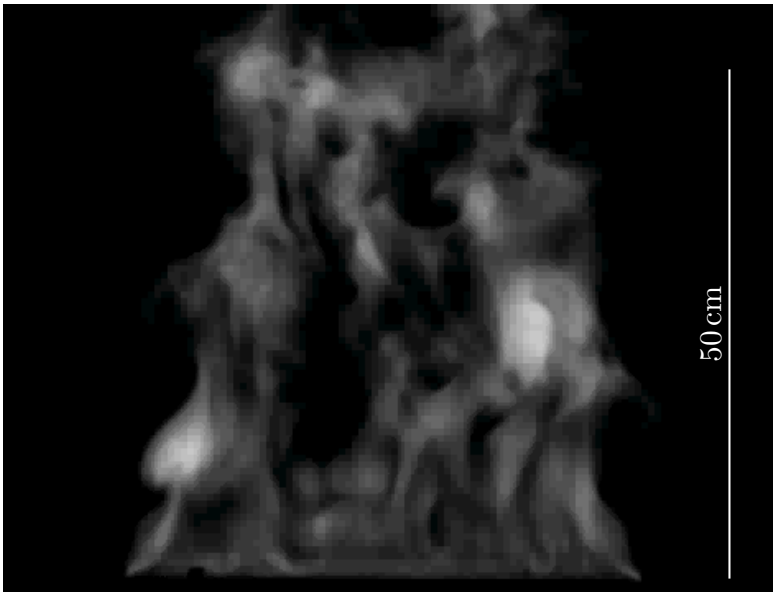

Figure 2.19: Sample infrared flame image.

flame is contained within the image and background interference is negligible. The flame shape is then resolved within each image, while the peripheral pixels around the flame (for which $I_{j,k} = F_{j,k} = 0$) do not affect the computation. The length-per-pixel in each frame is determined by placing an object with known length within the frame, which is then referenced during image processing.

The atmospheric transmissivity, $\tau_{j,k}$, in Eq. 2.27 is presently assumed to be unity for all point sources. This approximation is valid for the present configuration, where the heat flux transducer is relatively close to the flame, though for alternative conditions, such as those incorporating an increased presence of water-vapor (such as during water-mist suppression cases), the atmospheric transmissivity may be approximated using established methods [100]. Using Eq. 2.27 in conjunction with the recorded flame images and stated weighting factor conventions, χ_{rad} is evaluated from each $\dot{q}''_g$ measurement with an estimated uncertainty of roughly $\pm 4.5\%$.

Alternative to the multipoint model, the conventional single-point model characterizes the radiation source as a single isotropic point located at the flame centroid, yielding

$$\chi_{rad} = \frac{4\,\pi\,x_g^2\,\dot{q}_g''}{\dot{m}_{fuel}\,\Delta h_{comb}}. \tag{2.29}$$

which provides a simplified analogue to Eq. 2.27.

Taking the ratio of Eq. 2.27 divided by Eq. 2.29 then gives

$$\zeta = \frac{1}{x_g^3} \sum_{j=1}^{n_j} \sum_{k=1}^{n_k} \left(\frac{S_{j,k}^3}{F_{j,k}\,\tau_{j,k}} \right), \tag{2.30}$$

where ζ provides a measure of the relative agreement between the two source models, approaching a value of unity when the two models agree. Note that Eq. 2.30 is independent of $\dot{q}_g''$, and can be evaluated analytically as a function of transducer position (x_g, y_g, z_g), requiring only a spatially resolved image of the flame to define a representative $F_{j,k}$ array. Using two sample flame images from the present configuration with respective characteristic $L_f = 50\,\text{cm}$ and $L_f = 10\,\text{cm}$, ζ is plotted vs x_g $(y_g = y_{fr}/2, z_g = z_{fr}/2)$ in Fig. 2.20.

As shown in Fig. 2.20, the single-point model under-predicts the multipoint model with decreasing accuracy as the transducer is moved closer to the flame, an expected result that is consistent with previously reported results for axisymmetric flames [101]. For large x_g, where the single-point model is most valid, ζ correctly asymptotes toward unity. Comparing the trends for the two flames, the relative accuracy of the single-point model is shown to vary not only with x_g, but also with flame geometry, where differences in L_f also affect source model accuracy. Intuitively, a larger radiation source (increasing L_f) requires larger x_g to yield $\zeta \approx 1$.

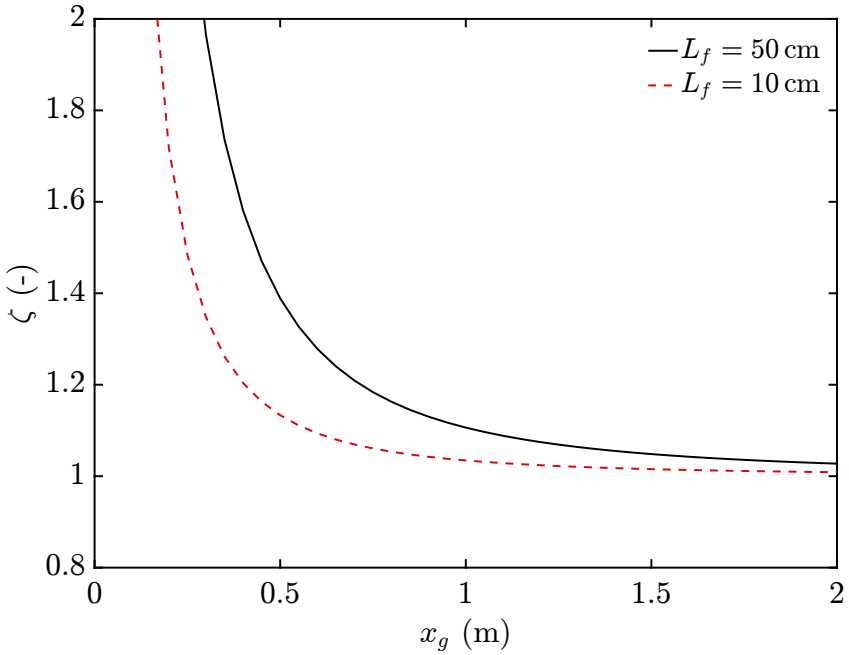

Figure 2.20: Ratio of multipoint to single-point radiation source models (ζ) plotted versus transducer position (x_g).

Applicable to any configuration, Eq. 2.30 may be combined with a representative image of the radiation source to determine a priori the appropriate transducer distance for accurate application of the simplified single-point source model. For the present configuration, where the transducer is located 1 m away from the flame, the single-point source model under-predicts the multipoint model by roughly 10% (see Fig. 2.20). In order to reduce this discrepancy to less than 1%, the transducer would need to be located more than 2 m away from the flame. Such large separation distances are not always feasible due to space constraints or limitations associated with achieving a measurable signal. For such situations, the multipoint model presents an attractive alternative, where Eq. 2.27 may be directly coupled with transducer measurements and resolved flame images to correct for source geometry affects.

2.3.4 Calorimetry

Rate of heat release ($\dot{Q}$) is generally regarded as the most important parameter available to characterize a fire hazard [102]. This parameter is useful and often essential in deriving various other fire properties including size, rate of growth/spread, material flammability and toxic species yields. Measurements of $\dot{Q}$ may also be used to evaluate combustion efficiency, η_{comb}, defined as

$$\eta_{comb} = \frac{\dot{Q}}{\dot{m}_{fuel}\,\Delta h_{comb}}, \tag{2.31}$$

which simply provides a dimensionless quantification of normalized flame strength and is an ideal metric for the assessment of suppression performance.

Despite its recognized importance, $\dot{Q}$ is typically difficult and costly to measure accurately, with only a limited set of feasible measurement techniques available. Of the available techniques, species-based calorimetry is widely recognized as the most appropriate [103, 104], whereby $\dot{Q}$ is derived from the rates of consumption and production of the major chemical species involved in the combustion reaction. The two standard formulations include oxygen-consumption (OC) or carbon-dioxide-generation (CDG) based methods [105–113].

Species-based calorimetry methods have been widely adopted by the fire testing and research communities and successfully employed in numerous studies [114–139], Unfortunately, most of these implementations utilize simplified formulations that rely on specific and often unstated assumptions. In particular, traditional formulations apply only to simple systems where the primary mass exchanges to/from

the combustion region are limited to the supply of fuel, entrainment of ambient air, and exhaust of combustion products. Certainly, this scenario adequately describes most fires, for which existing formulations have been shown to apply very well. However, for more complex systems with additional mass exchanges, such as those involving suppression agents or sprays, the existing formulations may not be applicable. The present configuration, which involves a diluted oxidizer with variable O_2 concentration, is a prime example of such a system.

Despite the wide body of existing literature, there is also a limited availability of general guidelines to direct the design and implementation of calorimetry measurements in complex applications. As a result, it can be difficult to confidently extend the traditional formulations to novel applications that may oppose their simplifying assumptions. In order to fill this need and permit highly accurate calorimetry measurements in the present configuration, a comprehensive derivation of the physical principles underlying species-based calorimetry and a corresponding generalized framework for the design of calorimetry measurement systems have been developed and are presented in Appendix A [140].

While more complex than the simplified expressions offered by traditional formulations, the framework presented in Appendix A is advantageous in that it is directly relatable to the physical principles from which species-based calorimetric methods are derived, offering transparency to the model formulation and the underlying assumptions. The formulations presented in Appendix A are also clearly representative of the conditions for which they have been developed, and may therefore be easily adapted to alternative applications requiring greater or lesser complexity.

To satisfy the calorimetry model presented in Appendix A, necessary measurements include the compositions and mass flow rates of the primary mass exchanges into and out of the combustion region. For the present configuration, the applicable control volume is depicted in Fig. 2.21, where mass exchanges include the fuel source ($\dot{m}_{fuel}$) with surrounding co-flowing oxidizer ($\dot{m}_{ox}$) and ambient air entrainment ($\dot{m}_a$). A reaction source term ($\dot{m}_k^{rxn}$) accounts for species consumption/generation due to combustion, while all $\dot{m}_{fuel}$, $\dot{m}_{ox}$, $\dot{m}_a$, and $\dot{m}_k^{rxn}$ are assumed totally captured within an exhaust collection system ($\dot{m}_e$).

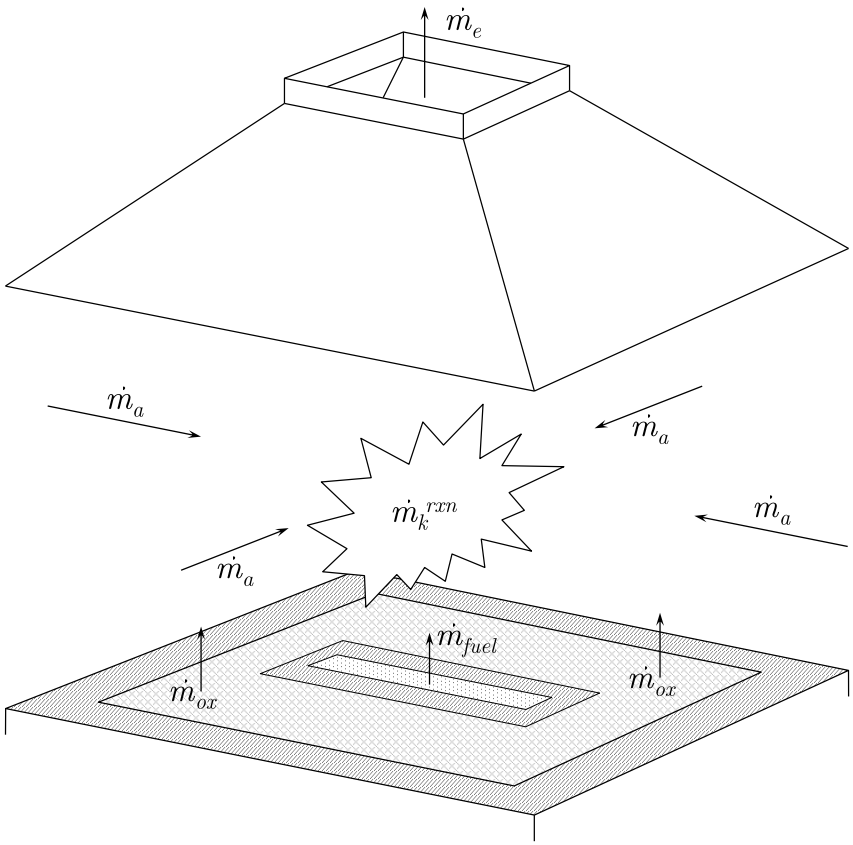

Figure 2.21: Control volume for species-based calorimetry analysis; a fuel source ($\dot{m}_{fuel}$) is located beneath an exhaust collection system ($\dot{m}_e$) with ambient air entrainment ($\dot{m}_a$), co-flowing oxidizer ($\dot{m}_{ox}$), and reaction source ($\dot{m}_k^{rxn}$). All $\dot{m}_{fuel}$, $\dot{m}_a$, $\dot{m}_{ox}$, and $\dot{m}_k^{rxn}$ are assumed totally captured within $\dot{m}_e$.

The experimental apparatus (Fig. 2.9) is centrally positioned roughly 1.1 m beneath a 2 m by 2 m fire-products collection hood connected to an exhaust evacuation system. A 60-cm-tall fiberglass curtain hangs from the perimeter of the hood to ensure total capture of all combustion products into the exhaust system. Within the exhaust system, measurement sensors are contained within a 3-m-long straight section of 28 cm inner-diameter round duct. All sensors are located roughly 5.2 m (18.5 diameters) downstream of the collection hood, such that sufficiently fully-developed and well-mixed flow conditions may be assumed.

A Veris Verabar V100 averaging pitot tube connected to a Setra Model 264 differential pressure transducer is used to measure the exhaust flow rate with an uncertainty of $\pm 1\%$ (see Eq. A.49, $C_f^e = 0.7530$). Adjacent to the pitot tube, an exposed-junction K-type thermocouple probe measures the exhaust temperature with an uncertainty of ± 2 K and response time of roughly 3 s.

A Michell Instruments PCMini52 relative humidity sensor is used to measure the exhaust H_2O content in situ with an uncertainty of $\pm 1\%$ RH and response time of roughly 10 s. The measured relative humidity is related to absolute humidity via a thermodynamic state equation for the saturation pressure of H_2O as a function of temperature [86]. This compensation is performed automatically by the sensor via simultaneous internal temperature measurement, significantly improving the accuracy and transient response of the measurement.

A sampling probe collects a portion of the exhaust flow for extractive composition measurements. The sampling probe consists of a 4.5 mm inner-diameter stainless-steel tube with 1.5 mm perforations spaced 1.27 cm uniformly along its

length, running the full diameter of the exhaust duct. A vacuum pump draws the exhaust sample from both ends of the probe, through a length of 3.2 mm inner-diameter tubing toward a rack of species analysis instrumentation. The sample passes through a 2 μm particulate filter, a section of Drierite^{TM} desiccant, and an additional 2 μm filter prior to analysis.

Composition measurements include O_2 content via a Rosemount Model 755 paramagnetic analyzer and CO_2 and CO content via a Siemens ULTRAMAT 23 infrared analyzer. Measurement uncertainties are ±1250 ppm O_2, ±1000 ppm CO_2, and ±100 ppm CO, with a response time of roughly 5 s for both analyzers. Prior to each experiment, all species analyzers are calibrated against reference mixtures with known composition to ensure measurement accuracy and minimize effects of calibration drift. The exhaust sampling system is also used to measure the ambient composition, which is assumed to remain constant at initial condition measured prior to each experiment.

Additional required measurements including the flow rates and compositions of the fuel and oxidizer are described in Sec. 2.2. In particular, unmeasured species in the oxidizer are estimated by assuming the oxidizer comprises a uniform mixture of ambient air with added suppressant. Measurements of $X_{O_2}^{ox}$ and $X_{H_2O}^{ox}$ (see Secs. 2.2.3 and 2.2.4 respectively) are then directly related to the mole fractions of CO_2 and CO in the oxidizer based on the measured composition of those species in the ambient. For anchored experiments (see Sec. 2.2.3), the O_2 flow introduced by the anchor is directly included as an additional term in the applicable expressions in the calorimetry formulation (see Appendix A).

2.4 Data Collection and Analysis

Experiments in the present configuration begin with the establishment of a stable unsuppressed flame in co-flowing oxidizer for either CH_4 or C_3H_8 fuel and for either non-anchored or anchored condition. From this initial state, the suppression potential of the oxidizer ($X_{O_2}^{ox}$ or Y_m^{ox}) is gradually increased, through introduction of either gaseous N_2 or fine water mist into the oxidizer, until the flame is extinguished. The rate of change in oxidizer suppression potential is sufficiently slow to ensure steady flame behavior is maintained at all incremental suppression conditions ($dX_{O_2}^{ox}/dt \approx 0.005\,\mathrm{min}^{-1}$, $dY_m^{ox}/dt \approx 0.01\,\mathrm{min}^{-1}$). Flame images and measurement data are recorded continuously throughout the duration of each experiment.

Measurement data are recorded using a National Instruments (NI) data acquisition (DAQ) system incorporating a SCXI-1600 USB DAQ module, a SCXI-1102 signal conditioner, and a SCXI-1303 terminal block, all integrated within a SCXI-1000 chassis. This system provides 32 measurement channels with a 16-bit analog-to-digital converter and a maximum data rate of 200,000 total samples per second. The signal conditioner provides a 2 Hz low-pass filter across each measurement channel to eliminate high-frequency fluctuations in the data signals. Data management and visualization are conducted using the DAQ system-associated NI LabVIEW software. Using this system, data for all instrumentation are recorded continuously at a rate of 10 Hz, where measurement response delays, due to differences in flow transport time to the various instruments, are compensated to provide synchronous data collection across all measurements.

Data are post-processed using a moving-average temporal filter with an averaging window of 10 s to further smooth fluctuations in the measured trends. The filtered data are then truncated to remove extraneous measurements recorded before the initiation of suppression and after the occurrence of extinguishment. The first data point in the truncated set is defined as the measurement recorded 10 s before the appropriate suppression potential metric ($X_{O_2}^{ox}$ or Y_m^{ox}) deviates by more than 0.1% from its initial ambient value. The final data point is then defined as the measurement recorded just before the fuel flow is shut off, where fuel shut-off is manually performed in each experiment immediately following flame extinction.

Uncertainties for all experimentally-derived quantities are estimated using a Monte-Carlo error propagation analysis [141]. By this method, every individual raw measurement is expanded to produce a one-dimensional array of $N+1$ values, with the first value in the array representing the actual measurement, and the remaining values in the array representing a random sample of N values drawn from a normal probability distribution with mean equal to the actual measurement, and standard deviation equal to the uncertainty of the recording instrument.

All mathematical operations performed on the raw measurements are then repeated for every value in the associated random sample of each measurement. Any quantity derived from the raw measurements then also includes an associated random sample, where the uncertainty in the derived quantity is defined as twice the associated sample standard deviation (representing a 95% confidence interval). For the present study, a random sample size of $N = 10,000$ has been found appropriate to provide converged uncertainty statistics for all experimentally-derived quantities.

Chapter 3: Simulation

3.1 Overview

Numerical simulations of the experiments are conducted using the Fire Dynamics Simulator (FDS), an open-source computational fluid dynamics (CFD) software tool developed by the National Institute of Standards and Technology [4]. FDS is widely used throughout the fire-safety consulting and design industries by practicing fire protection engineers and is thus a premier candidate for evaluation and improvement of its flame suppression predictive capabilities. A brief introduction to the primary features of the FDS numerical solver is presented in Sec. 3.2.

The present work seeks to evaluate the performance of and offer improvements to the baseline extinction and reignition models available within FDS, both of which use the concept of a critical flame temperature [142]. As applied in these models, a critical flame temperature should be viewed as an empirically-determined, fuel-specific quantity approximating the flame temperature at the limits of flammability (considering heat losses). Comparisons between simulated and experimental results provide a suitable metric to evaluate the capability of these models to describe flame suppression. A detailed description of the extinction and reignition treatments considered in the present work are provided respectively in Secs. 3.2.1 and 3.2.2.

Simulations are constructed to match as closely as possible the configuration of the present experimental facility, including all applicable geometric and boundary conditions. For the present study, simulations are limited to cases including the use of CH_4 fuel and the N_2 suppression system. Simulations of cases involving C_3H_8 fuel and the water-mist suppression system are left to future work. A detailed description of the numerical configuration is presented in Sec. 3.3, while considerations of the requirements for adequate numerical resolution in this configuration (for both the gas-phase flow solver and the radiative transfer solver) are discussed in Sec. 3.4.

3.2 Numerical Solver

FDS provides a variable density, low Mach-number Navier-Stokes solver tuned for buoyancy-driven flows with heat release. FDS features a block-structured, Cartesian staggered grid for numerical meshing capability and a parallel computing capability using MPI and OpenMP protocols. The numerics are generally second-order accurate with explicit time integration. Reaction chemistry is first-order accurate and time-split from transport, consistent with the classical eddy-dissipation concept (EDC) model [143, 144], which FDS uses to describe turbulent combustion. As applied in the present work, combustion is treated with a single-step, global reaction involving lumped species for the fuel, oxidizer, and products of combustion [145].

A large eddy simulation (LES) framework is employed for subgrid-scale turbulence modeling, where the LES residual stress and transport terms are closed via gradient diffusion coupled with a modified version of the Deardorff eddy-viscosity

model [146], using an algebraic model for the subgrid kinetic energy based on scale similarity [147], and constant values for the turbulent Schmidt and Prandtl numbers.

FDS models thermal radiation via the radiative transfer equation (RTE) using a discrete-ordinates, finite-volume method with gray absorption properties [148]. In the present study, the description of thermal radiation is further simplified by modeling flame emission using the concept of a global radiative loss fraction (χ_{rad}); where χ_{rad} is prescribed in the simulations a priori from experimental measurements.

For a comprehensive discussion detailing the mathematical models employed in the FDS solver, the reader is referred to the FDS technical reference guide [149]. Additional resources [150, 151], present an extensive catalog of verification and validation cases for the primary FDS models. Particularly relevant to the present work, the local volumetric heat release rate due to combustion, $\dot{Q}'''$, is given by

$$\dot{Q}''' = -\sum_k \dot{m}_k''' \, \Delta h_{f,k}^{\circ}, \tag{3.1}$$

where $\dot{m}_k'''$ is the volumetric mass reaction rate, and $\Delta h_{f,k}^{\circ}$ the mass-specific standard enthalpy of formation, for each lumped species, k, in the reaction. The volumetric mass reaction rate of fuel, $\dot{m}_{fuel}'''$, is evaluated as

$$\dot{m}_{fuel}''' = -\rho \frac{\min\left(Y_{fuel}, Y_{ox}/s\right)}{\tau_{mix}}, \tag{3.2}$$

where ρ is the local mass density, Y_{fuel} and Y_{ox} are the local mass fractions of fuel and oxidizer, and s is the stoichiometric oxidizer-to-fuel mass ratio. Other $\dot{m}_k'''$ are then determined from $\dot{m}_{fuel}'''$ based on stoichiometric reaction coefficients.

In Eq. 3.2, τ_{mix} is a modeled characteristic mixing time-scale for the reaction with alternate definitions based on the resolution of the flow-field [152]. For all

numerical resolutions considered in the present study (see Sec. 3.4), τ_{mix} is governed by turbulent advection and defined as

$$\tau_{mix} = \frac{C_u \, \Delta}{\sqrt{(2/3) \; k_{sgs}}}, \tag{3.3}$$

where $C_u = 0.4$ is a model coefficient calibrated to match experimental flame height measurements [151], $\Delta = (\Delta x \, \Delta y \, \Delta z)^{1/3}$ is the LES filter width defined by the local grid resolution $(\Delta x, \Delta y, \Delta z)$, and k_{sgs} is the modeled subgrid turbulent kinetic energy derived from the turbulence sub-model.

Using the Deardorff model [146], the turbulent viscosity, μ_t, is given by

$$\mu_t = \rho \, C_v \, \Delta \, \sqrt{k_{sgs}}, \tag{3.4}$$

where $C_v = 0.1$ is a model coefficient set to match a value reported in the literature [153]. Turbulent transport coefficients for mass and energy are then derived from μ_t via constant Schmidt and Prandtl numbers, $Sc_t = Pr_t = 0.5$.

The subgrid turbulent kinetic energy is evaluated as

$$k_{sgs} = \frac{1}{2}\Big((u - \hat{u})^2 + (v - \hat{v})^2 + (w - \hat{w})^2 \Big), \tag{3.5}$$

where $[u, v, w]$ are the cell-mean values of the x, y, and z-components of the local velocity field, and $[\hat{u}, \hat{v}, \hat{w}]$ are weighted averages of their respective cell-mean counterparts over the adjacent computational cells (representing a test-filtered velocity field over length scale 2Δ) [147, 149].

The fundamental limitation of the mixing-controlled combustion scheme presented in Eqs. 3.1–3.5, is that combustion is guaranteed to occur anywhere fuel and oxidizer are mixing, regardless of local conditions for temperature or fuel/oxidizer

dilution. This represents the characteristic 'mixed-is-burned' treatment adopted by the EDC framework and has the advantage that detailed heat transfer and chemical kinetics treatments are not necessary to achieve primary ignition. As a result however, additional modeling provisions must be made in order to account for flame extinction (Sec. 3.2.1) and prevent spurious reignition (Sec. 3.2.2).

3.2.1 Extinction Treatment

Accurate modeling of flame extinction in fire applications remains a significant challenge in modern CFD codes. This is because the physical phenomena that govern extinction are characterized by quantities, including the flame temperature and the fuel-oxidizer mixing rate at the flame sheet, that cannot be resolved numerically in configurations of practical interest. Still, much progress has been made in recent years toward meaningful improvement in the extinction modeling capability of open-source LES solvers [63–67].

According to the established extinction theory [31–46], diffusion flames may be extinguished according to three primary mechanisms, which include

1. Thermal quenching — characterized by flame weakening due to heat losses, such as that due to radiation, flame interaction with a cold boundary, or cooling induced by inert dilution and/or the latent evaporation of water droplets;

2. Aerodynamic quenching — characterized by flame weakening due to flow-induced perturbations, which increase the rate of fuel-oxidizer mixing beyond that capable of sustaining combustion; and

3. Kinetic quenching — characterized by flame weakening due to interactions between reaction intermediates and chemically active agents, which act to limit the chain-branching reactions responsible for self-sustaining combustion.

The flame extinction algorithm implemented in FDS uses the concept of a critical flame temperature, which adequately addresses the thermal quenching mechanism. The aerodynamic and kinetic quenching mechanisms however, are not represented in this model and FDS simulations applied to cases including these effects should not be expected to yield reasonable suppression performance. In the present configuration, thermal quenching acts as the dominant mode of extinction for either N_2 or water-mist suppression; therefore the baseline critical flame temperature based extinction model is sufficient.

The criterion for flame extinction in FDS incorporates an enthalpy balance where in order for combustion to occur, the potential combustion heat release must be sufficient to increase the mean temperature of the reaction mixture above a critical value, T_{ext}, defined as the critical flame temperature. Combustion is allowed to proceed if the inequality given by

$$\hat{Y}_{fuel}(h_{fuel}(T) + \Delta h_{comb}) + \hat{Y}_{ox}h_{ox}(T) + \hat{Y}_{pr}h_{pr}(T) > \hat{Y}_{fuel}h_{fuel}(T_{ext}) + \hat{Y}_{ox}h_{ox}(T_{ext}) + \hat{Y}_{pr}h_{pr}(T_{ext}), \quad (3.6)$$

is satisfied, where T is the initial cell temperature, $[\hat{Y}_{fuel}, \hat{Y}_{ox}, \hat{Y}_{pr}]$ and $[h_{fuel}, h_{ox}, h_{pr}]$ are, respectively, the mass fractions and mass-specific sensible enthalpies of the fuel, oxidizer, and products of combustion in the reaction mixture, and Δh_{comb} is the

mass-specific enthalpy of combustion of the fuel. Here, extinction occurs if the local concentrations of fuel and oxidizer and/or the local cell temperature are too low to support combustion (thermal quenching).

The reaction-mixture components in Eq. 3.6 are defined via the following,

$$\hat{Y}_{fuel} = \min\left(Y_{fuel}, Y_{ox}/s\right), \tag{3.7}$$

$$\hat{Y}_{ox} = s\,\hat{Y}_{fuel}, \tag{3.8}$$

$$\hat{Y}_{pr} = \left(\hat{Y}_{ox}/Y_{ox}\right)\left(Y_{fuel} - \hat{Y}_{fuel} + Y_{ox}\right), \tag{3.9}$$

where $[Y_{fuel}, Y_{ox}, Y_{pr}]$ are the local mass fractions of the fuel, oxidizer, and products of combustion in the computational cell at the beginning of the combustion time step (after transport) and s is the stoichiometric oxidizer-to-fuel mass ratio for combustion. These definitions for the reaction mixture components (Eqs. 3.7–3.9) have the effect that excess fuel is treated as a diluent but excess oxidizer is not. As a result of this convention, combustion is likely to occur in a cell having a small amount of fuel in excess oxidizer, but is likely to be suppressed in a cell having a small amount of oxidizer in excess fuel. This treatment accommodates reasonable combustion and extinction performance in relatively coarse computational cells, as are frequently used in simulations of practical-scale fire configurations.

The default critical flame temperature, $T_{ext} = 1600\,\mathrm{K}$, as used in the present study, is representative of typical hydrocarbon fuels [142]. If the criterion specified in Eq. 3.6 fails, combustion is suppressed and the reaction source terms for species generation/consumption and heat release are set to zero for that computational cell, at that time step ($\dot{Q}''' = \dot{m}_k''' = 0$ in Eqs. 3.1 and 3.2).

3.2.2 Reignition Treatment

Accurate CFD modeling of flame ignition and reignition in fire applications presents perhaps an even greater challenge than that for flame extinction. As with extinction, ignition phenomena are governed by quantities (flame temperature and fuel-oxidizer mixing rate) that cannot be resolved numerically in configurations of practical interest. Compounding this issue is the question of how to discern in the model the difference between primary ignition at the fuel source (which is often desirable and necessary to achieve a stabilized flaming condition) and spurious reignition occurring downstream of localized extinction events (which is undesirable when such reignition is non-physical).

By inspection of the combustion scheme presented in Eqs. 3.1–3.5, which is representative of the broader EDC combustion framework, it is apparent that spurious reignition may be an issue anywhere fuel and oxidizer mix downstream of a localized extinction event. Including consideration for the extinction criterion presented in Sec. 3.2.1, reignition occurs as long as fuel and oxidizer are locally present in sufficient quantities to satisfy Eq. 3.6, which is possible even for low initial cell temperatures near ambient condition. An example of this fact is the initial ignition of primary combustion at the start of a simulation, which desirably does not require any specification for an ignition source. Still, any non-physical, low-temperature reignition of previously extinguished fuel can significantly degrade the suppression performance of the extinction model. For applications in which suppression is the primary modeling interest, such spurious reignition must be prevented.

Restricting available solutions, any ignition or extinction criterion that is implemented to prevent spurious reignition cannot be generally applied in the model without also suppressing primary ignition at the fuel source. This issue may be circumvented by modeling primary ignition, though this would require an explicit ignition source coupled with detailed reaction kinetics and a highly-resolved treatment for heat transfer at the fuel source. Such an option is generally unavailable in fire applications which often include fuel sources that cannot be described with detailed reaction kinetics and complex configurations for which resolved heat transfer at the fuel source would require prohibitive computational cost. Despite these challenges, recent affiliated works have made notable progress in modeling and distinguishing ignition, extinction, and reignition processes in LES applications [64–67].

Simulations in the present configuration highlight the noted issues surrounding spurious reignition, including conditions for which flame extinction leads directly to non-physical reignition if explicit treatment preventing such reignition is not provided in the model. Proper reignition treatment may be guided by the established ignition theory [68–73], from which flame ignition and reignition phenomena may be classified according to three primary mechanisms, including

1. Autoignition — characterized by a spontaneous autoignition event in a fuel-oxidizer mixture (which may be initially premixed or non-premixed);

2. Edge flame propagation — characterized by the piloted ignition of a fuel-oxidizer mixture due to the propagation of a partially-premixed edge (triple) flame along the stoichiometric surface; and

3. Flame-flame interaction — characterized by the piloted ignition of a fuel-oxidizer mixture due to interaction with an adjacent flame in a direction normal to the stoichiometric surface.

It has not yet been demonstrated which of these mechanisms dominate reignition processes occurring in turbulent fire applications, though each likely plays a role. Existing insight suggests that these mechanisms are either temperature-controlled (mechanism 1) or mixing-controlled (mechanisms 2 and 3) [68]. As a preliminary modeling attempt, and following the convention of the critical flame temperature employed by the extinction criterion, a simple temperature-based ignition/reignition criterion may be written as

$$T > T_{ign}, \tag{3.10}$$

where T is the initial temperature of the computational cell (before the combustion time step) and T_{ign} is a critical temperature for reignition. As with the extinction criterion, if the inequality in Eq. 3.10 is unsatisfied, combustion is suppressed and the reaction source terms for species generation/consumption and heat release are set to zero for that cell, at that time step ($\dot{Q}''' = \dot{m}_k''' = 0$ in Eqs. 3.1 and 3.2).

As previously noted, Eq. 3.10 cannot be generally applied in the solver without requiring an explicit treatment for primary ignition at the fuel source. To avoid this complication, implementations with selective application of Eq. 3.10 that still permit spontaneous primary ignition are explored. Three simple modeling cases, respectively denoted M1, M2, and M3, and each utilizing Eqs. 3.6 and 3.10 to treat extinction and reignition in various capacities, are summarized as follows [67].

In each of the following cases, the baseline single-step global reaction scheme employed for primary combustion follows the EDC treatment and is defined as

$$\text{Fuel} + s\,\text{Oxidizer} \rightarrow (1+s)\,\text{Products}, \tag{R1}$$

where reaction R1 is allowed to proceed only if the inequalities in both Eqs. 3.6 and 3.10 are satisfied, subject to the respective temperature criteria T_{ext} and T_{ign}.

The first case, M1, represents the standard EDC behavior for which $T_{ext} = 1600\,\text{K}$ and $T_{ign} = 0\,\text{K}$ everywhere in the computational domain. Here, Eq. 3.10 is universally satisfied such that M1 includes no provision to prevent spurious reignition. As previously stated, spurious reignition may occur if, downstream of a region where Eq. 3.6 is unsatisfied (and therefore reaction R1 is suppressed), the resulting unburned fuel propagates to a region where Eq. 3.6 is satisfied such that reaction R1 then proceeds (potentially at non-physical low temperature).

The second case, M2, is a simple extension of M1, but including a small prescribed ignition zone near the fuel source within which $T_{ign} = 0\,\text{K}$. Elsewhere in the domain, $T_{ign} = 900\,\text{K}$, a value approximately equal to an experimentally measured auto-ignition temperature for CH_4 fuel [154]. Everywhere in the domain, $T_{ext} = 1600\,\text{K}$, consistent with M1. The ignition zone is defined within a region that extends 5 mm below, 5 mm around, and 2 cm above the surface of the fuel port. A diagram illustrating the bounds of the ignition zone is provided in Fig. 3.1.

The spatially-variable application of T_{ign} employed by M2 effectively eliminates the issue of spurious reignition. Reignition is allowed to occur, but only if the local cell temperature is high enough to support such a process (via Eq. 3.10).

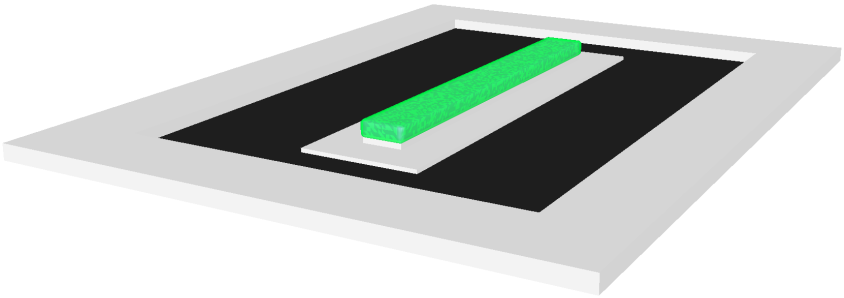

Figure 3.1: Diagram of the ignition zone applied in modeling case M2.

The confined region of the ignition zone permits the convenience and simplicity of spontaneous primary ignition, but does so without subjecting the bulk of the computational domain to this convention. Despite these advantages, the specification of this zone is somewhat arbitrary and guidelines for its size and location do not yet exist. These are subjects of interest in the present work.

The third case, M3, follows conventions developed in recent affiliated works [64–67], separating ignition and reignition using a tiered reaction mechanism. Including the primary reaction, R1, two additional reactions are introduced as

$$\text{Fuel} + s\,\text{Oxidizer} \rightarrow \text{Fuel}^* + s\,\text{Oxidizer}, \tag{R2}$$

$$\text{Fuel}^* + s\,\text{Oxidizer} \rightarrow (1+s)\,\text{Products}, \tag{R3}$$

where Fuel* is a secondary fuel species representing unburned fuel that has had the opportunity to react, but has been suppressed by Eq. 3.6. Here, reaction R2 acts as a mutually-exclusive alternate reaction pathway to reaction R1, transforming the primary Fuel into Fuel* if, and only if, R1 is suppressed. Reaction R3 then provides for the reignition of Fuel*, where the reignition criterion in Eq. 3.10 may be independently applied to R3 without affecting primary ignition in R1.

In M3, T_{ext} and T_{ign} apply uniformly throughout the domain but take different values for each reaction. For reaction R1, $T_{ext} = 1600\,\mathrm{K}$ and $T_{ign} = 0\,\mathrm{K}$, equivalent to the treatment in M1. For reaction R2, $T_{ext} = 0\,\mathrm{K}$ and $T_{ign} = 0\,\mathrm{K}$, signifying that R2 is always unrestricted whenever R1 is suppressed. For reaction R3, $T_{ext} = 1600\,\mathrm{K}$ and $T_{ign} = 900\,\mathrm{K}$, matching the treatment in M2 (outside the ignition zone). A summary of the critical temperature parameters, T_{ext} and T_{ign}, as presently applied in cases M1, M2, and M3 is displayed in Table 3.1.

The tiered reaction mechanism adopted in case M3 is advantageous in that it does not require an arbitrarily specified ignition zone and is therefore configuration independent. To its disadvantage however, M3 requires the additional complexity of reactions R2 and R3 and the computational expense of transporting an additional reacting species in Fuel*.

It is also important to recognize the implications of the stoichiometric requirement for oxidizer in the fuel transformation reaction, R2. This convention is necessary for the system of reactions R1–R3 to reduce back to the classical EDC treatment (R1) in cases of zero or total extinction; however, in situations where reaction R1 is extinguished and there is insufficient oxidizer to support reaction R2,

Table 3.1: Critical temperature parameters for model cases M1, M2, and M3.

Case	Reaction	T_{ext} (K)	T_{ign} (K)
M1	R1	1600	0
M2	R1	1600	900
M3	R1	1600	0
	R2	0	0
	R3	1600	900

fuel transformation will fail, permitting the persistence of the primary fuel in conditions of extinction, and providing the potential for spurious reignition to later occur (see Fig. 4.19 for a visualization of this effect). While technically permissible, this issue is limited to cases of extreme oxidizer dilution and in the majority of practical applications, M3 effectively eliminates spurious reignition.

As originally presented in previous work [64–66], no extinction criterion is applied to reaction R3 (equivalent to $T_{ext} = 0\,\mathrm{K}$), so that the only restriction on R3 is the ignition temperature criterion provided by Eq. 3.10. This treatment creates an issue in that reaction R3 may then permit combustion outside the limits of flammability, where heavily diluted fuel-oxidizer mixtures are allowed to burn if their initial temperature exceeds T_{ign}. This issue is limited to $T_{ign} < T_{ext}$, though such is typically the case. The convention adopted in the present work, where $T_{ext,R3} = T_{ext,R1}$ adequately prevents this issue and is therefore preferred.

3.3 Numerical Configuration

An illustration of the numerical configuration is depicted in Fig. 3.2, which visualizes the simulated flame at ambient condition. The computational domain is a 2.0-m-wide by 2.0-m-long by 2.0-m-tall box ($x \times y \times z$), which is large enough to prevent excessive boundary-condition effects on the simulated flame. This domain contains a numerical grid with two levels of refinement. The level-one refinement region comprises a 1.0-m-wide by 1.0-m-long by 1.0-m-tall box, centered around and above the experimental facility and flame. This region contains a uniform numerical

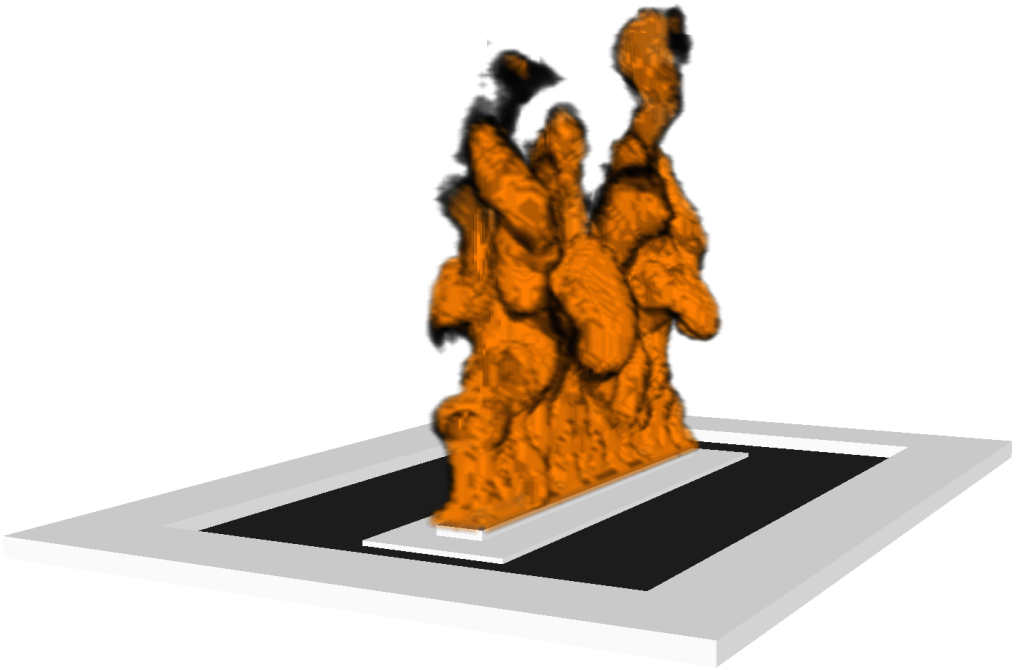

Figure 3.2: Illustration of the numerical configuration; a 50 kW CH_4 diffusion flame is visualized where the local volumetric heat release rate exceeds 200 kW/m^3.

grid in each coordinate direction with $\Delta x = \Delta y = \Delta z = 5.0$ mm. The level-two refinement region comprises the remainder of the computational domain, extending 1 m above and 0.5 m around the level-one refinement region in each direction and containing a uniform numerical grid with $\Delta x = 10.0$ mm. The total number of computational cells in both regions is 15 million.

A reduced computational domain comprising a 0.8-m-wide by 1.0-m-long by 1.0-m-tall box, having a baseline uniform numerical grid with $\Delta x = 5.0$ mm (total 6.4 million cells) is also employed for focused grid-convergence and model sensitivity studies (Secs. 3.4.1 and 4.3.2 respectively).

All edges of the computational domain feature an open, passive-flow boundary condition, with a background species of ambient air. The boundary conditions

at the fuel and oxidizer ports feature a prescribed mass-flux boundary condition (accounting for both convective and diffusive components), with values specified to match the experiment (fuel mass flow, $\dot{m}_{fuel} = 1\,\mathrm{g/s}$, and oxidizer mass flow, $\dot{m}_{ox} = 85\,\mathrm{g/s}$). The fuel and oxidizer, as well as any ambient entrainment, enter the domain with a constant temperature of $T_\infty = 293\,\mathrm{K}$. All solid surfaces within the domain, comprising the structural rim of the oxidizer apparatus and the ceramic fiberboard around the fuel port, are described as inert, isothermal objects with constant temperature, $T_\infty = 293\,\mathrm{K}$, and with zero-flow boundary condition. At initial condition, the interior of the domain includes a uniform composition of air at $T_\infty = 293\,\mathrm{K}$ with ambient relative humidity of 40%.

For comparison with N_2 suppression measurements, simulations feature controlled variation in the value of $X_{O_2}^{ox}$ applied at the oxidizer-port boundary condition. Variation in $X_{O_2}^{ox}$ is achieved by controlling the relative mass fluxes of air and N_2 leaving the oxidizer-port, which are varied to maintain a constant total oxidizer flow rate, $\dot{m}_{ox} = 85\,\mathrm{g/s}$. At the start of each simulation ($t = 0\,\mathrm{s}$), $X_{O_2}^{ox} = 0.21$, remaining constant at this value for the first 5 s of simulation time. This provides a sufficient duration to achieve steady conditions in the flame and oxidizer flow fields.

After $t = 5\,\mathrm{s}$, the value of $X_{O_2}^{ox}$ is steadily decreased at a rate of $dX_{O_2}^{ox}/dt = 0.002\,\mathrm{s}^{-1}$. Simulations are conducted for a total duration of 60 s so that $X_{O_2}^{ox} = 0.10$ at the end of the simulation, a value sufficient to achieve global flame extinction. Occurring concomitantly with the reduction in $X_{O_2}^{ox}$, the value of χ_{rad} also steadily decreases over the course of the simulation, with a prescribed trend matching that measured in the experiment (see Sec. 4.2.4).

In addition to the previously described transient simulations, which feature continuously variable $X_{O_2}^{ox}$, additional steady-state simulations are conducted to provide converged turbulent statistics at discrete $X_{O_2}^{ox}$ conditions. For these simulations, $X_{O_2}^{ox} = 0.21$ again for the first 5 s of the simulation to establish a stabilized ambient flaming condition. After $t = 5$ s, $X_{O_2}^{ox}$ is decreased rapidly over a 3 s duration to a final specified value, which is then held constant for the remainder of a 40 s duration simulation. Turbulent statistics are collected over the final 30 s of these simulations, during a period when the flow is statistically stationary.

Simulations are conducted using 60 processors (reduced-domain simulations use 40) on the University of Maryland Deepthought2 high-performance computing cluster, a large-scale Linux-based system of interconnected compute nodes. Typical simulations require roughly 2500 processor-hours using Intel Ivy Bridge E5-2680v2 2.80 GHz processors.

3.4 Numerical Resolution

3.4.1 Gas-Phase Flow Solver

To evaluate the numerical resolution requirement for a given configuration, it is necessary to consider the integral length scales characterizing the applicable flow field. For the present configuration, the integral length scales of interest include the flame height ($L_f \approx 50$ cm) and the flame width (approximated as the burner width, $W_b = 5$ cm). Here, the limiting length scale is the burner width, and for the baseline numerical resolution of $\Delta x = 5.0$ mm, $W_b/\Delta x = 10$, indicating that this length scale

is resolved over ten computational cells. This resolution may be considered marginal in the near-field region of the flame base (where $W_f \approx W_b$), but adequate in the intermediate and far-field regions within and above the bulk of the flame (where W_f increases with elevation so that $W_f > 10.0\,\text{mm}$ and $W_f/\Delta x > 20$ at mid-flame height, $z = 25\,\text{cm}$). Still, it may be questionable whether this resolution accurately captures the transition from laminar to turbulent flow near the flame base.

To evaluate grid-convergence in the present configuration, a series of simulations have been conducted featuring uniform grid resolution corresponding to $\Delta x = 20.0\,\text{mm}$, $10.0\,\text{mm}$, $5.0\,\text{mm}$, and $2.5\,\text{mm}$. These simulations are conducted using the reduced computational domain (see Sec. 3.3), with $X_{O_2}^{ox} = 0.21$ (no suppression), and each for a duration of 30 s. Selected diagnostics include vertical centerline (z-direction), and lateral cross-flame profiles (x-direction) of various locally computed quantities including volumetric heat release rate, gas-phase temperature, z-component of flow velocity, and the resolved and subgrid turbulent kinetic energies. Time-mean and root-mean-square (rms) statistics for each quantity are gathered over the final 25 s of each simulation. Run-time characteristics for each resolution case are presented in Table 3.2, comparing the total number of cells, processors, and computational cost applicable to each resolution.

Table 3.2: Run-time characteristics for simulations with varying grid resolution.

Δx (mm)	$W_b/\Delta x$ (-)	# Cells (-)	# Processors (-)	CPU Time (hr)
20.0	2.5	356,000	2	22
10.0	5.0	1,056,000	5	111
5.0	10.0	6,400,000	40	1,085
2.5	20.0	51,200,000	320	30,655

Figure 3.3 presents comparisons of vertical centerline and cross-flame profiles of the time-mean and rms volumetric heat release rate, $\dot{Q}'''$, among each resolution case. As shown, grid-convergence is not observed in mean $\dot{Q}'''$ for the presently considered resolutions, though variations are relatively slight ($\sim$10%), with maximum deviation in the peak mean value of $\dot{Q}'''$ on the order of 1000 kW/m^3 amongst all resolutions. Comparatively, $\dot{Q}'''_{rms}$ is significantly under-predicted by the coarser resolutions, with deviation in the peak value of more than 6000 kW/m^3 compared to the finest resolved case at $\Delta x = 2.5$ mm. These results indicate that significant unresolved turbulent fluctuations in the flame sheet location persist for $\Delta x \geq 2.5$ mm; however, the impact of these fluctuations on the mean field are comparatively slight. Certainly, the characteristic length scale of a turbulent flame sheet is on the order of 1 mm or less, and should not be expected to be resolved in the presently considered resolutions, nor in any typical large eddy simulation.

Figure 3.4 similarly presents comparisons of vertical centerline and cross-flame profiles of the time-mean and rms gas temperature, T. As shown, adequate grid-convergence is observed for $\Delta x \leq 5.0$ mm in the mean temperature field, though T_{rms} is again under-predicted on the order of 50 K compared to the finest resolved case at $\Delta x = 2.5$ mm. These results also indicate that there remain unresolved turbulent fluctuations in the temperature field for $\Delta x \geq 2.5$ mm, though these fluctuations negligibly impact the mean field. The simulated peak mean value of $T \approx 1200$ K also closely resembles a value of 1191 K predicted by an empirical correlation developed for line-fire geometries from corresponding experimental measurements in a similar configuration [155].

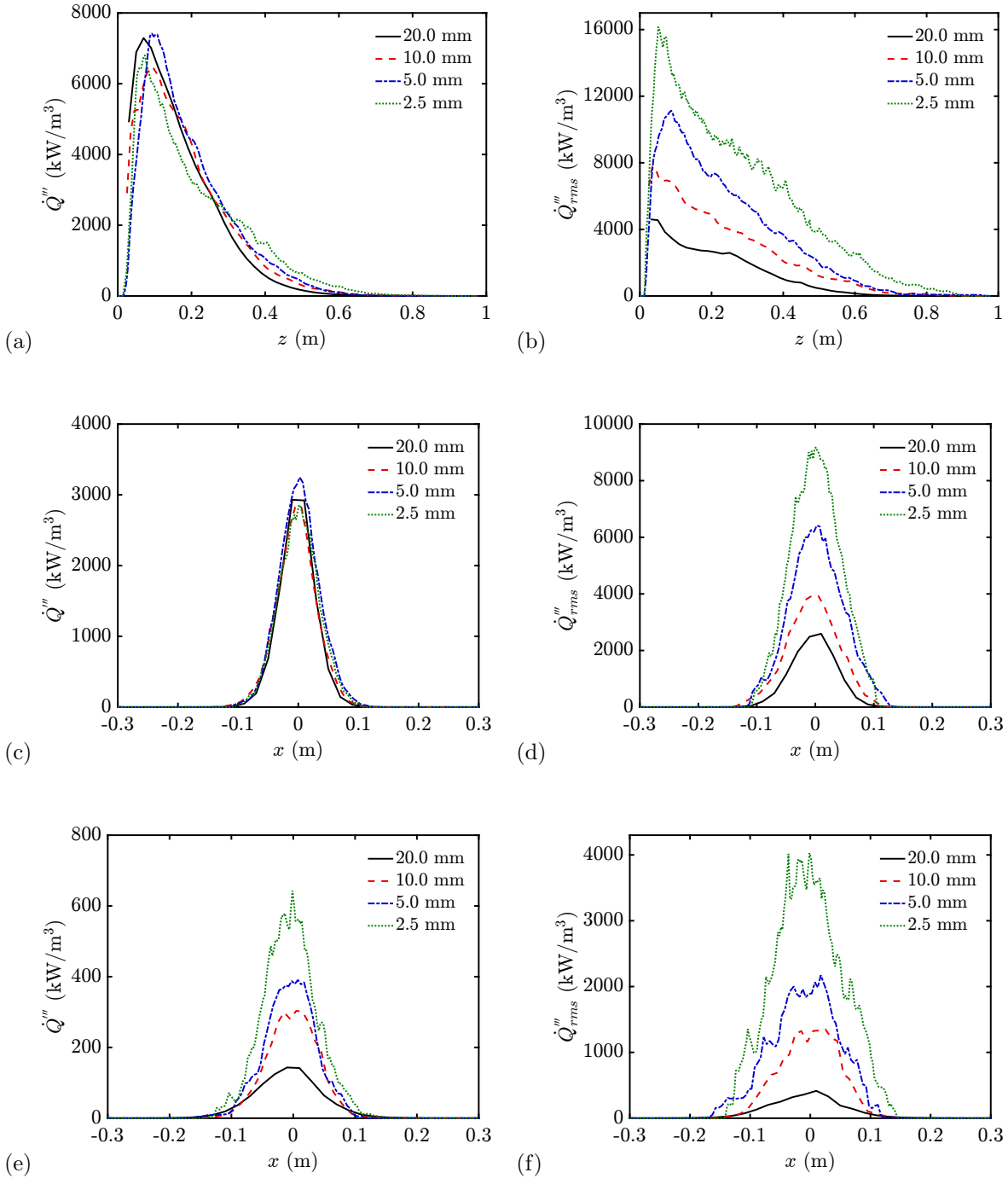

Figure 3.3: Simulated volumetric heat release rate ($\dot{Q}'''$) at selected grid resolutions; (a) mean z-profile, (b) rms z-profile, (c) mean x-profile at $z = 0.25\,\mathrm{m}$, (d) rms x-profile at $z = 0.25\,\mathrm{m}$, (e) mean x-profile at $z = 0.50\,\mathrm{m}$, (f) rms x-profile at $z = 0.50\,\mathrm{m}$.

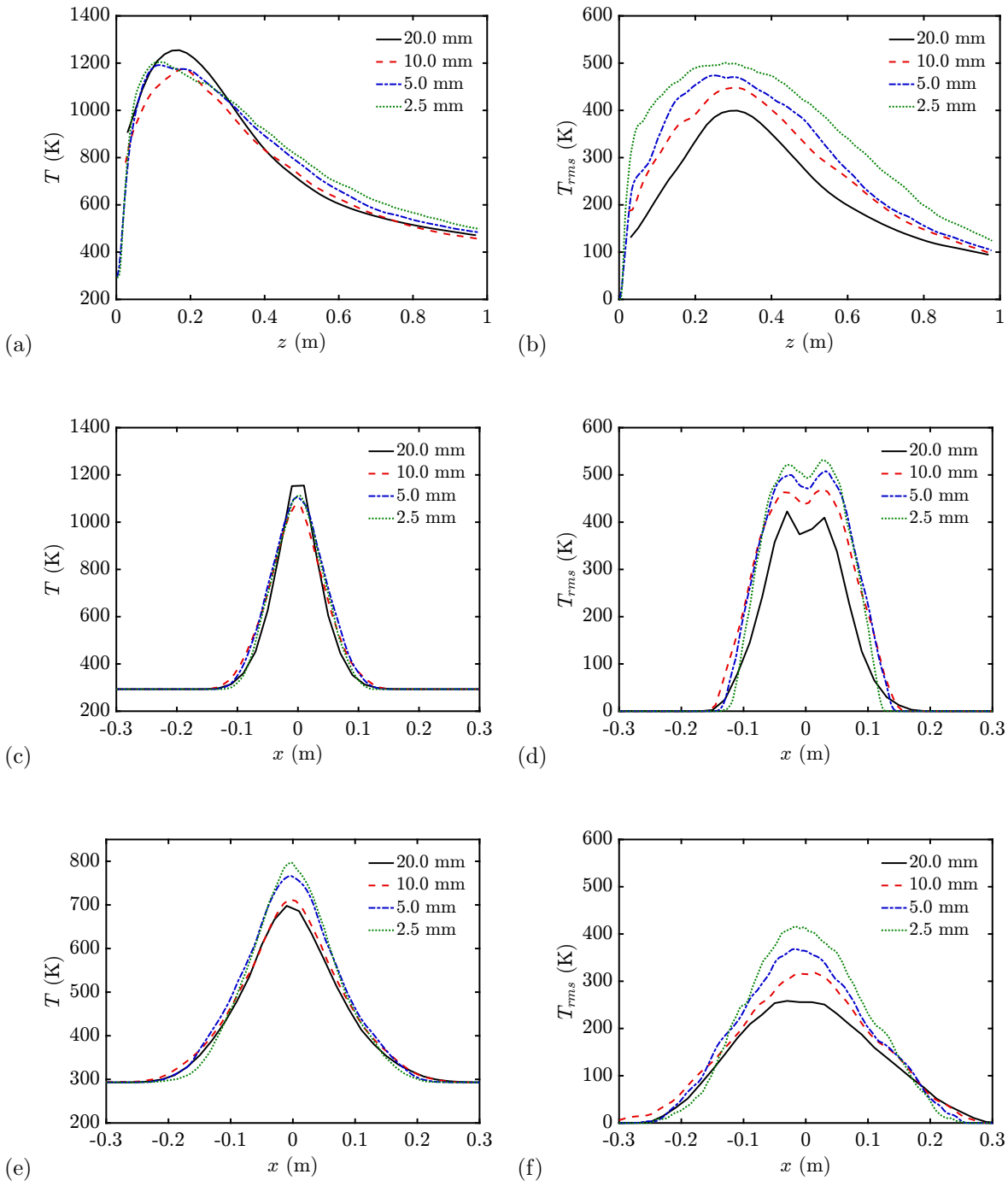

Figure 3.4: Simulated gas temperature (T) at selected grid resolutions; (a) mean z-profile, (b) rms z-profile, (c) mean x-profile at $z = 0.25\,\mathrm{m}$, (d) rms x-profile at $z = 0.25\,\mathrm{m}$, (e) mean x-profile at $z = 0.50\,\mathrm{m}$, (f) rms x-profile at $z = 0.50\,\mathrm{m}$.

Figure 3.5 presents resolution comparisons of the time-mean and rms z-velocity component magnitude, w. As shown, adequate grid-convergence is observed for $\Delta x \leq 5.0\,\text{mm}$ in both the mean and rms values. As with the results for temperature, the simulated far-field value of $w \approx 2.8\,\text{m/s}$ agrees well with a value of $2.88\,\text{m/s}$ predicted by empirical correlation [155].

Particularly noteworthy, the simulated results for $\Delta x = 20.0\,\text{mm}$ and $\Delta x = 10.0\,\text{mm}$ resolution, though not fully converged with the finest resolved results at $\Delta x = 2.5\,\text{mm}$, still approximate the mean T and w fields in the present configuration remarkably well. As shown in Table 3.2, these simulations accomplish this agreement with significantly reduced computational cost. These results suggest that while the flame width, W_f, may be the limiting length scale in the present configuration, the flame height, L_f, is perhaps the more dominant length scale in governing the behavior of the flame. Even for the coarsest presently considered case of $\Delta x = 20.0\,\text{mm}$, $L_f/\Delta x = 25$, indicating good resolution of this length scale.

An alternative scaling parameter [149], adapted to the present line-fire geometry and defined as

$$L^* = \left(\frac{\dot{Q}'}{\rho_\infty \, c_{p,\infty} \, T_\infty \, g^{1/2}} \right)^{2/3}, \tag{3.11}$$

provides a characteristic length scale based on buoyant plume scaling, where $\dot{Q}'$ is the flame heat release rate per-unit-length of the line source, ρ_∞, $c_{p,\infty}$, and T_∞ are respectively the mass density, heat capacity, and temperature of the ambient, and g is the gravitational acceleration constant. For the present configuration, $L^* \approx 0.2\,\text{m}$, which is also reasonably well-resolved in all of the presently considered cases.

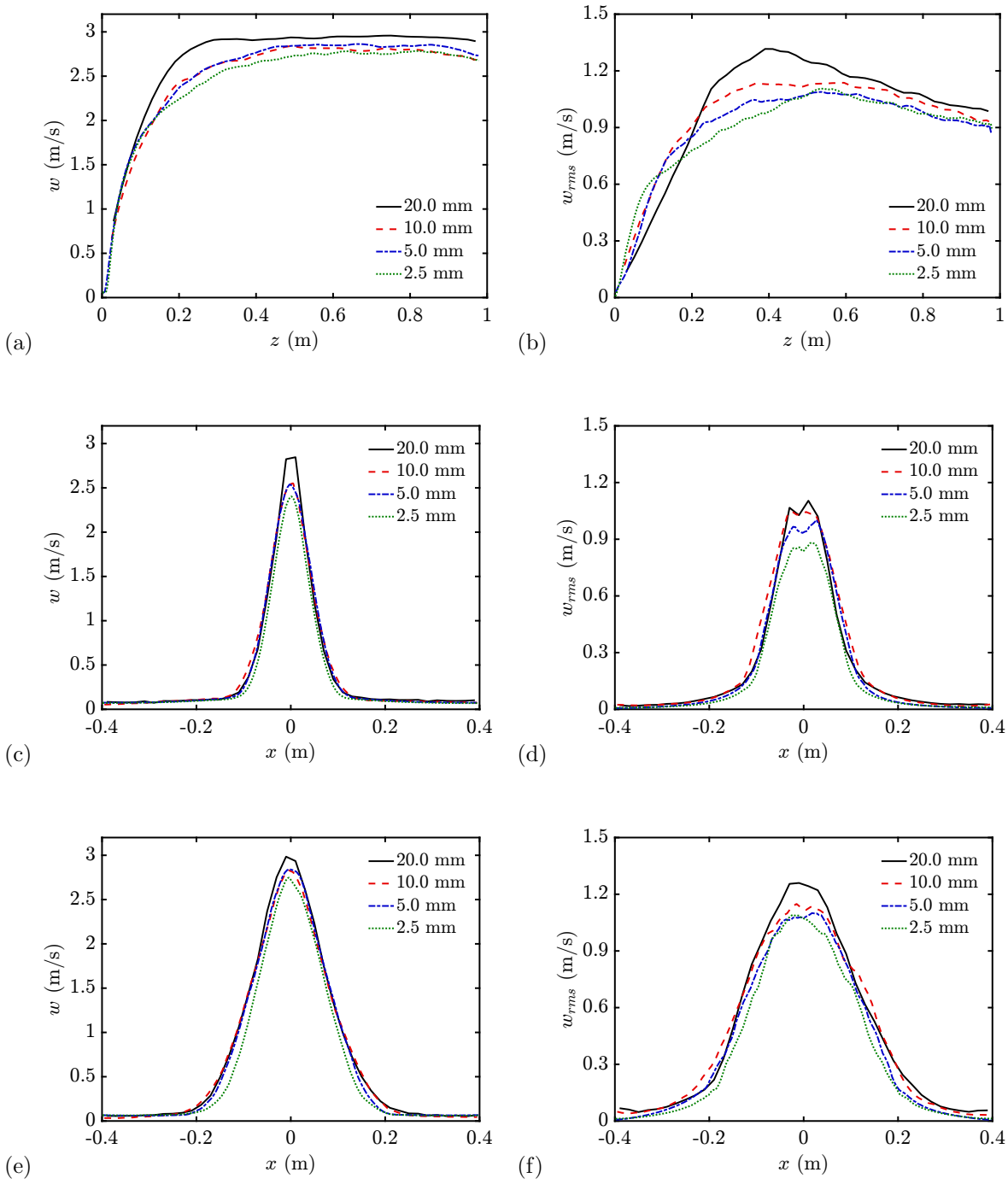

Figure 3.5: Simulated z-velocity magnitude (w) at selected grid resolutions; (a) mean z-profile, (b) rms z-profile, (c) mean x-profile at $z = 0.25\,\mathrm{m}$, (d) rms x-profile at $z = 0.25\,\mathrm{m}$, (e) mean x-profile at $z = 0.50\,\mathrm{m}$, (f) rms x-profile at $z = 0.50\,\mathrm{m}$.

The mean turbulent kinetic energy resolved by the numerical grid, k_t, may be approximated as

$$k_t = \frac{1}{2}\left(u_{rms}^2 + v_{rms}^2 + w_{rms}^2\right), \tag{3.12}$$

where u_{rms}, v_{rms}, and w_{rms}, are respectively the root-mean-square statistics for the x, y, and z components of the flow velocity. Vertical centerline and cross-flame profiles of k_t, as well as those for the unresolved subgrid turbulent kinetic energy, k_{sgs}, retrieved from the turbulence model (see Eq. 3.5), are presented in Fig. 3.6. As shown, values for k_t are reasonably well-converged amongst all considered resolutions, while values for k_{sgs} decrease steadily with decreasing Δx, due to diminishing influence of the turbulence model.

From these diagnostics, and following the conventions given in previous work [156], a characteristic resolution criterion, M, may be defined as

$$M = \frac{k_t}{k_t + k_{sgs}}, \tag{3.13}$$

where this ratio indicates the percentage of the modeled turbulent kinetic energy that is resolved by the numerical grid, taking a value of unity when k_{sgs} is negligible and decreasing toward zero as k_{sgs} begins to dominate k_t. Note that k_{sgs} is a modeled quantity and should not be expected to represent the true turbulent fluctuations in the unresolved flow. As a result, $M = 1$ does *not* imply that 100% of the turbulence in the flow is resolved by the grid. This criterion merely indicates the degree of influence that the turbulence model has on the flow field. Following established recommendations [153,156], $M \geq 0.8$ satisfies reasonably well-resolved LES. Vertical centerline and cross-flame profiles of M are presented in Fig. 3.7.

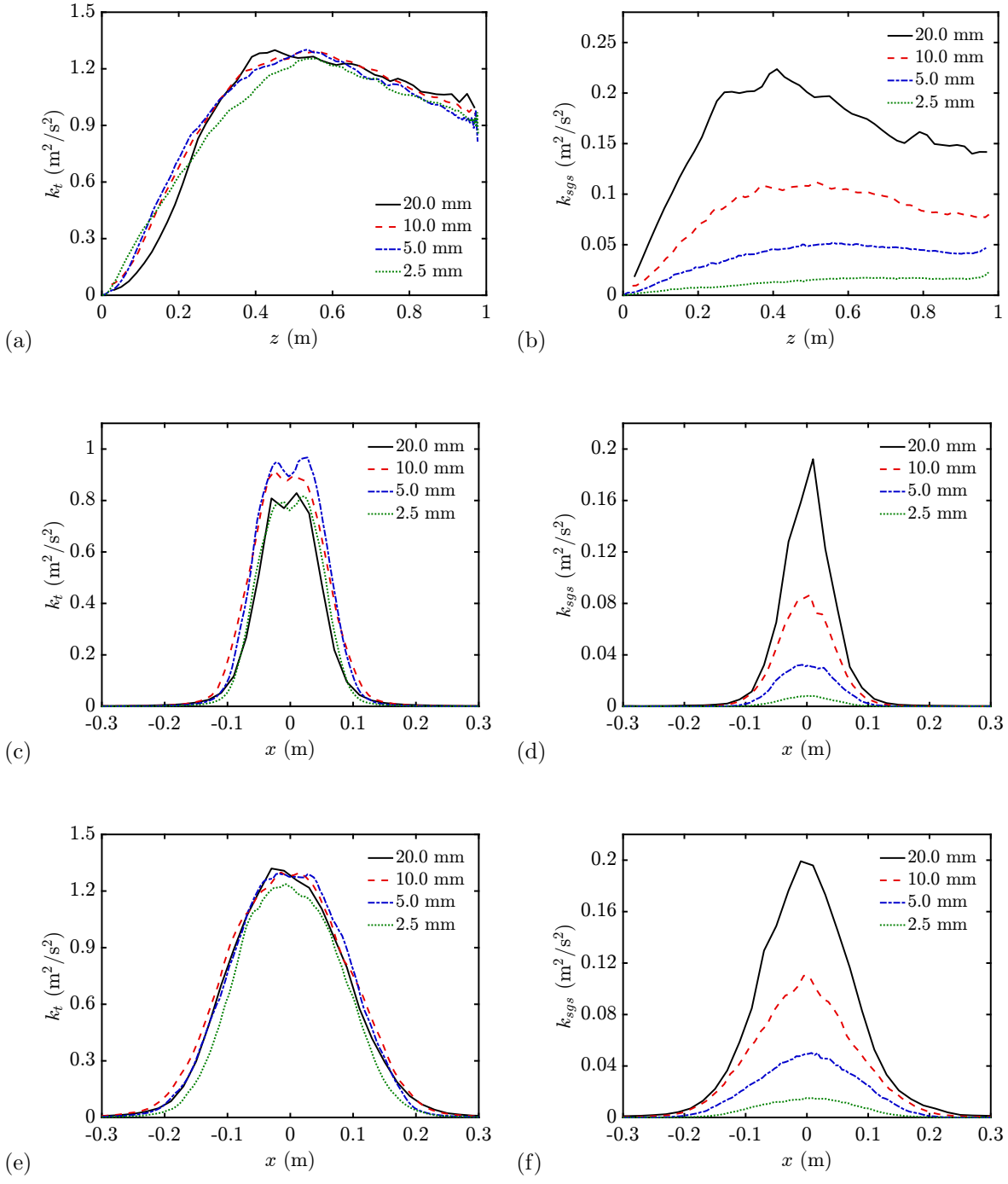

Figure 3.6: Simulated resolved (k_t) and unresolved (k_{sgs}) turbulent kinetic energy at selected grid resolutions; (a) k_t, mean z-profile, (b) k_{sgs}, mean z-profile, (c) k_t, mean x-profile at $z = 0.25\,\mathrm{m}$, (d) k_{sgs}, mean x-profile at $z = 0.25\,\mathrm{m}$, (e) k_t, mean x-profile at $z = 0.50\,\mathrm{m}$, (f) k_{sgs}, mean x-profile at $z = 0.50\,\mathrm{m}$.

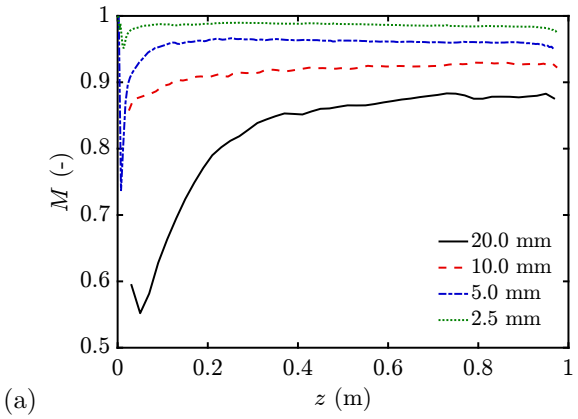

(a)

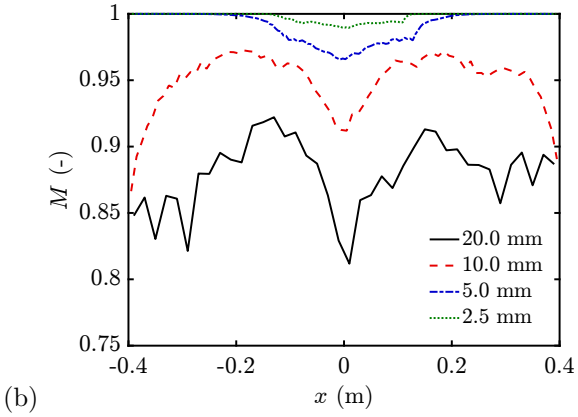

(b)

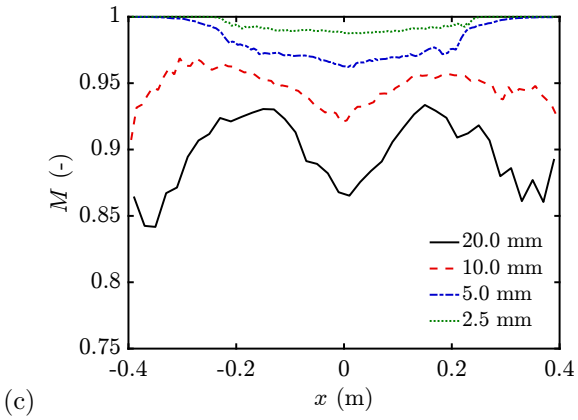

(c)

Figure 3.7: Simulated turbulence resolution criterion (M) at selected grid resolutions; (a) mean z-profile, (b) mean x-profile at $z = 0.25\,\mathrm{m}$, (c) mean x-profile at $z = 0.50\,\mathrm{m}$.

As shown in Fig. 3.7, for $\Delta x \leq 5.0\,\text{mm}$, $M \geq 0.8$ for all z along the flame centerline and for all x along representative cross-flame profiles, though for $\Delta x = 5.0\,\text{mm}$, there is a small region very near to the fuel port for which $M < 0.8$. This downward peak is attributed to the laminar-turbulent transition that occurs at the flame base (from Eq. 2.5, $1.2\,\text{cm} < z_{crit} < 2.7\,\text{cm}$). In consideration of this result and the preceding grid-convergence analysis, the $\Delta x = 5.0\,\text{mm}$ resolution is deemed adequate for the aims of the present study and this resolution is employed as the baseline in all of the presently conducted simulations.

Supplementing the preceding analysis, additional grid-convergence results including resolution comparisons for the simulated gas-phase mass density, perturbation pressure, x-component velocity magnitude, y-component velocity magnitude, and total flow kinetic energy are presented in Appendix B.

3.4.2 Radiative Transfer Solver

In addition to the preceding discussion, which considers the numerical discretization of the gas-phase flow field, and following recent affiliated work [65, 66], it is also worth considering the discretization in angular space used to resolve radiation transfer via the RTE. For the present configuration, which uses a heat flux transducer to measure radiative flame emissions, the integral length scales of interest are the flame surface area ($A_f = L_f \times L_b \approx 0.25\,\text{m}^2$) and the separation distance between the transducer and the flame ($x_g = 1\,\text{m}$). The angular region occupied by the flame, as viewed from the transducer is then given by the ratio, $A_f/x_g^2 = 0.25\,\text{sr}$.

In FDS, angular space (see Fig. 3.8) is discretized into N_θ polar bands and $N_\phi(\theta)$ azimuthal bands, where N_θ is an integer divisible by 2 and each $N_\phi(\theta)$ is an integer divisible by 4. The total number of solid angles, N_Ω, given by

$$N_\Omega = \sum_{i=1}^{N_\theta} N_\phi(\theta_i), \tag{3.14}$$

is determined based on computed values for N_θ and N_ϕ, which are set to yield N_Ω as close as possible to a user-specified value (subject to the preceding constraints for N_θ and N_ϕ and while maintaining equal solid angles so that $\Delta\Omega = 4\pi/N_\Omega$) [149].

A series of simulations featuring N_Ω ranging between 32–512 have been performed to evaluate the angular resolution requirements for convergence in the simulated transducer heat flux, $\dot{q}''_g$. Simulations are conducted with 5 mm grid resolution,

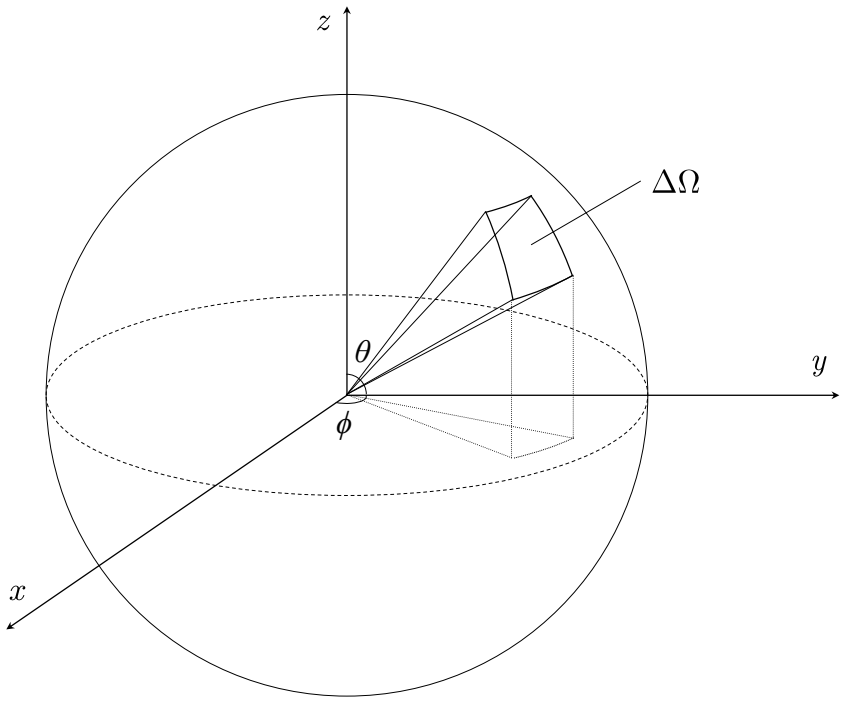

Figure 3.8: Illustration of the coordinate system used to discretize angular space for solution of the radiative transfer equation, as applied in the Fire Dynamics Simulator (FDS).

at $X_{O_2}^{ox} = 0.21$, and for a duration of 10 s. Time-mean simulated $\dot{q}_g''$, averaged over the final 8 s of each simulation, are plotted versus N_Ω in Fig. 3.9. As shown, simulated $\dot{q}_g''$ converge with the experimentally measured value for $N_\Omega \geq 320$.

For $N_\Omega = 320$, the angular resolution is given by $\Delta\Omega = 4\,\pi/N_\Omega \approx 0.04\,\text{sr}$, for which the region of interest, $A_f/x_g^2 = 0.25\,\text{sr}$ is resolved in roughly 6 solid angles, a result consistent with that reported in affiliated work [65, 66]. A general criterion for angular resolution requirement may then be suggested, corresponding to

$$N_\Omega \geq (6)\,\frac{4\,\pi\,r^2}{A}, \tag{3.15}$$

where A is the visible surface area of a radiation source and r is the radial distance between the source and the position of a sensor for which converged radiative intensity measurement is desired. In consideration of this result, $N_\Omega = 320$ angles is utilized for all simulations conducted in the present study.

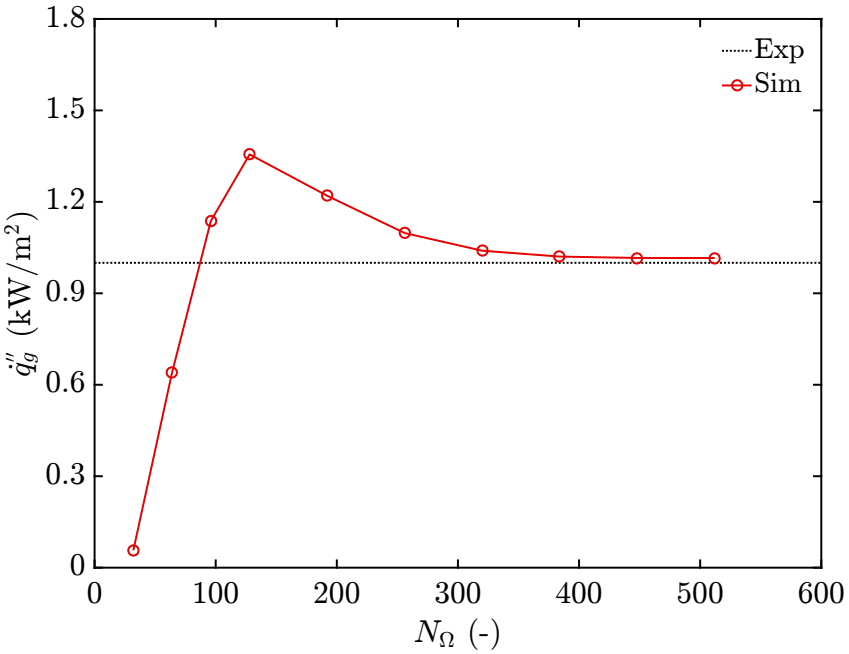

Figure 3.9: Simulated $\dot{q}_g''$ plotted versus angular RTE resolution; convergence is observed for $N_\Omega \geq 320$.

Chapter 4: Results and Discussion

4.1 Overview

Results for the present work showcase a range of detailed experimental and numerical analyses that offer insight and understanding into fire suppression phenomena. Experimental measurements of suppression effects and discussions thereof are presented in Sec. 4.2. Within, qualitative observations of visible flame structure and extinction behaviors are summarized in Sec. 4.2.1. Preliminary observations of water-mist suppression effects are included, though detailed measurements and analyses for this suppressant are deferred to future study. Following, Sec. 4.2.2 portrays a comparison of measured extinction limits for N_2 suppression with those reported in the literature, including a discussion of the dominant observed extinction mechanisms and their relevance to turbulent fire applications.

An analysis of visible flame height measurements is presented in Sec. 4.2.3, including measurement comparisons to classical scaling predictions. In Sec. 4.2.4, luminous and radiative flame emissions measurements are reported, where their comparison offers insight into the dominant form of flame radiative heat losses during suppression. Measurements of combustion efficiency and associated calorimetry-derived quantities are presented in Sec. 4.2.5, offering a quantitative evaluation

of suppression performance and providing a basis for understanding the dominant mode of flame extinguishment in the present configuration.

Following the experimental analysis, numerical simulation results are discussed in Sec. 4.3, including a comprehensive evaluation of the alternate flame extinction and reignition cases introduced in Sec. 3.2.2. Each modeling case is evaluated based on result comparisons with the measured experimental data (Sec. 4.3.1) and with regards to model sensitivity to input parameters and numerical resolution (Sec. 4.3.2). Simulation performance is summarized in Sec. 4.3.3, highlighting the significance of spurious reignition in determining the simulated suppression behavior, and identifying the relevant modeling issues that limit the broader applicability of the available extinction and reignition treatments.

4.2 Experiment

4.2.1 Flame Structure

Flame images depicting the results of preliminary burner configuration testing are presented in Fig. 4.1. In each of these images, fuel and oxidizer flow conditions are as specified in Sec. 2.2, except as otherwise stated. Images in Fig. 4.1 portray the observed flame structure for conditions (a) without the co-flowing oxidizer, (b) with the co-flowing oxidizer but without the ceramic fiberboard around the fuel port, and (c) including both the oxidizer and the board.

Figure 4.1(a) provides a baseline representation of the flame with no influence of the oxidizer. As shown, the flame appears sufficiently turbulent, with turbulent

(a)

(b)

(c)

Figure 4.1: Comparison of visible flame structure for varying oxidizer conditions; (a) no co-flowing oxidizer, (b) with co-flowing oxidizer, (c) with co-flowing oxidizer and ceramic fiberboard around fuel port.

flow structures developing very near to the fuel port (from Eq. 2.5, 1.2 cm $< z_{crit} <$ 2.7 cm). As shown in Fig. 4.1(b), and despite the design intent to the contrary, the co-flowing oxidizer appears to influence entrainment dynamics at the flame base, extending the laminar length of the flame by several factors ($z_{crit} \approx 7$ cm, as appears in the image). An effective deterrent to this influence is illustrated in Fig. 4.1(c), where inclusion of the ceramic fiberboard around the fuel port recovers and enhances buoyancy-induced turbulence at the flame base. This board encourages cross-flame directed entrainment flow at the flame base, a feature that more closely resembles the entrainment dynamics of realistic large-scale buoyant fires.

Cross-flame profiles (x-direction) of local thermocouple temperatures, T_{tc}, are presented in Fig. 4.2 for an unsuppressed flame condition. For these measurements, an array of exposed-junction, 1.0 mm bead-diameter K-type thermocouple probes (uncertainty ± 2 K, response time ~ 3 s) is suspended across the center of the fuel port at selected elevations corresponding to $z = 25$ cm ($\sim L_f/2$), $z = 50$ cm ($\sim L_f$), and $z = 75$ cm ($\sim 3\,L_f/2$). Reported thermocouple temperatures are uncompensated time-mean values, averaged over a duration of roughly 5 minutes.

As shown in Fig. 4.2, T_{tc} measurements exhibit expected symmetric Gaussian profiles across the width of the flame. Centerline peak temperatures decrease, while characteristic profile widths increase, with increasing elevation above the fuel port. The measured peak temperature of $T_{tc} \approx 1100$ K at $z = 25$ cm also closely matches previously reported measurements in a similar line-fire configuration [155]. A scaling correlation developed from those data predicts a peak temperature of 1191 K in the present configuration, in reasonable agreement with the present measurements.

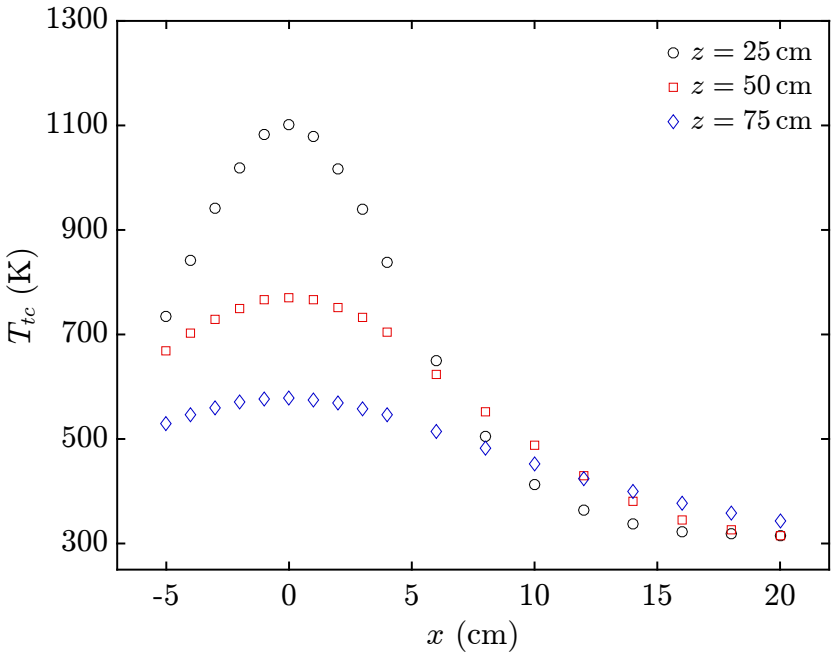

Figure 4.2: Time-mean cross-flame profiles (x-direction) of local thermocouple temperature (T_{tc}) at selected elevations above the fuel port.

Representative images depicting simultaneous front and end views of non-anchored flame quenching behavior due to N_2 suppression are presented in Fig. 4.3 for CH_4 fuel and Fig. 4.4 for C_3H_8 fuel. Camera exposure settings are fixed for these images, permitting comparable visibility of the dim blue flames observed near the extinction limit, but resulting in extensive saturation of the bright yellow unsuppressed flames. This marked difference in flame luminosity is explored through quantitative measurements in Sec. 4.2.4. Here, yellow and blue flame regions respectively indicate the local dominance of either soot incandescence or the luminescence of intermediate CH radicals. Shown in Figs. 4.3 and 4.4, as $X_{O_2}^{ox}$ is reduced for both fuels, soot incandescence diminishes, leading to a transition in flame color from yellow to blue, followed shortly thereafter by global flame extinguishment.

Figure 4.3: Simultaneous front and end-view CH_4 flame images at selected $X_{O_2}^{ox}$ for non-anchored condition; (a) $X_{O_2}^{ox} = 0.209$, (b) $X_{O_2}^{ox} = 0.181$, (c) $X_{O_2}^{ox} = 0.168$, (d) $X_{O_2}^{ox} = 0.158$, (e) $X_{O_2}^{ox} = 0.154$, (f) $X_{O_2}^{ox} = 0.152$; Exposure: 1/30 s, f/2.0, ISO 1250.

Figure 4.4: Simultaneous front and end-view C_3H_8 flame images at selected $X_{O_2}^{ox}$ for non-anchored condition; (a) $X_{O_2}^{ox} = 0.209$, (b) $X_{O_2}^{ox} = 0.172$, (c) $X_{O_2}^{ox} = 0.154$, (d) $X_{O_2}^{ox} = 0.144$, (e) $X_{O_2}^{ox} = 0.140$, (f) $X_{O_2}^{ox} = 0.139$; Exposure: 1/30 s, f/2.0, ISO 1250.

In the CH_4 flame (Fig. 4.3), there are minimal observable suppression effects for $X_{O_2}^{ox} > 0.18$ other than a reduction in flame luminosity (Fig. 4.3(b)). For $X_{O_2}^{ox} < 0.18$, a transition in flame color from yellow to blue begins to occur at the flame base. Around $X_{O_2}^{ox} \approx 0.17$ (Fig. 4.3(c)), soot incandescence diminishes rapidly, resulting in a progressive growth of the blue flame region until $X_{O_2}^{ox} \approx 0.16$, below which the flame appears entirely blue (Fig. 4.3(d)). Further reductions in $X_{O_2}^{ox}$ result in significant flame weakening, evidenced by drastic changes in flame structure and periods of localized detachment from the fuel port (Fig. 4.3(e)), owed to extensive localized quenching coupled with flame-base destabilization. Global extinction is immediately preceded by total detachment of the flame from the fuel port and subsequent liftoff, occurring at $X_{O_2}^{ox} = 0.152$ (Fig. 4.3(f)).

Shown in Fig. 4.4, suppression of the C_3H_8 flame occurs with a similar sequence, excepting that notable visual (color) transitions are extended to much lower $X_{O_2}^{ox}$. The unsuppressed C_3H_8 flame is visibly sootier than the CH_4 flame, evidenced by the faint envelope of smoke emanating from the flame sheet at ambient condition (Fig. 4.4(a)). Corresponding to this increased sooting propensity, initial bluing of the flame base does not occur until $X_{O_2}^{ox} < 0.155$ (Fig. 4.4(c)). With further reductions in $X_{O_2}^{ox}$, the flame rapidly deteriorates with respect to both soot incandescence and flame strength, as shown in Fig. 4.4(d) ($X_{O_2}^{ox} = 0.144$), which depicts a partially lifted C_3H_8 flame with roughly equal portions of yellow and blue. Transition to an entirely blue flame does not occur until $X_{O_2}^{ox} < 0.14$ (Fig. 4.4(e)), with global extinction following immediately thereafter at $X_{O_2}^{ox} = 0.139$ (Fig. 4.4(f)). As with the CH_4 flame, global extinction occurs as flame-base detachment and liftoff.

Comparing suppression observations for the two fuels, the CH_4 flame experiences complete suppression of soot radiation at relatively high $X_{O_2}^{ox} > 0.163$, then exhibits a prolonged period of stable, soot-free (blue) combustion between $X_{O_2}^{ox} = 0.163$ and $X_{O_2}^{ox} = 0.153$ prior to extinction. The C_3H_8 flame however, does not experience complete suppression of soot radiation until $X_{O_2}^{ox} < 0.14$ (if at all), in the midst of rampant localized flame quenching and structural instability, occurring immediately before global extinction at $X_{O_2}^{ox} = 0.139$. The observed discrepancies between the sooting tendencies of each fuel are attributed to respective differences in soot formation kinetics, where compared to the CH_4 flame, soot formation is favored in the C_3H_8 flame even for suppressed (low $X_{O_2}^{ox}$) conditions.

Additional representative images depicting front and end views of anchored flame quenching behavior due to N_2 suppression are presented in Fig. 4.5 for CH_4 fuel and Fig. 4.6 for C_3H_8 fuel. As shown in these figures, suppression observations for the anchored condition closely resemble those for the non-anchored condition, comprising a gradual reduction in flame luminosity and transition in flame color (due to diminishing soot incandescence), followed by global flame extinction.

Specific to the anchored condition, the O_2-anchor fosters a stabilized flame base that effectively prevents flame detachment and liftoff extinction for both fuels, also extending the domain of flammability to lower $X_{O_2}^{ox}$. Anchored extinguishment occurs as progressive localized extinction throughout the body of the flame (depicted in Fig. 4.5(e) for CH_4 and Fig. 4.6(e) for C_3H_8), where a condition is eventually reached where only a small pilot flame remains attached to the O_2-anchor, with no or minimal residual burning above the fuel port (Figs. 4.5(f) and 4.6(f)).

Figure 4.5: Simultaneous front and end-view CH_4 flame images at selected $X_{O_2}^{ox}$ for anchored condition; (a) $X_{O_2}^{ox} = 0.209$, (b) $X_{O_2}^{ox} = 0.175$, (c) $X_{O_2}^{ox} = 0.160$, (d) $X_{O_2}^{ox} = 0.149$, (e) $X_{O_2}^{ox} = 0.133$, (f) $X_{O_2}^{ox} = 0.122$; Exposure: 1/30 s, f/2.0, ISO 1250.

Figure 4.6: Simultaneous front and end-view C_3H_8 flame images at selected $X_{O_2}^{ox}$ for anchored condition; (a) $X_{O_2}^{ox} = 0.209$, (b) $X_{O_2}^{ox} = 0.152$, (c) $X_{O_2}^{ox} = 0.142$, (d) $X_{O_2}^{ox} = 0.139$, (e) $X_{O_2}^{ox} = 0.126$, (f) $X_{O_2}^{ox} = 0.122$; Exposure: 1/30 s, f/2.0, ISO 1250.

Images depicting preliminary results of water-mist suppression testing are presented in Figs. 4.7 and 4.8. Each figure portrays a reduced-size CH_4 flame ($\dot{Q} \approx 30\,\mathrm{kW}$) subjected to varying levels of mist loading, where variation in Y_m^{ox} is achieved by controlling the number of mist generators in operation (presently 0–6 generators, see Sec. 2.2.4 for details). For each case, the oxidizer flow rate is held fixed at a relatively low value ($\dot{m}_{ox} \approx 40\,\mathrm{g/s}$ in Fig. 4.7) or a relatively high value ($\dot{m}_{ox} \approx 85\,\mathrm{g/s}$ in Fig. 4.8) to achieve further variability in Y_m^{ox}. Decreasing $\dot{m}_{ox}$ increases Y_m^{ox} (for a given number of generators in operation), but restricts the extent of the mist to the base-region of the flame (recall that the relatively dense mist tends to sink in the ambient due to gravity, see Fig. 2.16). Increasing $\dot{m}_{ox}$ encourages mist delivery at higher elevations in the flame, but also reduces Y_m^{ox}.

For the low oxidizer-flow case (Fig. 4.7), the mist reaches a maximum of roughly 10–15 cm above the fuel port, covering the flame base, but leaving the top of the flame mist-free. For maximum mist loading at this condition ($Y_m^{ox} \approx 0.15$), the flame is extinguished within the mist layer, though a quasi-stabilized lifted flame continues to burn on top of the mist (Fig. 4.7(f)). Here, the observed extinguishing limit of $Y_m^{ox} \approx 0.15$ agrees with previously reported results [8, 53]. For the high oxidizer-flow case (Fig. 4.8), the mist reaches the mean flame height, but with reduced Y_m^{ox} insufficient for global flame quenching. Comparing results for the two cases, similar suppression effects are observed at different $\dot{m}_{ox}$, but corresponding to equivalent Y_m^{ox} (see Figs. 4.7(c) and 4.8(d)). This agreement demonstrates that the suppression potential of the mist-laden oxidizer is primarily determined by Y_m^{ox} and not by the total delivery rate of water to the flame.

Figure 4.7: Front-view CH_4 flame images ($\dot{Q} \approx 30\,\mathrm{kW}$, $\dot{m}_{ox} \approx 40\,\mathrm{g/s}$) at selected Y_m^{ox}; (a) $Y_m^{ox} = 0.00$, (b) $Y_m^{ox} \approx 0.02$, (c) $Y_m^{ox} \approx 0.05$, (d) $Y_m^{ox} \approx 0.09$, (e) $Y_m^{ox} \approx 0.12$, (f) $Y_m^{ox} \approx 0.15$.

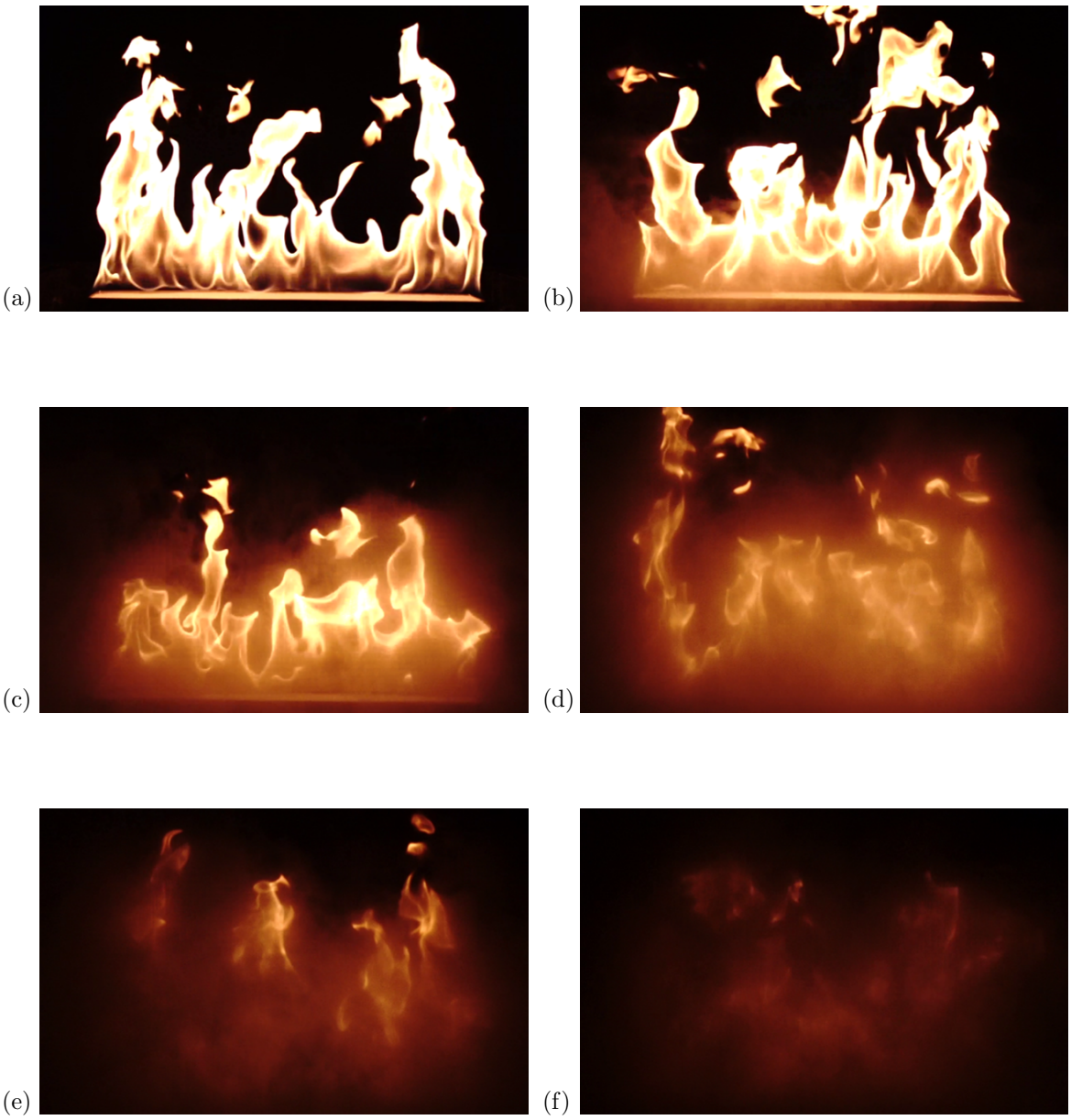

Figure 4.8: Front-view CH_4 flame images ($\dot{Q} \approx 30\,\text{kW}$, $\dot{m}_{ox} \approx 85\,\text{g/s}$) at selected Y_m^{ox}; (a) $Y_m^{ox} = 0.00$, (b) $Y_m^{ox} \approx 0.02$, (c) $Y_m^{ox} \approx 0.04$, (d) $Y_m^{ox} \approx 0.05$, (e) $Y_m^{ox} \approx 0.06$, (f) $Y_m^{ox} \approx 0.07$.

Shown in Figs. 4.7 and 4.8, the CH_4 flame experiences a significant reduction in luminosity with increasing Y_m^{ox}, similar to the observations reported for N_2 suppression (see Figs. 4.3–4.6). Unlike N_2 suppression however, no significant portions of the flame transition in color from yellow to blue, suggesting that soot production persists in spite of the suppression effects of the flame-mist interactions. The observed reduction in flame luminosity is then likely due to flame cooling, where the visible intensity of soot incandescence is strongly dependent on the flame temperature (see Fig. C.1 in Appendix C for a related discussion of spectral radiation). Though the observed reduction in luminosity is principally due to diminishing soot incandescence, there is notable attenuation of the visible emissions due to Mie scattering within the mist (see Figs. 4.8(c)–(f)).

As noted in Secs. 2.2.3 and 2.2.4, both N_2 and water mist achieve flame suppression primarily due to thermal quenching (reduction in flame temperature). Despite this similarity, the cooling potential of water mist is significantly greater than that for N_2 due to a greater sensible heat capacity and the latent contribution of evaporation (see Sec. 2.2.4). As a result of this difference, a greater amount of N_2 (and therefore a lower value of $X_{O_2}^{ox}$) is required to achieve comparable flame cooling to that of water mist. The observed differences in soot-suppression behaviors between N_2 and water mist are then best attributed to the lower $X_{O_2}^{ox}$ that are required for N_2 suppression, where soot production kinetics are highly sensitive to the local O_2 concentration [157–159].

From the present results, it is not discernible whether mist suppression is primarily due to latent cooling (evaporation) or sensible cooling (water-vapor dilution).

As mentioned in Sec. 2.2.4, this distinction is configuration dependent and primarily related to droplet size. Results from previous work suggest that for the mist utilized in the present configuration ($d_m \approx 10\,\mu$m), all drops should evaporate well outside the flame sheet and therefore sensible cooling effects should dominate [17, 53].

4.2.2 Extinction Limit

The flame extinction limit (LOI, see Sec. 2.2.3) is identified from recorded flame images as the condition for which the main visible flame ceases to exist. For non-anchored extinction, this condition corresponds to the flame liftoff event. For anchored extinction, this condition corresponds to the initiation of a prolonged total quenching of the main flame, though a small pilot flame may persist in the immediate vicinity of the O_2-anchor (see Figs. 4.5(f) and 4.6(f)).

The presently measured LOI are compared in Table 4.1 against similar measurements reported in the literature. Literature values comprise data from a range of experimental configurations having either opposed-flowing or co-flowing fuel-oxidizer streams, but all incorporating small laminar flames. Only the present study provides conditions for moderate-sized turbulent flames. Listed conditions for the present study include (1) the anchored condition, (2) the non-anchored condition, and (3) the non-anchored condition without the ceramic fiberboard around the fuel port (see Fig. 2.10). While present conditions (1) and (2) exhibit turbulence very near to the flame base, condition (3) provides an unprotected, extended laminar flame base (see Fig. 4.1(b)) and more closely resembles the laminar cup-burner configuration [30].

Table 4.1: LOI data for CH_4 and C_3H_8 flames extinguished in N_2-diluted air.

Source	Burner Type	Flame[a]	Flow[b]	LOI, CH_4	LOI, C_3H_8
Current (1)	TLB[c]	T	C	0.122 ± 0.002	0.122 ± 0.002
Current (2)	TLB[c]	T	C	0.152 ± 0.002	0.139 ± 0.002
Current (3)	TLB[c]	T	C	0.155 ± 0.002	0.142 ± 0.002
[18]	Porous	L	O	0.139	0.127
[25]	Tsuji	L	O	0.140 ± 0.001	0.128 ± 0.001
[20]	Tsuji	L	O	0.143	—
[21]	Opposed-Jet	L	O	0.150	0.137
[23]	Cup	L	C	0.153	0.139
[27]	Cup	L	C	0.155 ± 0.002	—
[24]	Cup	L	C	—	0.141
[22]	Cup	L	C	—	0.142 ± 0.003
[25]	Santoro	L	C	0.164 ± 0.001	0.151 ± 0.002

[a] Flame regime, laminar (L) or turbulent (T).
[b] Oxidizer flow condition, co-flow (C) or opposed-flow (O).
[c] Turbulent line burner.

From Table 4.1, the presently measured LOI in condition (3) for both CH_4 and C_3H_8 fuels are shown to closely match previously reported values from the cup-burner apparatus. As noted, this agreement is attributed to the similarities between these two configurations, which produce flames in a co-flowing oxidizer with laminar base regions and yield liftoff extinction events [22–29, 35].

Presently measured LOI for condition (2) are slightly lower than those for condition (3), attributed to the stabilizing influence of the ceramic fiberboard, which reduces strain and prevents vertically directed flow at the flame base, such as would promote detachment of the flame from the fuel port. Though condition (2) includes turbulence very near to the flame base, it is unclear if this turbulence impacts the flame destabilization process that leads to liftoff extinction. Certainly, at the location of the edge reaction kernel responsible for flame stabilization, the flow

remains laminar. This fact, the observation that extinction occurs as liftoff, and the relative agreement with the extinction limit in condition (3) all suggest that the condition (2) limit still represents a laminar quenching event, despite the bulk of the flame being turbulent.

The lowest presently measured LOI for either fuel corresponds to condition (1), which includes the flame-base strengthening influence of the O_2-anchor to prevent liftoff extinction events. This limit more clearly represents turbulent flame extinction, where global extinguishment occurs as a result of progressive localized quenching throughout the body of the turbulent flame (see Figs. 4.5 and 4.6). The LOI for condition (1) may be interpreted as a piloted extinction limit, corresponding to a condition where the small base-flame attached to the O_2-anchor can no longer reignite locally quenched fuel in the body of the flame. This condition relates to the extinction of large-scale turbulent fires, in which flame regions that experience localized quenching may be reignited due to interaction with adjacent burning regions [68–70]. For turbulent flames in particular, such interactions are significantly enhanced due to turbulent mixing, whereas such interactions may be much less likely to occur in small laminar flames.

Global extinguishment in a large-scale turbulent fire may then be interpreted to result from any one of three potential occurrences. First, extinguishment may be due to the progressive development of conditions throughout the flame for which piloted reignition cannot occur (represented by the condition (1) limit). Second, extinguishment may be due to a single localized quenching event that globally destabilizes the flame, potentially at a condition prior to the piloted extinction limit (represented

by liftoff, as in the condition (2) and (3) limits). A third case then accounts for a sudden global extinction event that quenches the entire flame simultaneously, which may be likely for small flames, but is certain to be unlikely for large-scale flames.

From the range of values presented in Table 4.1, it is readily shown that reported laminar LOI are configuration-dependent measurements that vary with burner geometry. Studies using opposed-flow configurations report lower LOI, while higher LOI are reported for co-flowing configurations, particularly for the Santoro burner. Relative trends in LOI across differing burner geometries are also identical for both CH_4 and C_3H_8 fuels. The large variations in LOI with burner geometry, which are well outside the respective uncertainties noted for each study, are most attributable to variations in flame strain-rate and conductive heat losses specific to each type of burner. It is suspected that the presently reported anchored LOI for condition (1), representing a more fundamental piloted extinction limit, should exhibit greater configuration independence, though this would need to be demonstrated through additional testing in a variety of configurations.

Despite the noted dependence of laminar LOI on burner geometry, LOI in the present configuration are found to be relatively invariant for fuel flow between 0.6–1.3 g/s and for oxidizer flow between 50–85 g/s (these ranges in flow conditions are included in the noted uncertainty bounds in Table 4.1). Similar results have been previously reported, limited to configurations with low-strain flames where the observed extinction limit is believed to be dominated by thermal effects rather than strain-related effects [18, 23, 25, 27]. As in these cases, thermal effects are believed to dominate the extinction limit in the present configuration.

Still, there are cases in which both strain and thermal effects impact extinction behavior, and within certain regimes, flow conditions can dominate the extinction limit. Such behaviors have been well summarized by previous work [35], in which flammability maps illustrate the effects of fuel and oxidizer flow variations on liftoff and extinction limits. Here, it is noted that these two limits need not correspond to the same condition, where a liftoff limit that precedes the extinction limit leads to a stabilized lifted flame elevated over the fuel source. For the present configuration, previous work does predict overlapping liftoff and extinction limits that remain relatively invariant with changes in fuel and oxidizer flow rate, matching the present results [35]. In any case, the piloted extinction limits reported for condition (1) are suspected to be most applicable to the suppression of realistic turbulent fires.

4.2.3 Flame Height

Measurements of mean visible flame height (L_f), derived via image-processing techniques described in Sec. 2.3.1, are plotted versus $X_{O_2}^{ox}$ for both fuels and for both non-anchored and anchored conditions in Fig. 4.9. As shown, L_f increases with reducing $X_{O_2}^{ox}$, in agreement with previous observations [13, 28]. This trend is rationalized that, as $X_{O_2}^{ox}$ decreases, a greater volume of oxidizer must be entrained to support complete combustion. In addition, buoyant entrainment should decrease due to suppression and reduced flame temperatures; therefore the flame must lengthen to entrain the additional required oxidizer, where entrainment rate increases with rising elevation along the flame.

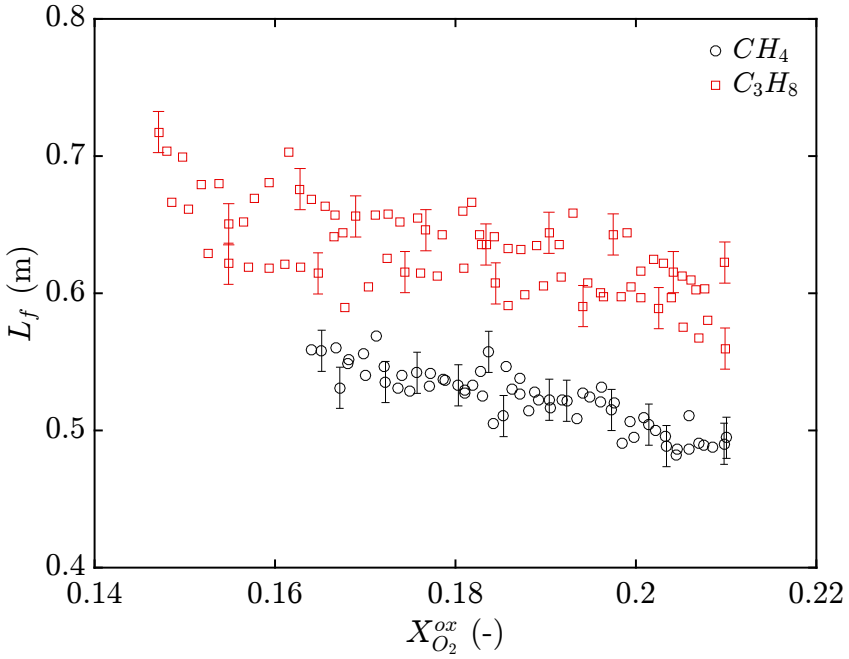

Figure 4.9: Measured flame height (L_f) plotted versus $X_{O_2}^{ox}$; with reducing $X_{O_2}^{ox}$, the flame lengthens to accommodate the additional entrainment required to support complete combustion.

Following the scaling relationship developed in Sec. 2.3.1 (Eq. 2.20), measured and scaling-predicted L_f are plotted in Fig. 4.10 versus the dimensionless scaling parameter, N. Values for N, as plotted in Fig. 4.10, are evaluated via Eq. 2.17 using presently measured values for χ_{rad} (see Sec. 4.2.4) and η_{comb} (see Sec. 4.2.5). A constant of proportionality of 22 is applied to Eq. 2.20 in order to fit the scaling relationship to the present data so that

$$\frac{L_f}{W_b} = 22\, N^{1/3}, \tag{4.1}$$

as plotted in Fig. 4.10. As shown, the predicted scaling reasonably matches the measured trends.

Recall that the present image-based measurements for L_f rely on luminous flame emissions, which are predominantly due to soot incandescence. Soot radiation

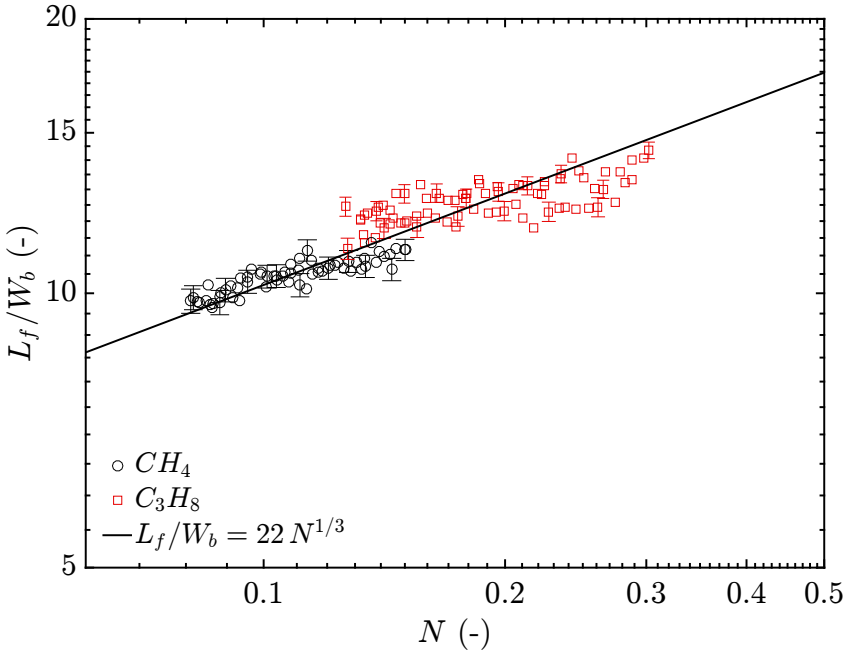

Figure 4.10: Normalized flame height (L_f/W_b) plotted versus scaling parameter, N; the solid line represents the scaling correlation given in Eq. 4.1, which exhibits reasonable agreement with the measured data.

should tend to increase the presently measured L_f because the soot burnout region extends beyond the location of the stoichiometric flame sheet. This effect is greatest in the unsuppressed C_3H_8 flame due to greater sooting propensity, helping to explain the higher measured L_f compared to the predicted trend for C_3H_8 at near-ambient $X_{O_2}^{ox}$. The inverse effect, occurring due to soot extinction and transition in flame color from yellow to blue, then helps to explain the slight over-predictions in L_f for the CH_4 flame below $X_{O_2}^{ox} = 0.180$ and for the C_3H_8 flame below $X_{O_2}^{ox} = 0.160$. Similarly declining visible flame height measurements coinciding with flame color transition have been reported in previous work [28].

Note that no presently measured L_f data are reported below $X_{O_2}^{ox} = 0.166$ for CH_4 fuel, or below $X_{O_2}^{ox} = 0.147$ for C_3H_8 fuel. Below these respective thresholds,

soot radiation in each flame diminishes rapidly, causing an overall reduction in luminosity and transition in flame color from yellow to blue (see Figs. 4.3–4.6). This transition, along with the development of increasingly intermittent flame structures, results in unreliably unsteady flame shape statistics (as derived using the present image-based technique). As a result of these processes and their combined effect on measurement uncertainty, L_f data are not reported for the affected conditions.

4.2.4 Flame Emissions

Flame luminosity ratio (LR, see Sec. 2.3.2) and radiative loss fraction (χ_{rad}, see Sec. 2.3.3) measurements for non-anchored CH_4 and C_3H_8 flames are plotted versus $X_{O_2}^{ox}$ in Fig. 4.11. As shown, LR decreases monotonically with declining $X_{O_2}^{ox}$ by at least six orders of magnitude for both fuels. This significant reduction in luminosity is readily discerned from the flame images presented in Sec. 4.2.1. From those images, three flame sooting regimes are identified, corresponding to transitions in flame color from entirely yellow, to transitional yellow-blue, to entirely blue. The yellow regime represents standard combustion with soot production and incandescence within the flame, while the yellow-blue regime represents the period during which soot production and radiation are diminished. The blue regime then represents soot-free combustion occurring beyond the extinction limit for soot production.

Notably, the boundaries of the three sooting regimes coincide well with sharp changes in the logarithmic LR trends. This agreement is noted for both fuels, despite their respective transitions occurring over different ranges of $X_{O_2}^{ox}$. Transitions for

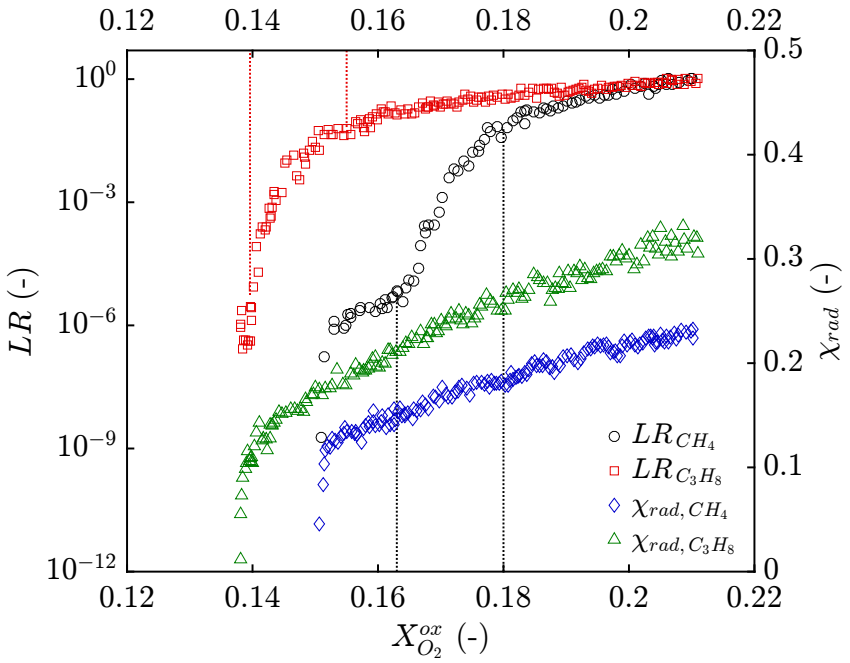

Figure 4.11: Measured flame luminosity ratio (LR) and radiative loss fraction (χ_{rad}) plotted versus $X_{O_2}^{ox}$ for the non-anchored condition; vertical dotted lines highlight $X_{O_2}^{ox}$ values where each flame transitions between sooting (color) regimes.

CH_4 occur at higher $X_{O_2}^{ox}$ (0.180 ± 0.002 for yellow to yellow-blue and 0.163 ± 0.002 for yellow-blue to blue) than those for C_3H_8 (0.155 ± 0.002 for yellow to yellow-blue and 0.140 ± 0.002 for yellow-blue to blue), owed to the greater sooting propensity of the C_3H_8 flame. Despite the difference in domain of transition, transitions for both fuels correspond to roughly equal LR, with yellow to yellow-blue transition occurring at roughly $LR = 7 \times 10^{-2}$ and yellow-blue to blue transition occurring at roughly $LR = 5 \times 10^{-6}$. These trends reinforce the concept that flame luminosity and soot volume fraction in the flame are correlated, as has been previously reported [91].

Unique to the CH_4 LR trend, there is an inflection point within the yellow-blue regime, after which the rapidly declining LR tapers for a prolonged period of steady, soot-free (blue) combustion between $X_{O_2}^{ox} = 0.163$ and $X_{O_2}^{ox} = 0.153$. Afterwards, LR

shows a steep decline coinciding with flame extinction. In comparison, the C_3H_8 LR trend experiences continuously sharpening decline throughout the yellow-blue and blue regimes. These trends agree well with the preceding flame image observations (see Sec. 4.2.1) and suggest that for the case of CH_4 suppression, soot radiation terminates independently of global flame extinction, whereas for C_3H_8 suppression, termination of soot radiation and flame extinction occur simultaneously, with the prospect that soot is still present at extinction. It is unclear what affect (if any) the continued presence of soot may have on the C_3H_8 extinction limit.

Also plotted in Fig. 4.11, χ_{rad} measurements are shown to decrease linearly for both fuels with declining $X_{O_2}^{ox}$. At ambient condition, χ_{rad} for the C_3H_8 flame (0.32 ± 0.014) is greater than that for the CH_4 flame (0.23 ± 0.010), consistent with previously reported measurements in an axisymmetric pool-fire configuration [160]. This increase is attributed to greater soot radiation in the C_3H_8 flame, where broad-band soot incandescence is detectable in both the visible and infrared spectra. The slope of χ_{rad} decline is then steeper for the C_3H_8 flame, with trends for both fuels approaching roughly equal χ_{rad} (0.13 ± 0.015) within their respective blue regimes. That the χ_{rad} measurements for both fuels agree once soot radiation terminates reinforces the notion that their disparity at higher $X_{O_2}^{ox}$ is principally due to differences in soot radiation. Still, partial quenching effects occurring within the blue regime of the C_3H_8 flame could complicate this interpretation.

A sharp change in the slope of linear χ_{rad} decline occurs, at $X_{O_2,\,crit}^{ox} \approx 0.153$ for CH_4 fuel and $X_{O_2,\,crit}^{ox} \approx 0.141$ for C_3H_8 fuel, in both cases coinciding with the rapid onset of extinction. Based on observations from the previously discussed flame

images (see Figs. 4.3 and 4.4), the terminal decline of χ_{rad} for both fuels is noted to occur over a period of intermittent flame structural instability, including localized lifting at the flame base and expansive quenching throughout the flame.

An interesting additional observation is made when comparing directly the LR and χ_{rad} data for the CH_4 flame (in Fig. 4.11). While measured LR decreases by four orders of magnitude throughout the yellow-blue transition regime and between sharp changes in the surrounding trend, over the same $X_{O_2}^{ox}$ range, χ_{rad} measures no remarkable change in its otherwise linear decline. This disparity suggests that soot radiation, which is the principal source of the visible emissions, is too weak to significantly impact the infrared emissions, where the latter must then be dominated by the gas-phase spectral emissions of heated combustion products (CO_2, H_2O) and unburned fuel. Similar behavior has been previously reported for laminar flames [43], but not for turbulent flames, as presently studied. Note that this result presently applies only to the CH_4 flame and is expected to be configuration dependent.

Though the disparity between LR and χ_{rad} trends is clear in the CH_4 flame, such behavior is only loosely present in the C_3H_8 flame, for which there is observed a slight variation in slope of χ_{rad} decline within the yellow-blue transition regime. This non-linearity could be attributed to variations in soot radiation, though the effect appears minor, suggesting that contributions from gas-phase emissions remain significant in the infrared spectrum. Causation between changing soot radiation and the observed tapering in the χ_{rad} trend is questionable however, as it is difficult to disassociate the effects of soot termination and global flame quenching which occur simultaneously in the blue regime of the C_3H_8 flame.

Measured LR and χ_{rad} for anchored CH_4 and C_3H_8 flames are plotted versus $X_{O_2}^{ox}$ in Fig. 4.12. As shown, trends in the anchored LR and χ_{rad} data closely resemble those for the non-anchored condition, with a few notable exceptions. With inclusion of the O_2-anchor, sooting regime transitions are shifted toward lower $X_{O_2}^{ox}$ (0.178 ± 0.002 and 0.155 ± 0.002 for CH_4 fuel; 0.152 ± 0.002 and 0.131 ± 0.002 for C_3H_8 fuel). These shifts are attributed to the direct influence of the O_2-anchor, where locally high $X_{O_2}^{ox}$ at the flame base stimulates increased soot production, resulting in greater soot radiation throughout the flame. Matching observations from the flame images (see Fig. 4.5), the lower plateau region in the LR trend for CH_4 fuel is considerably lengthened, representing stable soot-free (blue) combustion prior to extinction, and occurring between $X_{O_2}^{ox} = 0.155$ and $X_{O_2}^{ox} = 0.136$.

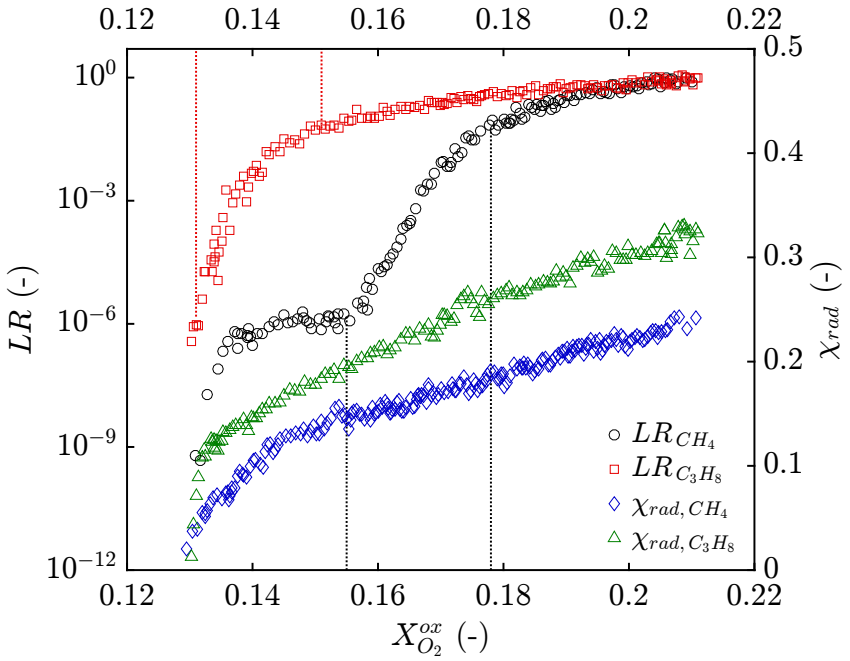

Figure 4.12: Measured flame luminosity ratio (LR) and radiative loss fraction (χ_{rad}) plotted versus $X_{O_2}^{ox}$ for the anchored condition; vertical dotted lines highlight $X_{O_2}^{ox}$ values where each flame transitions between sooting (color) regimes.

As with the non-anchored measurements, anchored χ_{rad} data decrease linearly with declining $X_{O_2}^{ox}$, also experiencing a notable transition in slope, though at lower $X_{O_2,crit}^{ox}$ for each fuel ($X_{O_2,crit}^{ox} \approx 0.143$ for CH_4 and $X_{O_2,crit}^{ox} \approx 0.135$ for C_3H_8). By preventing flame detachment and liftoff, the O_2-anchor additionally extends the domain of flammability for both fuels to lower $X_{O_2}^{ox}$, permitting continued measurement of χ_{rad} and LR beyond the non-anchored extinction limit.

4.2.5 Calorimetry

Measurements of total heat release rate ($\dot{Q}$) and combustion efficiency (η_{comb}) are derived via the calorimetry framework presented in Appendix A. In applying this framework, the standard oxygen-consumption (OC) and carbon-dioxide-generation (CDG) based formulations are utilized (neglecting soot), given respectively as

$$\dot{Q}_{OC} = -\Delta h_{O_2}\ \dot{m}_{O_2}^{rxn} + (\Delta h_{O_2} - \Delta h_{O_2,CO}) \left(\dot{m}_{CO}^{rxn}\ \frac{M_{O_2}}{2M_{CO}} \right), \tag{4.2}$$

$$\dot{Q}_{CDG} = \Delta h_{CO_2}\ \dot{m}_{CO_2}^{rxn} + (\Delta h_{CO_2} - \Delta h_{CO_2,CO}) \left(\dot{m}_{CO}^{rxn}\ \frac{M_{CO_2}}{M_{CO}} \right), \tag{4.3}$$

where values for the Δh parameters in Eqs. 4.2 and 4.3 are summarized in Table 4.2, using fuel-specific values for CH_4 and C_3H_8 (see Appendix A for details).

Table 4.2: Enthalpy parameters in the OC and CDG calorimetry expressions.

Parameter	Value (MJ/kg)
$\Delta h_{O_2}(CH_4)$	12.54
$\Delta h_{CO_2}(CH_4)$	18.23
$\Delta h_{O_2}(C_3H_8)$	12.77
$\Delta h_{CO_2}(C_3H_8)$	15.48
$\Delta h_{O_2,CO}$	17.69
$\Delta h_{CO_2,CO}$	6.43

As discussed in Sec. 2.3.4, and formalized in Appendix A, a premier advantage of the present calorimetry framework is its capacity to handle complex mass exchanges in the measurement system. Applied to the present configuration, this framework explicitly accounts for the variations in $X_{O_2}^{ox}$ that occur with N_2 dilution of the oxidizer. Due to their inherent simplifying assumptions, traditional calorimetry formulations found in the literature are unable to account for these effects.

To explore this distinction, $\dot{Q}$ measurements for an anchored CH_4 flame, derived using both the present and traditional calorimetry formulations, are plotted versus $X_{O_2}^{ox}$ in Fig. 4.13 for OC and Fig. 4.14 for CDG based methods. Model variants include (1) the present framework; (2) the present framework, but with $\dot{m}_{ox} = 0$ within the model, so as to artificially remove the influence of the diluted oxidizer; and (3) a traditional formulation for either OC [106] or CDG [109] based methods.

As shown in Fig. 4.13, $\dot{Q}_{OC}$ for all three models converge only at ambient $X_{O_2}^{ox}$, with models (2) and (3) remaining in close agreement for all $X_{O_2}^{ox}$. This agreement confirms that the present framework converges with the traditional formulation when the diluted oxidizer is neglected. Notably, models (2) and (3) significantly overpredict $\dot{Q}$, with deviations between these models and the reference model (1) increasing linearly with declining $X_{O_2}^{ox}$. This trend is due to the inherent sensitivity of the OC formulation to $X_{O_2}^{ox}$, which directly impacts the O_2 mass balance of the system. Specifically, as $X_{O_2}^{ox}$ is reduced, the O_2 deficit in the exhaust due to dilution of the oxidizer begins to dominate that due to O_2 consumption in the flame. As models (2) and (3) cannot account for oxidizer dilution, they incorrectly attribute the entire exhaust O_2 deficit to the combustion reaction, resulting in vastly overpredicted $\dot{Q}$.

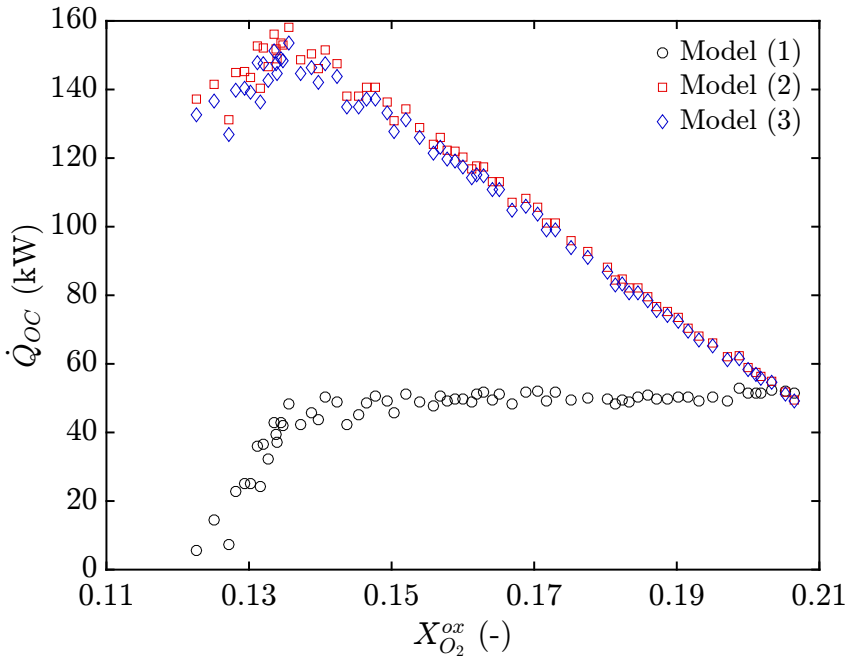

Figure 4.13: Measured $\dot{Q}_{OC}$ for an anchored CH_4 flame plotted versus $X_{O_2}^{ox}$ for varying calorimetry formulations; models include (1) the present formulation with $\dot{m}_{ox}$ as measured, (2) the present formulation with $\dot{m}_{ox} = 0$, and (3) a traditional OC formulation from the literature [106].

Contrary to the noted discrepancies in the OC formulations, $\dot{Q}_{CDG}$ for all three models converge for all $X_{O_2}^{ox}$ (see Fig. 4.14). This agreement is due to the relative insensitivity of the CDG formulation to variations in $X_{O_2}^{ox}$, where the CO_2 content of the oxidizer remains nearly negligible and does not deviate significantly from that in the ambient. As a result, variations in $X_{O_2}^{ox}$ do not significantly impact the CO_2 mass balance of the system, and surplus CO_2 in the exhaust is consistently dominated by that generated in the flame. Hence, models (2) and (3) maintain accurate predictions for $\dot{Q}$, despite neglecting the diluted oxidizer.

While the preceding result may be interpreted to suggest superiority of the CDG over the OC formulation, it must be noted that such a conclusion is configuration dependent. If, for example, oxidizer dilution in the present configuration were

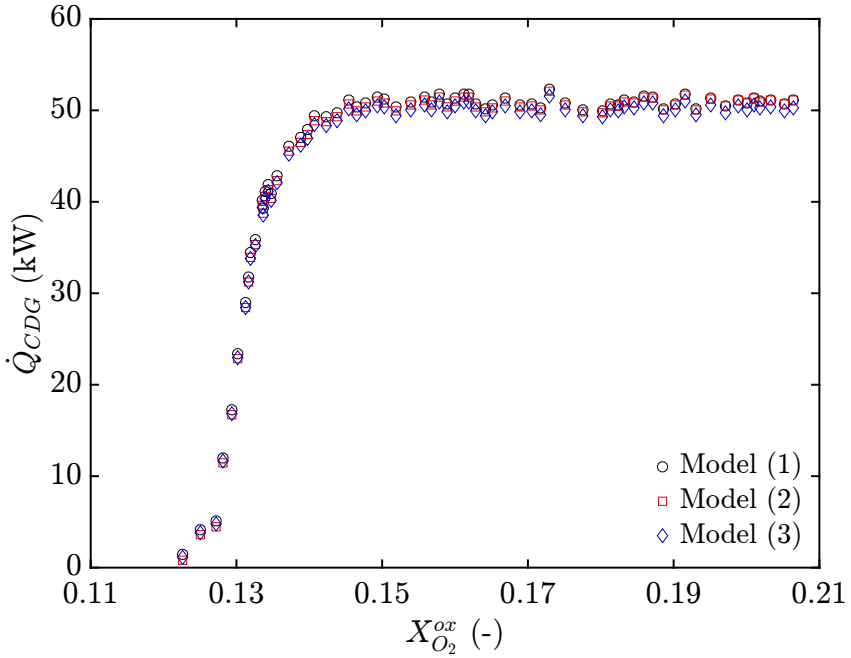

Figure 4.14: Measured $\dot{Q}_{CDG}$ for an anchored CH_4 flame plotted versus $X_{O_2}^{ox}$ for varying calorimetry formulations; models include (1) the present formulation with $\dot{m}_{ox}$ as measured, (2) the present formulation with $\dot{m}_{ox} = 0$, and (3) a traditional CDG formulation from the literature [109].

accomplished via CO_2 instead of N_2 addition, the CDG formulation would expectedly be significantly more sensitive to dilution of the oxidizer. For such a scenario, the traditional CDG formulation should not be expected to yield accurate results.

The model comparisons in Fig. 4.13 emphasize the importance of a comprehensive control-volume analysis in the derivation of any calorimetry framework, where the undue omission of applicable mass exchanges may significantly affect the accuracy of the model. However, comparisons in Fig. 4.14 highlight that for complex systems, not every applicable mass exchange need significantly influence both the OC and CDG formulations. Careful consideration of the mass balances in a given application may provide a useful means to determine a priori which formulation should be preferred and whether any omission of measurements may be acceptable.

Having demonstrated that the calorimetry framework presented in Appendix A is appropriate (and necessary) for accurate evaluation of heat release information in the present configuration, associated measurements for suppression analysis are presented as follows. Calorimetry-derived $\dot{Q}_{OC}$ and $\dot{Q}_{CDG}$ are plotted versus $X_{O_2}^{ox}$ in Fig. 4.15. Individual plots present data for the non-anchored CH_4 (Fig. 4.15(a)), anchored CH_4 (Fig. 4.15(b)), non-anchored C_3H_8 (Fig. 4.15(c)), and anchored C_3H_8 (Fig. 4.15(d)) flames. Also included in each plot are the corresponding combustion efficiency data, with η_{comb} as defined in Eq. 2.31.

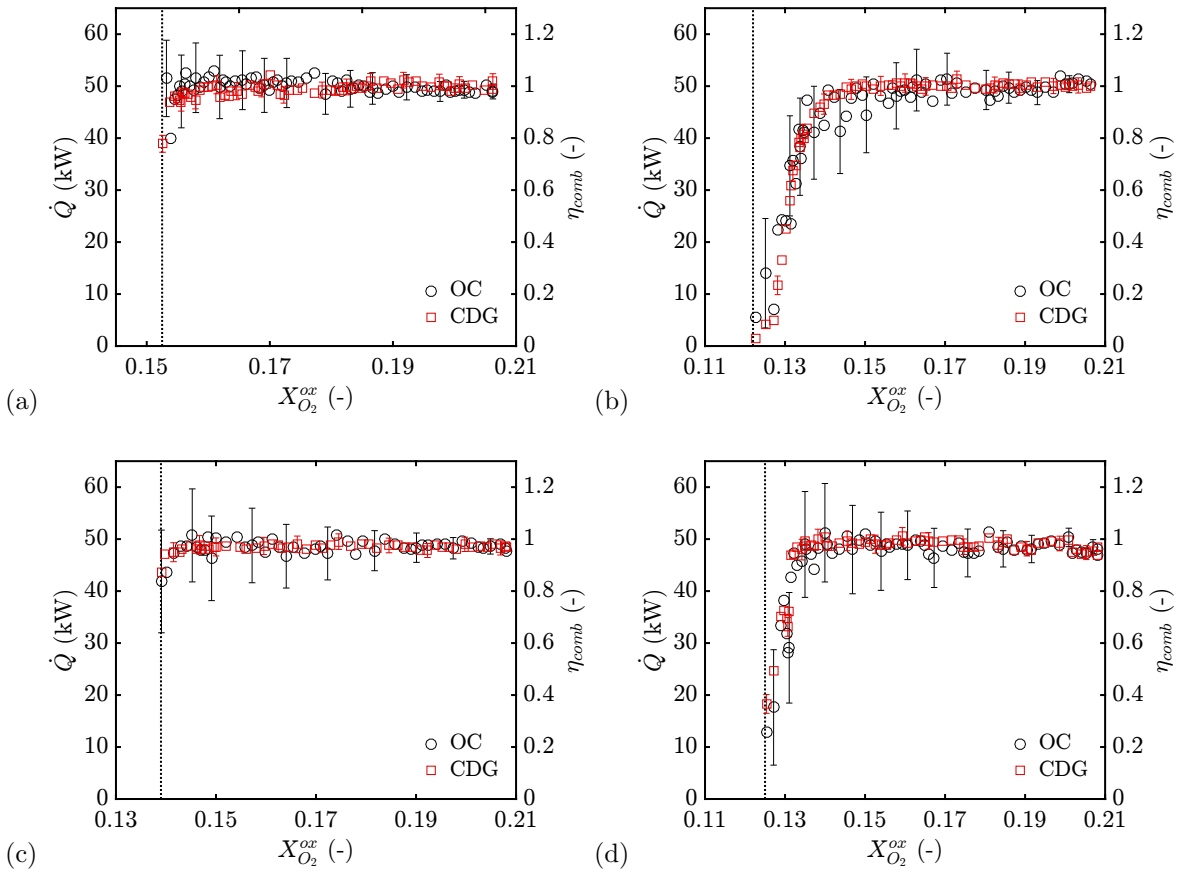

Figure 4.15: Calorimetry-derived heat release rate ($\dot{Q}$) and combustion efficiency (η_{comb}) plotted versus $X_{O_2}^{ox}$ for various flames; (a) non-anchored CH_4, (b) anchored CH_4, (c) non-anchored C_3H_8, (d) anchored C_3H_8.

As shown in Fig. 4.15, $\dot{Q}_{OC} \approx \dot{Q}_{CDG}$ for all $X_{O_2}^{ox}$ and for all four flames, indicating good agreement between the two formulations, as should be expected with the present framework. Notably, uncertainties in $\dot{Q}_{OC}$ and $\dot{Q}_{CDG}$ are initially comparable ($\pm 1.5\,\mathrm{kW}$) near ambient $X_{O_2}^{ox}$, but deviate with declining $X_{O_2}^{ox}$. Uncertainty in $\dot{Q}_{OC}$ gradually increases, eventually and significantly exceeding that in $\dot{Q}_{CDG}$ ($\pm 11\,\mathrm{kW}$ max for $\dot{Q}_{OC}$ versus $\pm 2\,\mathrm{kW}$ max for $\dot{Q}_{CDG}$). This trend is principally due to the heightened sensitivity of the OC formulation to uncertainties in the oxidizer composition and flow rate, for reasons previously discussed (see Fig. 4.13 discussion).

Also shown in Fig. 4.15, $\eta_{comb} \approx 1$ for all flames over a wide range of reduced $X_{O_2}^{ox}$. For the non-anchored flames (Figs. 4.15(a) and (c)), η_{comb} tapers only slightly, lowering to a value of roughly 0.8 for both fuels immediately before extinction. For these flames, extinction occurs as liftoff (see Figs. 4.3 and 4.4), whereby a potentially significant portion of the flame is still burning at initiation of the liftoff event. The extinction limit for each flame (LOI, see Table 4.1) is marked with a vertical dotted line in each figure, where LOI for the non-anchored flames are presently denoted as LOI_{na}. For the anchored flames (Figs. 4.15(b) and (d)), and for $X_{O_2}^{ox} > LOI_{na}$, $\dot{Q}$ and η_{comb} are equivalent to those measured for the non-anchored flames. For $X_{O_2}^{ox} < LOI_{na}$, the O_2-anchor prevents liftoff extinction, so that $\dot{Q}$ and η_{comb} reduce gradually with declining $X_{O_2}^{ox}$ due to progressive quenching until global extinction.

From the calorimetry-derived species reaction rates ($\dot{m}_k^{rxn}$, see Appendix A), the net combustion yield, y_k, of species k may be defined as

$$y_k = \frac{\dot{m}_k^{rxn}}{\dot{m}_{fuel}}. \tag{4.4}$$

Measured y_k for O_2, CO_2, H_2O, and CO are plotted versus $X_{O_2}^{ox}$ in Fig. 4.16. As before, individual plots present data for the non-anchored CH_4 (Fig. 4.16(a)), anchored CH_4 (Fig. 4.16(b)), non-anchored C_3H_8 (Fig. 4.16(c)), and anchored C_3H_8 (Fig. 4.16(d)) flames. Included in each plot are the reference stoichiometric yields for each species ($y_{k,st}$, shown as horizontal dashed lines), defined as

$$y_{k,st} = \nu_{k,st} \frac{M_k}{M_{fuel}}, \tag{4.5}$$

where $\nu_{k,st}$ is the stoichiometric molar reaction coefficient for species k in the balanced combustion mechanism for either fuel (see reaction R_0 in Appendix A).

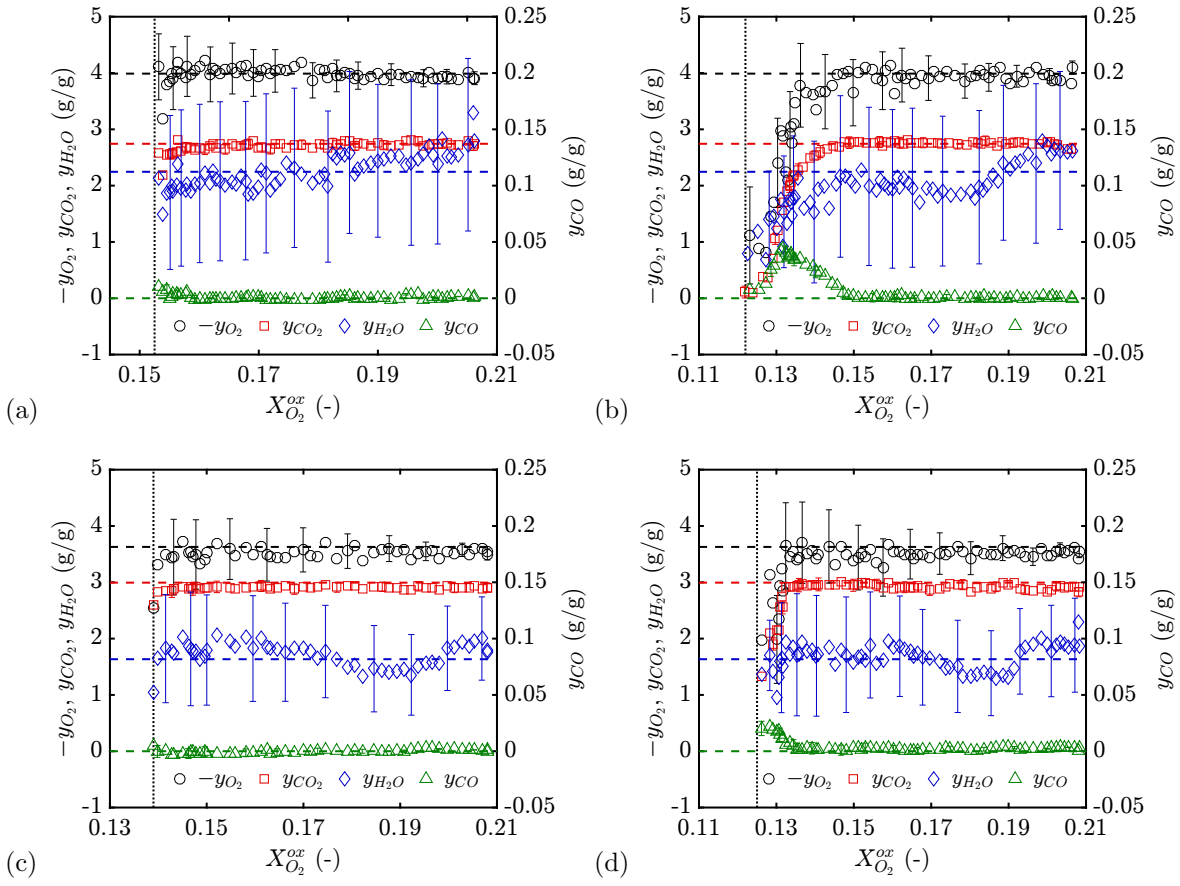

Figure 4.16: Calorimetry-derived net combustion yields (y_{O_2}, y_{CO_2}, y_{H_2O}, and y_{CO}) plotted versus $X_{O_2}^{ox}$ for various flames; (a) non-anchored CH_4, (b) anchored CH_4, (c) non-anchored C_3H_8, (d) anchored C_3H_8.

As shown in Fig. 4.16, $y_k \approx y_{k,st}$ for all species and for all four flames over a wide range of reduced $X_{O_2}^{ox}$. As expected, trends in y_{O_2} and y_{CO_2} closely match those noted for the $\dot{Q}_{OC}$ and $\dot{Q}_{CDG}$ measurements (see Fig. 4.15). Trends in y_{H_2O} resemble those for y_{O_2} and y_{CO_2}, though with significantly greater measurement uncertainty. Uncertainty in y_{H_2O} is principally attributed to the relative inaccuracy of the H_2O sensor, as compared to the highly accurate analyzers used for the other species (see Sec. 2.3.4). Despite the relatively high uncertainty, measured y_{H_2O} reasonably match the expected $y_{H_2O,st}$ for the present flames. As has been reported in previous works [107, 110, 112, 137], the OC and CDG calorimetry formulations are relatively insensitive to uncertainty in the H_2O measurements, therefore the noted uncertainty in y_{H_2O} does not significantly affect the other calorimetry-derived quantities.

Also shown in Fig. 4.16, $y_{CO} \approx 0$ for all four flames, indicating that there are no appreciable effects of incomplete combustion in the present suppression experiments. For the non-anchored flames (Figs. 4.16(a) and (c)), a small but nearly negligible increase in y_{CO} is observed at the moment of global extinction. A more pronounced increase in y_{CO} is measured for the anchored flames (Figs. 4.16(b) and (d)), where $y_{CO} > 0$ only for $X_{O_2}^{ox} < LOI_{na}$, increasing with declining $X_{O_2}^{ox}$ until reaching maxima of $y_{CO,max} = 0.045$ at $X_{O_2}^{ox} = 0.132$ for CH_4 and $y_{CO,max} = 0.022$ at $X_{O_2}^{ox} = 0.128$ for C_3H_8. With further reduction in $X_{O_2}^{ox}$, y_{CO} for either fuel diminishes as extinction effects begin to dominate any incomplete combustion.

Recalling the discussions presented in Secs. 4.2.1–4.2.4, previously described observations and measurements demonstrate significant effects of suppression in the present configuration through changes in visible flame structure and reductions in

radiative emissions with declining $X_{O_2}^{ox}$. Still, the presently measured trends in η_{comb} and y_k reveal that despite these other suppression effects, for all of the present flames and for $X_{O_2}^{ox} > LOI_{na}$, nearly all of the fuel continues to react and combustion products are produced in stoichiometric proportions. These results agree with speculations reported in previous studies [161–163], for which locally measured species concentrations suggested the persistence of complete combustion until the extinction limit, but validating combustion efficiency measurements were not provided. The present results establish a definitive confirmation of these behaviors.

To further investigate the significance of the present measurements, a direct comparison of the measured η_{comb} and χ_{rad} data is provided in Fig. 4.17. Recall that the present measurements comprise η_{comb} that remain constant near unity and χ_{rad} that decline linearly with reducing $X_{O_2}^{ox}$. Considering the discrepancy between these trends, it is apparent that in order for η_{comb} to remain near unity with declining $X_{O_2}^{ox}$, the measured reduction in χ_{rad} should occur with a concomitant increase in the convective fraction of the total heat release, χ_{conv}.

A measured estimate of χ_{conv} is also plotted in Fig. 4.17, defined as

$$\chi_{conv} = \frac{\dot{m}_e \, c_{p,e} \, (T_e - T_\infty)}{\dot{m}_{fuel} \, \Delta h_{comb}}, \tag{4.6}$$

where $\dot{m}_e$ is the mass flow rate, T_e the temperature, and $c_{p,e}$ the heat capacity of the exhaust gases in the fire-products collection system (see Sec. 2.3.4), with other terms as previously defined. Here, $c_{p,e}$ is estimated as the corresponding value for ambient air, evaluated at temperature T_e. Also included in Fig. 4.17 is the sum,

$$\chi_{sum} = \chi_{conv} + \chi_{rad}. \tag{4.7}$$

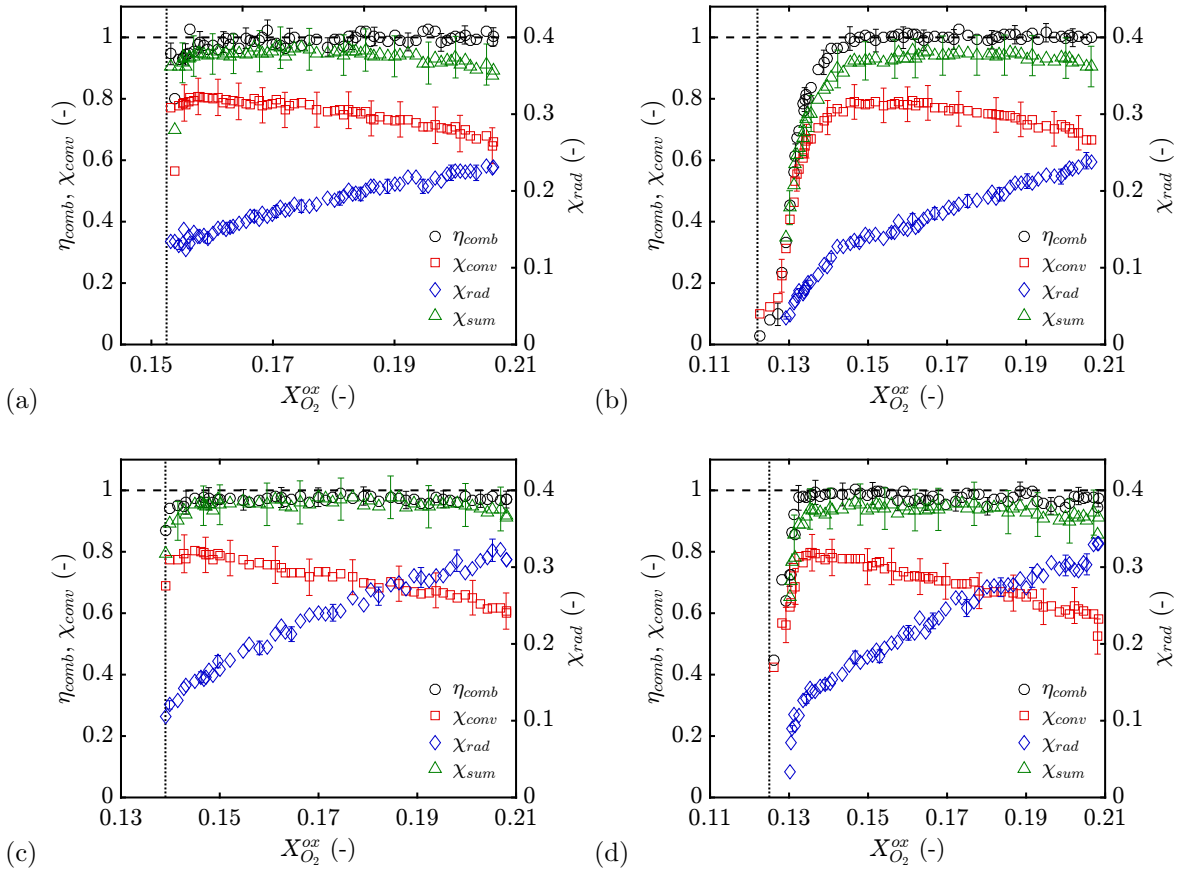

Figure 4.17: Comparison of measured η_{comb} (species calorimetry derived), χ_{rad} (thermally derived), and χ_{conv} (thermally derived) plotted versus $X_{O_2}^{ox}$ for various flames; (a) non-anchored CH_4, (b) anchored CH_4, (c) non-anchored C_3H_8, (d) anchored C_3H_8.

As shown in Fig. 4.17, measured χ_{conv} increase quasi-linearly with declining $X_{O_2}^{ox}$ for all four flames, due primarily to associated increases in T_e. The increasing trend in χ_{conv} is nearly perfectly offset by the decreasing trend in χ_{rad}, so that χ_{sum} closely matches η_{comb}. The χ_{sum} trend slightly, but consistently under-predicts the η_{comb} trend, attributed to heat losses that are not accounted for in the χ_{conv} and χ_{rad} measurements. Such losses likely include conduction losses at the flame base to the burner or additional losses to the walls of the exhaust system. In comparing the

offset between η_{comb} and χ_{sum}, these losses are suggested to be small and unaffected by declining $X_{O_2}^{ox}$, though such agreement is likely configuration dependent.

The agreement between the present η_{comb} and χ_{sum} measurements offers two additional conclusions. First, χ_{sum}, which is based entirely on thermal measurements, provides an independent validation of the species-based calorimetry principles used to evaluate η_{comb}, where the calorimetry-derived heat release rate is determined using mass-conservation analyses and species measurements only and includes no actual thermal measurements.

Second, because of the measurement complexity required for accurate species-based calorimetry (see Appendix A), the present results suggest that coupled measurements of χ_{rad} (requiring only a heat flux transducer and resolved flame images) and χ_{conv} (requiring only a thermocouple and the collection and measurement of the exhaust flow rate) may provide an attractive and inexpensive alternative method for global heat release rate measurements, particularly for cases where qualitative trends are desired and a systematic offset in quantitative result due to heat losses may be acceptable. For suppression studies in particular, qualitative η_{comb} trends inferred from χ_{conv} and χ_{rad} measurements may potentially be calibrated to yield quantitative results, provided η_{comb} at an unsuppressed condition is known and any offset due to heat losses may be assumed to be independent of suppression effects.

Summarizing the present experimental results, it is expected that the primary effect of the N_2-diluted oxidizer is to reduce the flame temperature, where the increasing presence of inert N_2 in the reacting mixture dissipates heat from the combustion reaction. Because the radiative flame emissions scale with temperature

to the fourth power, χ_{rad} is most sensitive to this effect and reduces linearly with declining $X_{O_2}^{ox}$. Despite the reducing flame temperature, η_{comb} has been found to remain close to unity until the extinction limit is reached, suggesting a constant rate of heat release into the reacting mixture. With less of that heat lost to radiation, a greater fraction is convected away from the flame into the plume, resulting in increased plume and exhaust temperatures. In this fashion, the reduction in flame temperature that may be intuitively expected during flame suppression can also be (somewhat counter-intuitively) expected to cause increasing plume temperatures. This result could perhaps have implications for the design of fire suppression systems. The observed changes in the visible flame structure (see Figs. 4.3–4.6) are then the limited result of diminishing soot incandescence where soot inception is highly sensitive to both flame temperature and dilution effects [157–159].

4.3 Simulation

The present investigation considers three alternative treatments for modeling extinction and reignition in numerical simulations of the experiments. The primary features of these cases are summarized in the following (see Sec. 3.2.2 for details).

1. M1 — baseline case featuring the standard EDC combustion model with a temperature-based extinction criterion, but no explicit reignition treatment.

2. M2 — extension of case M1, including a prescribed ignition zone that permits spontaneous combustion at the fuel port, but applies a temperature-based reignition criterion elsewhere in the computational domain.

3. M3 — advanced case featuring a tiered combustion mechanism, where secondary and tertiary reactions respectively allow the transformation of primary fuel to secondary fuel (upon extinction of the primary reaction) and the reignition of secondary fuel (subject to a temperature-based reignition criterion).

Each of the preceding cases include an extinction criterion (Eq. 3.6) with critical temperature parameter, T_{ext}, and a reignition criterion (Eq. 3.10) with critical temperature parameter, T_{ign}. The values of these parameters as specifically applied within each case are described in Table 3.1. Applied to the preceding cases, simulations consider only N_2 suppression of the anchored CH_4 flame, where the use of CH_4 fuel permits the model assumption that combustion occurs with zero net soot yield, and use of the anchored condition avoids the complexity associated with liftoff extinction events (which are not expected to be modeled adequately).

4.3.1 Measurement Comparisons

A preliminary validation of each modeling case against measured thermocouple temperatures (T_{tc}) and local O_2 mole fractions (X_{O_2}) is presented in Fig. 4.18. Measured and simulated data are reported as lateral cross-flame profiles (x-direction) at selected elevations corresponding to $z = 12.5\,\text{cm}$ ($\sim L_f/4$) and $z = 25.0\,\text{cm}$ ($\sim L_f/2$) above the fuel port, for a partially-diluted oxidizer condition of $X_{O_2}^{ox} = 0.18$. This validation condition serves to evaluate the influence that each extinction and reignition treatment may have on the flame structure for a partially suppressed condition where complete combustion is still expected.

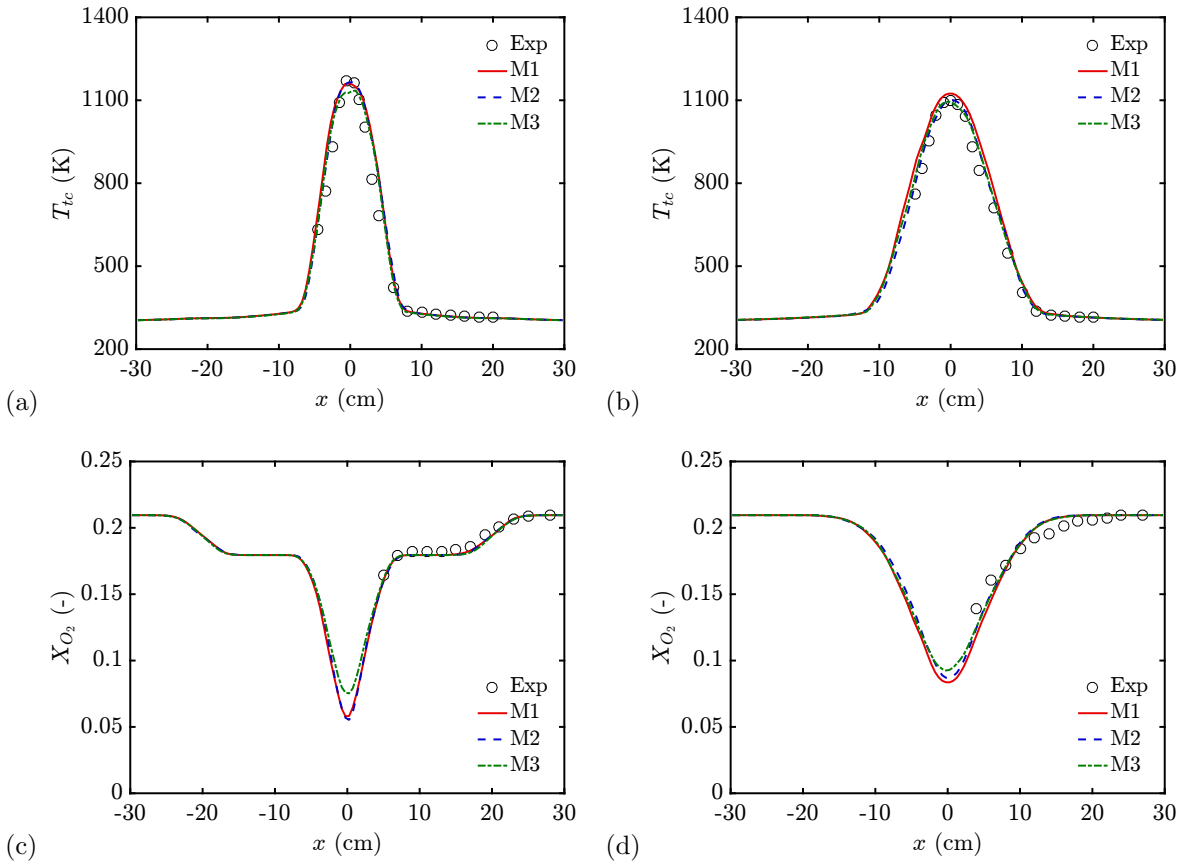

Figure 4.18: Simulated and measured mean x-profiles of local thermocouple temperature (T_{tc}) and O_2 mole fraction (X_{O_2}) at selected elevations above the fuel port, and for $X_{O_2}^{ox} = 0.18$; (a) T_{tc} at $z = 12.5\,\text{cm}$, (b) T_{tc} at $z = 25.0\,\text{cm}$, (c) X_{O_2} at $z = 12.5\,\text{cm}$, (d) X_{O_2} at $z = 25.0\,\text{cm}$.

As shown in Fig. 4.18, simulated T_{tc} and X_{O_2} for all three cases agree reasonably well with the measured values. In particular, peak T_{tc} at both $z = 12.5\,\text{cm}$ and $z = 25.0\,\text{cm}$ show good agreement, though the simulated profiles are slightly wider than measured at both elevations. Agreement for X_{O_2} at $z = 12.5\,\text{cm}$ is also good, though the simulated trends at $z = 25.0\,\text{cm}$ are slightly sharper than measured. These results validate that each case yields mean temperature and mixing fields resembling those measured in the experiment, confirming that the simulated flame structures are not unreasonably skewed by the extinction and reignition treatments.

A preliminary verification test to evaluate the capacity for spurious reignition in each case is depicted in Fig. 4.19, which visualizes each simulated flame at $X_{O_2}^{ox} = 0$ (pure N_2 co-flowing oxidizer). For this condition, total flame extinction is definitively expected with no possibility of reignition, corresponding to simulated $\eta_{comb} = 0$. Here, the simulated η_{comb} is defined as

$$\eta_{comb} = \frac{1}{\tau\, \dot{m}_{fuel}\, \Delta h_{comb}} \int_{\tau} \int_{V} \dot{Q}''' \, dV \, dt, \tag{4.8}$$

where $\dot{Q}'''$ is the local volumetric heat release rate in each computational cell, $\dot{m}_{fuel}$ is the mass flow rate of primary fuel from the fuel port, V is the volume of the computational domain, and τ is a time-averaging window.

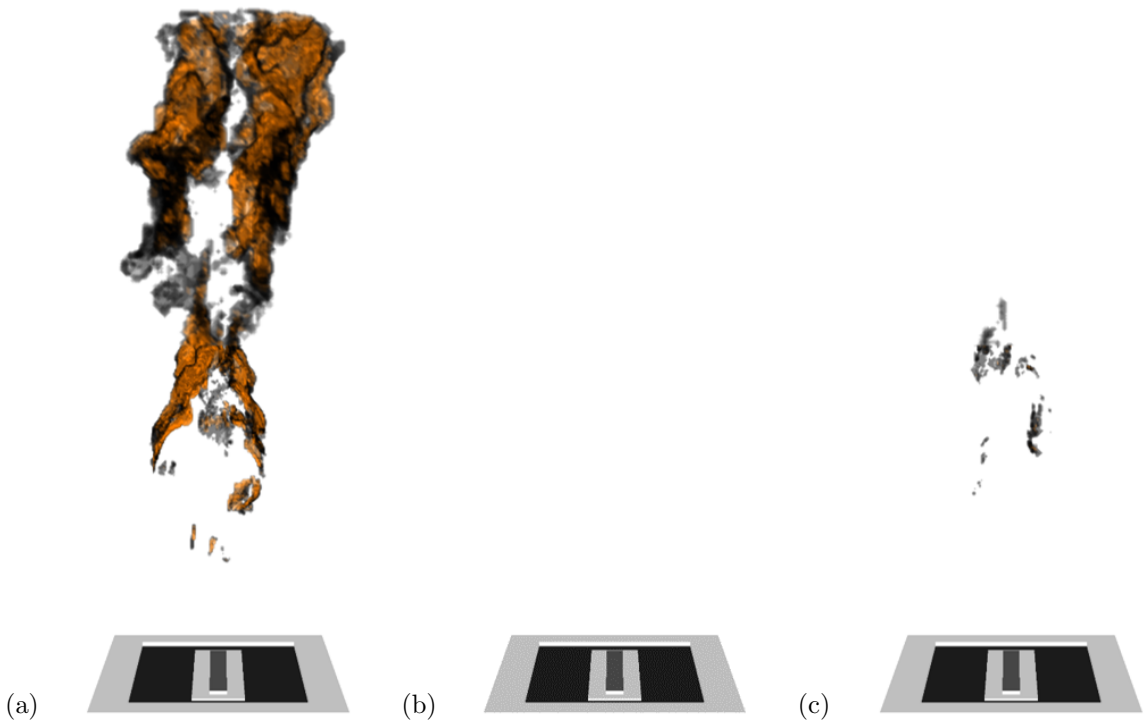

Figure 4.19: Spurious reignition in each modeling case for $X_{O_2}^{ox} = 0$; (a) M1 suffers significant spurious reignition ($\eta_{comb} = 0.69$), (b) M2 thoroughly eliminates spurious reignition ($\eta_{comb} = 0$), (c) M3 suffers slight, but nearly negligible spurious reignition ($\eta_{comb} = 0.01$).

For case M1 in Fig. 4.19(a), as expected, there is significant spurious reignition and $\eta_{comb} = 0.69$. As shown, extinction is correctly predicted within the region of influence of the diluted oxidizer; however, as soon as the plume of unburned fuel mixes with sufficient air from the surrounding ambient (roughly 1 m above the fuel port) the inequality in Eq. (3.6) is satisfied and combustion proceeds spontaneously.

For case M2 in Fig. 4.19(b), there is no spurious reignition and $\eta_{comb} = 0$. For M3 however, in Fig. 4.19(c), there is a nearly negligible, but still finite occurrence of spurious reignition ($\eta_{comb} = 0.01$). This is due to the tiered reaction scheme implemented in M3, where the fuel transformation reaction (R2) includes a stoichiometric requirement for air. As there is no air present in the oxidizer at $X_{O_2}^{ox} = 0$, reaction R2 fails within the diluted oxidizer, allowing the extinguished primary fuel to persist within the domain. Upon initial mixing with air in the ambient, most but not all of this primary fuel is eventually transformed to secondary fuel (via the extinction model). Spurious reignition in case M3 is thus significantly reduced compared to M1, though it is not as thoroughly eliminated as in M2.

Figure 4.20 presents simulated η_{comb} for each case plotted versus $X_{O_2}^{ox}$ and compared against experimental data (derived via CDG calorimetry, see Sec. 4.2.5). Compared to the measured data, all simulated cases match the initial plateau in η_{comb} for $X_{O_2}^{ox} > 0.14$. For $X_{O_2}^{ox} < 0.14$, M1 fails to follow the experimental trend and significantly over-predicts η_{comb}, primarily due to the occurrence of spurious reignition, as illustrated in Fig. 4.19(a). Notably, M1 does not predict deviation from $\eta_{comb} \approx 1$ until $X_{O_2}^{ox} < 0.12$, where the experimental data (and M2 and M3) show global extinction. Also noteworthy, M1 fails to ever predict extinguishment.

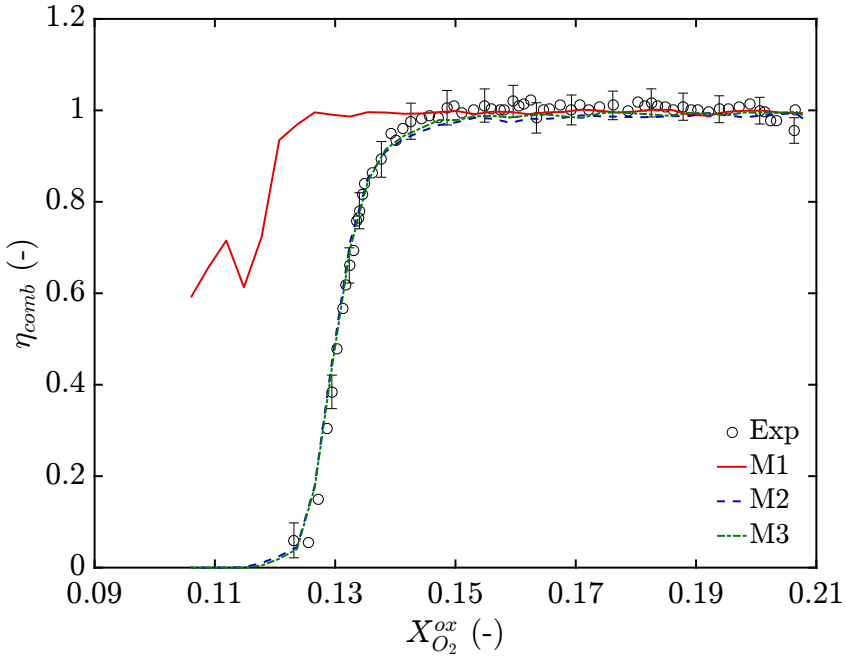

Figure 4.20: Simulated and measured combustion efficiency (η_{comb}) plotted versus $X_{O_2}^{ox}$; M1, which permits spurious reignition, fails to match the measured trend, while M2 and M3, which include provisions to prevent spurious reignition, match the measured data well.

As shown in Fig. 4.20, cases M2 and M3 follow the experimental η_{comb} trend very well, falling within measurement uncertainty (± 0.04), and matching the extinction limit at $LOI \approx 0.12$. Despite their different approaches at addressing spurious reignition (M2 via spatially defined ignition zone, and M3 via tiered reaction mechanism), the two cases also agree with one another remarkably well. In both cases, this agreement is achieved using relatively simple temperature-based extinction and reignition treatments, with established critical temperature values ($T_{ext} = 1600\,\mathrm{K}$ and $T_{ign} = 900\,\mathrm{K}$). The results in Fig. 4.20 demonstrate the significance of adequately preventing spurious reignition in simulations with localized flame suppression.

Supplemental measurement comparisons for the simulated flame height (L_f) and flame radiative heat flux ($\dot{q}_g''$) are presented respectively in Figs. 4.21 and 4.22.

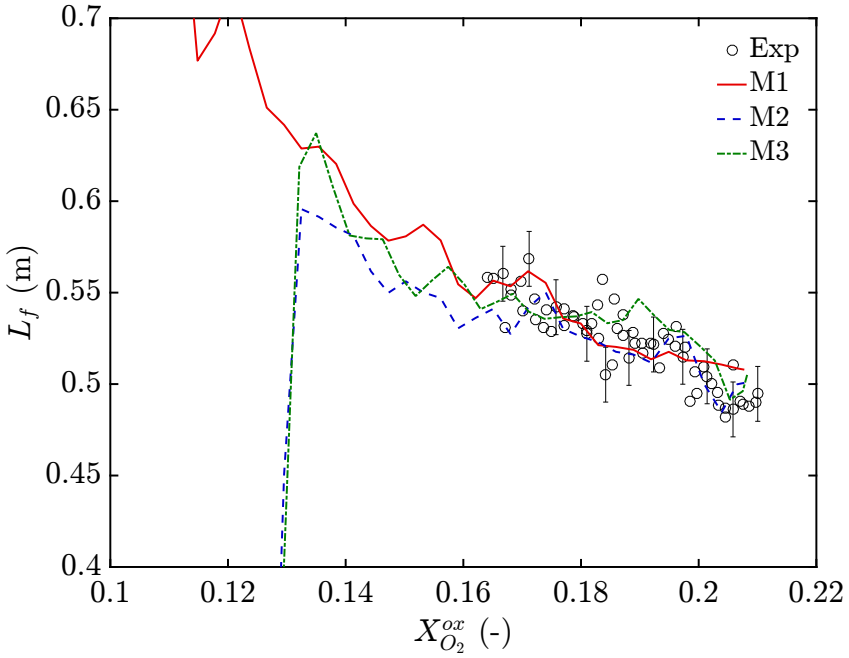

Figure 4.21: Simulated and measured flame height (L_f) plotted versus $X_{O_2}^{ox}$; measured L_f is derived via visible flame emissions, simulated L_f is derived via peak local volumetric heat release rate.

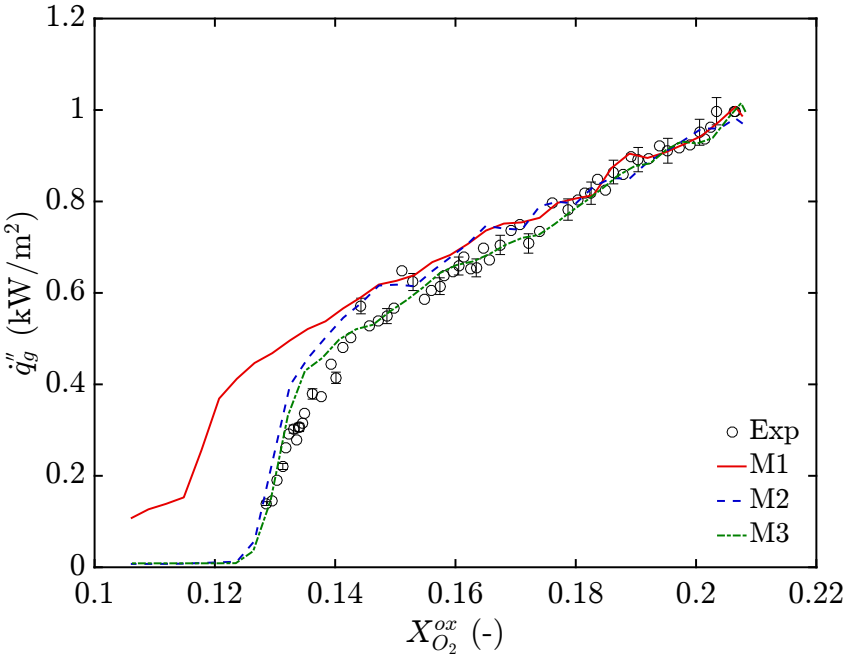

Figure 4.22: Simulated and measured flame radiative heat flux ($\dot{q}_g''$) plotted versus $X_{O_2}^{ox}$; agreement between measured and simulated results is expected because the measured χ_{rad} is prescribed in the simulations.

As plotted in Fig. 4.21, the simulated flame height is defined via

$$L_f = \frac{1}{\tau\, A} \int_{\tau} \int_{A} \max\left(z \mid \dot{Q}''' > \dot{Q}'''_{crit}\right)\, dA\, dt, \tag{4.9}$$

where A is the cross-sectional area of the computational domain, $\dot{Q}'''_{crit}$ is a critical value for the local volumetric heat release rate defining the extent of the flame, and other terms are as previously defined (see Eq. 4.8). Here, $\dot{Q}'''_{crit} = 1\,\mathrm{kW/m^3}$, is selected to produce agreement between the simulated and measured L_f at ambient $X^{ox}_{O_2}$. Sensitivity of the simulated L_f to $\dot{Q}'''_{crit}$ is relatively slight, such that variation in $\dot{Q}'''_{crit}$ between 0.1–10 $\mathrm{kW/m^3}$ yields deviation in the simulated L_f of roughly 4 cm.

Shown in Fig. 4.21, measured and simulated L_f among all three cases agree reasonably well for $X^{ox}_{O_2} > 0.16$ (where measured data are available). With declining $X^{ox}_{O_2}$, simulated L_f match the measured increasing trend, indicating that oxidizer entrainment in the simulated flames correctly responds to conditions of oxidizer dilution. For $X^{ox}_{O_2} < 0.16$, simulated L_f for all three cases continue to increase until $X^{ox}_{O_2} \approx 0.13$, at which point L_f for M2 and M3 rapidly decline due to flame extinction. Contrarily for case M1, L_f increases monotonically due to continuous spurious reignition at high elevations in the domain.

Depicted in Fig. 4.22, very good agreement is obtained between the measured and simulated $\dot{q}''_g$. This agreement is expected, where the measured χ_{rad} (which is derived from the measured $\dot{q}''_g$) is prescribed in the simulations (so that the simulated $\dot{q}''_g$ is derived from the prescribed χ_{rad}). The observed agreement then serves as a verification of consistency between the measured and prescribed trends in χ_{rad}, and that the angular RTE resolution in the simulation is sufficient (see Sec. 3.4.2).

With its tiered reaction mechanism, case M3 permits additional detailed diagnostics to compare the relative contributions of heat release from either primary combustion (reaction R1) or reignition (reaction R3). These results are presented in Fig. 4.23. As shown, combustion is initially dominated by R1 at ambient $X_{O_2}^{ox}$, though there is considerable reignition heat release from R3 ($\sim$30%), indicating that even at ambient conditions, M3 predicts localized extinction (though later reignition satisfies total $\eta_{comb} \approx 1$). As $X_{O_2}^{ox}$ is reduced, $\eta_{comb,\,R1}$ steadily and monotonically decreases while $\eta_{comb,\,R3}$ gradually increases. For $X_{O_2}^{ox} > 0.14$, these trends offset, resulting in constant total simulated $\eta_{comb} \approx 1$. Near $X_{O_2}^{ox} \approx 0.135$, $\eta_{comb,\,R3}$ attains a peak value of roughly 80%, dropping off abruptly with further declining $X_{O_2}^{ox}$. Along with the continuous decline in $\eta_{comb,\,R1}$, total η_{comb} also decreases, tapering once $\eta_{comb,\,R3}$ drops to zero, occurring just before global extinction.

In agreement with the results of recent affiliated work [66], these trends clearly demonstrate that reignition treatment can dominate simulated suppression performance, where $\eta_{comb,\,R3}$ is maximized and significantly greater than $\eta_{comb,\,R1}$ throughout the region of rapidly declining η_{comb} in advance of the extinction limit. The simulated result that $\eta_{comb,\,R3} > 0$ at ambient $X_{O_2}^{ox}$ additionally suggests that local extinction and reignition events may be prevalent in turbulent fires, even for unsuppressed conditions. While these insights are interesting, it must be noted that no experimental measurements presently exist which could corroborate any distribution of total heat release amongst primary combustion and reignition. The present results are then useful to evaluate model performance, but should not be construed to represent actual flame behaviors until supporting measurements are made available.

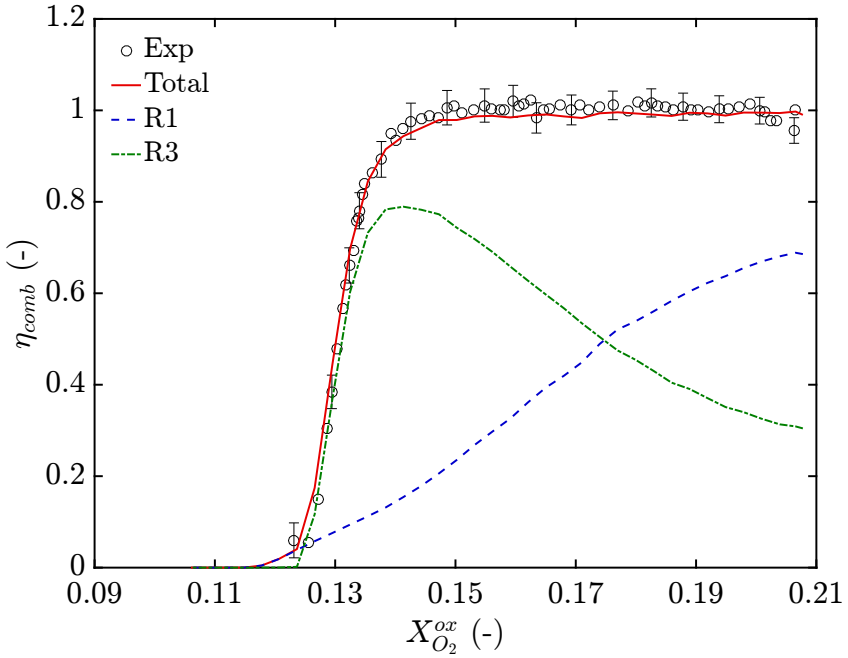

Figure 4.23: Simulated and measured combustion efficiency (η_{comb}) among tiered reactions in modeling case M3; reaction R1 represents primary combustion, while reaction R3 represents reignition.

4.3.2 Model Sensitivity

The sensitivity of modeling cases M1, M2, and M3 to variations in input parameters is examined in Fig. 4.24, which primarily compares simulated η_{comb} trends for each case among T_{ext} between 1500–1700 K, and T_{ign} between 800–1000 K. Specific to case M2, an additional sensitivity study considering the influence of the size of the prescribed ignition zone has also been performed.

Shown in Figs. 4.24(a), (c), and (e), respectively for cases M1, M2, and M3, a shift of T_{ext} by 100 K in either direction produces a corresponding shift in LOI by roughly 0.015. The same also results in a shift in the value of $X_{O_2}^{ox}$ at the inflection point of η_{comb} decline ($X_{O_2,crit}^{ox}$) by roughly 0.015, such that the entire η_{comb} trend is synchronously shifted to higher or lower $X_{O_2}^{ox}$ with variation in T_{ext}. Similarly

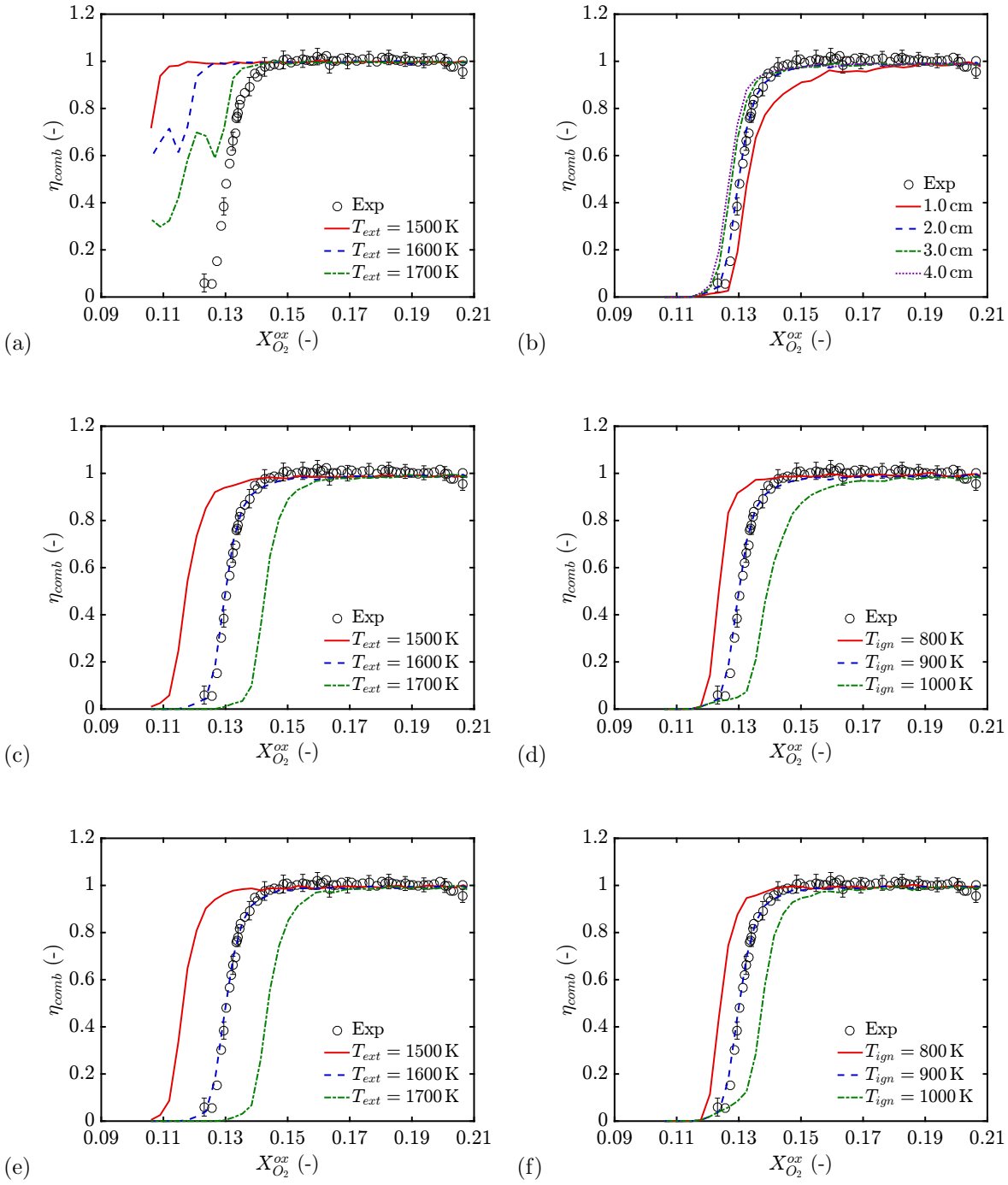

Figure 4.24: Sensitivity of simulated combustion efficiency (η_{comb}) to varying model parameters; (a) M1 T_{ext} sensitivity, (b) M2 ignition-zone size sensitivity, (c) M2 T_{ext} sensitivity, (d) M2 T_{ign} sensitivity, (e) M3 T_{ext} sensitivity, (f) M3 T_{ign} sensitivity.

shown in Figs. 4.24(d) and (f), respectively for cases M2 and M3, a shift of T_{ign} by 100 K in either direction results in a negligible change in LOI, but a shift in $X^{ox}_{O_2,\,crit}$ of roughly 0.01 (with M2 slightly more sensitive to variation in T_{ign} than M3). Shown in Fig. 4.24(b) (case M2), variations in ignition-zone elevation between 1.0–4.0 cm lead to a negligible change in LOI, with changes in $X^{ox}_{O_2,\,crit}$ of less than 0.005. Simulated suppression performance in each case is then most sensitive to T_{ext}, less sensitive to T_{ign}, and for M2, even less sensitive to ignition zone size.

Note that while simulated suppression performance is relatively insensitive to increasing size of the ignition zone, as shown in Fig. 4.24(b), there does exist a minimum effective size for the ignition zone below which spontaneous primary ignition is not achieved. For the present configuration, this ineffectiveness limit corresponds to an ignition zone one computational-cell high, extending 5 mm above the fuel port. This minimum size is likely to depend on the configuration of the fuel source, the selected value for T_{ign}, and the grid resolution (see Fig. 4.25 below), though no numerical or theoretical basis for its recommendation has yet been determined. A maximum size for the ignition zone however, may be intuitively discerned relative to the mean flame volume at ambient condition, where a size of one-tenth the mean flame volume may be considered as a suitable initial limit.

The sensitivity of each modeling case to variations in grid resolution is explored in Fig. 4.25, including comparisons between the baseline resolution, $\Delta x = 5.0$ mm, and coarsened resolutions, $\Delta x = 10.0$ mm and $\Delta x = 20.0$ mm (the refined resolution of $\Delta x = 2.5$ mm is deemed prohibitively expensive for the present analysis, with an estimated computational cost of more than 100,000 processor-hours).

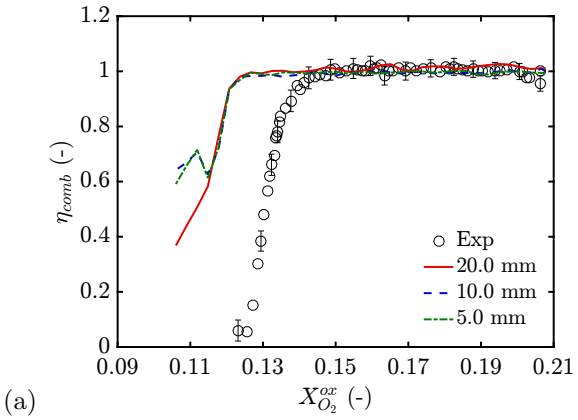

(a)

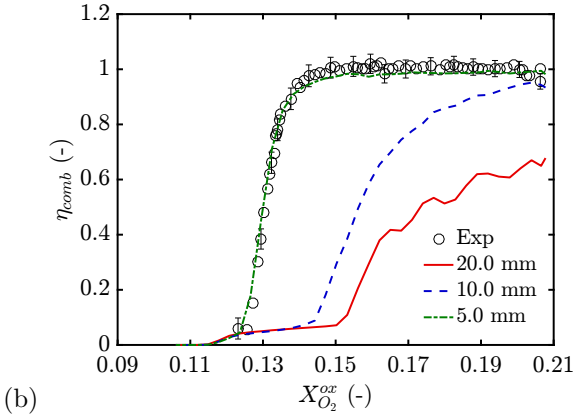

(b)

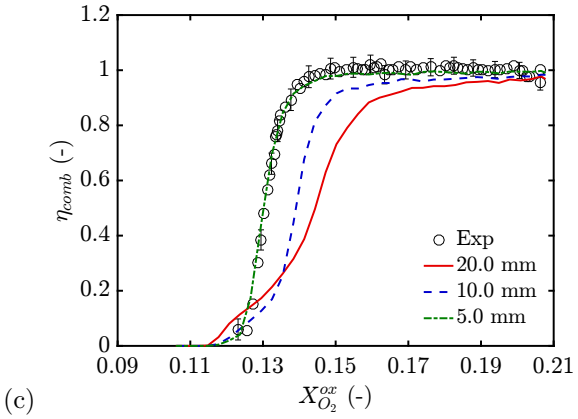

(c)

Figure 4.25: Sensitivity of simulated combustion efficiency (η_{comb}) to varying grid resolution; (a) case M1, (b) case M2, (c) case M3.

As depicted in Fig. 4.25(a), grid sensitivity in case M1 is relatively negligible, attributed to the dominance of spurious reignition over extinction within the domain. Comparatively, grid sensitivity in cases M2 and M3 is significant, respectively shown in Figs. 4.25(b) and (c). In both cases, grid coarsening leads to an over-prediction of suppression, attributed to the inherent grid sensitivity of the gas-phase cell temperature on which the reignition criterion is solely based and which tends to be under-predicted in coarse grids. Grid sensitivity is greatest in case M2, attributed to the bounds of the specified ignition zone, whose size does not scale with the underlying grid resolution so that for coarse grids, the relative size of the ignition zone becomes too small (contains too few cells) to support primary ignition.

4.3.3 Model Performance

Drawing from the present simulation results, a set of target objectives for modeling extinction and reignition in fire applications could include the following.

1. When desirable, fuel should be allowed to ignite spontaneously without the need to model complex ignition physics.

2. Combustion should be extinguished wherever extinction conditions are encountered, as determined by the chosen extinction model.

3. Following extinction events, fuel should not spuriously reignite once non extinction conditions are encountered elsewhere in the computational domain.

4. The model should ideally be free of arbitrary user input.

5. When desirable, the model should also be able to handle non-burning fuel sources, such as fuel leakages.

Here, objective (1) is necessary for reasons described in Sec. 3.2.2, where the modeling of primary ignition is generally unavailable in fire applications, which often include fuels that cannot be described with detailed reaction kinetics and complex configurations for which resolved heat transfer at the fuel source would require prohibitive computational cost. The current state-of-the-art solution to objective (1) in the classical EDC combustion treatment is to completely neglect ignition, where fuel burns spontaneously upon mixing with oxidizer. This convention then necessitates objectives (2) and (3), respectively for the provision of flame extinction and the prevention of spurious reignition, where the significance of objective (3) is readily demonstrated in the simulation results presented in Sec. 4.3.1.

Objective (4) recognizes the desire for a model that requires no arbitrary or configuration-dependent user input, while objective (5) accommodates potential specialized applications whose interests may include the modeling of fuel transport through a domain with spontaneous ignition occurring at a specified location other than the location of fuel injection. Note that objectives (4) and (5) are likely to conflict with one another, as user input is sure to be necessary to distinguish between a fuel source where spontaneous ignition is desired and a fuel leakage, where spontaneous ignition may be undesirable.

Of the presently considered cases, all incorporate EDC mixing-controlled combustion, by which objective (1) is satisfied. Each case additionally includes a sim-

ple extinction criterion based on the concept of a critical flame temperature (see Sec. 3.2.1), satisfying objective (2). As discussed in Sec. 3.2.2 (and demonstrated in Sec. 4.3.1), this combination of EDC combustion treatment with simplistic extinction modeling unfortunately leads to spurious reignition and thus the potential failure of objective (3), as demonstrated in case M1, which includes no explicit treatment to prevent spurious reignition.

While the present case M2 passes objective (3), it does so with the requirement that a prescribed ignition region be explicitly specified within the computational domain. While a prescribed ignition zone may be desirable in some applications (as recognized in objective (5), which only M2 passes), its requirement will be undesirable in many more cases where the appropriate spatial bounds of the ignition zone are not easily discernible. In general, the size and shape of the ignition zone must relate to the physical configuration of the fuel source and therefore no one-size-fits-all approach may be advised. Additional model sensitivities to the size of the ignition region and its performance dependency on grid resolution must also be considered (see Sec. 4.3.2). For these reasons, case M2 fails objective (4).

Case M3 addresses objective (3) using a configuration-independent tiered reaction mechanism (see Sec. 3.2.2), which avoids the constraint of arbitrary user input and therefore passes objective (4). Still, case M3 does require the added computational expense associated with the solution of an additional transport equation for the secondary fuel species. Additionally, though M3 adequately prevents spurious reignition in most situations, there are cases for which it fails to do so (see Fig. 4.19(c)). For this reason, M3 only qualifies objective (3).

The performance of each of the presently investigated extinction/reignition cases with respect to the stated modeling objectives is summarized in Table 4.3, where ✓, ×, and O respectively indicate a passed, failed, or qualified objective.

From Table 4.3, it is readily apparent that there is no simple and generally applicable approach to achieve accurate modeling of extinction and reignition within the limitations of the EDC combustion framework. In the present configuration, for which objective (3) has been shown to be paramount to achieve reasonable simulated suppression performance, cases M2 and M3 (which pass or qualify this objective) are shown to yield accurate results when compared to measured global combustion efficiency data (see Fig. 4.20). While the reignition treatments adopted in these cases are simplistic, they produce significant improvements in model performance with manageable added complexity and computational cost.

The present results offer incentive to open new dialogues regarding the issue of spurious reignition in EDC combustion models, which until this investigation, have received limited or no attention in the broader research community, with all existing focus paid exclusively to extinction. The present results highlight that extinction modeling, while key to model performance, can be significantly affected and potentially dominated by the chosen reignition treatment.

Table 4.3: Summary of objective performance for model cases M1, M2, and M3.

Objective	M1	M2	M3
(1)	✓	✓	✓
(2)	✓	✓	✓
(3)	×	✓	O
(4)	✓	×	✓
(5)	×	✓	×

Chapter 5: Conclusion

5.1 Summary

The present work features a fundamental investigation of fire suppression phenomena, wherein a buoyant, turbulent, methane (CH_4) or propane (C_3H_8) diffusion flame is suppressed via either nitrogen dilution of the oxidizer or application of a fine water mist. The carefully designed laboratory-scale facility comprises a slot burner centrally located within a co-flowing oxidizer. The oxidizer provides controlled delivery of either suppressant to achieve a range of conditions from unsuppressed combustion through total flame extinguishment. An optional O_2-anchor establishes a strengthened flame base that resists liftoff extinction, permitting the study of weakened turbulent flames applicable to realistic fire suppression scenarios.

A variety of non-intrusive, integral diagnostics are used to develop detailed analyses examining flame-suppressant interactions and the underlying suppression processes. Primary measurements include oxidizer composition analysis to monitor suppression potential, flame imaging to observe suppression response and quantify visible flame structure, flame emissions measurements (luminous and radiative) to assess sooting propensity and heat losses, and species-based calorimetry to evaluate global heat release rate and combustion efficiency.

Measured results reveal a variety of interesting suppression behaviors including transition in flame color from bright yellow to dim blue (due to diminishing soot incandescence), expansion in flame height (due to diluted oxidizer entrainment), structural intermittency (due to localized quenching effects), and reduction in radiative heat emissions (due to to lowering flame temperature). Despite these effects, metrics of global suppression performance indicate the persistence of stoichiometric combustion and total consumption of available fuel, with an abrupt transition to complete extinguishment occurring only at the extinction limit.

Experimental measurements are compared with the results of large eddy simulations performed using the Fire Dynamics Simulator (FDS), an open-source computational fluid dynamics (CFD) software tool. These comparisons provide a basis for evaluating the performance of available extinction and reignition models with respect to their ability to accurately predict fire suppression. The present simulations utilize the concept of a critical flame temperature to individually treat flame extinction and reignition processes. These treatments are uniquely applied within three modeling cases, each addressing flame reignition in a different capacity.

Simulations in the present configuration highlight a key combustion modeling issue in the occurrence of spurious reignition, which may follow localized extinction and can significantly degrade model performance. Applied to the present simulations, models including provisions to prevent spurious reignition are found to produce excellent agreement with measured trends in the global combustion efficiency. By comparison, models that do not address spurious reignition fail to produce reasonable suppression performance.

5.2 Highlights

Primary findings derived from the present measurements and simulations are summarized in the following. Detailed discussions regarding the interpretation and significance of these findings may be found in associated sections of the dissertation.

Nitrogen Suppression Observations

- As $X_{O_2}^{ox}$ is reduced for either CH_4 or C_3H_8 fuel, soot radiation diminishes, visualized through a significant reduction in flame luminosity and a transition in flame color from yellow to blue.

- The CH_4 flame exhibits a prolonged period of stable, soot-free (blue) combustion prior to extinction, whereas the C_3H_8 flame experiences suppression of soot production simultaneously with global extinction.

- Non-anchored flames are extinguished via flame-base detachment and liftoff ($LOI = 0.152$ for CH_4, $LOI = 0.139$ for C_3H_8), while anchored flames are extinguished via progressive localized quenching throughout the main combustion region ($LOI = 0.122$ for CH_4 and C_3H_8).

Water Mist Suppression Observations

- Water-mist suppression potential is primarily determined by Y_m^{ox} and not by the total delivery rate of water to the flame.

- As Y_m^{ox} is increased for CH_4 fuel, flame luminosity decreases significantly, but without a transition in flame color from yellow to blue.

- Localized flame quenching is observed for $Y_m^{ox} \approx 0.15$, a limit in agreement with previously reported results [8, 53].

Turbulent Flame Extinction

- Non-anchored LOI in the present facility are found to closely resemble previously reported results in the laminar cup-burner configuration; these laminar liftoff limits are established to be highly configuration-dependent measurements and are not expected to represent realistic turbulent flame extinction.

- Anchored LOI in the present facility, representing piloted extinction, are suspected to offer a more appropriate measure of the turbulent extinction limit.

- Global extinguishment in large-scale turbulent fires is suspected to result from any of three potential occurrences: (1) a progressive growth of multiple localized quenching events throughout the main combustion region, (2) a single localized quenching event that globally destabilizes the flame, or (3) a sudden global quenching event that extinguishes the entire flame simultaneously.

Flame Height

- Mean visible flame height is found to increase with reducing $X_{O_2}^{ox}$, in agreement with classical scaling predictions, and previously reported observations [13,28].

Flame Emissions

- Flame luminosity decreases significantly with declining $X_{O_2}^{ox}$, by at least six orders of magnitude for both CH_4 and C_3H_8; sharp bends in the logarithmic luminosity trend coincide with transitions in flame sooting behavior between regimes identified by changes in flame color: yellow, yellow-blue, and blue.

- Radiative loss fraction (χ_{rad}) is found to decrease linearly with declining $X_{O_2}^{ox}$ for both CH_4 and C_3H_8, where the value of χ_{rad} at ambient conditions and the ensuing slope of linear decline is dependent on fuel sooting propensity.

- For the CH_4 flame, radiative and luminous flame emissions are uncoupled, suggesting that the radiative emissions are dominated by the spectral emissions of heated gas-phase combustion products, while soot incandescence is dominant only in the visible spectrum.

Calorimetry

- The omission of applicable mass exchanges in the derivation of a calorimetry formulation may significantly affect the accuracy of the formulation; however, careful consideration of the mass balances in a given configuration may provide a useful means to determine a priori whether omission of measurements may be acceptable or whether oxygen-consumption or carbon-dioxide-generation based formulations should be preferred.

- Global combustion efficiency (η_{comb}) is found to remain constant near unity with declining $X_{O_2}^{ox}$ for both CH_4 and C_3H_8, decreasing abruptly only upon global flame extinction; until the extinction limit is reached, nearly all fuel continues to react and primary combustion species (O_2, CO_2, H_2O) are consumed/produced in stoichiometric proportions.

- With declining $X_{O_2}^{ox}$, net yields of CO remain close to zero for both CH_4 and C_3H_8, but increase slightly near the extinction limit; there is no significant presence of incomplete combustion in the presently studied flames.

- The convective heat release fraction (χ_{conv}) is found to increase linearly with declining $X_{O_2}^{ox}$ for both CH_4 and C_3H_8 due to increasing combustion exhaust temperature, in agreement with the measured trends in η_{comb} and χ_{rad}.

- Measured η_{comb}, which are derived via species-based calorimetry, are found to closely match the measured sum $\chi_{sum} = \chi_{conv} + \chi_{rad}$, which are derived via thermal measurements (respectively exhaust temperature and flame emissive heat flux); this agreement provides a validation of the calorimetry principles used to evaluate η_{comb}, which include no actual thermal measurements.

- For applications where species-based calorimetry measurements may be prohibitively difficult or costly, carefully measured χ_{rad}, requiring only a heat flux gauge and resolved flame images, and χ_{conv}, requiring only a thermocouple and collection/measurement of combustion exhaust, may provide an attractive and inexpensive alternative for measurement of the global heat release rate.

Extinction/Reignition Modeling

- Numerical results highlight the importance of reignition, where models that prevent spurious reignition yield results that match experimental data, while those that permit spurious reignition fail to predict flame extinction.

- Extinction modeling, while key to suppression performance, can be significantly affected and potentially dominated by reignition behavior.

- No simple and generally applicable approach is available to accurately model extinction and reignition within the limitations of a mixing-controlled combustion framework; the requirement for arbitrary user input to treat ignition and reignition is inevitable for certain applications using these types of models.

5.3 Contributions

A major contribution of the present work is the development of the turbulent line burner (TLB) measurement facility. The TLB facility represents a canonical laboratory-scale configuration that has been carefully designed to produce controlled flames with the complex features necessary for relation to realistic fire applications. The facility also provides well-characterized and controlled inlet and boundary conditions that are easily represented within CFD fire simulations. With its current suppression capabilities, the TLB configuration facilitates isolation of flame-suppressant interactions and provides for a variety of detailed and non-intrusive diagnostics to observe and quantify suppression performance. Beyond its use in the present work,

the TLB facility is well poised for an expanding role in a variety of future investigations, supporting potential innovations in fire suppression technologies.

Demonstrated through a variety of experimental diagnostics, the present work also contributes a number of advanced analytical methods for measurement analysis:

- A robust image-processing technique has been developed for consistent measurement of mean visible flame height (L_f), avoiding the subjective complications associated with manual flame observations. Supplementing this development, a complimentary L_f scaling analysis has been extended to consider non-standard ambient conditions, adaptable to a variety of fire configurations in alternative environments (see Sec. 2.3.1).

- For evaluation of radiative flame emissions, a novel weighted, two-dimensional multipoint radiation source model has been developed, providing meaningful improvement over the traditional single-point source model when source geometry effects are important. Derived from the model, a simple procedure has also been established to evaluate whether measurement conditions are appropriate for use of the less complex single-point model (see Sec. 2.3.3).

- A generalized framework for species-based calorimetry analysis has been formalized. Unlike the overly simplified treatments in existing formulations, this framework is directly relatable to the physical principles from which it is derived, offering transparency to its formulation and underlying assumptions. This model may also be more easily adapted to complex applications opposing the simplifying assumptions in traditional formulations (see Appendix A).

With its well-characterized configuration, detailed measurements within the TLB facility are particularly useful as validation data to supporting the development of advanced fire suppression models. All measurements reported in the present work represent an additional contribution to the fire modeling community, where the present data are made available in an open-source repository provided for the inaugural meeting of the IAFSS Working Group on Measurement and Computation of Fire Phenomena (the MaCFP Working Group) [164, 165]. The availability of these measurements represents a meaningful expansion in the library of validation data applicable to CFD fire suppression models, where the quantity and quality of existing data are notably limited.

The reignition treatments developed and analyzed in this work represent further contributions for the notable performance improvements they afford when applied in a configuration subjected to spurious reignition. As spurious reignition is likely to be a modeling issue in most realistic fire configurations, these reignition models are particularly useful for their potential applicability to such scenarios.

5.4 Future Work

Following the contributions and progress of the present study, select recommendations for future work are summarized in the following.

- The continued analysis of water-mist suppression measurements within the TLB facility would provide potential insight for water-mist suppression behavior, as well as useful validation data for comparison with CFD fire models.

- Detailed local measurements of flame temperature or flow velocity would provide additional useful data both for the evaluation of flame suppression response and for the validation of CFD fire models.

- A detailed investigation of the anchored extinction condition, including extensions to additional configurations, would provide clarity regarding its relevance to the extinction of realistic turbulent fires.

- The presently advocated treatments for modeling extinction and reignition could be further evaluated via comparisons with: the existing N_2 suppression measurements for C_3H_8 fuel in the present configuration, future water-mist suppression measurements in the present configuration, or other suppression cases in alternative configurations.

- The present simulations could be reevaluated with fully modeled flame emission, replacing the prescribed χ_{rad} approach adopted in the present work.

- The TLB facility could be enhanced to accommodate alternative suppressants, including inert agents, water-mist additives, or some combination thereof.

- The TLB facility could be enhanced to accommodate alternative fuel sources, particularly liquid or gaseous fuels incorporating the additional physics of heat-feedback driven fuel pyrolysis; such an enhancement would provide for potentially interesting suppression observations, as well as enhanced relatability of the measurements to realistic fire conditions.

Appendix A: General Framework for Species-Based Calorimetry

A.1 Overview

The foundation for species-based calorimetry is the thermodynamic concept that the heat released by a chemical reaction is directly related to the rates of consumption and production of the major chemical species involved. In any species-based calorimetry application, it is necessary to first determine the applicable combustion chemistry. The major species present in the assumed reaction determine which species must be considered in the enthalpy balance for the reaction (Sec. A.2), tracked in the mass-conservation analysis that follows (Sec. A.3), and that must eventually be measured in the calorimetry system (Sec. A.4).

The principal tenants of the present calorimetry framework follow.

1. Determine the appropriate global combustion chemistry, as in Eq. A.1.

2. Develop a formulation for the reaction enthalpy balance; for standard applications, the established expressions in Eqs. A.27 and A.31 or a novel formulation in Eq. A.36 may be used; for special applications including complex reactions or exotic combustion species, Eq. A.6 may be used, or an alternative case-specific formulation may be derived via the methods discussed in Sec. A.2.

3. Determine appropriate values for the parameters in the chosen enthalpy formulation; for applications with known fuel chemistry, these may be evaluated via Eqs. A.2 and A.15; or for applications with unknown fuel chemistry, standard reference values may be used, subject to accuracy limitations (see Table A.2).

4. Develop a control-volume-based mass-conservation analysis applicable to the measurement configuration that considers all relevant mass exchanges and from this analysis, derive Eqs. A.38 and A.40.

5. With considerations for Eqs. A.38–A.49, determine and implement the appropriate configuration of instrumentation necessary to close this system of expressions, including any necessary modifications for specific applications.

6. Using available measurements and following the solution framework presented at the end of Sec. A.4, solve the system of Eqs. A.38–A.49 to evaluate the desired combustion heat release rate.

General assumptions utilized in the present analysis that are necessary for any species-based calorimetry application include the following.

1. The assumed global combustion chemistry comprises all major species actually present in *considerable* quantities before and after the reaction; 'before' referring to an initially non-reacting fuel-oxidizer mixture, and 'after' referring to the mixed products of combustion far downstream from the combustion region.

2. The system in which the reaction occurs remains at constant pressure and any work done by the system on its surroundings is limited to expansion work.

3. The assumed control volume completely characterizes *all* unique compositions of mass exchanged across its boundaries.

4. The reaction occurs entirely within the assumed control volume.

Optional simplifying assumptions applied in the present analysis also include the following. Omission of these assumptions may be possible, but could considerably complicate the analytical and/or measurement requirements. Further simplifications are available, but would require additional assumptions.

5. Nitrogen in the ambient is conserved and unaffected by the reaction.

6. Any soot produced by combustion consists of pure graphitic carbon.

7. All flow streams crossing the boundaries of the control volume are quasi-steady, and therefore any net accumulation or reduction of total mass within the control volume is neglected.

8. No mass is lost from the system (except that exiting through the monitored exhaust pathway).

9. All flow streams are well-mixed at the locations in which they are measured.

10. For flow measurement via differential pressure methods (Eq. A.49), compressibility effects are neglected and ideal gas behavior is assumed, also neglecting the mass contributions of any condensed-phase species or particulates to the mixed-stream density.

A.2 Combustion Treatment

A.2.1 General Formulation

Considering the combustion of a simple organic fuel in air, a global single-step reaction perspective gives

$$C_x H_y O_z + \nu_{O_2} O_2 + \nu_{N_2} N_2 \rightarrow \nu_{H_2O} H_2O + \nu_{CO_2} CO_2 + \nu_{CO} CO + \nu_{C_{(s)}} C_{(s)} + \nu_{UHC} UHC + \nu_{N_2} N_2, \quad \text{(A.1)}$$

where ν_k are the molar reaction coefficients for each species, k, involved in the reaction. In this mechanism, an arbitrary fuel compound ($C_x H_y O_z$) and oxygen (O_2) are consumed to produce water-vapor (H_2O) and carbon-dioxide (CO_2), while carbon-monoxide (CO), soot ($C_{(s)}$), and unburned hydrocarbons (UHC) are included as potential products of incomplete combustion. Nitrogen (N_2) and any other inert species that may be present are assumed to be globally unaffected by the reaction.

Detailed reaction kinetics are safely neglected in Eq. A.1 via Hess's law, where the total enthalpy change over the course of a chemical reaction, ΔH, is independent of the reaction pathway and given by

$$\Delta H = \sum_{k,\, products} \left(\nu_k \, \Delta \bar{h}^\circ_{f,k}\right) - \sum_{k,\, reactants} \left(\nu_k \, \Delta \bar{h}^\circ_{f,k}\right), \quad \text{(A.2)}$$

where $\Delta \bar{h}^\circ_{f,k}$ are the mole-specific standard enthalpies of formation for each species, k, involved in the reaction. Via Eq. A.2, the global reaction perspective is appropriate, so long as the primary species included in the assumed reaction mechanism (Eq. A.1) indeed represent the major species actually present in *considerable* quan-

tities at the initial and final states of the reaction. Here, the initial state refers to an initially non-reacting fuel-oxidizer mixture and the final state refers to the mixed products of combustion far downstream from the reaction zone. Any species present in insignificant quantities may be safely neglected.

The mechanism in Eq. A.1 adequately applies to most fire applications. For special applications in which complex fuel chemistry, involvement of other reactive compounds, or any other factor leads to the net consumption or production of additional species in *considerable* quantities, those additional species should be accounted for in the assumed mechanism and included in the analysis that follows.

For the mechanism assumed in Eq. A.1, Eq. A.2 becomes

$$\Delta H = \nu_{H_2O}\,\Delta\bar{h}^\circ_{f,H_2O} + \nu_{CO_2}\,\Delta\bar{h}^\circ_{f,CO_2} + \nu_{CO}\,\Delta\bar{h}^\circ_{f,CO} + \nu_{UHC}\,\Delta\bar{h}^\circ_{f,UHC} - \Delta\bar{h}^\circ_{f,fuel}, \quad \text{(A.3)}$$

where $\Delta\bar{h}^\circ_{f,fuel}$ is the mole-specific standard enthalpy of formation for the fuel species ($C_xH_yO_z$) and terms for O_2, N_2, and $C_{(s)}$ are dropped because $\Delta\bar{h}^\circ_{f,k} = 0$ for these species. Reference $\Delta\bar{h}^\circ_f$ for typical combustion species are presented in Table A.1.

Table A.1: Reference $\Delta\bar{h}^\circ_f$ for standard combustion species.

Species, k	$\Delta\bar{h}^\circ_{f,k}$ (kJ/mol)
CH_4	-74.87
C_3H_8	-104.70
O_2	0
N_2	0
H_2O	-241.83
CO_2	-393.51
CO	-110.53
$C_{(s)}$	0

Direct solution of Eq. A.3 requires knowledge of $\Delta\bar{h}_f^\circ$ for each species involved in the reaction. These values are known for most combustion species (see Table A.1), but may be unknown for the fuel ($C_xH_yO_z$) and are ill-defined for unburned hydrocarbons (UHC).

The appropriate treatment for $\Delta\bar{h}_{f,UHC}^\circ$ depends on available measurement methods. If UHC are suspected to be negligible or if measurement is unavailable, this term should be neglected. If UHC species are individually measured, such as via infrared detectors, this term should be split into individual terms for each measured hydrocarbon species, where $\Delta\bar{h}_f^\circ$ for each may be determined from reference values (as in Table A.1). If UHC are measured in total, such as via flame ionization detector, measured UHC should be treated with a representative hydrocarbon species, typically CH_4 or C_3H_8. Care must be taken in selecting this representative species because $\Delta\bar{h}_f^\circ$ for hydrocarbons do not scale directly with number of C atoms (as does the measured signal from a flame ionization detector). As a result, if UHC are represented by a low (high) carbon-count hydrocarbon relative to what is actually being measured, $\Delta\bar{h}_{f,UHC}^\circ$ will be over (under)-estimated.

Solution of Eq. A.3 additionally requires knowledge of all ν_k in the stoichiometrically balanced combustion reaction. While an idealized combustion reaction may be easily balanced, reactions involving products of incomplete combustion cannot be balanced unless yields for CO, $C_{(s)}$, and UHC are known. As a result, all ν_k cannot be generally determined a priori.

To circumvent this issue, each ν_k may be evaluated from experimentally measured species reaction rates following the concepts developed in previous work [111],

and defined by

$$\nu_k = \frac{\dot{m}_k^{rxn}\, M_{fuel}}{\dot{m}_{fuel}\, M_k}, \tag{A.4}$$

where $\dot{m}_{fuel}$ is the mass flow rate of fuel, $\dot{m}_k^{rxn}$ is the mass reaction rate of species k, and M_{fuel} and M_k are respectively the molar masses of the fuel and species k. Using Eq. A.4, each ν_k may be dynamically evaluated from the measured time-history for each $\dot{m}_k^{rxn}$ (see Sec. A.3 for determination of $\dot{m}_k^{rxn}$), provided the fuel composition is known and the mass flow rate of fuel is measured.

Once all ν_k and $\Delta\bar{h}^\circ_{f,k}$ are known, ΔH may be evaluated via Eq. A.3, and the reaction heat release rate, $\dot{Q}$, may be defined as

$$\dot{Q} = \Delta H\, \frac{\dot{m}_k^{rxn}}{\nu_k\, M_k}, \tag{A.5}$$

where by the first law of thermodynamics, $\Delta H = \Delta Q$, provided the system in which the reaction occurs remains at constant pressure and any work done by the system on its surroundings is limited to expansion work.

Combination of Eqs. A.3–A.5 then gives

$$\dot{Q} = \dot{m}_{H_2O}^{rxn}\, \frac{\Delta\bar{h}^\circ_{f,H_2O}}{M_{H_2O}} + \dot{m}_{CO_2}^{rxn}\, \frac{\Delta\bar{h}^\circ_{f,CO_2}}{M_{CO_2}} + \dot{m}_{CO}^{rxn}\, \frac{\Delta\bar{h}^\circ_{f,CO}}{M_{CO}} + \dot{m}_{UHC}^{rxn}\, \frac{\Delta\bar{h}^\circ_{f,UHC}}{M_{UHC}} - \dot{m}_{fuel}\, \frac{\Delta\bar{h}^\circ_{f,fuel}}{M_{fuel}}. \tag{A.6}$$

Equation A.6 provides for the direct determination of $\dot{Q}$ from experimentally measured $\dot{m}_k^{rxn}$. This formulation is advantageous in that it requires no presumption of the reaction stoichiometry and may be easily extended to include additional combustion species. It may be best applied in applications involving complex combustion mechanisms where additional or exotic reactant and product species are

present. For such applications, Eqs. A.1, A.3, and A.6 may be directly extended to include those additional species, provided each additional $\Delta\bar{h}^{\circ}_{f,k}$ may be determined, and each additional $\dot{m}^{rxn}_{k}$ may be measured.

Despite this advantage, Eq. A.6 may be applied only in applications where $\dot{m}_{fuel}$ is measured and the fuel composition is known ($\Delta\bar{h}^{\circ}_{f,fuel}$ and M_{fuel} must be known). Furthermore, Eq. A.6 is highly sensitive to the mass reaction rates of all major combustion products, including $\dot{m}^{rxn}_{H_2O}$, which is not easily or accurately measured in most calorimetry systems. As these limitations are prohibitive for most fire applications, alternative more generally-applicable enthalpy formulations are desirable.

Toward this goal, let Eq. A.1 be simplified to give the following baseline combustion reaction,

$$C_xH_yO_z + \nu_{O_2}\,O_2 \rightarrow \nu_{H_2O}\,H_2O + \nu_{CO_2}\,CO_2 + \nu_{CO}\,CO + \nu_{C_{(s)}}\,C_{(s)}, \qquad (R_0)$$

where terms involving N_2 are dropped for brevity (N_2 is assumed inert and does not participate in the reaction) and UHC are neglected to simplify the analysis that follows.

Reaction R_0 may then be divided into the following three sub-reactions,

$$C_xH_yO_z + \nu^{R_1}_{O_2}\,O_2 \rightarrow \nu^{R_1}_{H_2O}\,H_2O + \nu^{R_1}_{CO_2}\,CO_2, \qquad (R_1)$$

$$C_xH_yO_z + \nu^{R_2}_{O_2}\,O_2 \rightarrow \nu^{R_2}_{H_2O}\,H_2O + \nu^{R_2}_{CO}\,CO, \qquad (R_2)$$

$$C_xH_yO_z + \nu^{R_3}_{O_2}\,O_2 \rightarrow \nu^{R_3}_{H_2O}\,H_2O + \nu^{R_3}_{C_{(s)}}\,C_{(s)}, \qquad (R_3)$$

which may be directly stoichiometrically balanced to give

$$C_xH_yO_z + \left(x + \frac{y}{4} - \frac{z}{2}\right) O_2 \rightarrow \frac{y}{2} H_2O + x\, CO_2, \tag{R_1b}$$

$$C_xH_yO_z + \left(\frac{x}{2} + \frac{y}{4} - \frac{z}{2}\right) O_2 \rightarrow \frac{y}{2} H_2O + x\, CO, \tag{R_2b}$$

$$C_xH_yO_z + \left(\frac{y}{4} - \frac{z}{2}\right) O_2 \rightarrow \frac{y}{2} H_2O + x\, C_{(s)}, \tag{R_3b}$$

where x, y, and z are respectively the number of carbon, hydrogen, and oxygen atoms in the applicable fuel species.

Here, sub-reactions R_1, R_2, and R_3 are specifically defined so that their sum yields the original combustion mechanism given in reaction R_0. That is, let each sub-reaction, R_n, be multiplied by a weighting factor, F_n, defined as

$$F_n = \frac{\dot{m}_k^{R_n}\, \nu_k}{\dot{m}_k^{rxn}\, \nu_k^{R_n}}, \tag{A.7}$$

and satisfying

$$\sum_n F_n = 1, \tag{A.8}$$

so that

$$\dot{m}_k^{rxn} = \sum_n \dot{m}_k^{R_n}, \tag{A.9}$$

$$\nu_k = \sum_n \left(F_n\, \nu_k^{R_n}\right), \tag{A.10}$$

and via Hess's law,

$$\Delta H = \sum_n \left(F_n\, \Delta H_{R_n}\right), \tag{A.11}$$

where $\dot{m}_k^{R_n}$ and $\nu_k^{R_n}$ are respectively the mass reaction rate and molar reaction coefficient of species k in sub-reaction R_n, and ΔH_{R_n} is the enthalpy of reaction of sub-reaction R_n.

Combining Eqs. A.7 and A.11 into Eq. A.5 and simplifying the resulting expression then gives

$$\dot{Q} = \sum_{n} \left(\Delta H_{R_n} \frac{\dot{m}_k^{R_n}}{\nu_k^{R_n} M_k} \right). \tag{A.12}$$

The value of Eq. A.12 is realized in that the heat release rate for an arbitrarily complex combustion mechanism may be determined via the sum of a series of simpler sub-reactions. As long as these sub-reactions are balanceable, each $\nu_k^{R_n}$ may be directly determined and each ΔH_{R_n} may be evaluated by applying Eq. A.2 to each sub-reaction.

In addition, the following identity may be defined,

$$\frac{\dot{m}_{k_1}^{R_n}}{\nu_{k_1}^{R_n} M_{k_1}} = \frac{\dot{m}_{k_2}^{R_n}}{\nu_{k_2}^{R_n} M_{k_2}}, \tag{A.13}$$

where k_1 and k_2 are any two species participating in any stoichiometrically balanced reaction, R_n. Combining Eq. A.13 into Eq. A.12 then gives

$$\dot{Q} = \sum_{n} \left(\Delta H_{R_n} \frac{\dot{m}_{k_n}^{R_n}}{\nu_{k_n}^{R_n} M_{k_n}} \right), \tag{A.14}$$

where k_n is any species participating in reaction R_n. Each summation term in Eq. A.14 may therefore be individually applied to any species appearing in each sub-reaction. That is, the terms in Eq. A.14 need not be limited to include only the same species across all sub-reactions.

By defining a mass-specific enthalpy of reaction, given by

$$\Delta h_{k_n}^{R_n} = \frac{\Delta H_{R_n}}{\nu_{k_n}^{R_n} M_{k_n}}, \tag{A.15}$$

Eq. A.14 may also be re-expressed as

$$\dot{Q} = \sum_{n} \left(\dot{m}_{k_n}^{R_n} \Delta h_{k_n}^{R_n} \right). \tag{A.16}$$

Equation A.16 shares all the noted benefits of Eqs. A.12 and A.14, but has been presented in simpler form. The primary limitation of Eq. A.16 is realized in that each $\dot{m}_{k_n}^{R_n}$ is generally unknown and must therefore be related to some measured $\dot{m}_k^{rxn}$ using Eqs. A.9 and A.13. Depending on the complexity of the combustion mechanism and the resulting number of sub-reactions, R_n, extensive algebraic manipulations may be required to derive a usable form of Eq. A.16. It is for this reason that the previous formulation leading to Eq. A.6 may be preferred for applications involving complex reactions. Fortunately, the preceding system of sub-reactions R_1–R_3 is relatively simple and general enthalpy formulations for combustion mechanisms resembling reaction R_0 may be derived, as summarized in the following sections.

A.2.2 Oxygen-Consumption (OC) Formulation

Applying Eq. A.16 to sub-reactions R_1–R_3, and selecting the O_2 term in each gives a preliminary formulation for an oxygen-consumption (OC) based determination of the combustion heat release rate,

$$\dot{Q}_{OC} = \dot{m}_{O_2}^{R_1} \Delta h_{O_2}^{R_1} + \dot{m}_{O_2}^{R_2} \Delta h_{O_2}^{R_2} + \dot{m}_{O_2}^{R_3} \Delta h_{O_2}^{R_3}. \tag{A.17}$$

Applying Eq. A.9 to the first term in Eq. A.17 yields

$$\dot{Q}_{OC} = \dot{m}_{O_2}^{rxn} \Delta h_{O_2}^{R_1} + \dot{m}_{O_2}^{R_2} \left(\Delta h_{O_2}^{R_2} - \Delta h_{O_2}^{R_1} \right) + \dot{m}_{O_2}^{R_3} \left(\Delta h_{O_2}^{R_3} - \Delta h_{O_2}^{R_1} \right), \tag{A.18}$$

while applying Eq. A.13 to the second and third terms in Eq. A.18 then allows the substitution of $\dot{m}_{O_2}^{R_2}$ for $\dot{m}_{CO}^{R_2}$ and $\dot{m}_{O_2}^{R_3}$ for $\dot{m}_{C_{(s)}}^{R_3}$ respectively.

The advantage of this substitution is realized in that via Eq. A.9, $\dot{m}_{CO}^{R_2} = \dot{m}_{CO}^{rxn}$ and $\dot{m}_{C_{(s)}}^{R_3} = \dot{m}_{C_{(s)}}^{rxn}$ (CO only appears in sub-reaction R_2 and $C_{(s)}$ only appears in

sub-reaction R_3). Performing these operations gives

$$\dot{Q}_{OC} = \dot{m}^{rxn}_{O_2}\,\Delta h^{R_1}_{O_2} + \dot{m}^{rxn}_{CO}\,\left(\Delta h^{R_2}_{O_2} - \Delta h^{R_1}_{O_2}\right)\,\frac{\nu^{R_2}_{O_2}\,M_{O_2}}{\nu^{R_2}_{CO}\,M_{CO}} + \dot{m}^{rxn}_{C_{(s)}}\,\left(\Delta h^{R_3}_{O_2} - \Delta h^{R_1}_{O_2}\right)\,\frac{\nu^{R_3}_{O_2}\,M_{O_2}}{\nu^{R_3}_{C_{(s)}}\,M_{C_{(s)}}}. \quad \text{(A.19)}$$

It is at this point useful to introduce two supplemental sub-reactions,

$$CO + \frac{1}{2}\,O_2 \rightarrow CO_2, \quad (R_4)$$

$$C_{(s)} + O_2 \rightarrow CO_2, \quad (R_5)$$

defined such that

$$R_1 = R_2 + \nu^{R_1}_{CO_2}\,R_4, \quad \text{(A.20)}$$

$$R_1 = R_3 + \nu^{R_1}_{CO_2}\,R_5, \quad \text{(A.21)}$$

and therefore, via Hess's law,

$$\Delta H_{R_1} = \Delta H_{R_2} + \nu^{R_1}_{CO_2}\,\Delta H_{R_4}, \quad \text{(A.22)}$$

$$\Delta H_{R_1} = \Delta H_{R_3} + \nu^{R_1}_{CO_2}\,\Delta H_{R_5}, \quad \text{(A.23)}$$

and via Eq. A.15

$$\Delta h^{R_1}_{k_1}\,\nu^{R_1}_{k_1}\,M_{k_1} = \Delta h^{R_2}_{k_2}\,\nu^{R_2}_{k_2}\,M_{k_2} + \Delta h^{R_4}_{k_4}\,\nu^{R_1}_{CO_2}\,\nu^{R_4}_{k_4}\,M_{k_4}, \quad \text{(A.24)}$$

$$\Delta h^{R_1}_{k_1}\,\nu^{R_1}_{k_1}\,M_{k_1} = \Delta h^{R_3}_{k_3}\,\nu^{R_3}_{k_3}\,M_{k_3} + \Delta h^{R_5}_{k_5}\,\nu^{R_1}_{CO_2}\,\nu^{R_5}_{k_5}\,M_{k_5}. \quad \text{(A.25)}$$

Applying Eqs. A.24 and A.25 to the second and third terms in Eq. A.19 re-

spectively yields

$$\dot{Q}_{OC} = \dot{m}_{O_2}^{rxn}\,\Delta h_{O_2}^{R_1} + \dot{m}_{CO}^{rxn}\left(\Delta h_{O_2}^{R_1}\,\left(\nu_{O_2}^{R_1} - \nu_{O_2}^{R_2}\right) - \Delta h_{O_2}^{R_4}\,\nu_{CO_2}^{R_1}\,\nu_{O_2}^{R_4}\right)\frac{M_{O_2}}{\nu_{CO}^{R_2}\,M_{CO}} + \dot{m}_{C_{(s)}}^{rxn}\left(\Delta h_{O_2}^{R_1}\,\left(\nu_{O_2}^{R_1} - \nu_{O_2}^{R_3}\right) - \Delta h_{O_2}^{R_5}\,\nu_{CO_2}^{R_1}\,\nu_{O_2}^{R_5}\right)\frac{M_{O_2}}{\nu_{C_{(s)}}^{R_3}\,M_{C_{(s)}}}. \quad \text{(A.26)}$$

Inserting values for all $\nu_k^{R_n}$ in Eq. A.26, which are obtained from the balanced sub-reactions R_1b–R_3b as well as the supplemental sub-reactions R_4 and R_5, the end result becomes

$$\dot{Q}_{OC} = \dot{m}_{O_2}^{rxn}\,\Delta h_{O_2}^{R_1} + \dot{m}_{CO}^{rxn}\,\left(\Delta h_{O_2}^{R_1} - \Delta h_{O_2}^{R_4}\right)\frac{M_{O_2}}{2\,M_{CO}} + \dot{m}_{C_{(s)}}^{rxn}\,\left(\Delta h_{O_2}^{R_1} - \Delta h_{O_2}^{R_5}\right)\frac{M_{O_2}}{M_{C_{(s)}}}, \quad \text{(A.27)}$$

where all $\dot{m}_k^{R_n}$ have been substituted for measurable $\dot{m}_k^{rxn}$, and all resulting $\nu_k^{R_n}$ have been eliminated from the expression (so that no fuel-dependent x, y, or z terms remain in the final expression).

Equation A.27 presents the familiar formulation for OC calorimetry [105–113], where the heat release rate for any combustion reaction resembling the originally assumed mechanism (R_0) may be evaluated from measurements of $\dot{m}_{O_2}^{rxn}$, $\dot{m}_{CO}^{rxn}$, and $\dot{m}_{C_{(s)}}^{rxn}$, and using the enthalpy parameters $\Delta h_{O_2}^{R_1}$, $\Delta h_{O_2}^{R_4}$, and $\Delta h_{O_2}^{R_5}$. Each enthalpy parameter may be determined by applying Eqs. A.2 and A.15 to the appropriate balanced sub-reaction R_n. Note that $\Delta h_{O_2}^{R_4}$ and $\Delta h_{O_2}^{R_5}$ are defined via reactions R_4 and R_5, which are independent of fuel composition and may therefore be treated as configuration-independent constants.

The parameter $\Delta h_{O_2}^{R_1}$, which represents the sole configuration-dependent pa-

rameter in Eq. A.27, is defined via reaction R_1, representing the stoichiometrically complete combustion of the applicable fuel species. Though $\Delta h_{O_2}^{R_1}$ may be accurately determined only if the fuel composition is known, values for $\Delta h_{O_2}^{R_1}$ have been demonstrated in previous work to remain relatively constant amongst a wide range of fuel species (of the general form $C_x H_y O_z$) [166–169]. As a result, an average value for $\Delta h_{O_2}^{R_1}$ may be assumed (see Table A.2) and Eq. A.27 may be applied with reasonable accuracy to applications with unknown fuel composition.

A.2.3 Carbon-Dioxide-Generation (CDG) Formulation

By similar methods to those presented in Sec. A.2.2, Eq. A.16 may be applied to the system of sub-reactions R_1–R_3, now selecting the carbon-containing product species in each reaction (CO_2 in R_1, CO in R_2, and $C_{(s)}$ R_3). The result gives

$$\dot{Q}_{CDG} = \dot{m}_{CO_2}^{R_1} \Delta h_{CO_2}^{R_1} + \dot{m}_{CO}^{R_2} \Delta h_{CO}^{R_2} + \dot{m}_{C_{(s)}}^{R_3} \Delta h_{C_{(s)}}^{R_3}, \tag{A.28}$$

which provides a preliminary formulation for a carbon-dioxide-generation (CDG) based determination of the combustion heat release rate.

Applying Eq. A.9 to all three terms in Eq. A.28 and noting, as before, that $\dot{m}_{CO_2}^{R_1} = \dot{m}_{CO_2}^{rxn}$, $\dot{m}_{CO}^{R_2} = \dot{m}_{CO}^{rxn}$, and $\dot{m}_{C_{(s)}}^{R_3} = \dot{m}_{C_{(s)}}^{rxn}$ then yields

$$\dot{Q}_{CDG} = \dot{m}_{CO_2}^{rxn} \Delta h_{CO_2}^{R_1} + \dot{m}_{CO}^{rxn} \Delta h_{CO}^{R_2} + \dot{m}_{C_{(s)}}^{rxn} \Delta h_{C_{(s)}}^{R_3}. \tag{A.29}$$

Equation A.29 presents the familiar formulation for CDG based calorimetry [105–113]; however, this formulation is undesirable because it contains three configuration-dependent parameters in $\Delta h_{CO_2}^{R_1}$, $\Delta h_{CO}^{R_2}$, and $\Delta h_{C_{(s)}}^{R_3}$, all of which bear

sensitivity to the composition of the applicable fuel species. In order to alleviate this sensitivity, further manipulation of Eq. A.29 may be performed as follows.

Applying Eqs. A.24 and A.25 to the second and third terms in Eq. A.29 respectively gives

$$\begin{aligned}\dot{Q}_{CDG} = \dot{m}^{rxn}_{CO_2}\,\Delta h^{R_1}_{CO_2} \\ + \dot{m}^{rxn}_{CO}\,\left(\Delta h^{R_1}_{CO_2} - \Delta h^{R_4}_{CO_2}\,\nu^{R_4}_{CO_2}\right)\,\frac{\nu^{R_1}_{CO_2}\,M_{CO_2}}{\nu^{R_2}_{CO}\,M_{CO}} \\ + \dot{m}^{rxn}_{C_{(s)}}\,\left(\Delta h^{R_1}_{CO_2} - \Delta h^{R_5}_{CO_2}\,\nu^{R_5}_{CO_2}\right)\,\frac{\nu^{R_1}_{CO_2}\,M_{CO_2}}{\nu^{R_3}_{C_{(s)}}\,M_{C_{(s)}}},\end{aligned} \quad \text{(A.30)}$$

to which values for all $\nu_k^{R_n}$, again obtained from the balanced sub-reactions R_1b–R_3b, R_4, and R_5, may be inserted to yield

$$\begin{aligned}\dot{Q}_{CDG} = \dot{m}^{rxn}_{CO_2}\,\Delta h^{R_1}_{CO_2} + \dot{m}^{rxn}_{CO}\,\left(\Delta h^{R_1}_{CO_2} - \Delta h^{R_4}_{CO_2}\right)\,\frac{M_{CO_2}}{M_{CO}} \\ + \dot{m}^{rxn}_{C_{(s)}}\,\left(\Delta h^{R_1}_{CO_2} - \Delta h^{R_5}_{CO_2}\right)\,\frac{M_{CO_2}}{M_{C_{(s)}}}.\end{aligned} \quad \text{(A.31)}$$

Equation A.31, which is analogous to the OC formulation in Eq. A.27, is preferential over Eq. A.29 because the enthalpy parameters $\Delta h^{R_4}_{CO_2}$ and $\Delta h^{R_5}_{CO_2}$, unlike $\Delta h^{R_2}_{CO_2}$ and $\Delta h^{R_3}_{CO_2}$ (and like $\Delta h^{R_4}_{O_2}$ and $\Delta h^{R_5}_{O_2}$), are independent of fuel composition and may be treated as configuration-independent constants. With a definition analogous to that of $\Delta h^{R_1}_{O_2}$, $\Delta h^{R_1}_{CO_2}$ is then the sole configuration-dependent parameter in Eq. A.31. As with $\Delta h^{R_1}_{O_2}$, values for $\Delta h^{R_1}_{CO_2}$ have been similarly demonstrated to remain relatively constant amongst a wide variety of fuel species [169]. Equation A.31 may then also be applied with reasonable accuracy to applications with unknown fuel composition, provided an average value of $\Delta h^{R_1}_{CO_2}$ is assumed (see Table A.2).

A.2.4 Alternative Formulations

Recalling the previously stated notion that Eq. A.16 may be applied to any species appearing in each sub-reaction, the presently formulated OC and CDG expressions (respectively Eqs. A.27 and A.31) represent only two of the possible derivations of Eq. A.16. For a system of n sub-reactions containing n_k species, the number of unique calorimetry formulations that may be derived is determined via

$$N = \frac{n_k!}{n!\ (n_k - n)!}. \tag{A.32}$$

For the present system of three sub-reactions containing six species (R_1–R_3), $N = 20$. Most of these formulations are of questionable value, requiring species measurements that are not easily performed ($\dot{m}^{rxn}_{H_2O}$) or including enthalpy parameters, that unlike $\Delta h^{R_1}_{O_2}$ and $\Delta h^{R_1}_{CO_2}$, may not be reliably estimated using average values. Any formulation involving H_2O or the fuel species may then be disregarded (though for applications of interest, such formulations may still be derived following the methods exemplified in Secs. A.2.2 and A.2.3), leaving a system of three sub-reactions containing four species, for which $N = 4$.

The OC formulation (O_2, CO, and $C_{(s)}$) and the CDG formulation (CO_2, CO, and $C_{(s)}$) represent two of those four combinations. The remaining two combinations include the species O_2, CO, and $C_{(s)}$, or the species O_2, CO_2, and CO. In most calorimetry systems, O_2, CO_2, and CO are measured with relative ease and accuracy, while $C_{(s)}$ measurements are comparatively difficult and undesirable. This last combination is then of particular interest and is derived as follows.

Beginning with the preliminary OC formulation presented in Eq. A.17, and now applying Eq. A.9 to the third term (instead of the first term, as was performed previously) gives

$$\dot{Q} = \dot{m}_{O_2}^{rxn}\,\Delta h_{O_2}^{R_3} + \dot{m}_{O_2}^{R_1}\,\left(\Delta h_{O_2}^{R_1} - \Delta h_{O_2}^{R_3}\right) + \dot{m}_{O_2}^{R_2}\,\left(\Delta h_{O_2}^{R_2} - \Delta h_{O_2}^{R_3}\right). \tag{A.33}$$

Again applying Eqs. A.9 and A.13 to the second and third terms in Eq. A.33 then allows the substitution of $\dot{m}_{O_2}^{R_1}$ for $\dot{m}_{CO_2}^{rxn}$ and $\dot{m}_{O_2}^{R_2}$ for $\dot{m}_{CO}^{rxn}$ respectively. Performing these operations gives

$$\begin{aligned}\dot{Q} = \dot{m}_{O_2}^{rxn}\,\Delta h_{O_2}^{R_3} &+ \dot{m}_{CO_2}^{rxn}\,\left(\Delta h_{O_2}^{R_1} - \Delta h_{O_2}^{R_3}\right)\,\frac{\nu_{O_2}^{R_1}\,M_{O_2}}{\nu_{CO_2}^{R_1}\,M_{CO_2}} \\ &+ \dot{m}_{CO}^{rxn}\,\left(\Delta h_{O_2}^{R_2} - \Delta h_{O_2}^{R_3}\right)\,\frac{\nu_{O_2}^{R_2}\,M_{O_2}}{\nu_{CO}^{R_2}\,M_{CO}}.\end{aligned} \tag{A.34}$$

Applying Eqs. A.24 and A.25 to the second and third terms in Eq. A.34 respectively yields

$$\begin{aligned}\dot{Q} = \dot{m}_{O_2}^{rxn}\,\Delta h_{O_2}^{R_3} &+ \dot{m}_{CO_2}^{rxn}\,\left(\Delta h_{O_2}^{R_3}\left(\frac{\nu_{O_2}^{R_3} - \nu_{O_2}^{R_1}}{\nu_{CO_2}^{R_1}}\right) + \Delta h_{O_2}^{R_5}\,\nu_{O_2}^{R_5}\right)\,\frac{M_{O_2}}{M_{CO_2}} \\ &+ \dot{m}_{CO}^{rxn}\,\left(\Delta h_{O_2}^{R_3}\left(\frac{\nu_{O_2}^{R_3} - \nu_{O_2}^{R_2}}{\nu_{CO_2}^{R_1}}\right) - \Delta h_{O_2}^{R_4}\,\nu_{O_2}^{R_4} + \Delta h_{O_2}^{R_5}\,\nu_{O_2}^{R_5}\right)\,\frac{\nu_{CO_2}^{R_1}\,M_{O_2}}{\nu_{CO}^{R_2}\,M_{CO}}.\end{aligned} \tag{A.35}$$

Inserting values for all $\nu_k^{R_n}$, again obtained from the balanced sub-reactions R_1b–R_3b, R_4, and R_5, Eq. A.35 becomes

$$\begin{aligned}\dot{Q} = \dot{m}_{O_2}^{rxn}\,\Delta h_{O_2}^{R_3} &+ \dot{m}_{CO_2}^{rxn}\,\left(\Delta h_{O_2}^{R_5} - \Delta h_{O_2}^{R_3}\right)\,\frac{M_{O_2}}{M_{CO_2}} \\ &+ \dot{m}_{CO}^{rxn}\,\left(2\,\Delta h_{O_2}^{R_5} - \Delta h_{O_2}^{R_4} - \Delta h_{O_2}^{R_3}\right)\,\frac{M_{O_2}}{2M_{CO}}.\end{aligned} \tag{A.36}$$

As with the preceding OC and CDG formulations, Eq. A.36 evaluates the combustion heat release rate via measured mass reaction rates ($\dot{m}_{O_2}^{rxn}$, $\dot{m}_{CO_2}^{rxn}$, and $\dot{m}_{CO}^{rxn}$) and reference enthalpy parameters ($\Delta h_{O_2}^{R_3}$, $\Delta h_{O_2}^{R_4}$, and $\Delta h_{O_2}^{R_5}$). As in the OC formulation, $\Delta h_{O_2}^{R_4}$ and $\Delta h_{O_2}^{R_5}$ may be treated as configuration-independent constants. Unlike the OC formulation, which contains the configuration-dependent parameter $\Delta h_{O_2}^{R_1}$, Eq. A.36 contains the configuration-dependent parameter $\Delta h_{O_2}^{R_3}$, representing the stoichiometric combustion of the applicable fuel species to H_2O and $C_{(s)}$ (instead of H_2O and CO_2).

From Eq. A.25, $\Delta h_{O_2}^{R_3}$ may be related to the more well-known $\Delta h_{O_2}^{R_1}$ via

$$\Delta h_{O_2}^{R_3} = \Delta h_{O_2}^{R_1} + \frac{2x}{\frac{y}{2} - z} \left(\Delta h_{O_2}^{R_1} - \Delta h_{O_2}^{R_5} \right), \tag{A.37}$$

where x, y, and z are the numbers of carbon, hydrogen, and oxygen atoms in the applicable fuel species. Using Eq. A.37, an average value for $\Delta h_{O_2}^{R_3}$ may be estimated from an existing tabulation of $\Delta h_{O_2}^{R_1}$ data. A collection of average values and corresponding standard deviations for $\Delta h_{O_2}^{R_1}$, $\Delta h_{CO_2}^{R_1}$, and $\Delta h_{O_2}^{R_3}$, determined from existing data spanning a collection of roughly 150 basic hydrocarbon compounds [169], is presented in Table A.2. Note that for certain compounds such as formaldehyde (CH_2O), for which $z = y/2$, sub-reaction R_3b contains no requirement for O_2, and $\Delta h_{O_2}^{R_3}$ is undefined. Such compounds are omitted from the reported averages.

As shown in Table A.2, the standard deviation in $\Delta h_{O_2}^{R_3}$ is comparable to, but slightly larger than that in $\Delta h_{CO_2}^{R_1}$ (both being greater then that in $\Delta h_{O_2}^{R_1}$). From this result, Eq. A.36 may also be applied with reasonable accuracy to applications with unknown fuel composition, provided an average value for $\Delta h_{O_2}^{R_3}$ is assumed.

Table A.2: Measured and theoretical averages for reaction enthalpy parameters.

Parameter	Measured [169] (MJ/kg)	Theoretical (MJ/kg)
$\Delta h_{O_2}^{R_1}$	13.1 ± 0.6	12.89 ± 0.24
$\Delta h_{CO_2}^{R_1}$	13.6 ± 1.1	13.37 ± 1.12
$\Delta h_{O_2}^{R_3}$	14.7 ± 1.4[a]	14.38 ± 1.14
$\Delta h_{O_2}^{R_4}$	—	17.69[b]
$\Delta h_{O_2}^{R_5}$	—	12.30[b]
$\Delta h_{CO_2}^{R_4}$	—	6.43[b]
$\Delta h_{CO_2}^{R_5}$	—	8.94[b]

[a] Not measured, evaluated from measured $\Delta h_{O_2}^{R_1}$ using Eq. A.37.
[b] Fuel-independent constant.

The primary advantage of Eq. A.36 is that it contains no requirement for the measurement of $C_{(s)}$, which can be difficult to measure accurately in most applications. Still, Eq. A.36 has been derived from reaction R_0, which includes consideration for $C_{(s)}$ production. Equation A.36 therefore includes implicitly a correction for the enthalpy associated with the production of $C_{(s)}$, without requiring actual $C_{(s)}$ measurements. This is accomplished by leveraging the balanced stoichiometry of the presumed system of sub-reactions (R_1–R_3), where it may be recognized that distinct amounts of O_2 are required for the stoichiometric production of either CO_2, CO, or $C_{(s)}$ ($\nu_{O_2}^{R_1} \neq \nu_{O_2}^{R_2} \neq \nu_{O_2}^{R_3}$). By measuring total O_2 consumption, combined with measurements of CO_2 and CO production, $C_{(s)}$ production may be inferred from these stoichiometric relationships. The novel formulation presented in Eq. A.36 may then be particularly desirable for applications in which $C_{(s)}$ production is considerable, but accurate $C_{(s)}$ measurements are unavailable.

It should be emphasized that the enthalpy parameters in each of the presently derived formulations are defined based on stoichiometrically idealized reactions (R_1–R_5), which may not be fully realized in actual combustion conditions. Average values for the enthalpy parameters ($\Delta h_{O_2}^{R_1}$, $\Delta h_{CO_2}^{R_1}$, and $\Delta h_{O_2}^{R_3}$) are then most appropriately based on theoretically derived values, and not experimental measurements. This is because any combustion experiment pursuing the measurement of these parameters likely includes some effects of incomplete combustion. These effects are configuration dependent and are therefore undesirable in the pursuit of generally representative values for each parameter. Any experimental deviations from ideal behavior likely involve the under-consumption of O_2 or the under-production of CO_2, effects which lead to over-prediction of the enthalpy parameters.

Instead, theoretical values for $\Delta h_{O_2}^{R_1}$, $\Delta h_{CO_2}^{R_1}$, and $\Delta h_{O_2}^{R_3}$ may be evaluated using Eqs. A.2 and A.15 for any number of fuel species, provided the chemical composition ($C_xH_yO_z$) and enthalpy of formation ($\Delta\bar{h}^{\circ}_{f,fuel}$) of the fuel may be determined. Theoretical average values for $\Delta h_{O_2}^{R_1}$, $\Delta h_{CO_2}^{R_1}$, and $\Delta h_{O_2}^{R_3}$ are also presented in Table A.2, evaluated for the same collection of hydrocarbon compounds used to produce the measured averages [169]. As shown, measured values for each parameter indeed overpredict the theoretical values by roughly 2%.

It is important to note that the presently derived formulations, Eq. A.27 for OC-based and Eq. A.31 for CDG-based calorimetry, as well as the novel formulation presented in Eq. A.36 (and any of the 17 other available formulations not presently derived), apply only to reactions resembling the originally assumed mechanism given by R_0. Here, combustion products are limited to H_2O, CO_2, CO, and $C_{(s)}$, while

UHC are neglected. These reaction-enthalpy formulations should not generally be applied to mechanisms including significant yields of additional or exotic species as these may substantially alter the enthalpy of reaction. For such applications, the simple formulation presented in Eq. A.6 may be utilized, or the preceding derivation framework may be applied to the applicable combustion mechanism.

While the familiar OC and CDG calorimetry formulations in Eqs. A.27 and A.29 are somewhat intuitive and have been firmly established in the existing literature [105–113], the present analysis demonstrates that the derivation of these expressions from first principles is non-trivial. The present derivations not only reinforce the general validity of these expressions, but also offer clarity into the assumptions inherent in their formulation and the most appropriate definitions for their characteristic parameters. This analysis also highlights the flexibility in the derivation framework, revealing the existence of potentially attractive alternative formulations such as the novel expression given in Eq. A.36.

A.3 Mass Conservation Analysis

The primary duty of a calorimetry measurement system is the accurate determination of the species mass reaction rates, $\dot{m}_k^{rxn}$, present in the applicable reaction-enthalpy formulation (see Sec. A.2). These reaction rates are most appropriately derived via a control-volume-based mass-conservation analysis applied to the measurement system. A model control volume is depicted in Fig. A.1, representing a simple open combustion system comprising a fuel source ($\dot{m}_{fuel}$) placed beneath an

exhaust collection system ($\dot{m}_e$) with ambient air entrainment ($\dot{m}_a$). Matching the experimental configuration utilized in the present work, an additional mass source is included, representing a co-flowing oxidizer around the fuel source ($\dot{m}_{ox}$). Systems lacking this source may simply ignore associated terms in the analysis that follows. More complex systems may also be considered, where additional or alternative mass exchanges must be included. It is *essential* that the assumed control volume completely characterize all unique compositions of mass actually exchanged across its boundaries.

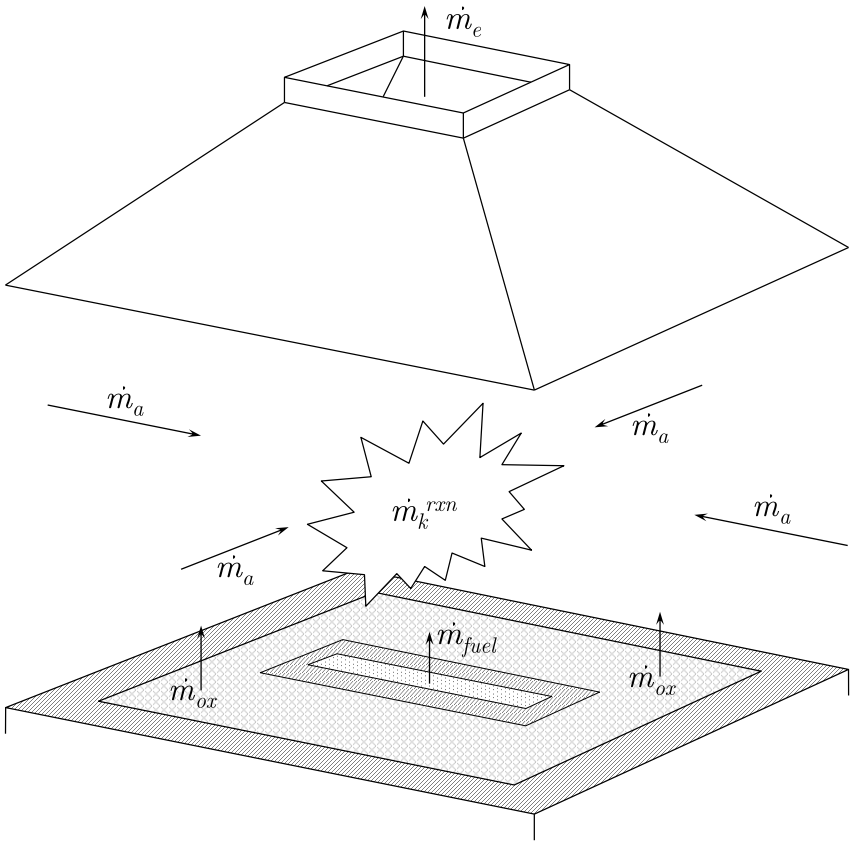

Figure A.1: Control volume for species-based calorimetry analysis; a fuel source ($\dot{m}_{fuel}$) is located beneath an exhaust collection system ($\dot{m}_e$) with ambient air entrainment ($\dot{m}_a$), co-flowing oxidizer ($\dot{m}_{ox}$), and reaction source ($\dot{m}_k^{rxn}$). All $\dot{m}_{fuel}$, $\dot{m}_a$, $\dot{m}_{ox}$, and $\dot{m}_k^{rxn}$ are assumed totally captured within $\dot{m}_e$.

Conservation of total mass within a control volume gives

$$0 = \sum_j \dot{m}_j + \frac{dm}{dt}, \tag{A.38}$$

where $\dot{m}_j$ is the mass flow rate of stream j across the boundary of the control volume and dm/dt accounts for the accumulation or reduction of mass within the control volume due to unsteady flow at the boundaries. This term is typically important only for very large systems where the flow-through time of the control volume is significantly greater than the measurement time-scales of interest. Recent studies have explored calorimetry measurements in applications where such dm/dt effects are important, with limited success [121, 126, 127].

For the control volume depicted in Fig. A.1 and including a steady-state assumption where dm/dt effects are neglected, Eq. A.38 simplifies to

$$\dot{m}_e = \dot{m}_{fuel} + \dot{m}_a + \dot{m}_{ox}, \tag{A.39}$$

where it is additionally assumed that there be no loss of mass from the system except through the exhaust flow. As most system designs include measurement instrumentation in the exhaust stream, this limitation ensures that all products of combustion are collected and measured. Alternative configurations are possible, but may considerably complicate measurement requirements.

Conservation of species mass within a control volume gives

$$\dot{m}_k^{rxn} = \sum_j \dot{m}_k^j + \frac{dm_k}{dt}, \tag{A.40}$$

where $\dot{m}_k^{rxn}$ is the mass reaction rate of species k, $\dot{m}_k^j$ is the mass flow rate of species k within stream j, and m_k is the mass of species k contained in the control volume.

Applied to the control volume in Fig. A.1 and including a steady-state assumption where dm_k/dt effects are neglected, Eq. A.40 simplifies to

$$\dot{m}_k^{rxn} = \dot{m}_k^e - \dot{m}_k^{fuel} - \dot{m}_k^a - \dot{m}_k^{ox}. \tag{A.41}$$

Equation A.41 may be further simplified through assumptions limiting the constituent species in each flow stream. For example, the fuel stream usually consists of pure fuel and products of incomplete combustion are usually negligible in the ambient, though some applications may feature complex or diluted fuel mixtures or significant ambient vitiation. In general, no simplifying assumptions need be made regarding the composition of each flow stream unless the measurement capabilities to fully characterize those streams are unavailable.

Species mass flow rates within each stream may be expressed in terms of the stream composition via

$$\dot{m}_k^j = X_k^j \, \dot{m}_j \, \frac{M_k}{M_j}, \tag{A.42}$$

where X_k^j is the mole fraction of species k within stream j, M_k is the molar mass of species k, and M_j is the mixed molar mass of stream j, which can also be expressed in terms of the stream composition as

$$M_j = \sum_k \left(X_k^j \, M_k \right), \tag{A.43}$$

provided that

$$\sum_k X_k^j = 1, \tag{A.44}$$

must also be satisfied.

By direct application of Eq. A.39, $\dot{m}_j$ for one of the flow streams in the system may be obtained provided all others are known. For open systems, $\dot{m}_a$ is typically

difficult or impossible to measure, and therefore all $\dot{m}_j$ except $\dot{m}_a$ should be measured. Alternatively, assuming non-reactivity of N_2 ($\dot{m}^{rxn}_{N_2} = 0$), Eq. A.41 may be re-expressed as

$$\dot{m}^{a}_{N_2} = \dot{m}^{e}_{N_2} - \dot{m}^{fuel}_{N_2} - \dot{m}^{ox}_{N_2}, \tag{A.45}$$

and inserted into an inverted form of Eq. A.42, expressed as

$$\dot{m}_a = \frac{\dot{m}^{a}_{N_2}}{X^{a}_{N_2}} \frac{M_a}{M_{N_2}}. \tag{A.46}$$

When available, Eqs. A.45 and A.46 typically provide a more accurate determination of $\dot{m}_a$, than direct use of Eq. A.39, with the stipulation that $\dot{m}^{j}_{N_2}$ must be measured or estimated for all N_2-containing flow streams (which usually also requires measurement of all $\dot{m}_j$ except $\dot{m}_a$). Similar formulations may be derived for applications where other inert species are present.

An additional simplification is noted in Eq. A.44, where X^{j}_{k} for one of the constituent species in each flow stream (considered as the background species) may be obtained provided all others are known. In the exhaust and ambient, N_2 is typically the most appropriate species to omit measurement, and thus all relevant species except N_2 should be measured for these streams. The appropriate background species for any additional flow streams may vary, dependent on the stream composition.

Required composition measurements may be further simplified via assumptions limiting the constituent species in each stream (*i.e.* $X^{a}_{CO} = 0$, $X^{e}_{H_2O} = X^{a}_{H_2O}$, $X^{e}_{C_{(s)}} = 0$, *etc.*). However, if such assumptions are unwarranted, the accuracy of the mass-conservation analysis may be impacted and any affected $\dot{m}^{rxn}_{k}$ may then be significantly misrepresented.

An additional mass-conservation statement may also be applied to the combustion reaction, giving

$$\sum_k \dot{m}_k^{rxn} = 0, \tag{A.47}$$

which states that there can be no net change in mass within the control volume due to chemical reaction. This expression may be used as a simple check on mass conservation to verify that all $\dot{m}_k^{rxn}$ indeed sum to zero, but is perhaps more useful as a means of evaluating $\dot{m}_k^{rxn}$ for one species provided all others are known. Though useful, this expression is more complex to implement than the preceding simplifications, requiring an iterative procedure where the composition of the unmeasured species must first be estimated in order to determine $\dot{m}_k^{rxn}$ for the others.

Eqs. A.38–A.47 provide the necessary mass-conservation framework for any calorimetry measurement system, where the desired species reaction rates, $\dot{m}_k^{rxn}$, as appear in the reaction-enthalpy formulation, may be determined from measurements of the compositions (X_k^j) and total mass flow rates ($\dot{m}_j$) of the applicable mass exchanges in the system. Additional considerations for the measurement of these quantities are presented in Sec. A.4.

A.4 Measurement Considerations

In a typical calorimetry system, composition instrumentation is installed in the exhaust stream using an extractive sampling system leading to various species analyzers. For most analyzers, the flow sample must be conditioned via filtration to remove soot and other particulates and a combination of cold-traps and desiccation

to remove H_2O. Note that Drierite^{TM}, which is the most appropriate desiccant for H_2O removal in calorimetry applications, is known to also interact with CO_2 and can impede CO_2 measurement response in samples with transient CO_2 content [170,171]. The amount of Drierite^{TM} used for sample conditioning should be minimized to alleviate such effects.

The removal of any species from the sample presents additional challenge because the analyzer-measured sample composition sans the removed species does not accurately represent the true stream composition. Analyzer composition measurements must then be corrected to account for sample conditioning via

$$X_k^j = X_{k,A}^j \left(1 - \sum_{k,\, rmv} X_k^j \right), \tag{A.48}$$

where $X_{k,A}^j$ is the analyzer-measured mole fraction of species k in the stream j sample. The summation in Eq. A.48 is performed over any species k that is removed from the sample during conditioning (usually only H_2O removal is necessary), where X_k^j for any such species must be directly measured via either in situ sensors or extractive analyzers installed upstream of the applicable sample conditioning.

Mass flow rates may be measured by numerous techniques, the proper choice of which depends on the applicable flow characteristics. For applications using solid or liquid fuel sources, a load-cell may be employed to measure the rate of fuel pyrolysis. For applications using pressurized gaseous fuels, direct measurement instruments such as mass flow meters or rotameters may be used. Such instruments are viable for low-flow, high-pressure applications, but are not suitable for high-flow, low-pressure conditions as typically encountered in calorimetry exhaust systems.

For calorimetry applications, differential pressure methods are preferred, for which a differential pressure sensing device is placed in the applicable flow stream and the flow rate is determined as

$$\dot{m}_j = C_f^j \, A_j \left(\frac{2 \, \Delta P_j \, P_j \, M_j}{R \, T_j} \right)^{1/2}, \tag{A.49}$$

where A_j is the cross-sectional area of the flow stream, ΔP_j is the sensor-measured differential pressure, P_j is the static pressure of the flow, T_j is the temperature of the flow, M_j is the molar mass of the flow mixture, R is the ideal gas constant, and C_f^j is a flow coefficient characterizing the velocity profile across the cross-section of the stream. All of these quantities must be evaluated at the location of the probe.

Note that Eq. A.49 relies on Bernoulli's principle to relate the measured differential pressure to the flow velocity, hence compressibility effects are neglected. The flow velocity is related to the mass flow rate via the flow density, which is estimated from the stream composition, pressure, and temperature via the ideal gas law. As a result, condensed-phase contributions to the stream mass, such as soot and other particulates or condensed forms of H_2O and UHC, are neglected.

The flow coefficient, C_f^j, may be determined by calibrating the differential pressure sensor to a condition with known flow rate. A suitable procedure may include passing an accurately measured flow of some species into the flow stream, while accurately measuring the concentration of that species using an available species analyzer. The total flow rate may then be obtained by relating the known species flow to the background flow required to yield the measured concentration. Sensors with known and constant C_f^j are also available, which require no calibration.

A number of previous works have advocated the treatment of C_f^j as a calibration factor applicable to the entire calorimetry system, whereby C_f^j is determined by placing a calibration burner with known heat release in the measurement system. The value of C_f^j is then fixed so that the system returns the correct heat release rate. This type of calibration procedure should be avoided because it lumps any and all extraneous factors affecting the measurement into a single factor that has no physical relationship to many of the effects that may be included. Such effects may vary for measuring conditions different from the calibration test, potentially resulting in significant unidentifiable errors in the measurements. It is highly recommended that C_f^j be determined via independent flow calibration and not using a calibration burner.

The solution procedure for the preceding mass-conservation analysis requires first the determination of the compositions of all applicable flow streams using an appropriate configuration of species analyzers. This includes measuring X_k^j for any species removed during sample conditioning, measuring $X_{k,A}^j$ for all remaining species, correcting all $X_{k,A}^j$ via Eq. A.48, obtaining X_k^j for each selected background species via Eq. A.44, and determining each M_j via Eq. A.43. Next, $\dot{m}_j$ for all flow streams (typically with the exception of $\dot{m}_a$) are either directly measured or are determined via Eq. A.49. Using the now available M_j, $\dot{m}_j$, and X_k^j, available $\dot{m}_k^j$ are obtained via Eq. A.42. Typically unavailable for direct measurement, $\dot{m}_a$ is obtained via Eqs. A.45 and A.46 using all $\dot{m}_{N_2}^j$. Next, all $\dot{m}_k^a$ are determined via Eq. A.42. With all $\dot{m}_k^j$ now available, the desired $\dot{m}_k^{rxn}$ are determined via Eq. A.41, from which $\dot{Q}$ may be evaluated using the appropriate reaction-enthalpy formulation.

Appendix B: Supplemental Results for Grid Convergence Study

B.1 Overview

The following sections present supplemental results evaluating numerical grid-convergence in large eddy simulations (LES) of the present turbulent line-fire configuration. A detailed description of the experimental facility is presented in Sec. 2.2, while a discussion of the numerical configuration is presented in Sec. 3.3. A description of the numerical solver, the Fire Dynamics Simulator (FDS), is presented in Sec. 3.2, with primary grid-convergence results included in Sec. 3.4.

Grid-convergence simulations feature a uniform numerical grid with varying resolution corresponding to $\Delta x = 20.0\,\text{mm}$, $10.0\,\text{mm}$, $5.0\,\text{mm}$, and $2.5\,\text{mm}$, in a computational domain comprising a 0.8-m-wide by 1.0-m-long by 1.0-m-tall box ($x \times y \times z$) surrounding the flame (see Fig. 3.2). Simulations are conducted for a duration of 30 s, where time-mean and root-mean-square (rms) statistics for each quantity are gathered over the final 25 s of each simulation, during a period when the flow is statistically stationary. A comparison of run-time characteristics for these simulations is presented in Table 3.2. Supplemental results include statistics for gas-phase mass density (ρ), perturbation pressure (p), x-component velocity magnitude (u), y-component velocity magnitude (v), and total flow kinetic energy (k).

B.2 Density

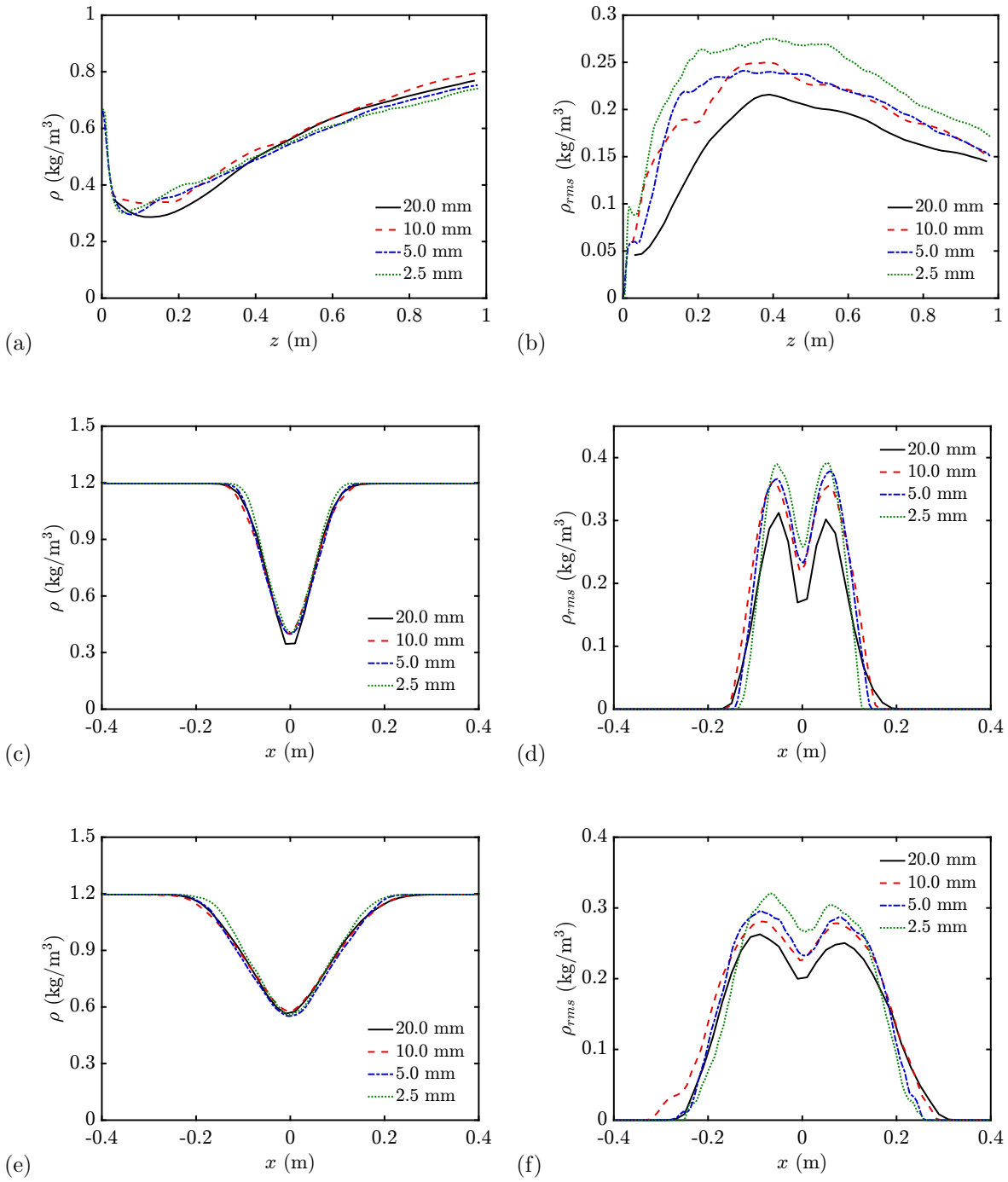

Figure B.1: Simulated mass density (ρ) at selected grid resolutions; (a) mean z-profile, (b) rms z-profile, (c) mean x-profile at $z = 0.25\,\text{m}$, (d) rms x-profile at $z = 0.25\,\text{m}$, (e) mean x-profile at $z = 0.50\,\text{m}$, (f) rms x-profile at $z = 0.50\,\text{m}$.

B.3 Perturbation Pressure

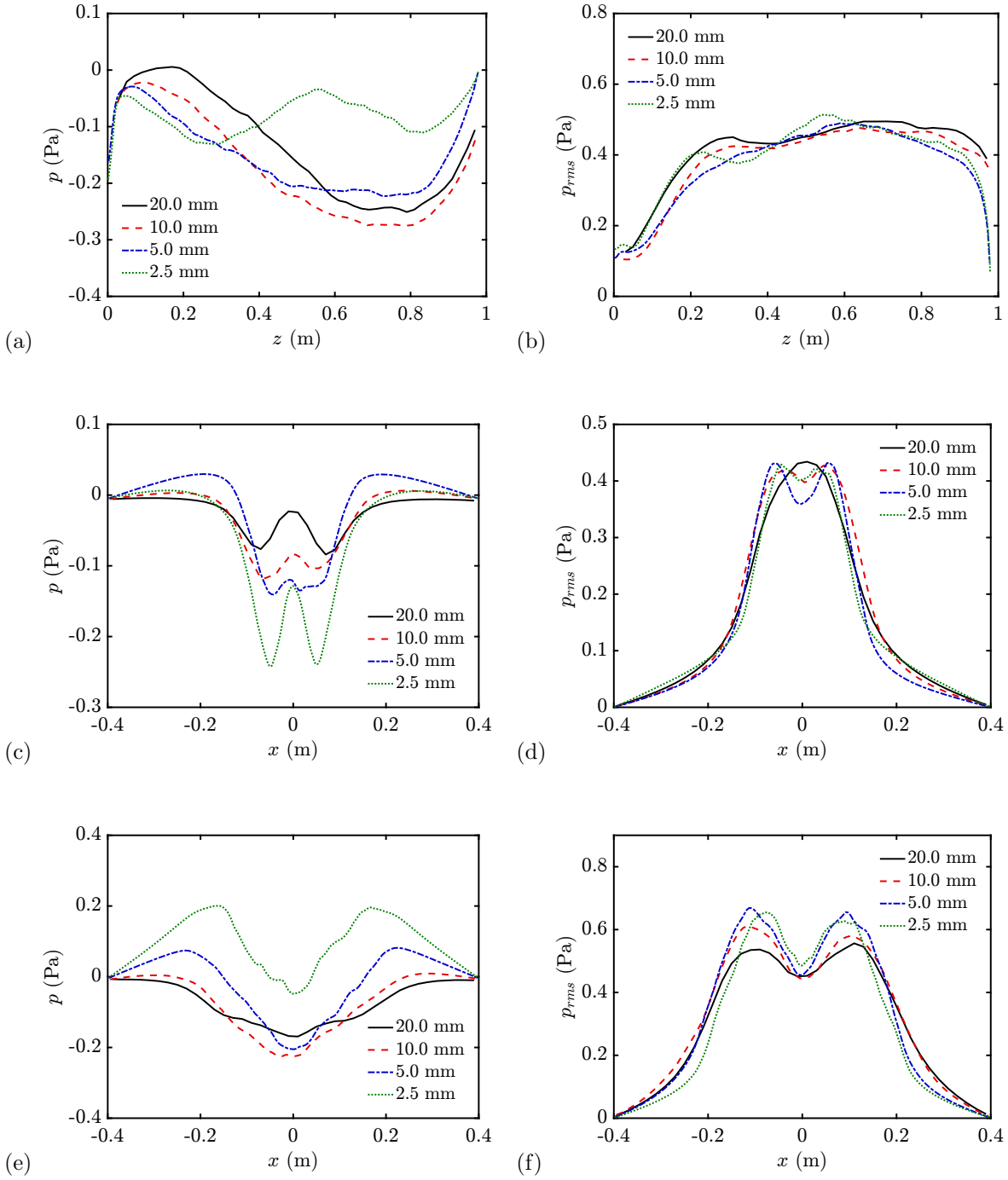

Figure B.2: Simulated perturbation pressure (p) at selected grid resolutions; (a) mean z-profile, (b) rms z-profile, (c) mean x-profile at $z = 0.25\,\mathrm{m}$, (d) rms x-profile at $z = 0.25\,\mathrm{m}$, (e) mean x-profile at $z = 0.50\,\mathrm{m}$, (f) rms x-profile at $z = 0.50\,\mathrm{m}$.

B.4 x-Velocity Magnitude

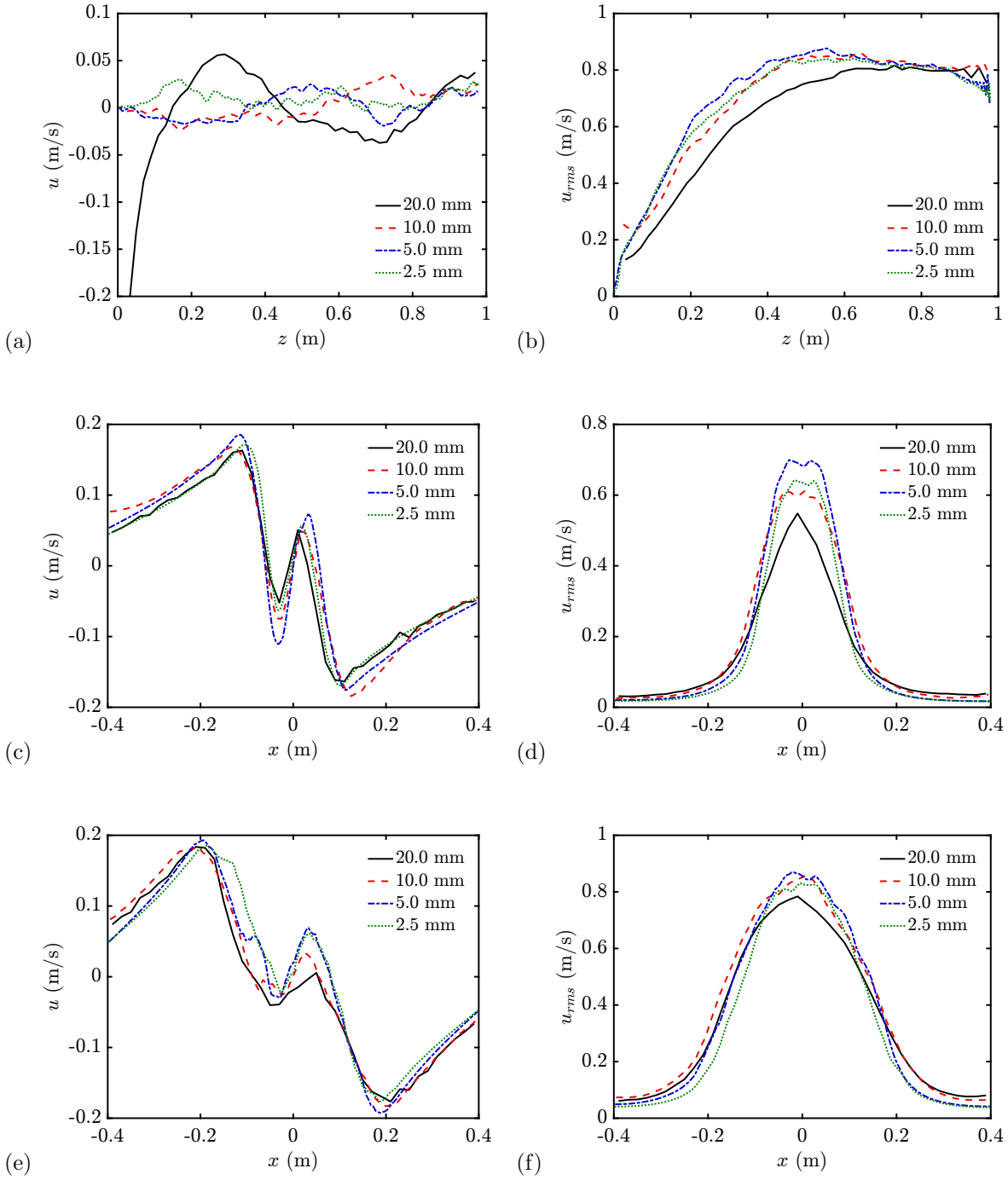

Figure B.3: Simulated x-velocity magnitude (u) at selected grid resolutions; (a) mean z-profile, (b) rms z-profile, (c) mean x-profile at $z = 0.25\,\mathrm{m}$, (d) rms x-profile at $z = 0.25\,\mathrm{m}$, (e) mean x-profile at $z = 0.50\,\mathrm{m}$, (f) rms x-profile at $z = 0.50\,\mathrm{m}$.

B.5 y-Velocity Magnitude

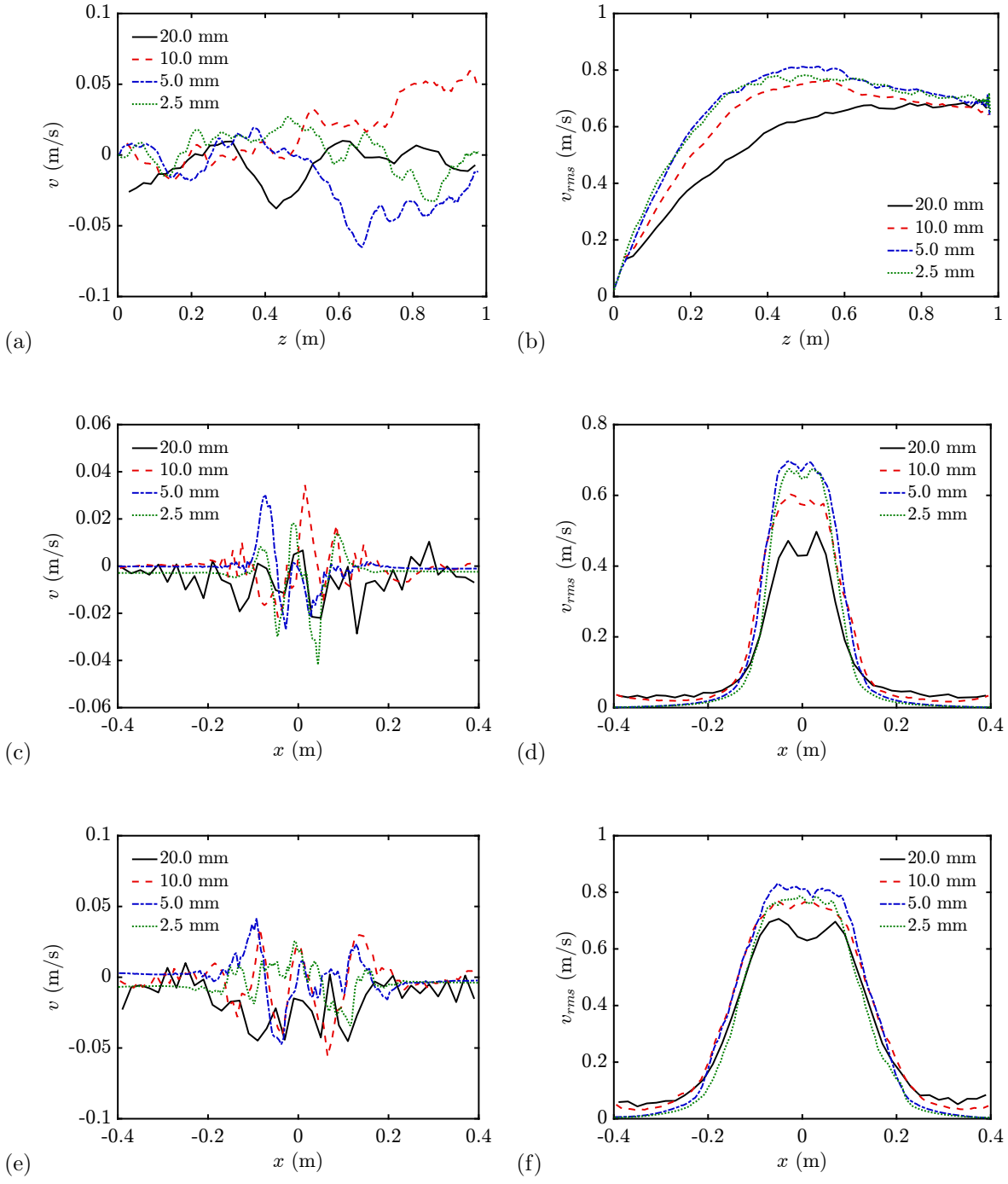

Figure B.4: Simulated y-velocity magnitude (v) at selected grid resolutions; (a) mean z-profile, (b) rms z-profile, (c) mean x-profile at $z = 0.25\,\text{m}$, (d) rms x-profile at $z = 0.25\,\text{m}$, (e) mean x-profile at $z = 0.50\,\text{m}$, (f) rms x-profile at $z = 0.50\,\text{m}$.

B.6 Total Kinetic Energy

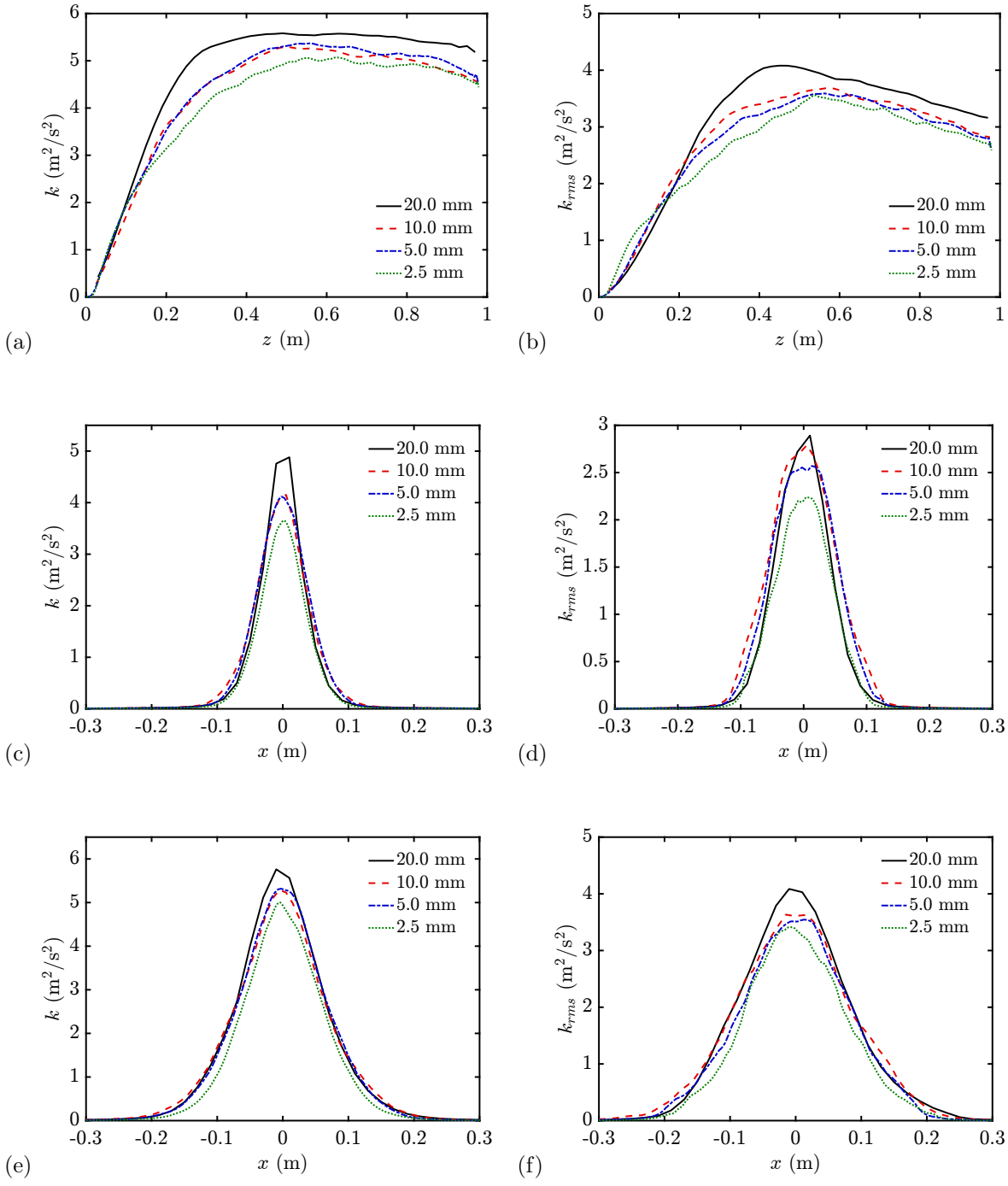

Figure B.5: Simulated total kinetic energy (k) at selected grid resolutions; (a) mean z-profile, (b) rms z-profile, (c) mean x-profile at $z = 0.25\,\text{m}$, (d) rms x-profile at $z = 0.25\,\text{m}$, (e) mean x-profile at $z = 0.50\,\text{m}$, (f) rms x-profile at $z = 0.50\,\text{m}$.

Appendix C: Spectral Resolution of the Radiative Transfer Equation

C.1 Overview

The following presents an investigation of different treatments of spectral resolution for evaluation of the radiative transfer equation (RTE). Common methods, in order of decreasing accuracy (and computational cost), include line-by-line, narrow-band, wide-band, and gray calculations. Line-by-line calculations treat individually each and every absorption/emission line across the spectrum of interest (typically in the millions), and are prohibitively expensive for most applications. Narrow-band calculations provide a drastic reduction in computational cost by dividing the spectrum into a series of only hundreds or thousands of narrow bands, with each band typically spanning hundreds or thousands of individual lines. Wide-band calculations further coalesce the spectrum into much wider bands, with the full spectrum typically divided into only several bands. Gray calculations provide the least expensive option by treating the entire spectrum as a single band, neglecting any variation in radiative properties over the spectrum.

The present study features a comparison of the narrow-band model used within RadCal, a stand-alone RTE solver [172], and a standard gray model, solved using simple hand calculations. A description of the narrow-band formulation included

in the RadCal solver is presented in Sec. C.2, while the gray formulation is discussed in Sec. C.3. Careful analysis of the differences between the mathematical frameworks for each of these models provides guidance toward which applications the gray formulation is most appropriate (Sec. C.4). Comparisons between model results then highlight and quantify the various penalties in accuracy that result from the simplifying assumptions employed in the gray formulation (Sec. C.5).

C.2 RadCal Formulation

RadCal evaluates a one-dimensional RTE with narrow-band spectral resolution in a configuration comprising a series of homogeneous gas layers. Radiative emission and absorption within the layers are considered, though scattering effects are neglected. The boundary condition for the system consists of background irradiation from an infinitely-far blackbody at specified temperature. Other specified quantities include the number of layers along the radiation path, the path length, temperature, and composition of each layer, and the bounds of the spectral domain.

The radiation spectrum is discretized in terms of a spectral variable, usually either wavelength, λ (μm), or wavenumber, ω (cm^{-1}). Reference values for each of these quantities, corresponding to the bounds of the visible and infrared spectra are provided in Table C.1. The narrow-band resolution for RadCal computations is $5\,\mathrm{cm}^{-1}$ in the range ($50 < \omega < 1100$), $25\,\mathrm{cm}^{-1}$ in the range ($1100 < \omega < 5000$), and $50\,\mathrm{cm}^{-1}$ in the range ($5000 < \omega < 10000$). Wavenumber is the spectral variable of choice for the present study and is also the default used for RadCal computations.

Table C.1: Reference values for bounds of the visible and infrared spectra.

Spectrum	Wavelength (λ, μm)	Wavenumber (ω, cm^{-1})
Far Infrared (FIR)	1000 – 10	10 – 1000
Mid Infrared (MIR)	10 – 2.5	1000 – 4000
Near Infrared (NIR)	2.5 – 0.75	4000 – 13300
Visible	0.75 – 0.38	13300 – 26300

RadCal-computed quantities, each evaluated over the total radiation path, include the end-path received intensity ($\bar{I}$), the effective absorption coefficient ($\bar{\kappa}_E$), the Planck mean absorption coefficient ($\bar{\kappa}_P$), the total transmissivity ($\bar{\tau}$), and the total emissivity ($\bar{\varepsilon}$). Each of these quantities are defined as follows.

The end-path received intensity is given by

$$\bar{I} = \int_{\omega_{min}}^{\omega_{max}} \Big(B_\omega(T_B)\, \tau_\omega(L) + B_\omega(T_l) \left(1 - \tau_\omega(L)\right) \Big) d\omega, \tag{C.1}$$

where B_ω is the spectral blackbody intensity (Planck distribution), τ_ω is the spectral transmissivity of the gas layer, L is the path length, T_l is the temperature of the gas layer, and T_B is the temperature of the boundary blackbody. The first term on the right-hand side of Eq. C.1 represents background irradiation reduced by absorption within the layer, while the second term represents emission from within the layer. The integral in this expression is evaluated over the range of discrete spectral bands within the domain bounded by ($\omega_{min} < \omega < \omega_{max}$).

The spectral Planck distribution is defined as a function of temperature via

$$B_\omega(T) = \frac{2\, h_P\, c_0^2\, \omega^3}{\exp\left(\frac{h_P\, c_0\, \omega}{k_B\, T}\right) - 1}, \tag{C.2}$$

where h_P is the Planck constant ($6.6261 \times 10^{-34}\,\mathrm{J\,s}$), c_0 is the speed of light in vacuum ($2.9979 \times 10^8\,\mathrm{m/s}$), and k_B is the Boltzmann constant ($1.3807 \times 10^{-23}\,\mathrm{J/K}$).

The effective absorption coefficient is defined by

$$\bar{\kappa}_E = -\frac{1}{L} \ln \left(\frac{\int_{\omega_{min}}^{\omega_{max}} I_\omega - B_\omega(T_l)\, d\omega}{\int_{\omega_{min}}^{\omega_{max}} B_\omega(T_B) - B_\omega(T_l)\, d\omega} \right), \tag{C.3}$$

where I_ω is the end-path spectral radiative intensity, defined as the integrand from Eq. C.1.

The Planck mean absorption coefficient is then defined as

$$\bar{\kappa}_P = \frac{\int_{\omega_{min}}^{\omega_{max}} B_\omega(T_l) \sum_k \kappa_{\omega,k}\, P_k\, d\omega}{\int_0^\infty B_\omega(T_l)\, d\omega}, \tag{C.4}$$

where $\kappa_{\omega,k}$ is the spectral absorption coefficient and P_k the partial pressure of species k in the gas layer. Here, $\kappa_{\omega,k}$ is referenced from either line-by-line calculations or fitted experimental data. As defined in Eq. C.4, $\bar{\kappa}_P$ is a function of the local gas temperature and composition only and is independent of the path length. This desirable trait allows $\bar{\kappa}_P$ to be treated as a pseudo optical property of the medium.

The total transmissivity and emissivity of the gas layer are defined via

$$\bar{\tau} = \frac{\int_{\omega_{min}}^{\omega_{max}} \tau_\omega(L)\, B_\omega(T_B)\, d\omega}{\int_{\omega_{min}}^{\omega_{max}} B_\omega(T_B)\, d\omega}, \tag{C.5}$$

$$\bar{\varepsilon} = 1 - \exp\left(-\bar{\kappa}_E\, L\right), \tag{C.6}$$

where $\bar{\varepsilon}$ is derived from the computed effective absorption coefficient, $\bar{\kappa}_E$, while $\bar{\tau}$ is determined based on the narrow-band modeled spectral transmissivity, τ_ω.

Narrow-band modeled τ_ω are defined via the following expressions, taking different definitions based on the participating radiative species present in each gas layer. For the case of blackbody spectral behavior, which is applicable only for soot,

$$\tau_{\omega,k} = \exp\left(-\kappa_{\omega,k}\, L\right). \tag{C.7}$$

For gas-phase species, τ_ω is determined using one of the following expressions, which provide alternate statistical representations of the average radiative properties over each narrow band. In these expressions, terms are as previously defined, where $\beta_{\omega,k}$ is a spectral band-overlap parameter for species k, referenced from either line-by-line calculations or fitted experimental data.

By the Elsasser model,

$$\tau_{\omega,k} = 1 - \mathrm{erf}\left(\frac{\sqrt{\pi}\,\kappa_{\omega,k}\,P_k\,L}{2\sqrt{1+\frac{\pi\,\kappa_{\omega,k}\,P_k\,L}{16\,\beta_{\omega,k}}}}\right), \tag{C.8}$$

which assumes that all spectral lines have equivalent strengths, widths, and spacing. These strong assumptions are typically only valid for very light gaseous species so that within RadCal, Eq. C.8 is applied only for CH_4.

By the Goody model,

$$\tau_{\omega,k} = \exp\left(\frac{-\kappa_{\omega,k}\,P_k\,L}{\sqrt{1+\frac{\kappa_{\omega,k}\,P_k\,L}{4\,\beta_{\omega,k}}}}\right), \tag{C.9}$$

which assumes an exponential distribution of line strengths within the narrow-band. The Goody model is generally superior to the Elsasser model, though the assumption of an exponential distribution of line strengths substantially underestimates the number of low-intensity lines. Within RadCal, Eq. C.9 is applied for H_2O, CO_2, and CO.

By the Malkmus model,

$$\tau_{\omega,k} = \exp\left(-2\,\beta_{\omega,k}\left(\sqrt{1+\frac{\kappa_{\omega,k}\,P_k\,L}{\beta_{\omega,k}}}-1\right)\right), \tag{C.10}$$

which assumes an exponential-tailed distribution of line strengths that varies proportionally to inverse line strength. The Malkmus model is generally recognized

as the most suitable statistical narrow-band model for polyatomic gases. Within RadCal, Eq. C.10 is applied for all remaining species, primarily polyatomic fuels.

For a gas layer with multiple participating radiative species, the total effective transmissivity is determined via

$$\tau_\omega = \prod_k \tau_{\omega,k}, \tag{C.11}$$

where the applicable $\tau_{\omega,k}$ are determined using Eqs. C.7–C.10, depending on which participating species are present in the layer.

The solution procedure for the RadCal narrow-band formulation requires first the specification of all relevant initial and boundary conditions for temperature and composition of the applicable gas layer. In addition, any participating radiative species must have spectral absorption coefficients, $\kappa_{\omega,k}$, and band-overlap parameters, $\beta_{\omega,k}$, defined for each narrow-band. For most primary combustion species, these quantities are inherent to the RadCal solver and need not be specified by the user. Depending on the participating species, spectral transmissivities, $\tau_{\omega,k}$, are evaluated for each band from the tabulated $\kappa_{\omega,k}$ and $\beta_{\omega,k}$ via one of Eqs. C.7–C.10. From these $\tau_{\omega,k}$, effective τ_ω are determined using Eq. C.11, and the total layer transmissivity, $\bar{\tau}$, is determined via Eq. C.5. Next, the end-path intensity, $\bar{I}$, is evaluated using Eq. C.1. From $\bar{I}$ and the path length, L, the effective absorption coefficient, $\bar{\kappa}_E$, is determined via Eq. C.3. Finally, the total emissivity, $\bar{\varepsilon}$, is evaluated from $\bar{\kappa}_E$ and L using Eq. C.6. The Planck mean absorption coefficient, $\bar{\kappa}_P$, is additionally computed from $\kappa_{\omega,k}$ values using Eq. C.4, but is not explicitly used in any of the narrow-band calculations.

C.3 Gray Formulation

The following formulation provides gray-resolution radiative properties for comparison against the narrow-band resolved quantities defined in Sec. C.2. The standard gray model requires an estimate of an effective absorption coefficient for the medium, which is here referenced from the RadCal-computed Planck mean absorption coefficient, $\bar{\kappa}_P$, defined in Eq. C.4. Here, $\bar{\kappa}_P$ is selected over the effective absorption coefficient, $\bar{\kappa}_E$, due to its path-length independence and treatability as a pseudo optical property of the medium. As defined, the numerator term in Eq. C.4 is integrated over the spectral domain bounded by ($\omega_{min} < \omega < \omega_{max}$), while the denominator term is integrated over the full spectrum ($0 < \omega < \infty$). As a result of this convention, RadCal-computed $\bar{\kappa}_P$ are artificially reduced when evaluated over limited spectral domains. To correct for this, a modified Planck mean absorption coefficient, $\tilde{\kappa}_P$, for use in the following gray formulation is defined as

$$\tilde{\kappa}_P = \bar{\kappa}_P \frac{\int_0^\infty B_\omega(T_l)\, d\omega}{\int_{\omega_{min}}^{\omega_{max}} B_\omega(T_l)\, d\omega}, \tag{C.12}$$

where the indefinite integral is approximated as

$$\int_0^\infty B_\omega(T)\, d\omega = \frac{\sigma\, T^4}{\pi}, \tag{C.13}$$

and σ is the Stefan-Boltzmann constant ($5.6704 \times 10^{-8}\,\mathrm{W/m^2/K^4}$).

From the modified Planck mean absorption coefficient, $\tilde{\kappa}_P$, defined in Eq. C.12, gray-resolved end-path intensity, total transmissivity, and total emissivity are defined respectively via

$$\tilde{I} = \exp\left(-\tilde{\kappa}_P\, L\right) \int_{\omega_{min}}^{\omega_{max}} B_\omega(T_B)\, d\omega + \Big(1 - \exp\left(-\tilde{\kappa}_P\, L\right)\Big) \int_{\omega_{min}}^{\omega_{max}} B_\omega(T_l)\, d\omega, \tag{C.14}$$

$$\tilde{\tau} = \exp\left(-\tilde{\kappa}_P\, L\right), \tag{C.15}$$

$$\tilde{\varepsilon} = 1 - \exp\left(-\tilde{\kappa}_P\, L\right). \tag{C.16}$$

The solution procedure for the gray formulation requires first the evaluation of the modified Planck mean absorption coefficient, $\tilde{\kappa}_P$, using the RadCal-computed $\bar{\kappa}_P$ within Eq. C.12. Next, the gray-resolved end-path intensity, $\tilde{I}$, total transmissivity, $\tilde{\tau}$, and total emissivity, $\tilde{\varepsilon}$, are determined via Eqs. C.14–C.16. Because the gray formulation makes use of the RadCal-computed $\bar{\kappa}_P$, all initial and boundary conditions for the gray-resolved quantities must match those employed for the narrow-band computations. Note that the only spectral information utilized within the gray formulation is that which is modeled by $\tilde{\kappa}_P$.

C.4 Key Discrepancies Between Formulations

In comparing the narrow-band and gray formulations (respectively described in Secs. C.2 and C.3), four primary discrepancies between the two formulations may be identified. These discrepancies are described as follows and are further explored in the detailed result comparisons presented in Sec. C.5.

The first discrepancy (1) arises from details in the narrow-band modeled spectral transmissivity, which are neglected in the gray formulation. In the narrow-band formulation, $\tau_{\omega,k}$ for gas-phase species are calculated via Eqs. C.8–C.10 as functions of not only $\kappa_{\omega,k}$, but $\beta_{\omega,k}$ as well. From the forms of Eqs. C.8–C.10, it is apparent that any influence of $\beta_{\omega,k}$ is negligible for short path length, L, but increases with the pressure path length (defined as the product $P_k\, L$). The gray-formulated trans-

missivity, given via Eq. C.15 (and influenced by Eqs. C.4 and C.12), contains no information on $\beta_{\omega,k}$ and therefore fails to correctly model this behavior. Note that $\beta_{\omega,k}$ is defined only for gas-phase species, and thus discrepancy (1) is negligible for media where the principal participating species is soot.

The second discrepancy (2) is due to an erroneous reversal of mathematical operations used to evaluate the gray-formulated $\tilde{\tau}$. In the narrow-band formulation, τ_ω is determined directly from $\kappa_{\omega,k}$ via Eqs. C.7–C.11. The narrow-band $\bar{\tau}$ is then evaluated by integrating τ_ω over the spectrum via Eq. C.5. The order of operations for the narrow-band $\bar{\tau}$ is then $\int f(\kappa_\omega)\, d\omega$. In the gray formulation, $\bar{\kappa}_P$ is defined by integrating $\kappa_{\omega,k}$ over the spectrum via Eq. C.4. The gray-formulated $\tilde{\tau}$ is then determined from $\bar{\kappa}_P$ via Eqs. C.12 and C.15. The order of operations for the gray-formulated $\tilde{\tau}$ is then $f\left(\int \kappa_\omega\, d\omega\right)$. In general, $\int f(\kappa_\omega)\, d\omega \neq f\left(\int \kappa_\omega\, d\omega\right)$, where equality is satisfied only for certain functions and integration domains.

The third discrepancy (3) results from the temperature dependence of the Planck distribution, B_ω, which is used as a weighting function for spectral integrations in both formulations. In the narrow-band formulation, $\bar{\tau}$ is determined via Eq. C.5 as a weighted spectral average of τ_ω, where B_ω is evaluated at the background blackbody temperature, T_B. As used in the gray formulation, $\bar{\kappa}_P$ is determined via Eq. C.4 as a weighted spectral average of $\kappa_{\omega,k}$, where B_ω is evaluated at the layer temperature, T_l. Because the shape of the Planck distribution varies significantly with temperature (see Fig. C.1), any discrepancy between T_l and T_B can cause significant inaccuracy in the gray formulation, where $\bar{\kappa}_P$ is then skewed by the offset shape of B_ω.

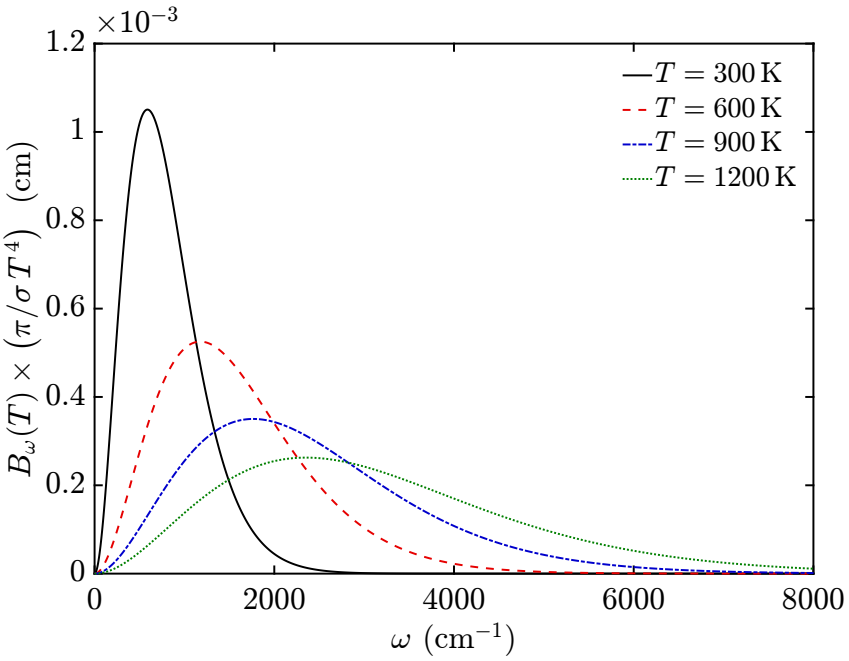

Figure C.1: Normalized Planck distribution (B_ω) evaluated at selected temperatures and plotted versus wavenumber (ω).

The fourth discrepancy (4) arises from the gray formulation's direct use of Kirchhoff's law in the evaluation of the total emissivity. By Eqs. C.15 and C.16, $\tilde{\tau}$ and $\tilde{\varepsilon}$ are related via $\tilde{\tau} + \tilde{\varepsilon} = 1$. Kirchhoff's law, which dictates that the spectral absorptivity, α_ω, and emissivity, ε_ω, of a medium be equal, generally applies only discretely to monochromatic radiation, but extends to the full spectrum for media or objects that exhibit blackbody behavior. It is also valid that if the reflectivity of a medium is negligible, radiation that is not absorbed, must be transmitted, yielding $\alpha_\omega + \tau_\omega = 1$. But from Kirchhoff's law, $\alpha_\omega = \varepsilon_\omega$, and therefore $\tau_\omega + \varepsilon_\omega = 1$. This result is valid for individual spectral lines, but is generally invalid when extended across the full spectrum. This discrepancy can lead to inconsistencies between the gray-formulated $\tilde{\tau}$ and $\tilde{\varepsilon}$ (unless the medium exhibits blackbody behavior).

Discrepancies (1) through (4) are a direct result of the simplifying assumptions inherent to the gray formulation. The primary advantage of the gray formulation is that it neglects spectral variations in the computed quantities and requires only a single calculation to cover the entire spectrum. This is accomplished by modeling all spectral information within $\bar{\kappa}_P$, which is defined solely via local properties of the medium and is independent of path length and boundary conditions. While their effects may be minimized by limiting use of the gray formulation to certain scenarios, these discrepancies cannot be fundamentally corrected without also crippling the computational advantages that they afford.

C.5 Formulation Performance

The present analysis considers one-dimensional radiative transfer through a single homogeneous gas layer for varying property scenarios. The considered scenarios include variation of the spectral domain over which computations are performed, variation of the path length and thus optical depth of the layer, and alternation between a scenario involving dominance of gas-layer emission relative to background radiation (low T_B, high T_l) and dominance of gas-layer absorption (high T_B, low T_l).

The spectral domains considered include 1400–1600 cm^{-1}, 1200–2200 cm^{-1}, 1000–4500 cm^{-1}, and 50–10000 cm^{-1}. Path lengths range from 0.5–50 cm. For the scenario involving layer emission dominance (scenario 1), the background and layer temperatures are respectively 300 K and 800 K, while for the scenario involving layer absorption dominance (scenario 2), respective temperatures are 800 K and 300 K.

Calculations for each scenario are conducted within four principal test cases, each investigating a different radiative species. Differentiation between these cases is meant to clearly identify the previously defined formulation discrepancies as well as quantify their effects on the computed radiative properties.

Case 1 considers a modified (hypothetical) soot species for which both $\kappa_{\omega,k}$ and $\tau_{\omega,k}$ are constant across the spectrum. Case 2 considers a modified (hypothetical) water-vapor species for which $\kappa_{\omega,k}$ is constant, while $\tau_{\omega,k}$ varies non-linearly across the spectrum. Case 3 considers soot, for which $\kappa_{\omega,k}$ varies linearly, while $\tau_{\omega,k}$ varies non-linearly across the spectrum. Finally, case 4 considers water-vapor, for which $\kappa_{\omega,k}$ and $\tau_{\omega,k}$ both vary sharply and non-linearly across the spectrum.

All cases consider a homogeneous gas layer at atmospheric pressure. Layer composition for cases 1 and 3 comprises respective mole fractions of N_2 and O_2 of 0.80 and 0.20, with a soot volume fraction of 1 ppm. Layer composition for cases 2 and 4 comprises respective mole fractions of N_2, O_2, and H_2O of 0.75, 0.20, and 0.05. In all cases, the excess N_2 and O_2 act as an inert background and do not participate in the radiation transfer (but are important for collision broadening effects).

Results for case 1 are presented in Fig. C.2, representing a trivial condition for which $\kappa_{\omega,k}$ and $\tau_{\omega,k}$ are both invariant across the full spectrum. As a result, the narrow-band and gray formulations reduce to mathematically equivalent forms and all four of the previously noted formulation discrepancies do not apply. This is illustrated in Fig. C.2, which shows that the narrow-band and gray-formulated end-path intensities, transmissivities, and emissivities respectively agree across all computed conditions, in agreement with expectations.

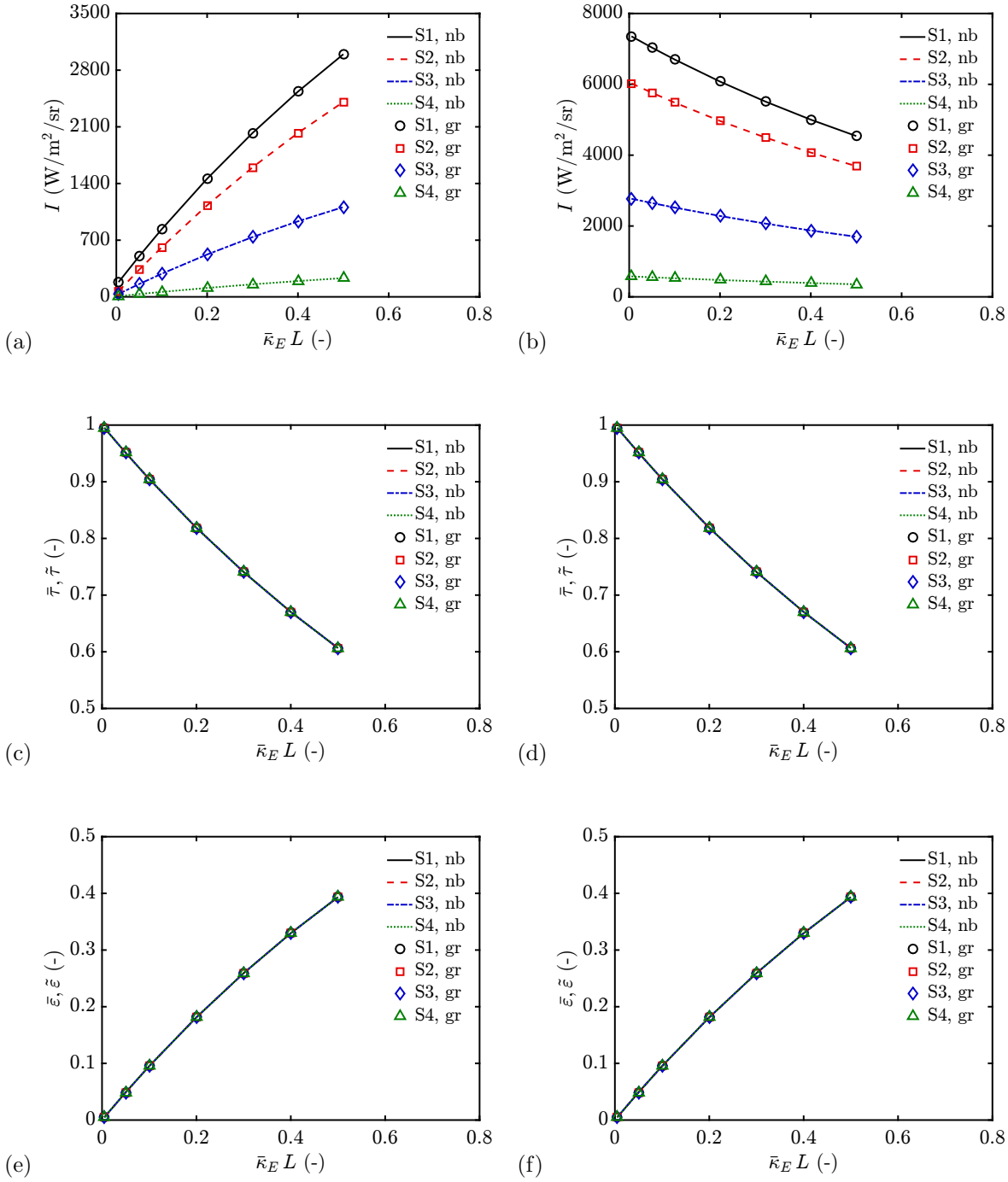

Figure C.2: Case 1 comparison of narrow-band (nb) and gray (gr) formulated end-path intensity (I), transmissivity (τ), and emissivity (ε) for layer emission dominance (scenario 1) or layer absorption dominance (scenario 2), plotted versus effective optical depth ($\bar{\kappa}_E L$); S1: 50–10000 cm^{-1}, S2: 1000–4500 cm^{-1}, S3: 1200–2200 cm^{-1}, S4: 1400–1600 cm^{-1}; (a) I, scenario 1, (b) I, scenario 2, (c) τ, scenario 1, (d) τ, scenario 2, (e) ε, scenario 1, (f) ε, scenario 2.

Results in Figs. C.2(c)-(f) show that $\bar{\varepsilon}$ and $\bar{\tau}$ are independent of the width of the spectral domain over which they are computed. In addition, $\bar{\varepsilon}$ and $\bar{\tau}$ computed for scenario 1 are equivalent to those for scenario 2, indicating no variation of behavior with dominance of absorption or emission within the layer. These observations are consistent with $\kappa_{\omega,k}$ being invariant across the spectrum. Intuitively, $\bar{\tau}$ decreases and $\bar{\varepsilon}$ increases, both with increasing optical depth of the layer.

The observed variations in the computed end-path intensities with changing spectral domain, as shown in Figs. C.2(a)-(b), are also expected. These differences occur because, as the width of the computed spectrum increases, the energy contained within that spectrum must also increase. Supporting this explanation, plotted intensities increase with increasing width of the computed spectrum.

For scenario 1 results, end-path intensities increase with increasing optical depth of the layer, due to the dominance of emission within the layer, where a thicker layer yields greater emission. For scenario 2, end-path intensities decrease with increasing optical depth of the layer due to the dominance of absorption within the layer, where a thicker layer yields greater absorption of the background radiation.

Results for case 2 are presented in Fig. C.3, representing a more complex condition then case 1, where $\kappa_{\omega,k}$ remains constant across the spectrum, but $\tau_{\omega,k}$ does not. This results from the dependence of $\tau_{\omega,k}$ on $\beta_{\omega,k}$, which also varies across the spectrum due to Doppler broadening effects. Results for case 2 highlight the effects of discrepancy (1) when comparing the narrow-band and gray-formulated results. As in case 1, because $\kappa_{\omega,k}$ is constant across the spectrum, discrepancies (2), (3), and (4) do not apply.

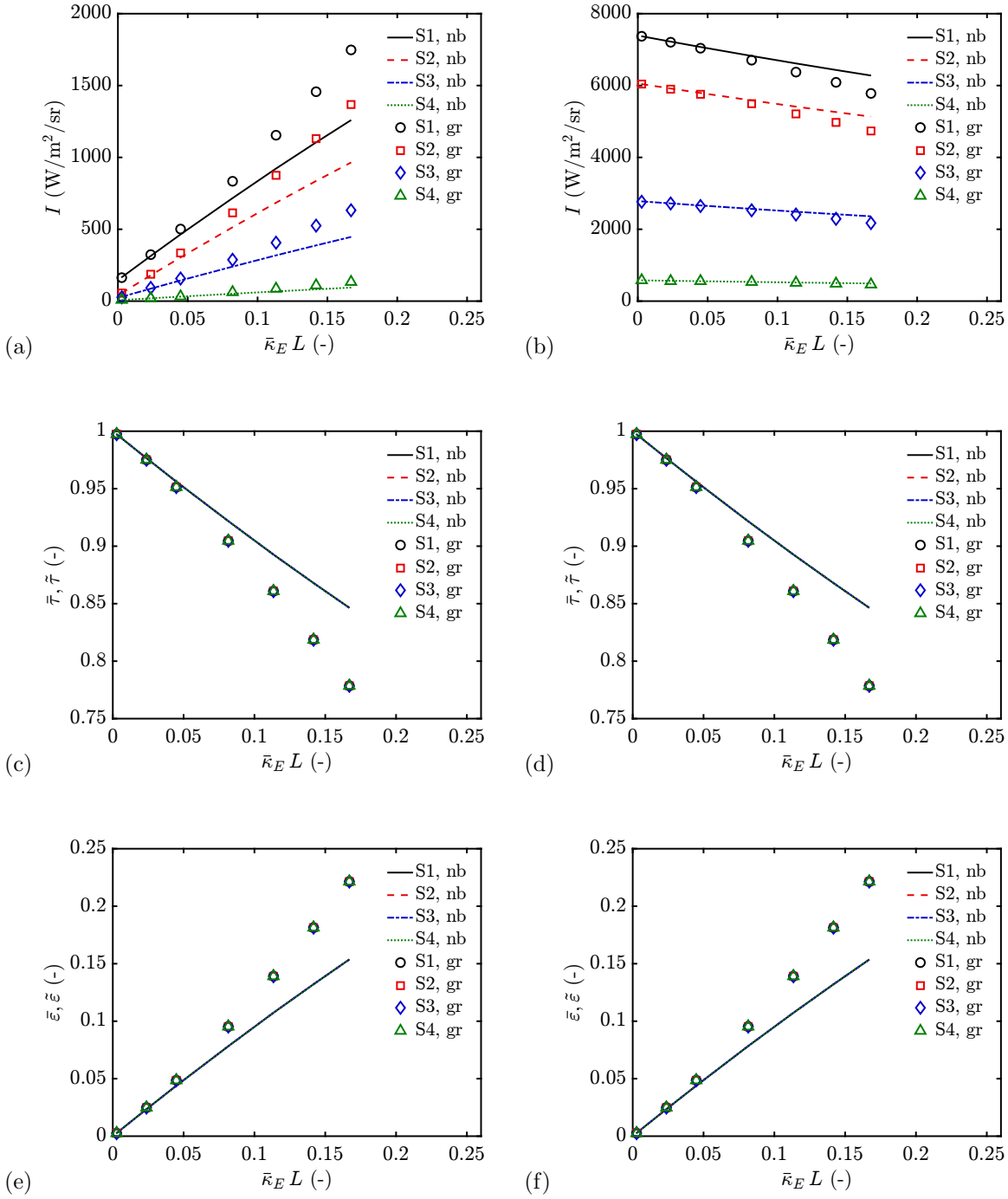

Figure C.3: Case 2 comparison of narrow-band (nb) and gray (gr) formulated end-path intensity (I), transmissivity (τ), and emissivity (ε) for layer emission dominance (scenario 1) or layer absorption dominance (scenario 2), plotted versus effective optical depth ($\bar{\kappa}_E L$); S1: 50–10000 cm^{-1}, S2: 1000–4500 cm^{-1}, S3: 1200–2200 cm^{-1}, S4: 1400–1600 cm^{-1}; (a) I, scenario 1, (b) I, scenario 2, (c) τ, scenario 1, (d) τ, scenario 2, (e) ε, scenario 1, (f) ε, scenario 2.

For case 2, $\tau_{\omega,k}$ is modeled via Eq. C.9, from which it is apparent that the asymptotic behavior follows $-\ln(\tau_{\omega,k}) \approx \kappa_{\omega,k} P_k L$ for short pressure paths and $-\ln(\tau_{\omega,k}) \approx \sqrt{4\beta_{\omega,k}\kappa_{\omega,k} P_k L}$ for long pressure paths. From Eq. C.15, it is apparent that the gray formulation assumes the short pressure path asymptotic behavior independent of the actual path length. Matching the results shown in Fig. C.3, it is expected that the gray results initially agree with the narrow-band results for short pressure paths, then deviate with increasing path length.

Despite the observed deviations between the narrow-band and gray-formulated results, general trends in the computed quantities are in agreement with those noted for case 1. Considering the deviations, end-path intensities are consistently over-predicted by the gray formulation for scenario 1 (emission dominance) and under-predicted for scenario 2 (absorption dominance). Independent of the scenario, $\tilde{\tau}$ are consistently under-predicted by the gray formulation, while $\tilde{\varepsilon}$ are consistently over-predicted. Computed transmissivities and emissivities for both formulations are independent of the bounds of the computed spectrum, and are equivalent between scenarios 1 and 2. These results are consistent with those reported for case 1 and are again the direct result of $\kappa_{\omega,k}$ being invariant across the spectrum.

Results for case 3 are presented in Fig. C.4, representing a more complex condition for which $\kappa_{\omega,k}$ varies linearly across the spectrum. From Eq. C.7 (which is here applicable because the layer contains only soot), $\tau_{\omega,k}$ varies as the exponential of $\kappa_{\omega,k}$. Because $\tau_{\omega,k}$ is here defined by blackbody behavior, and not a statistical narrow-band model, discrepancies (1) and (4) do not apply to this case. Still, because of the noted spectral variations in $\kappa_{\omega,k}$, discrepancies (2) and (3) are present.

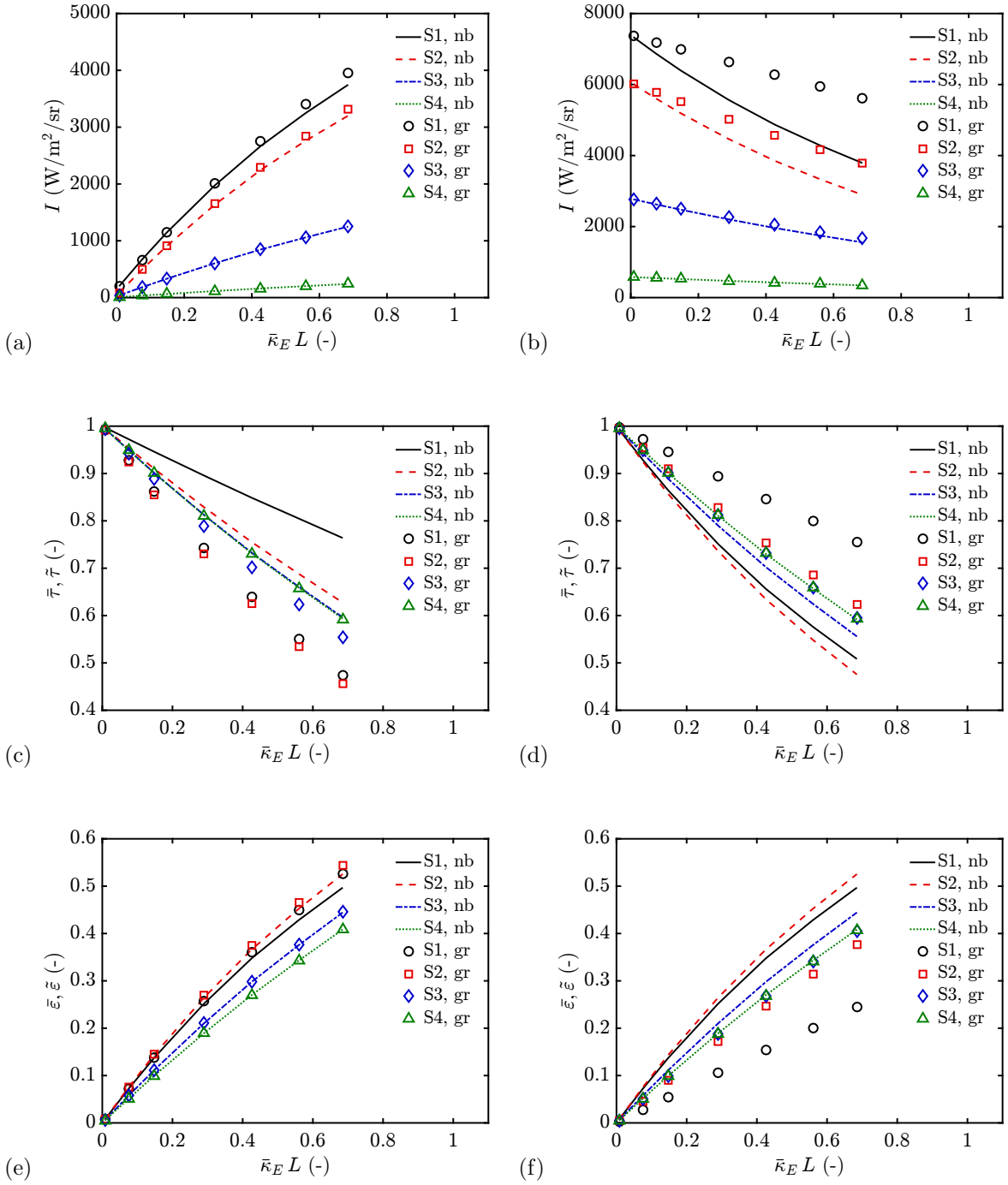

Figure C.4: Case 3 comparison of narrow-band (nb) and gray (gr) formulated end-path intensity (I), transmissivity (τ), and emissivity (ε) for layer emission dominance (scenario 1) or layer absorption dominance (scenario 2), plotted versus effective optical depth ($\bar{\kappa}_E L$); S1: 50–10000 cm^{-1}, S2: 1000–4500 cm^{-1}, S3: 1200–2200 cm^{-1}, S4: 1400–1600 cm^{-1}; (a) I, scenario 1, (b) I, scenario 2, (c) τ, scenario 1, (d) τ, scenario 2, (e) ε, scenario 1, (f) ε, scenario 2.

As shown in Fig. C.4, general trends in the computed quantities are in agreement with those observed in the preceding cases. Additional deviations between the narrow-band and gray results generally increase with both increasing width of the computed spectrum and with increasing optical depth, consistent with errors that result from discrepancies (2) and (3).

While the narrow-band formulation resolves spectral variations in κ_ω, the gray formulation does not. Rather, the gray formulation assumes that a constant, mean value of $\tilde{\kappa}_P$ applies over each computed spectrum. While it is generally the case that there exists an effective mean value, $\bar{\kappa}_E$, that accurately models spectral variations in κ_ω, such a value cannot be accurately computed while retaining the simplifying assumptions of the gray formulation. Certainly, $\tilde{\kappa}_P$ deviates from $\bar{\kappa}_E$ due to discrepancies (2) and (3). Agreement between $\tilde{\kappa}_P$ (or any other mean value of κ_ω) and $\bar{\kappa}_E$ generally deteriorates as the width of the computed spectrum increases. In addition, any effect of such a disagreement on computed results is amplified as the path length is increased. These rules match the trends depicted in Fig. C.4.

As shown in Fig. C.4(a), end-path intensities are well approximated with the gray formulation for scenario 1, whereas from Fig. C.4(b), end-path intensities are approximated comparably poorly for scenario 2. From Figs. C.4(e) and (f), an analogous observation is obtained from the emissivity results. Contrastingly, from Figs. C.4(c) and (d), transmissivities are approximated poorly for both scenarios.

These observations are a direct result of discrepancy (3), where the only change between scenarios 1 and 2 are the layer and background temperatures. In particular, the emission spectrum of the gas layer is well represented by $\tilde{\kappa}_P$, which assumes

blackbody behavior evaluated at the layer temperature. Comparatively, the absorption spectrum of the gas layer is poorly represented by $\tilde{\kappa}_P$, because the appropriate absorption spectrum depends not on the layer temperature, but on the layer boundary condition, which is typically unavailable when $\tilde{\kappa}_P$ is determined. The net effect of this result is that $\tilde{\kappa}_P$ always favors accuracy of emission over absorption, in particular for layers that exhibit blackbody behavior. Caution should thus necessarily be taken when attempting to employ a $\tilde{\kappa}_P$ based gray formulation to model a configuration involving primarily absorption of external radiation.

The observation that $\tilde{\tau}$ results poorly match the narrow-band solutions for both scenarios is supported by the notion that $\tilde{\kappa}_P$ poorly represents absorption behavior. Contrarily, $\tilde{\varepsilon}$ are well matched for scenario 1 (layer emission dominance) because $\tilde{\kappa}_P$ represents emission behavior well. The poorly matched $\tilde{\varepsilon}$ results for scenario 2 (layer absorption dominance) are then also due to the dominance of background radiation, which is not well represented by $\tilde{\kappa}_P$.

Shown in Figs. C.4(c) and (d), $\tilde{\tau}$ under-predict the narrow-band solutions for scenario 1 ($T_l > T_B$) and over-predict them for scenario 2 ($T_l < T_B$), consistent with the temperature differences in each scenario. Careful comparison of Figs. C.4(c) and (d) also suggests that, were $\bar{\kappa}_P$ to be evaluated at T_B instead of T_l (see Eq. C.4), $\tilde{\tau}$ would more accurately match the narrow-band solutions. Such a convention cannot generally be employed however, because boundary-incident radiation at an arbitrary location within a medium cannot typically be known prior to solution of the RTE.

Results for case 4 are presented in Fig. C.5, representing the most complex of the presently considered cases.

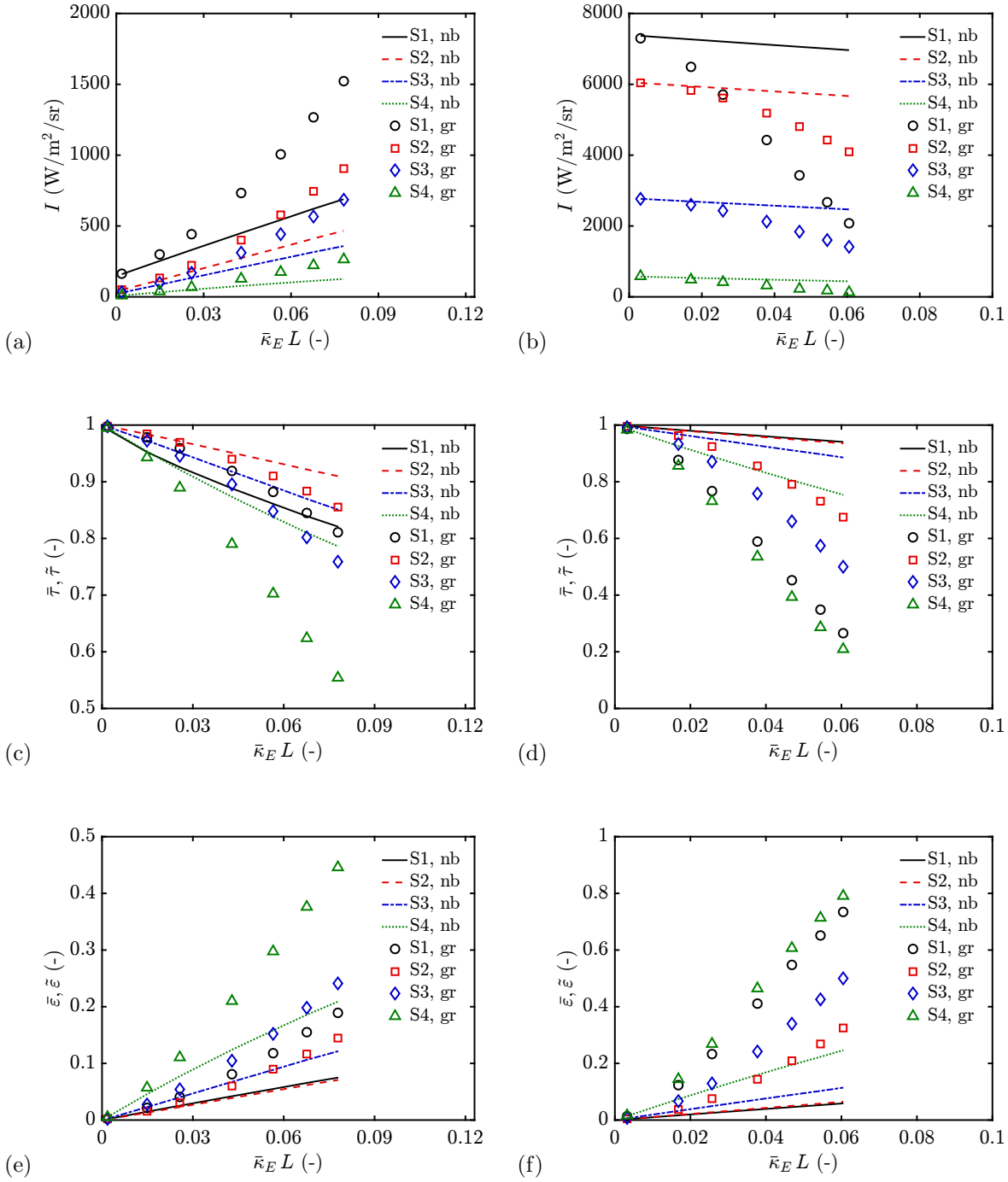

Figure C.5: Case 4 comparison of narrow-band (nb) and gray (gr) formulated end-path intensity (I), transmissivity (τ), and emissivity (ε) for layer emission dominance (scenario 1) or layer absorption dominance (scenario 2), plotted versus effective optical depth ($\bar{\kappa}_E L$); S1: 50–10000 cm^{-1}, S2: 1000–4500 cm^{-1}, S3: 1200–2200 cm^{-1}, S4: 1400–1600 cm^{-1}; (a) I, scenario 1, (b) I, scenario 2, (c) τ, scenario 1, (d) τ, scenario 2, (e) ε, scenario 1, (f) ε, scenario 2.

For case 4, $\kappa_{\omega,k}$ and $\tau_{\omega,k}$ both vary sharply, non-monotonically, and non-linearly across the spectrum. As a result, all four of the previously described formulation discrepancies apply and compound on one another. From the plotted results (see Fig. C.5), agreement between the narrow-band and gray formulations is found only at low optical depth. Also shown, agreement is not necessarily improved with narrowing of the computed spectrum. General trends in the computed quantities agree with the preceding cases, but with significantly increased discrepancy between the narrow-band and gray formulations. Certainly, for conditions dominated by the spectral characteristics of a radiative species such as water vapor, the gray formulation should be employed only for clearly optically thin conditions.

The preceding analysis highlights the effects that the aforementioned formulation discrepancies (see Sec. C.4) can have on radiative transfer computations in a range of conditions. While the narrow-band formulation provides more accurate results in all scenarios, there are situations for which the gray formulation may be appropriate. As the gray formulation offers significant advantages in terms of simplicity and computational cost, there are clear motivations toward its use in place of a more resolved or more accurate radiation model. Based on the present results, the gray formulation should be reliably implemented only in cases where (1) the dominant participating radiative species exhibit principally blackbody behavior, (2) the dominant role of the medium is to emit rather than absorb radiation, and most importantly (3) the optical depth (path length) through the medium is sufficiently low. Actual deviations between gray-formulated results and the correct behavior will depend on the specific scenario being modeled.

Bibliography

[1] NFPA 13, Standard for the installation of sprinkler systems, NFPA, www.nfpa.org (2016).

[2] NFPA 750, Standard on water mist fire protection systems, NFPA, www.nfpa.org (2015).

[3] NFPA 2001, Standard on clean agent fire extinguishing systems, NFPA, www.nfpa.org (2015).

[4] Fire Dynamics Simulator, NIST, http://firemodels.github.io/fds-smv/ (2016).

[5] FireFOAM, FM Global, https://github.com/fireFoam-dev (2016).

[6] OpenFOAM, OpenFOAM Foundation, www.openfoam.org (2016).

[7] G. Grant, J. Brenton, D. Drysdale, Fire suppression by water sprays, Progress in Energy and Combustion Science 26 (2) (2000) 79–130.

[8] H.-Z. Yu, J. S. Newman, Theory of fire extinguishment, in: A. E. Cote (Ed.), NFPA Fire Protection Handbook, 20th Edition, National Fire Protection Association, 2008, pp. 79–92.

[9] P. E. Santangelo, P. Tartarini, Fire control and suppression by water-mist systems, Open Thermodynamics Journal 4 (4) (2010) 167–184.

[10] J. R. Mawhinney, B. Z. Dlugogorski, A. K. Kim, A closer look at the fire extinguishing properties of water mist, in: Fire Safety Science–Proceedings of the Fourth International Symposium, IAFSS, 1994, pp. 47–60.

[11] B. Downie, C. Polymeropoulos, G. Gogos, Interaction of a water mist with a buoyant methane diffusion flame, Fire Safety Journal 24 (4) (1995) 359–381.

[12] J. Suh, A. Atreya, The effect of water vapor on counterflow diffusion flames, in: International Conference on Fire Research and Engineering, NIST, 1995, pp. 103–108.

[13] C. C. Ndubizu, R. Ananth, P. A. Tatem, V. Motevalli, On water mist fire suppression mechanisms in a gaseous diffusion flame, Fire Safety Journal 31 (3) (1998) 253–276.

[14] B. Yao, W. Fan, G. Liao, Interaction of water mists with a diffusion flame in a confined space, Fire Safety Journal 33 (2) (1999) 129–139.

[15] A. Atreya, T. Crompton, J. Suh, A study of the chemical and physical mechanisms of fire suppression by water, in: Fire Safety Science–Proceedings of the Sixth International Symposium, IAFSS, 2000, pp. 493–504.

[16] S. C. Kim, H. S. Ryou, An experimental and numerical study on fire suppression using a water mist in an enclosure, Building and Environment 38 (11) (2003) 1309–1316.

[17] B. T. Fisher, A. R. Awtry, R. S. Sheinson, J. W. Fleming, Flow behavior impact on the suppression effectiveness of sub-10-μm water drops in propane/air co-flow non-premixed flames, Proceedings of the Combustion Institute 31 (2) (2007) 2731–2739.

[18] R. F. Simmons, H. G. Wolfhard, Some limiting oxygen concentrations for diffusion flames in air diluted with nitrogen, Combustion and Flame 1 (2) (1957) 155–161.

[19] R. Hirst, K. Booth, Measurement of flame-extinguishing concentrations, Fire Technology 13 (4) (1977) 296–315.

[20] S. Ishizuka, H. Tsuji, An experimental study of effect of inert gases on extinction of laminar diffusion flames, Proceedings of the Combustion Institute 18 (1) (1981) 695–703.

[21] I. K. Puri, K. Seshadri, Extinction of diffusion flames burning diluted methane and diluted propane in diluted air, Combustion and Flame 65 (2) (1986) 137–150.

[22] A. Hamins, G. Gmurczyk, W. Grosshandler, R. G. Rehwoldt, I. Vazquez, T. Cleary, C. Presser, K. Seshadri, Flame suppression effectiveness, Tech. Rep. SP861, NIST (1994).

[23] E. A. Ural, Measurement of the extinguishing concentration of gaseous fuels using the cup-burner apparatus, in: Halon Options Technical Working Conference, NMERI, 1999, pp. 275–283.

[24] M. Babb, S. R. Gollahalli, C. M. Sliepcevich, Extinguishment of liquid heptane and gaseous propane diffusion flames, Journal of Propulsion and Power 15 (2) (1999) 260–265.

[25] W. M. Pitts, R. A. Bryant, J. C. Yang, Thermal agent extinguishment of two types of diffusion flames, in: Proceedings of the Second Joint Meeting of the US Sections of the Combustion Institute, CI, 2001, pp. 1–16.

[26] F. Takahashi, G. T. Linteris, V. R. Katta, Flame extinguishment in a cup-burner apparatus, in: Proceedings of the Fourth Joint Meeting of the US Sections of the Combustion Institute, CI, 2005, pp. 1–6.

[27] F. Takahashi, G. T. Linteris, V. R. Katta, Extinguishment mechanisms of coflow diffusion flames in a cup-burner apparatus, Proceedings of the Combustion Institute 31 (2) (2007) 2721–2729.

[28] J. Min, F. Baillot, H. Guo, E. Domingues, M. Talbaut, B. Patte-Rouland, Impact of CO_2, N_2 or Ar diluted in air on the length and lifting behavior of a laminar diffusion flame, Proceedings of the Combustion Institute 33 (1) (2011) 1071–1078.

[29] F. Takahashi, V. R. Katta, G. T. Linteris, O. C. Meier, Cup-burner flame structure and extinguishment by CF_3Br and C_2HF_5 in microgravity, Proceedings of the Combustion Institute 34 (2) (2013) 2707–2717.

[30] M. L. Robin, T. F. Rowland, Development of a standard cup-burner apparatus: NFPA and ISO standard methods, in: Halon Options Technical Working Conference, NMERI, 1999, pp. 284–292.

[31] F. Takahashi, W. J. Schmoll, Lifting criteria of jet diffusion flames, Proceedings of the Combustion Institute 23 (1) (1991) 677–683.

[32] R. Azzoni, S. Ratti, S. K. Aggarwal, I. K. Puri, The structure of triple flames stabilized on a slot burner, Combustion and Flame 119 (1) (1999) 23–40.

[33] A. Lock, A. M. Briones, S. K. Aggarwal, I. K. Puri, U. Hegde, Liftoff and extinction characteristics of fuel- and air-stream-diluted methane–air flames, Combustion and Flame 149 (4) (2007) 340–352.

[34] A. Wyzgolik, F. Baillot, Response of the non-premixed lifted flame to coaxial jet mixing layers, Proceedings of the Combustion Institute 31 (1) (2007) 1583–1590.

[35] J. Min, F. Baillot, Experimental investigation of the flame extinction processes of nonpremixed methane flames inside an air coflow diluted with CO_2, N_2, or Ar, Combustion and Flame 159 (12) (2012) 3502–3517.

[36] B. H. Chao, C. K. Law, J. S. T'ien, Structure and extinction of diffusion flames with flame radiation, Proceedings of the Combustion Institute 23 (1) (1991) 523–531.

[37] J. Du, R. L. Axelbaum, The effects of flame structure on extinction of CH_4-O_2-N_2 diffusion flames, Proceedings of the Combustion Institute 26 (1) (1996) 1137–1142.

[38] S. H. Chan, J. Q. Yin, B. J. Shi, Structure and extinction of methane-air flamelet with radiation and detailed chemical kinetic mechanism, Combustion and Flame 112 (3) (1998) 445–456.

[39] J. L. Rhatigan, H. Bedir, J. S. T'ien, Gas-phase radiative effects on the burning and extinction of a solid fuel, Combustion and Flame 112 (1) (1998) 231–241.

[40] R. Chen, R. L. Axelbaum, Scalar dissipation rate at extinction and the effects of oxygen-enriched combustion, Combustion and Flame 142 (1) (2005) 62–71.

[41] K. J. Santa, B.-H. Chao, P. B. Sunderland, D. L. Urban, D. P. Stocker, R. L. Axelbaum, Radiative extinction of gaseous spherical diffusion flames in microgravity, Combustion and Flame 151 (4) (2007) 665–675.

[42] P. Narayanan, A. Trouvé, Radiation-driven flame weakening effects in sooting turbulent diffusion flames, Proceedings of the Combustion Institute 32 (1) (2009) 1481–1489.

[43] P. Narayanan, H. R. Baum, A. Trouvé, Effect of soot addition on extinction limits of luminous laminar counterflow diffusion flames, Proceedings of the Combustion Institute 33 (2) (2011) 2539–2546.

[44] P. G. Arias, H. G. Im, P. Narayanan, A. Trouvé, A computational study of non-premixed flame extinction by water spray, Proceedings of the Combustion Institute 33 (2) (2011) 2591–2597.

[45] V. Lecoustre, P. Narayanan, H. R. Baum, A. Trouvé, Local extinction of diffusion flames in fires, in: Fire Safety Science–Proceedings of the Tenth International Symposium, IAFSS, 2011, pp. 583–595.

[46] V. R. Lecoustre, P. G. Arias, S. P. Roy, Z. Luo, D. C. Haworth, H. G. Im, T. F. Lu, A. Trouvé, Direct numerical simulations of non-premixed ethylene–air flames: Local flame extinction criterion, Combustion and Flame 161 (11) (2014) 2933–2950.

[47] K. Prasad, C. Li, K. Kailasanath, C. C. Ndubizu, R. Ananth, P. A. Tatem, Numerical modeling of water mist suppression of methane-air diffusion flames, Combustion Science and Technology 132 (1998) 325–364.

[48] A. M. Lentati, H. K. Chelliah, Dynamics of water droplets in a counterflow field and their effect on flame extinction, Combustion and Flame 115 (1) (1998) 158–179.

[49] A. M. Lentati, H. K. Chelliah, Physical, thermal, and chemical effects of fine-water droplets in extinguishing counterflow diffusion flames, Proceedings of the Combustion Institute 27 (2) (1998) 2839–2846.

[50] K. Prasad, C. Li, K. Kailasanath, Simulation of water mist suppression of small scale methanol liquid pool fires, Fire Safety Journal 33 (3) (1999) 185–212.

[51] A. K. Lazzarini, R. H. Krauss, H. K. Chelliah, G. T. Linteris, Extinction conditions of non-premixed flames with fine droplets of water and water/NaOH solutions, Proceedings of the Combustion Institute 28 (2) (2000) 2939–2945.

[52] G. O. Thomas, The quenching of laminar methane-air flames by water mists, Combustion and Flame 130 (1) (2002) 147–160.

[53] R. Ananth, R. C. Mowrey, Ultra-fine water mist extinction dynamics of a co-flow diffusion flame, Combustion Science and Technology 180 (9) (2008) 1659–1692.

[54] A. Yoshida, T. Uendo, R. Takasaki, H. Naito, Y. Saso, Water droplets behavior in extinguishing methane-air counterflow diffusion flames, in: Fire Safety Science–Proceedings of the Tenth International Symposium, IAFSS, 2011, pp. 569–582.

[55] I. Sakurai, J. Suzuki, Y. Kotani, H. Naito, A. Yoshida, Extinguishment of propane/air co-flowing diffusion flames by fine water droplets, Proceedings of the Combustion Institute 34 (2) (2013) 2727–2734.

[56] A. Yoshida, K. Kashiwa, S. Hashizume, H. Naito, Inhibition of counterflow methane/air diffusion flame by water mist with varying mist diameter, Fire Safety Journal 71 (2015) 217–225.

[57] E. Blanchard, S. Desanghere, P. Boulet, Quantification of energy balance during fire suppression by water mist in a mid-scale test tunnel, in: Fire Safety Science–Proceedings of the Tenth International Symposium, IAFSS, 2011, pp. 119–132.

[58] A. Jenft, A. Collin, P. Boulet, G. Pianet, A. Breton, A. Muller, Experimental and numerical study of pool fire suppression using water mist, Fire Safety Journal 67 (2014) 1–12.

[59] Y. Xin, K. V. Meredith, Characterization of fire suppression of an idealized commodity using uniform water fluxes, in: Fire Safety Science–Proceedings of the Eleventh International Symposium, IAFSS, 2014, pp. 1208–1221.

[60] Y. Wang, K. V. Meredith, X. Zhou, P. Chatterjee, Y. Xin, M. Chaos, N. Ren, S. B. Dorofeev, Numerical simulation of sprinkler suppression of rack storage fires, in: Fire Safety Science–Proceedings of the Eleventh International Symposium, IAFSS, 2014, pp. 1170–1183.

[61] T. M. Jayaweera, H.-Z. Yu, Scaling of fire cooling by water mist under low drop Reynolds number conditions, Fire Safety Journal 43 (1) (2008) 63–70.

[62] H.-Z. Yu, Physical scaling of water mist suppression of wood crib fires in enclosures, in: Fire Safety Science–Proceedings of the Eleventh International Symposium, IAFSS, 2014, pp. 1222–1235.

[63] J. Vaari, J. Floyd, R. McDermott, CFD simulations on extinction of co-flow diffusion flames, in: Fire Safety Science–Proceedings of the Tenth International Symposium, IAFSS, 2011, pp. 781–793.

[64] S. Vilfayeau, N. Ren, Y. Wang, A. Trouvé, Numerical simulation of under ventilated liquid-fueled compartment fires with flame extinction and thermally-driven fuel evaporation, Proceedings of the Combustion Institute 35 (3) (2015) 2563–2571.

[65] S. Vilfayeau, Large eddy simulation of fire extinction phenomena, Ph.D. thesis, University of Maryland, College Park (2015).

[66] S. Vilfayeau, J. P. White, P. B. Sunderland, A. W. Marshall, A. C. Trouvé, Large eddy simulation of flame extinction in turbulent line fire exposed to air-nitrogen co-flow, Fire Safety Journal, submitted for publication.

[67] J. P. White, S. Vilfayeau, A. W. Marshall, A. C. Trouvé, R. J. McDermott, Modeling flame extinction and reignition in large eddy simulations with fast chemistry, Fire Safety Journal, submitted for publication.

[68] J. C. Hewson, A. R. Kerstein, Local extinction and reignition in nonpremixed turbulent $CO/H_2/N_2$ jet flames, Combustion Science and Technology 174 (5-6) (2002) 35–66.

[69] H. Pitsch, C. M. Cha, S. Fedotov, Flamelet modelling of non-premixed turbulent combustion with local extinction and re-ignition, Combustion Theory and Modelling 7 (2) (2003) 317–332.

[70] P. Sripakagorn, S. Mitarai, G. Kosály, H. Pitsch, Extinction and reignition in a diffusion flame: A direct numerical simulation study, Journal of Fluid Mechanics 518 (2004) 231–259.

[71] R. Venugopal, J. Abraham, A 2-D DNS investigation of extinction and reignition dynamics in nonpremixed flame–vortex interactions, Combustion and Flame 153 (3) (2008) 442–464.

[72] R. Venugopal, J. Abraham, Numerical investigations of reignition in vortex-perturbed n-heptane nonpremixed flames, AIAA Journal 46 (10) (2008) 2479–2497.

[73] R. Venugopal, J. Abraham, Numerical studies of vortex-induced extinction/reignition relevant to the near-field of high-Reynolds number jets, Physics of Fluids 21 (5) (2009) 1–11.

[74] Y. Hasemi, M. Nishihata, Fuel shape effect on the deterministic properties of turbulent diffusion flames, in: Fire Safety Science–Proceedings of the Second International Symposium, IAFSS, 1989, pp. 275–284.

[75] M. A. Delichatsios, Transition from momentum to buoyancy-controlled turbulent jet diffusion flames and flame height relationships, Combustion and Flame 92 (4) (1993) 349–364.

[76] R. J. Forstrom, E. M. Sparrow, Experiments on the buoyant plume above a heated horizontal wire, International Journal of Heat and Mass Transfer 10 (3) (1967) 321–331.

[77] R. G. Bill, B. Gebhart, The transition of plane plumes, International Journal of Heat and Mass Transfer 18 (4) (1975) 513–526.

[78] S. Kimura, A. Bejan, Mechanism for transition to turbulence in buoyant plume flow, International Journal of Heat and Mass Transfer 26 (10) (1983) 1515–1532.

[79] S. Wakitani, H. Yosinobu, Transition to turbulence in a plane plume above a horizontal heat source: Measurement of flow properties and flow visualization, Fluid Dynamics Research 2 (4) (1988) 243–259.

[80] K. Noto, K. Teramoto, T. Nakajima, Spectra and critical Grashof numbers for turbulent transition in a thermal plume, Journal of Thermophysics and Heat Transfer 13 (1) (1999) 82–90.

[81] X. Yao, A. W. Marshall, Quantitative salt-water modeling of fire-induced flow, Fire Safety Journal 41 (7) (2006) 497–508.

[82] G. Heskestad, Turbulent jet diffusion flames: Consolidation of flame height data, Combustion and Flame 118 (1) (1999) 51–60.

[83] L. I. Gaby, Hot-wire smoke streams for visualization of air flow patterns, Journal of Scientific Instruments 43 (5) (1966) 334.

[84] K. C. Adiga, R. F. Hatcher, R. S. Sheinson, F. W. Williams, S. Ayers, A computational and experimental study of ultra fine water mist as a total flooding agent, Fire Safety Journal 42 (2) (2007) 150–160.

[85] P. E. Santangelo, Characterization of high-pressure water-mist sprays: Experimental analysis of droplet size and dispersion, Experimental Thermal and Fluid Science 34 (8) (2010) 1353–1366.

[86] W. Wagner, A. Pruß, The IAPWS formulation 1995 for the thermodynamic properties of ordinary water substance for general and scientific use, Journal of Physical and Chemical Reference Data 31 (2) (2002) 387–535.

[87] E. E. Zukoski, B. M. Cetegen, T. Kubota, Visible structure of buoyant diffusion flames, Proceedings of the Combustion Institute 20 (1) (1985) 361–366.

[88] G. Heskestad, Peak gas velocities and flame heights of buoyancy-controlled turbulent diffusion flames, Proceedings of the Combustion Institute 18 (1) (1981) 951–960.

[89] G. Heskestad, Luminous heights of turbulent diffusion flames, Fire Safety Journal 5 (2) (1983) 103–108.

[90] B. S. Grove, J. G. Quintiere, Calculating entrainment and flame height in fire plumes of axisymmetric and infinite line geometries, Journal of Fire Protection Engineering 12 (3) (2002) 117–137.

[91] A. J. Giovanetti, D. P. Hoult, J. C. Keck, A. F. Sarofim, Flame luminosity and unburned hydrocarbon measurements in swirling combustion, Tech. Rep. 2295-80-1, MIT (1980).

[92] J. P. White, E. D. Link, A. C. Trouvé, P. B. Sunderland, A. W. Marshall, J. A. Sheffel, M. L. Corn, M. B. Colket, M. Chaos, H.-Z. Yu, Radiative emissions measurements from a buoyant, turbulent line flame under oxidizer-dilution quenching conditions, Fire Safety Journal 76 (2015) 74–84.

[93] G. Hankinson, B. J. Lowesmith, A consideration of methods of determining the radiative characteristics of jet fires, Combustion and Flame 159 (3) (2012) 1165–1177.

[94] G. H. Markstein, Radiative energy transfer from gaseous diffusion flames, Proceedings of the Combustion Institute 15 (1) (1975) 1285–1294.

[95] G. H. Markstein, Radiative energy transfer from turbulent diffusion flames, Combustion and Flame 27 (1976) 51–63.

[96] G. H. Markstein, Scaling of radiative characteristics of turbulent diffusion flames, Proceedings of the Combustion Institute 16 (1) (1977) 1407–1419.

[97] A. T. Modak, Thermal radiation from pool fires, Combustion and Flame 29 (1977) 177–192.

[98] G. H. Markstein, Relationship between smoke point and radiant emission from buoyant turbulent and laminar diffusion flames, Proceedings of the Combustion Institute 20 (1) (1985) 1055–1061.

[99] G. H. Markstein, J. De Ris, Wall-fire radiant emission. Part 1: Slot-burner flames, comparison with jet flames, Proceedings of the Combustion Institute 23 (1) (1991) 1685–1692.

[100] S. P. Fuss, A. Hamins, An estimate of the correction applied to radiant flame measurements due to attenuation by atmospheric CO_2 and H_2O, Fire Safety Journal 37 (2) (2002) 181–190.

[101] Y. Sivathanu, J. Gore, Total radiative heat loss in jet flames from single point radiative flux measurements, Combustion and Flame 94 (3) (1993) 265–270.

[102] V. Babrauskas, R. D. Peacock, Heat release rate: The single most important variable in fire hazard, Fire Safety Journal 18 (3) (1992) 255–272.

[103] K. D. Steckler, Estimation of rate of heat release by means of oxygen consumption measurements, in: D. R. Lide (Ed.), A Century of Excellence in Measurements, Standards, and Technology, CRC Press, 2001, pp. 280–282.

[104] J. R. Lawson, SFPE classic paper review: A review of classic work by Dr William J. Parker on heat release rate measurements by oxygen consumption, Journal of Fire Protection Engineering 22 (2012) 5–9.

[105] W. J. Parker, Calculations of the heat release rate by oxygen consumption for various applications, Journal of Fire Sciences 2 (5) (1984) 380–395.

[106] M. L. Janssens, Measuring rate of heat release by oxygen consumption, Fire Technology 27 (3) (1991) 234–249.

[107] B. Z. Dlugogorski, J. R. Mawhinney, V. Huu Duc, The measurement of heat release rates by oxygen consumption calorimetry in fires under suppression, in: Fire Safety Science–Proceedings of the Fourth International Symposium, IAFSS, 1994, pp. 877–888.

[108] A. Tewarson, Heat release rate in diffusion flames, Thermochimica Acta 278 (1996) 19–37.

[109] S. Brohez, C. Delvosalle, G. Marlair, A. Tewarson, Soot generation in fires: An important parameter for accurate calculation of heat release, in: Fire Safety Science–Proceedings of the Sixth International Symposium, IAFSS, 2000, pp. 265–276.

[110] S. Brohez, C. Delvosalle, G. Marlair, A. Tewarson, The measurement of heat release from oxygen consumption in sooty fires, Journal of Fire Sciences 18 (5) (2000) 327–353.

[111] H. Biteau, T. Steinhaus, C. Schemel, A. Simeoni, G. Marlair, N. Bal, J. L. Torero, Calculation methods for the heat release rate of materials of unknown composition, in: Fire Safety Science–Proceedings of the Ninth International Symposium, IAFSS, 2008, pp. 1165–1176.

[112] S. Brohez, C. Delvosalle, Carbon dioxide generation calorimetry–errors induced by the simplifying assumptions in the standard test methods, Fire and Materials 33 (2) (2009) 89–97.

[113] W. K. Chow, S. S. Han, Heat release rate calculation in oxygen consumption calorimetry, Applied Thermal Engineering 31 (2) (2011) 304–310.

[114] V. Babrauskas, Development of the cone calorimeter–a bench-scale heat release rate apparatus based on oxygen consumption, Fire and Materials 8 (2) (1984) 81–95.

[115] H. C. Tran, R. H. White, Burning rate of solid wood measured in a heat release rate calorimeter, Fire and Materials 16 (4) (1992) 197–206.

[116] S. Brohez, G. Marlair, C. Delvosalle, Fire calorimetry relying on the use of the fire propagation apparatus. Part I: Early learning from use in Europe, Fire and Materials 30 (2) (2006) 131–149.

[117] S. Brohez, G. Marlair, C. Delvosalle, Fire calorimetry relying on the use of the fire propagation apparatus. Part II: Burning characteristics of selected chemical substances under fuel rich conditions, Fire and Materials 30 (1) (2006) 35–50.

[118] H. Biteau, A. Fuentes, G. Marlair, S. Brohez, J. L. Torero, Ability of the fire propagation apparatus to characterise the heat release rate of energetic materials, Journal of Hazardous Materials 166 (2) (2009) 916–924.

[119] P. Ribière, S. Grugeon, M. Morcrette, S. Boyanov, S. Laruelle, G. Marlair, Investigation on the fire-induced hazards of Li-ion battery cells by fire calorimetry, Energy & Environmental Science 5 (2012) 5271–5280.

[120] C. Fourneau, C. Delvosalle, H. Breulet, S. Brohez, Characterization of highly under-ventilated fires using the cone calorimeter, Fire and Materials 40 (3) (2016) 434–444.

[121] J. S. Newman, C. Wieczorek, J. M. Troup, Application of building-scale calorimetry, in: Fire Safety Science–Proceedings of the Eighth International Symposium, IAFSS, 2005, pp. 1425–1434.

[122] S. C. Kim, M. Bundy, Numerical model of a large-scale oxygen consumption fire calorimeter, Journal of Thermal Analysis and Calorimetry 93 (3) (2008) 1013–1019.

[123] A. Hamins, E. Johnsson, M. Donnelly, A. Maranghides, Energy balance in a large compartment fire, Fire Safety Journal 43 (3) (2008) 180–188.

[124] P.-A. Santoni, F. Morandini, T. Barboni, Determination of fireline intensity by oxygen consumption calorimetry, Journal of Thermal Analysis and Calorimetry 104 (3) (2011) 1005–1015.

[125] Y. J. Ko, R. Michels, G. V. Hadjisophocleous, Instrumentation design for HRR measurements in a large-scale fire facility, Fire Technology 47 (4) (2011) 1047–1061.

[126] H. Pretrel, W. Le Saux, L. Audouin, Determination of the heat release rate of large scale hydrocarbon pool fires in ventilated compartments, Fire Safety Journal 62 (2013) 192–205.

[127] H. Pretrel, W. Le Saux, L. Audouin, Experimental determination of fire heat release rate with OC and CDG calorimetry for ventilated compartments fire scenario, Fire and Materials 38 (4) (2014) 474–506.

[128] ASTM E1354 - 15a, Standard test method for heat and visible smoke release rates for materials and products using an oxygen consumption calorimeter, ASTM International, www.astm.org (2015).

[129] ASTM E2058 - 13a, Standard test methods for measurement of material flammability using a fire propagation apparatus (FPA), ASTM International, www.astm.org (2013).

[130] ASTM E2067 - 15, Standard practice for full-scale oxygen consumption calorimetry fire tests, ASTM International, www.astm.org (2015).

[131] ISO 5660-1:2015, Reaction-to-fire tests – heat release, smoke production and mass loss rate – Part 1: Heat release rate (cone calorimeter method) and smoke production rate (dynamic measurement), ISO, www.iso.org (2015).

[132] J. Qin, B. Yao, W. K. Chow, Experimental study of suppressing cooking oil fire with water mist using a cone calorimeter, Hospitality Management 23 (5) (2004) 545–556.

[133] J. Qin, W. K. Chow, Bench-scale tests on PMMA fires with water mist, Polymer Testing 24 (1) (2005) 39–63.

[134] W. K. Chow, J. Qin, S. S. Han, Bench-scale tests on controlling plastic fires with water mists, Chemical Engineering & Technology 28 (9) (2005) 1041–1047.

[135] J. Qin, W. K. Chow, S. S. Han, Bench-scale studies on suppressing ghee fires with water mist, in: Fire Safety Science–Proceedings of the Tenth International Symposium, IAFSS, 2011, pp. 111–118.

[136] R. W. Yeager, Uncertainty analysis of energy release rate measurement for room fires, Journal of Fire Sciences 4 (4) (1986) 276–296.

[137] P. A. Enright, C. M. Fleischmann, Uncertainty of heat release rate calculation of the ISO 5660-1 cone calorimeter standard test method, Fire Technology 35 (2) (1999) 153–169.

[138] S. Brohez, Uncertainty analysis of heat release rate measurement from oxygen consumption calorimetry, Fire and Materials 29 (6) (2005) 383–394.

[139] R. A. Bryant, G. W. Mulholland, A guide to characterizing heat release rate measurement uncertainty for full-scale fire tests, Fire and Materials 32 (3) (2008) 121–139.

[140] J. P. White, E. D. Link, A. C. Trouvé, P. B. Sunderland, A. W. Marshall, A general calorimetry framework for measurement of combustion efficiency in a suppressed turbulent line fire, Fire Safety Journal, submitted for publication.

[141] J. F. Ogilvie, A Monte-Carlo approach to error propagation, Computers & Chemistry 8 (3) (1984) 205–207.

[142] C. Beyler, Flammability limits of premixed and diffusion flames, in: P. DiNenno (Ed.), SFPE Handbook of Fire Protection Engineering, 4th Edition, National Fire Protection Association, 2008, pp. 194–210.

[143] B. F. Magnussen, B. H. Hjertager, On mathematical modeling of turbulent combustion with special emphasis on soot formation and combustion, Proceedings of the Combustion Institute 16 (1) (1977) 719–729.

[144] T. Poinsot, D. Veynante, Theoretical and Numerical Combustion, 2nd Edition, RT Edwards, Inc., 2005.

[145] R. J. McDermott, J. E. Floyd, Enforcing realizability in explicit multicomponent species transport, Fire Safety Journal 78 (2015) 180–187.

[146] J. W. Deardorff, Stratocumulus-capped mixed layers derived from a three-dimensional model, Boundary-Layer Meteorology 18 (4) (1980) 495–527.

[147] J. Bardina, J. H. Ferziger, W. C. Reynolds, Improved subgrid-scale models for large-eddy simulation, in: 13th Fluid and Plasma Dynamics Conference, AIAA, 1980, pp. 1–10.

[148] S. Hostikka, K. B. McGrattan, A. Hamins, Numerical modeling of pool fires using LES and finite volume method for radiation, in: Fire Safety Science–Proceedings of the Seventh International Symposium, IAFSS, 2003, pp. 383–394.

[149] K. McGrattan, S. Hostikka, R. McDermott, J. Floyd, C. Weinschenk, K. Overholt, Fire Dynamics Simulator Technical Reference Guide Volume 1: Mathematical Model, 6th Edition, NIST, 2016.

[150] K. McGrattan, S. Hostikka, R. McDermott, J. Floyd, C. Weinschenk, K. Overholt, Fire Dynamics Simulator Technical Reference Guide Volume 2: Verification, 6th Edition, NIST, 2016.

[151] K. McGrattan, S. Hostikka, R. McDermott, J. Floyd, C. Weinschenk, K. Overholt, Fire Dynamics Simulator Technical Reference Guide Volume 3: Validation, 6th Edition, NIST, 2016.

[152] R. J. McDermott, K. B. McGrattan, J. E. Floyd, A simple reaction time scale for under-resolved fire dynamics, in: Fire Safety Science–Proceedings of the Tenth International Symposium, IAFSS, 2011, pp. 809–820.

[153] S. B. Pope, Turbulent Flows, Cambridge University Press, 2000.

[154] C. Robinson, D. B. Smith, The auto-ignition temperature of methane, Journal of Hazardous Materials 8 (3) (1984) 199–203.

[155] L.-M. Yuana, G. Cox, An experimental study of some line fires, Fire Safety Journal 27 (2) (1996) 123–139.

[156] S. B. Pope, Ten questions concerning the large-eddy simulation of turbulent flows, New Journal of Physics 6 (35) (2004) 1–24.

[157] K. C. Smyth, J. H. Miller, R. C. Dorfman, W. G. Mallard, R. J. Santoro, Soot inception in a methane/air diffusion flame as characterized by detailed species profiles, Combustion and Flame 62 (2) (1985) 157–181.

[158] J. Du, R. L. Axelbaum, The effect of flame structure on soot-particle inception in diffusion flames, Combustion and Flame 100 (3) (1995) 367–375.

[159] R. A. Dobbins, Soot inception temperature and the carbonization rate of precursor particles, Combustion and Flame 130 (3) (2002) 204–214.

[160] A. Hamins, K. Konishi, P. Borthwick, T. Kashiwagi, Global properties of gaseous pool fires, Proceedings of the Combustion Institute 26 (1) (1996) 1429–1436.

[161] G. Santo, M. A. Delichatsios, Effects of vitiated air on radiation and completeness of combustion in propane pool fires, Fire Safety Journal 7 (2) (1984) 159–164.

[162] J. H. Morehart, E. E. Zukoski, T. Kubota, Characteristics of large diffusion flames burning in a vitiated atmosphere, in: Fire Safety Science–Proceedings of the Third International Symposium, IAFSS, 1991, pp. 575–583.

[163] J. H. Morehart, E. E. Zukoski, T. Kubota, Chemical species produced in fires near the limit of flammability, Fire Safety Journal 19 (2) (1992) 177–188.

[164] Working group on measurement and computation of fire phenomena, IAFSS, http://www.iafss.org/macfp/ (2016).

[165] Measurement and computation of fire phenomena database, IAFSS, https://github.com/MaCFP/macfp-db (2016).

[166] W. M. Thornton, The relation of oxygen to the heat of combustion of organic compounds, Philosophical Magazine 33 (194) (1917) 196–203.

[167] C. Huggett, Estimation of rate of heat release by means of oxygen consumption measurements, Fire and Materials 4 (2) (1980) 61–65.

[168] R. N. Walters, S. M. Hackett, R. E. Lyon, Heats of combustion of high temperature polymers, Fire and Materials 24 (5) (2000) 245–252.

[169] A. Tewarson, Generation of heat and gaseous, liquid, and solid products in fires, in: P. DiNenno (Ed.), SFPE Handbook of Fire Protection Engineering, 4th Edition, National Fire Protection Association, 2008, pp. 109–194.

[170] M. Elia, T. McDonald, A. Crisp, Errors in measurements of CO_2 with the use of drying agents, Clinica Chimica Acta 158 (3) (1986) 237–244.

[171] C. R. White, S. J. Portugal, G. R. Martin, P. J. Butler, Respirometry: Anhydrous Drierite equilibrates with carbon dioxide and increases washout times, Physiological and Biochemical Zoology 79 (5) (2006) 977–980.

[172] W. L. Grosshandler, RadCal: A narrow-band model for radiation calculations in a combustion, environment, Tech. Rep. TN1402, NIST (1993).